Dynamics and microstructure of colloidal complex fluids: A lattice Boltzmann study

Eunhye Kim

Thesis submitted in for the degree of Doctor of Philosophy
School of Physics
University of Edinburgh

2009

Abstract

The lattice Boltzmann (LB) method is a versatile way to model complex fluids with hydrodynamic interactions through solving the Navier-Stokes equations. It is well-known that the role of hydrodynamic interactions is ignorable in studying the Boltzmann equilibrium of colloidal (Brownian) particles. However, full hydrodynamic interactions play an important role in their dynamics. In the LB framework for moving colloids, the "bounce-back on links" method is used to calculate the hydrodynamic forces. In this thesis, three kinds of colloidal complex fluids with full hydrodynamic interactions are simulated by lattice Boltzmann methods: colloids in a binary fluid, magnetic colloids in a single fluid and magnetic colloids in a binary fluid.

First, we have done extensive simulations of nanoparticles in a binary fluid, following up previous work[1] which predicted formation of a "bijel" (bicontinuous interfacially jammed emulsion gel) in symmetric fluid quenches. Our work in this thesis focuses on the analysis of the dynamics after nanoparticles become arrested on the fluid-fluid interfaces under conditions varying from a symmetric quench to a strongly asymmetric quench. Although these new simulations extend the time window studied by a factor of two, slow domain growth is still observed. Our new analyses address the mechanics of the slow residual dynamics which involves cooperative motion of the nanoparticles at the fluid-fluid interfaces.

The second topic is the LB simulation of colloidal ferrofluids to see the effect of full hydrodynamic interactions among magnetic colloids. The main focus is on how the hydrodynamic interaction affects both the equilibrium dynamics of these dipolar systems and also their transient dynamics to form clusters. Numerically, magnetic colloids are implemented with the long-range dipolar interactions described by Ewald summation. To check the effect of full hydrodynamic interactions, Brownian dynamics without any hydrodynamic interaction has been done for comparison: Monte Carlo results are also reported. We confirm that our LB generates the Boltzmann distribution for static equilibrium properties, by comparison with these methods. However, the equilibrium dynamics is altered: hydrodynamic interactions make the structural relaxations slower in both the short-time and the long-time regime. This slow relaxation rate is also found for transient motions.

The third topic addresses magnetic colloids in a binary fluid. In contrast with the preceding two systems which correspond directly to laboratory experiments, this last system is so far only predicted by the LB results in this thesis. To explore this hypothetical new material by the LB method, the basic structures are investigated in terms of both domain growth morphology and the arrangement of magnetic colloids. Under conditions varying from a symmetric quench to an asymmetric quench, a chainlike arrangement is observed for dipoles jammed on the surfaces, but the basic morphology of domains is still maintained regardless of the dipolar strength. In addition, applying external field affects the morphology of domains and the stability of domain structures.

Declaration

I do hereby declare that this thesis was composed by myself and that the work described within is my own, except where explicitly stated otherwise.

Eunhye Kim
March 2009

Acknowledgements

I would sincerely like to thank my first supervisor Prof. Mike Cates for all his support, encouragement and good ideas during my PhD period. Without his enthusiasm, our projects and this thesis would never have been completed. I would also like to express my gratitude to my second supervisor Dr. Kevin Stratford, who is always caring to me, for his all support and encouragement. I would like to say that I have been very happy to work with them.

I am deeply indebted to the Scottish Universities Physics Alliance and the Overseas Research Students Award Scheme for scholarships. I would like to thank Mrs. Avril Manners (director of Grad School SUPA) for all support.

I wish to thank Dr. Philip Camp, who always opens his mind toward students, for encouragement and discussion about the research of magnetic colloids. It is a pleasure to thank experimentalists in the soft matter group: Dr. Paul Clegg, Dr. Eva Herzig and Dr. Kathryn White for fruitful discussions about bijel; Miss Danielle Van't Zand and Dr. Laurence Wilson for exciting laboratory tours.

Many thanks to Mrs. Jane Patterson, who is mother to postgraduates in School of Physics, for all her support. Thanks to many friends in Physics. I would like to thank Neelofer and Dilek for your kindness. Thank Iain for the correction of my English writing and feeding me with cakes and meals, Toni (as the regular caffeine sponsor during my PhD) for a lot of entertainment and kindness, Iris (as the suspicious dancing teacher) for kindness and all members of the Korean Society badminton club for energetic game.

I am grateful to the Kempton family, Emily and Annelise, who are invaluable in my Edinburgh life.

I wish to express my warm and sincere thanks to Prof. Bongsoo Kim, Prof. Sung Jong Lee and Prof. Kyunghee Lui for encouragement and all support.

Lastly, huge thanks to father and mother for their love, and thanks to other twelve families for being together. I would sincerely like to thank Sangha Jung-Am for the guidance in my life.

Contents

List of Figures

List of Tables

Chapter 1

Introduction

Complex fluids[16, 17] are single or multiphase fluids whose components couple different length scales. Many are composite materials having internal coexistence of two or more than two phases, e.g. solid-liquid, liquid-gas, liquid-liquid; familiar examples are found broadly in our daily products such as foods, shampoo and cosmetics. From mixing different materials, complex fluids arise with distinctive microstructures which lead to distinguished physical properties macroscopically and mechanically. The simplest examples, containing two different local phases, are colloidal dispersions, emulsions and foams.

Colloidal dispersions are one of the archetypes of complex fluids. They are solid/liquid composites which have two different scales: solid colloids with size about 10^{-6}m $\sim$ 10^{-9}m, and a liquid molecule that has a length less than 10^{-9}m. Dilute colloids in a thermal solvent are dispersed, obeying Brownian motion as described by the Stokes-Einstein relation. Common products using colloidal dispersions are paint and ink. The properties of colloidal dispersions depend on the interaction potentials of the colloids. By designing these interaction potentials, their structure and dynamics are controllable: for example, the particular aggregation structure, "nose-to-tail" or "head-to-tail", is found for magnetic colloids with long-range dipolar interactions. (In this Thesis, simulations using magnetic colloids have been done and will be discussed later.) The second example, emulsions, consist of two immiscible liquids such as water/oil and such composites are found as butter and cream. By agitating two liquids, a homogeneous microstructure can arise where one liquid disperses in the other liquid. Mechanically, emulsions are still flexible, but more sticky than the original two liquids. For stabilisation of emulsions, usually surfactants such as amphiphilic molecules are added, to reduce the interfacial tension of fluid-fluid interfaces. Instead of the addition of surfactants, colloids can make oil/water emulsions stabilised, forming "Pickering emulsions". This colloid-stabilised emulsion can be simulated by our LB (lattice Boltzmann) method; this will be discussed later in detail. In contrast with the composition of emulsions, foams have gas bubbles dispersed in a liquid or solid. (An example is beer foams.)

Due to the diverse utilities of complex fluids, predictions for novel materials have been of great interests for a long time. Recently, after developing the numerical methods and the computational hardware, simulations for complex fluids have contributed to design for novel materials and understanding their physics.

In this Thesis, colloidal systems including full hydrodynamic interactions are investigated via lattice Boltzmann methods: colloids (or magnetic colloids) are studied in a single or binary fluid. Among many competing numerical methods[18, 19], most ignore hydrodynamic interactions in colloidal systems, although indirect hydrodynamic forces can be introduced in Brownian dynamics methods[19, 20, 21], and Stokesian dynamics introduces many-body hydrodynamic interactions when solving the Langevin equation[22, 23]. The lattice Boltzmann framework is very efficient when adapted for simulations of composite complex fluid systems while including many-body hydrodynamic interactions, e.g. a binary fluid[24, 25], amphiphilic fluids[26, 27], liquid crystal[28], or colloids in a binary fluid[12].

The following section will discuss the experimental systems of colloidal complex fluids considered in this Thesis. First, colloid-stabilised emulsions will be discussed including a special emulsion "bijel" whose structure was initially predicted by LB simulation[1]. Secondly, magnetic colloids in a single fluid (so-called "colloidal ferrofluids") will be discussed to study the effect of long-range dipolar interactions. Finally, the prediction of a novel complex fluid (the magnetic bijel) will be briefly discussed.

1.1 Pickering emulsions and "bijels"

Pickering emulsions[29, 30, 31] are stabilised by solid particles and characterised by the contact angle θ_{ow} of three-phase contact for the particle at oil-water interfaces shown in Figure 1.1(a). The contact angle θ_{ow} is defined by three interfacial tensions: γ_{po} (particle-oil), γ_{pw} (particle-water) and γ_{ow} (oil-water), and explained by Young's equation[32]: $\cos\theta_{ow} = (\gamma_{po} - \gamma_{pw})/\gamma_{ow}$. This contact angle can be determined from the hydrophobic or hydrophilic property of particles. For hydrophilic particles, θ_{ow} is less than 90°, while $\theta_{ow} > 90^\circ$ is observed for hydrophobic particles at oil-water interfaces. These situations for particles partially absorbed at interfaces are called "non-neutral wetting". For 90° wetting angle, it is called "neutral wetting". Neutral wetting particles are optimal for stabilising Pickering emulsions.

Removing a particle from oil-water interfaces requires an energy depending on contact angle θ_{ow}[33]:

$$\Delta E = \pi r^2 \gamma_{ow} (1 \pm \cos\theta_{ow})^2, \tag{1.1}$$

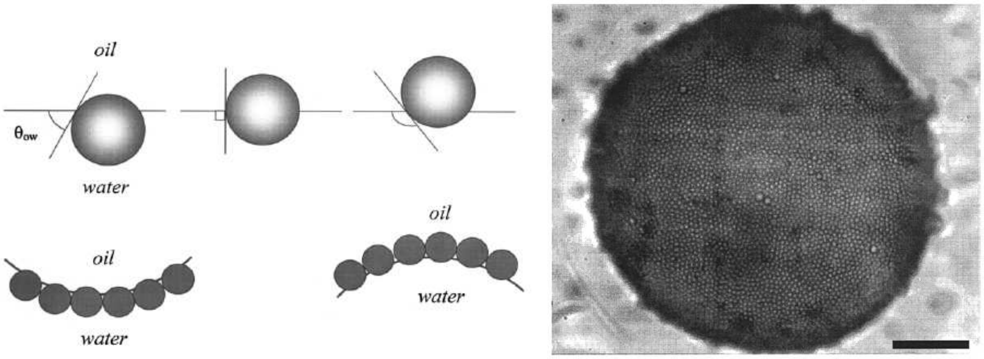

(a) (b)

Figure 1.1: (a) Contact angle (from [2]). Three different angles, $\theta_{ow} < 90°$, $\theta_{ow} = 90°$ and $\theta_{ow} > 90°$ are shown from left to right. The interfacial curvature is determined by a particle's contact angle. (b) Microscopy image of a Pickering emulsion (from [3]), a water-in-cyclohexane droplet stabilised by monodisperse particles of radius 1.6μm. The scale bar on the bottom of right corresponds to 50μm.

where the sign in the bracket is positive for removal into oil and negative for removal into water. From this equation, the energy for a neutral wetting particle can be estimated: for 0.5μm as a radius of particle and $\gamma_{ow} = 50$mN/m as oil-water interfacial tension, ΔE is obtained as $10^7 k_B T$ which means this particle is irreversibly absorbed at interfaces. Figure 1.1(b) shows an optical image of a Pickering emulsion droplet in a lab experiment; a single layer of particles is seen on the surface.

Using this idea of colloids at the fluid-fluid interfaces, a bicontinuous emulsion, the so-called "bijel" (bicontinuous interfacially jammed emulsion gel), was achieved in lab experiments[4, 34, 35, 36]. Initially, the structure of the bijel was predicted by LB simulation[1] using neutral wetting nanoparticles in a quench of two well-mixed fluids at equal volume fraction. Then the arrested fluids were monitored with a particular morphology: each fluid percolates other and jammed colloids are observed at the fluid-fluid interfaces. Moreover, this LB prediction also gave insight on the mechanism to form the arrested morphology; the experimental work confirms the mechanism suggested by LB simulations. Figure 1.2 shows the time-evolution of bijel formation in a recent experiment; after a quench of the single-phase fluids, the phase separation sweeps out domains with colloids trapped at interfaces, and then coalescing domains result in decreasing surface area and particles jammed together at interfaces. However, in contrast with the experimental bijel which maintains a stable formation during a few weeks, the LB simulations failed to reach the fully arrested state. Instead, slowly growing domains were observed.

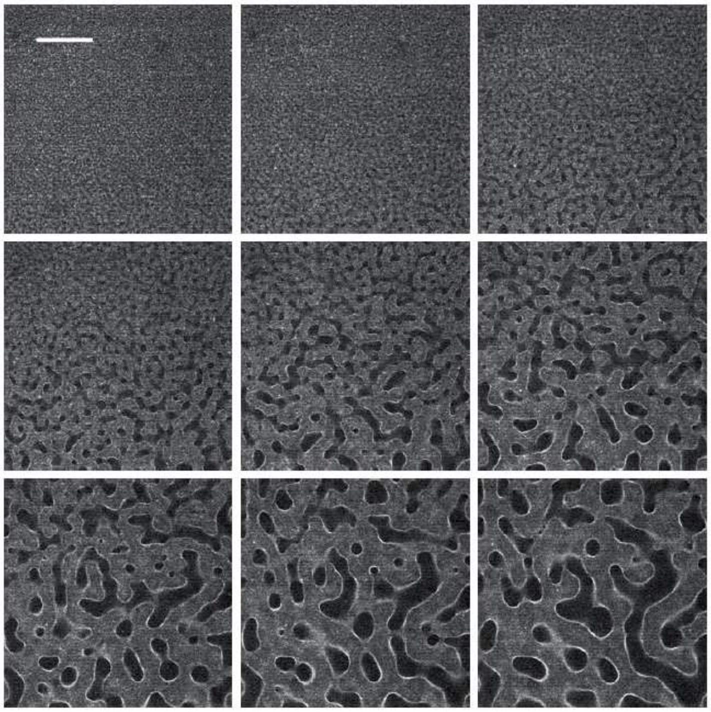

Figure 1.2: Time-evolution of bijel formation in experiment[4]: fluorescence confocal microscopy images of a 2,6-lutidine-water composition with 2% particle fraction. The time interval between images is 0.7s. White is particles while dark parts are liquids: the domains are distinguished by the difference in the shade of grey. The scale bar corresponds to 100μm.

In this Thesis, we will present new LB simulations that extend the previous study[1]. Especially, our extended work focuses on analyses of the dynamics after nanoparticles are arrested on the fluid-fluid interfaces, under conditions ranging from a symmetric quench to a strong asymmetric quench. Besides, through the new analyses, we will interpret the mechanism of the slow residual dynamics.

1.2 Colloidal ferrofluids

Magnetic colloids[37] of nano-sized diameter have a permanent magnet core, such as cobalt, iron oxide or magnetite (Fe_3O_4), coated with a molecular layer, e.g. a surfactant; the size of this magnet core determines the strength of dipolar moment. Principally due to such a small particle size, thermal fluctuation of a solvent maintains particles suspended, showing Brownian motion despite the long-range dipolar interactions, and the coated layer prevents particles to stick to each other.

According to the alignment of magnetic spins (or magnetic moments) of atoms in a material, its magnetic properties are determined as either ferromagnetic or paramagnetic; in ferromagnetism, magnetic spins have a long-range ordering, while any long-range ordering is not observed in paramagnetism. Basically bulk ferromagnetic materials consist of multi-crystalline domains to minimise internal field energy[38]. However, if a sample of material is of nanometer scale, a single crystalline domain is found; the critical size between a single magnetic domain and multiple domains is theoretically predicted by Kittel as around 15nm[39]. In contrast to multiple domains with zero net magnetisation, this small crystallite is magnetised in one direction with a finite value of the magnetic domain moment; the long-range dipolar interactions originate from magnetic fields generated by these magnetic domain moments. In simulations, this magnetic domain moment is chosen to model magnetic colloids. (Section 2.4.2. will discuss this in detail.)

For magnetic colloids in a thermal solvent, thermal energy can change the direction of their magnetic domain moment (magnetic colloids undergo Brownian motion) but is not high enough to fluctuate magnetic spins of individual atoms. In addition, magnetic domain moments respond to an external field. In terms of the macroscopical behaviour of magnetic colloids, their motion shows a similar behaviour to paramagnetism; this is called "superparamagnetism"[37, 40, 41], and arises at any temperature below the Curie temperature. In the absence of an external field, magnetic colloids are free to rotate; after applying the external field, their magnetic diplar moment tend to align along the direction of the external field although individual magnetic spins of atoms are not directly affected by the external field. The saturation magnetisation under the external field can be explained by Langevin theory according to the ratio of thermal fluctuation and strength of magnetic field acting on magnetic particles.

Ferromagnetic colloids in a carrier liquid, named "colloidal ferrofluids"[42, 43] show particular aggregation structures of the magnetic colloids, and unusual phase behaviour due to long-range dipolar interactions, even in the absence of external field. In 1970, de Gennes and Pincus[44] discussed the trend of aggregated structures like chains and predicted a van der Waals-like phase diagram. This tendency to form chainlike structure is the key issue in studies of ferrofluids phase equilibrium and dynamics. In experiment, chain structures were first observed by Hess and Parker using electron microscopy[45], but the quantitative experiments for ferromagnetic colloids made by iron and magnetite have been done by Philipse and co-works[46, 47, 5] using cryogenic transmission electron microscopy (cryo-TEM). Figure 1.3 presents the recent measurement of aggregated structures in 2 dimensions by Klokkenburg *et al.*; on increasing pair interaction energy between magnetic particles, chains and rings are monitored in the cases B and C, whereas clusters are also seen at A with lower interaction energy.

While there are only a few observations of microstructures in experiments, many

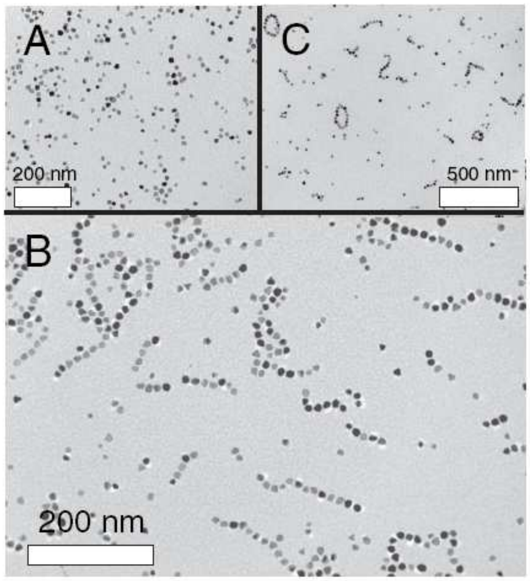

Figure 1.3: The cryo-TEM images of magnetite dispersions[5]. A: surface fraction is 0.14 and pair interaction energy is $-4k_BT$. (The surface fraction is defined as NA_p/A_I, where N is the total number of particles in the images, A_p is the cross-sectional area of a particle, and A_I is the total area of all images.) B and C are $-9k_BT$ for pair interaction energy with surface fraction 0.14 and 0.03 respectively.

numerical works have confirmed the structural characteristics in both 2D and 3D. To study ferrofluids, a simple interaction potential is introduced as the sum of a short-range interaction and a long-range interaction; for spherical magnetic colloids, the interaction of two magnetic colloids with point dipolar moments, $\mathbf{s}_i$ and $\mathbf{s}_j$, is given as

$$U(\mathbf{r}_{ij}; \mathbf{s}_i, \mathbf{s}_j) = U^{SR}(\mathbf{r}_{ij}) + \frac{1}{r_{ij}^3}\left[\mathbf{s}_i \cdot \mathbf{s}_j - \frac{3(\mathbf{s}_i \cdot \mathbf{r}_{ij})(\mathbf{s}_j \cdot \mathbf{r}_{ij})}{r_{ij}^2}\right], \tag{1.2}$$

where $\mathbf{r}_{ij}$ is the distance of centre-to-centre of magnetic colloids and U^{SR} is the short-range potential. In ferrofluids, this short-range interaction influences the phase diagram. Three kinds are mostly used: hard-sphere, soft-sphere and Lennard-Jones potentials. For analytical calculation, the dipolar hard-sphere (DHS) [48, 49] is taken as a simple model. The other models which consider soft-repulsive short-range potential are the dipolar soft-sphere (DSS) [50, 51, 52, 53] and the Stockmayer fluid (SMF) [54, 55]. An aggregate structure based on "nose-to-tail" originates from the long-range dipolar interactions which strongly depend on the directions of dipolar moment: in the simple case of DHS, two close dipoles aligned "nose-to-tail" have a much lower energy ($-2\mu^2/d^3$) than aligning side by side with antiparallel moments ($-\mu^2/d^3$). (Here, μ is the strength of the dipole moment and d is the particle diameter.) That means dipoles prefer the “nose-to-tail” structure energetically.

Figure 1.4 presents the phase diagram for microstructures of DHS according to the density and the strength of the dipole moment. In bulk ferrofluids, similar phase behaviour to nonmagnetic colloids and atomic models is found for weak dipolar strength with the range $\mu^2/k_BTd^3 < 1$. This has been confirmed in experiments on citrate coated maghemite particles[56]. In simulations, dispersion of monomers are clearly observed at $\mu^2/k_BTd^3 < 2$. In analytical calculations, mean-field model and simple statistical models[6, 57, 58, 43] can predict magnetic properties such as susceptibility at weak dipolar strength and high density. But for strong dipole moment, the anisotropic term of the dipolar interactions increases so that this mean-field approximation is not available. Around $\mu^2/k_BTd^3 \geq 2.5$ at low densities[48, 8], magnetic colloids start to form small chains; on increasing the density, the fraction of chains and the cluster size increase. At $\rho^* \simeq 0.06$, a network is formed with long chains. At higher density $\rho^* \geq 0.2$, the phase becomes like the normal liquid instead of the network structure. Above $\rho^* \geq 0.6$, the system has a ferroelectric phase[8] which has long-range orientational orderings[9].

Applying these characteristics, magnetic colloids have been very significant material, for modern data recording and storage devices, e.g. music tape and computer hard-disks, for a long time. Recently, formulations using ferrofluids have been of great interest for biotechnological applications such as cancer detection[59, 60, 61] and as a carrier for drug delivery[59, 62]. Especially in biomedical applications like drug delivery systems, hydrodynamics plays an important role. However, none of many numerical studies on ferrofluids include full hydrodynamic interactions. In contrast to other numerical methods which have been used to simulate colloidal ferrofluids, LB provides the full calculation of hydrodynamics of colloids. In Chapter 4, we will present LB simulations for colloidal ferrofluids, comparing with the simulations of Brownian dynamics and Monte Carlo and we will discuss the role of hydrodynamic interactions in both equilibrium and nonequilibrium situations.

1.3 Prediction of a new composite

In Chapter 5 of this Thesis, we present simulations of new complex fluids, comprising magnetic colloids in a binary fluid mixture, which experiences spinodal decomposition. This composite has not yet been implemented in lab experiment, but magnetic Pickering emulsions have been made by Meller *et al.*[63], using paramagnetic colloids. To explore this new composite, we quantify the same basic properties as are measured in the other two systems of this Thesis; especially, their microstructures, such as morphology of fluid domains and dipolar structure of magnetic colloids, are one of the most interesting issues in this study. Additionally, the effects of external fields will be discussed in terms

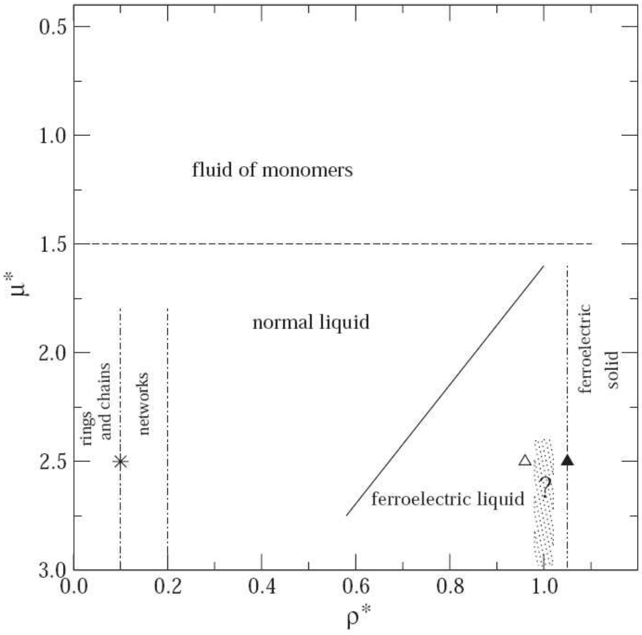

Figure 1.4: Schematic phase diagram of 3D dipolar hard-sphere[6, 7] in simulations. The parameters on each axes are the reduced density and the reduced dipolar moment defined as $\rho^* = N\sigma^3/V$ (N: number of particles, V: volume of the system, σ: characteristic length of the hard core) and $\mu^* = (\mu^2/\sigma^3 k_B T)^{1/2}$. The dimensionless dipolar coupling constant is defined as $\lambda = \mu^{*2}$. The star symbol indicates the critical point of a condensation[8, 9]. The open triangle marks the limits of mechanical stability of the bct(body-centered tetragonal) structure and the filled triangle signs that of the fcc (face-centered-cubic) structure[10].

of the stability conditions for stable emulsions, as linking to the experiment work[63].

1.4 Thesis layout

To investigate colloidal complex fluids, described in the above introduction, the next chapter (Chapter 2) will introduce the simulation methods including the lattice Boltzmann (LB) framework, from the basic single fluids to colloids in LB, and the interacting potentials to design magnetic or non-magnetic colloids.

The next three chapters will mostly present the simulation results found by LB simulations. In Chapter 3, the simulation results for “colloids in a binary fluid” will be discussed through extensive analyses of slow dynamics after particles are arrested at interfaces. Chapter 4 will discuss the hydrodynamic interactions in colloidal ferrofluids in equilibrium and nonequilibrium, comparing with the data from BD and MC. Transient motion to form clusters will be also discussed to quantify the statistics for cluster size at various conditions controlled the strength of magnetic moment and particle fraction. In Chapter 5, we will present the simulation results of magnetic colloids in a binary fluid and some discussions.

Lastly, Chapter 6 summarises our LB simulation results and discusses further works possible in the future.

Chapter 2

Simulation Methods

This chapter describes the numerical methods used: the LB framework[64], solid particles in LB and interaction potentials for particles. All work in this thesis has been done using the LB code *Ludwig*[11] which includes the LB scheme not only for a single fluid and a binary fluid with and without particles, but also for thermally fluctuating fluids to implement the Brownian motion of particles. For magnetic colloids, the Ewald summation is set up within *Ludwig* for the long-range dipolar interactions in a periodic boundary box.

In LB, distribution functions for discrete fluid particles on a lattice provide an efficient way to solve the kinetic equations of fluids. The lattice approach can also be easily developed for parallel computing. Section 2.1 below will discuss the simple LB idea in Stokes flow for a single fluid, and then fluctuating LB for thermal fluids is also discussed. In Section 2.2, the theoretical approach for a binary fluid will be explained and then the LB framework including the kinetic equation for a binary fluid will be shown.

In Section 2.3, the description of colloids on the lattice will be discussed and then the bounce-back on links algorithm will be shown to characterise moving colloids in lattice fluids. The lubrication correction will be discussed for colloids and the updating algorithm for colloidal motion will be shown at the end of this section.

Finally, Section 2.4 will talk about the interaction potentials for the short-range and long-range interactions. The modified soft-core potential for short-range interaction will be discussed. For magnetic colloids, the long-range dipolar interactions are derived from the external field of a magnetic source. For a periodic boundary system, the Ewald summation is used to calculate the long-range dipolar interaction.

2.1 Kinetics of a fluid and lattice Boltzmann

The fluid motion represents the flow of physical quantities[65], e.g. density, momentum and energy, in time and space. A closed system obeys conservation laws for the total density and the total momentum. The continuity equation describes the time-dependent local density flow:

$$\frac{\partial \rho}{\partial t} + \nabla \cdot (\rho \mathbf{v}) = 0 \tag{2.1}$$

where ρ is a local density at $(\mathbf{r}, t)$ and $\mathbf{v}$ is the velocity. The momentum transfer in an incompressible viscous fluid is described by the Navier-Stokes equation,

$$\rho\left(\partial_t \mathbf{v} + (\mathbf{v} \cdot \nabla)\mathbf{v}\right) = \eta \nabla^2 \mathbf{v} - \nabla p + \mathbf{f}. \tag{2.2}$$

Here η is a shear viscosity and p is a pressure. Incompressible fluids in the absence of a body force (e.g. gravity) have zero as the force term $\mathbf{f}$. However to deal with the fluctuating fluid or a binary fluid, the space dependent force tensor term $\mathbf{f}$ has to be set up to be nonzero. For fluctuating fluids, the random stress is added in terms of a tensor whose divergence is $\mathbf{f}$. In the case of a binary fluid, the term $\mathbf{f}$ is from interfaces of fluids. These will be shown in following consecutive sections for fluctuating fluids and a binary fluid.

Using the isothermal and incompressible conditions, the space differential term in equation (2.2) is rewritten using the stress tensor $\Pi_{\alpha\beta}$ in Cartesian coordinates:

$$\Pi_{\alpha\beta} = \rho v_\alpha v_\beta + p\delta_{\alpha\beta} - \eta_{\alpha\beta\gamma\epsilon} \nabla_\gamma v_\epsilon. \tag{2.3}$$

The subscripts, α, β and γ denote the Cartesian coordinate components. The pressure $p = \rho c_s^2$, where c_s is a speed of sound and $c_s = 1/\sqrt{3}$ in lattice units. Tensor viscosities $\eta_{\alpha\beta\gamma\epsilon}$ for Newtonian fluid are given as $\eta_{\alpha\beta\gamma\epsilon} = \eta\delta_{\alpha\gamma}\delta_{\beta\epsilon} + \eta\delta_{\beta\gamma}\delta_{\alpha\epsilon} + \zeta\delta_{\alpha\beta}\delta_{\gamma\epsilon}$ where ζ is a bulk viscosity, η is a shear viscosity and $\delta_{\alpha\beta}$ is the Kronecker delta.

Therefore, equation (2.2) combined with the stress tensor $\Pi_{\alpha\beta}$ is

$$\frac{\partial \rho v_\alpha}{\partial t} + \nabla_\beta \Pi_{\alpha\beta} = f_\alpha. \tag{2.4}$$

Solving the continuous equations (2.1) and (2.2) or (2.4) characterises the fluid motion. Numerically, LB gives the solutions of these equations by following the route which can be defined from the pseudo particles on lattice points. On each lattice point, one defines a distribution function $f_i(\mathbf{r}, t)$ associated with the discrete velocities $\mathbf{c}_i$ of these particles. For one time step Δt, the displacement $\mathbf{c}_i \Delta t$ represents either the displacement to neighbour lattice sites or the null displacement.

This spatially discrete approach to fluid dynamics on underlying grids has to satisfy symmetry conditions in order to recover hydrodynamic behaviour with full rotational symmetry of space[66]. To satisfy the appropriate symmetries, the moments of the set of lattice vector $\mathbf{c}_i$ must obey

$$\begin{aligned}
&\sum_{i=0}^{n} \omega_i = 1, \\
&\sum_{i=0}^{n} \omega_i c_{i\alpha} = 0, \\
&\sum_{i=0}^{n} \omega_i c_{i\alpha} c_{i\beta} = \rho c_s^2 \delta_{\alpha\beta}, \\
&\sum_{i=0}^{n} \omega_i c_{i\alpha} c_{i\beta} c_{i\gamma} = 0, \\
&\sum_{i=0}^{n} \omega_i c_{i\alpha} c_{i\beta} c_{i\gamma} c_{i\epsilon} = (\rho c_s^2)^2 (\delta_{\alpha\beta}\delta_{\gamma\epsilon} + \delta_{\alpha\gamma}\delta_{\beta\epsilon} + \delta_{\alpha\epsilon}\delta_{\beta\gamma}).
\end{aligned}$$

Here, ω_i is the quadrature weight for each velocity vector $\mathbf{c}_i$.

The type of LB model is denoted by $DdQn$ which indicates $d-$dimensions and an n discrete velocity vector set which can include the zero velocity. The most frequent models are $D1Q3$, $D2Q9$, $D3Q15$ and $D3Q19$. Figure 2.1 shows the velocity vector set in $D3Q15$ and $D3Q19$, frequently used models in 3D. The velocity vectors including the zero velocity and the weight factors in $D3Q15$ and $D3Q19$ respectively are given as

$$\begin{aligned}
\mathbf{c}_i &= (\mathbf{c}_1, \mathbf{c}_2, \mathbf{c}_3, \mathbf{c}_4, \mathbf{c}_5, \mathbf{c}_6, \mathbf{c}_7, \mathbf{c}_8, \mathbf{c}_9, \mathbf{c}_{10}, \mathbf{c}_{11}, \mathbf{c}_{12}, \mathbf{c}_{13}, \mathbf{c}_{14}, \mathbf{c}_{15}) \\
&= \begin{pmatrix}
0 & 1 & 1 & 1 & 1 & 1 & 0 & 0 & 0 & 0 & -1 & -1 & -1 & -1 & -1 \\
0 & 1 & 1 & 0 & -1 & -1 & 1 & 0 & 0 & -1 & 1 & 1 & 0 & -1 & -1 \\
0 & 1 & -1 & 0 & 1 & -1 & 0 & 1 & -1 & 0 & 1 & -1 & 0 & 1 & -1
\end{pmatrix}, \\
\omega_i &= \left(\frac{16}{72}, \frac{1}{72}, \frac{1}{72}, \frac{8}{72}, \frac{1}{72}, \frac{1}{72}, \frac{8}{72}, \frac{8}{72}, \frac{8}{72}, \frac{8}{72}, \frac{1}{72}, \frac{1}{72}, \frac{8}{72}, \frac{1}{72}, \frac{1}{72}\right),
\end{aligned}$$

and

$$\begin{aligned}
\mathbf{c}_i &= (\mathbf{c}_1, \mathbf{c}_2, \mathbf{c}_3, \mathbf{c}_4, \mathbf{c}_5, \mathbf{c}_6, \mathbf{c}_7, \mathbf{c}_8, \mathbf{c}_9, \mathbf{c}_{10}, \mathbf{c}_{11}, \mathbf{c}_{12}, \mathbf{c}_{13}, \mathbf{c}_{14}, \mathbf{c}_{15}, \mathbf{c}_{16}, \mathbf{c}_{17}, \mathbf{c}_{18}, \mathbf{c}_{19}) \\
&= \begin{pmatrix}
0 & 1 & 1 & 1 & 1 & 1 & 0 & 0 & 0 & 0 & 0 & 0 & 0 & 0 & -1 & -1 & -1 & -1 & -1 \\
0 & 1 & 0 & 0 & 0 & -1 & 1 & 1 & 1 & 0 & 0 & -1 & -1 & -1 & 1 & 0 & 0 & 0 & -1 \\
0 & 0 & 1 & 0 & -1 & 0 & 1 & 0 & -1 & 1 & -1 & 1 & 0 & -1 & 0 & 1 & 0 & -1 & 0
\end{pmatrix}, \\
\omega_i &= \left(\frac{12}{36}, \frac{1}{36}, \frac{1}{36}, \frac{2}{36}, \frac{1}{36}, \frac{1}{36}, \frac{1}{36}, \frac{2}{36}, \frac{1}{36}, \frac{2}{36}, \frac{2}{36}, \frac{1}{36}, \frac{2}{36}, \frac{1}{36}, \frac{1}{36}, \frac{1}{36}, \frac{2}{36}, \frac{1}{36}, \frac{1}{36}\right).
\end{aligned}$$

Using the velocity distribution function $f_i(\mathbf{r}, t)$, the local physical values in equation

(2.1)-(2.4) can be defined:

$$\rho(\mathbf{r},t) = \sum_i f_i(\mathbf{r},t), \tag{2.5}$$

$$\rho v_\alpha(\mathbf{r},t) = \sum_i f_i(\mathbf{r},t)c_{i\alpha}, \tag{2.6}$$

$$\Pi_{\alpha\beta}(\mathbf{r},t) = \sum_i f_i(\mathbf{r},t)c_{i\alpha}c_{i\beta}, \tag{2.7}$$

where $c_{i\alpha}c_{i\beta}$ is a dyadic product.

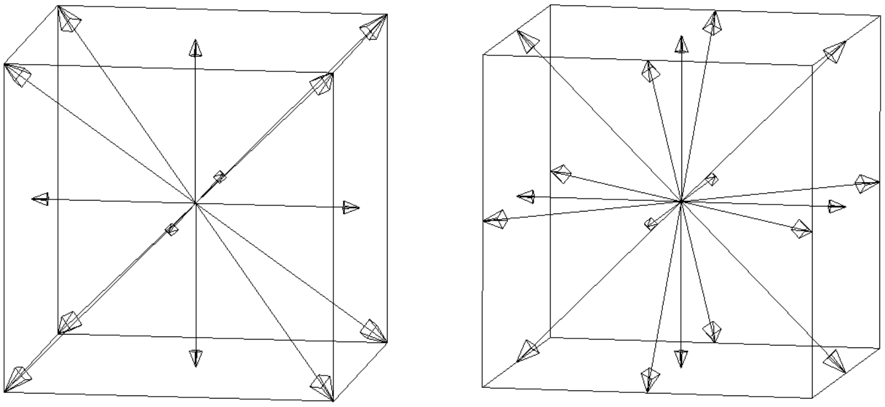

(a) $D3Q15$ (b) $D3Q19$

Figure 2.1: The lattice Boltzmann models in 3D (from [11]).

2.1.1 Dynamic equation of LB for a single fluid

With the local values defined by f_i, the dynamic equation for the computation is constructed by two parts, collision and propagation:

$$f_i(\mathbf{r}+\mathbf{c}_i\Delta t, t+\Delta t) - f_i(\mathbf{r},t) = \sum_j L_{ij}(f_j(\mathbf{r},t) - f_j^{eq}(\mathbf{r},t)). \tag{2.8}$$

The right-side term is the collision process. The L_{ij} is a collision matrix often chosen as the lattice BGK matrix δ_{ij}/τ with a single relaxation time τ. Its relaxation time τ determines the viscosity η as $\eta = (2\tau - 1)\rho/6$. After each time step, the local f_i is relaxed towards the distribution which describes the local equilibrium. The $f_j^{eq}(\mathbf{r},t)$ is an equilibrium distribution which depends on the local values of $\rho(\mathbf{r},t)$ and $\mathbf{v}(\mathbf{r},t)$ written here as

$$f_j^{eq} = \omega_j \left(\rho + \frac{\rho v_\alpha c_{j\alpha}}{c_s^2} + \frac{\rho v_\alpha v_\beta Q_{j\alpha\beta}}{2c_s^4} \right), \tag{2.9}$$

where $Q_{j\alpha\beta}$ is the kinetic projector, defined as $Q_{j\alpha\beta} = c_{j\alpha}c_{j\beta} - p\delta_{\alpha\beta} = c_{j\alpha}c_{j\beta} - \rho c_s^2 \delta_{\alpha\beta}$. More generally, instead of choosing the BGK collision matrix, δ_{ij}/τ, a multiple-relaxation-time operator[67] is used for the lattice Boltzmann equation, because different relaxation times for each mode can achieve more stability; using the conservation laws for mass and momentum, two or more relaxation times can be chosen via the stress tensor and ghost modes, described in next section for fluctuating LB.

The second part of the dynamic evolution is the propagation on the left hand side of equation (2.8), $f_i(\mathbf{r}+\mathbf{c}_i\Delta t, t+\Delta t) - f_i(\mathbf{r}, t)$, which means each distribution function f_i passes along the next lattice links as $\mathbf{c}_i\Delta t$ at each time step.

2.1.2 Fluctuating lattice Boltzmann

Brownian colloidal particles in thermal solvents are set in motion by random forces generated from the surrounding fluctuating fluids. These random forces acting on particles in LB were first described by Ladd[68]. He introduced the LB equation containing the stochastic term $\xi_i^H(\mathbf{r}, t)$ to represent thermal fluctuation:

$$f_i(\mathbf{r}+\mathbf{c}_i\Delta t, t+\Delta t) = f_i(\mathbf{r}, t) + L_{ij}(f_i(\mathbf{r}, t) - f_i^0(\mathbf{r}, t)) + \xi_i^H(\mathbf{r}, t), \tag{2.10}$$

where ξ_i^H is only determined by the fluctuating stress moment $\hat{S}_{\alpha\beta}(\mathbf{r}, t) = \sum_i \xi_i^H c_{i\alpha}c_{i\beta}$. Recalling equation (2.3), the shear tensor including $\hat{S}_{\alpha\beta}$ is rewritten as

$$\Pi_{\alpha\beta} = \rho v_\alpha v_\beta + p\delta_{\alpha\beta} - \eta_{\alpha\beta\gamma\epsilon}\nabla_\gamma v_\epsilon - \hat{S}_{\alpha\beta}. \tag{2.11}$$

The $\hat{S}_{\alpha\beta}$ is a random Gaussian distribution whose mean is zero and variance satisfies with the fluctuation-dissipation theorem (FDT), $\langle \hat{S}_{\alpha\beta}(\mathbf{r}, t)\hat{S}_{\alpha\beta}(\mathbf{r}', t')\rangle = 2k_B T\eta_{\alpha\beta\gamma\epsilon}\delta(\mathbf{r}-\mathbf{r}')\delta(\mathbf{t}-\mathbf{t}')$. In the $D3Q19$ model used here, Ladd's algorithm only applies noise to 10 hydrodynamic quantities: one is the local density ρ, 3 are the momentum components in x, y, and z, and 6 modes are entries in the stress tensor which is symmetric. This leaves 9 degrees of freedom undefined; these are called "ghost" modes. However, the FDT in Ladd's approach is only satisfied by the continuous model with hydrodynamic limit $q \to 0$ which corresponds to the infinite size of a colloidal particle. Moreover, in a fluid without particles, the algorithm by Ladd fails to obtain the Boltzmann statistics on the local equilibrium of physical values, e.g. density, momentum and stress tensor, at nonzero q[69].

To improve this fault, Adhikari *et al.* accomplished the fully consistent equations including the fluctuating nonlinear hydrodynamic modes which are “ghosts”. Adhikari *et al.*[69] introduce noise for the full set.

Therefore, the dynamic equation for the improved FLB is completed by adding the extra stochastic term ξ_i^G contributed by the ghost modes in equation (2.10):

$$f_i(\mathbf{r}+\mathbf{c}_i\Delta t, t+\Delta t) = f_i(\mathbf{r},t) + L_{ij}(f_i(\mathbf{r},t) - f_i^0(\mathbf{r},t)) + \xi_i(\mathbf{r},t), \tag{2.12}$$

where $\xi_i = \xi_i^H + \xi_i^G$. The extra stochastic term, ξ_i^G, is determined by the noise structure through the concepts of statistical mechanics. Previously, it was mentioned that the velocity distribution function, $f_i(\mathbf{r},t)$, includes information on the physical quantities of the fluids. That means that the number of these physical quantities can be anything up to the total number of velocity vectors, c_i, where $i = 1, 2, 3, ..., n$. (Here $n = 19$.) From this, the local kinetic modes can be written down as

$$M^a(\mathbf{r},t) = \sum_i^n m_i^a f_i(\mathbf{r},t), a = 1...n. \tag{2.13}$$

Here m_i^a is the ath eigenvector so that the set of m_i^a is a $(n \times n)$ matrix. Inversely, the velocity distribution $f_i(\mathbf{r},t)$ is defined:

$$f_i(\mathbf{r},t) = \sum_a N^a \omega_i m_i^a M^a(\mathbf{r},t). \tag{2.14}$$

Here N^a is found from $N^a \sum_i \omega_i m_i^a m_i^b = \delta_{ab}$. M^a are the kinetic quantities: ρ, ρv_α, $\Pi_{\alpha\beta}$ and ghosts. Using the equation (2.13) and conservation laws for mass and momentum, the total fluctuating distribution ξ_i is finally obtained as

$$\begin{aligned} \xi_i &= \textstyle\sum_{a=0}^{10} \omega_i m_i^a \hat{\xi}^a(\mathbf{r},t) N^a + \sum_{g=11}^{19} \omega_i m_i^g \hat{\xi}^g(\mathbf{r},t) N^g \\ &= \omega_i \tfrac{Q_{i\alpha\beta}\hat{S}_{\alpha\beta}(\mathbf{r},t)}{2c_s^4} + \textstyle\sum_{g=11}^{19} \omega_i m_i^g \hat{\xi}^g(\mathbf{r},t) N^g. \end{aligned} \tag{2.15}$$

Here the first term on the right side is the noise, ξ_i^H, defined by Ladd[68]. The other term on the right side is ξ_i^G, the noise term for “ghost”modes.

To calculate the ghost noise ξ_i^G, this improved algorithm derives the amplitude of the extra noise from the FDT relation:

$$\langle \hat{\xi}^a \hat{\xi}^b \rangle = \frac{\tau_a \tau_b - 1}{\tau_a \tau_b} \langle \delta M^a \delta M^b \rangle, \tag{2.16}$$

where τ_a and τ_b are relaxation times for the modes, M^a and M^b in equation (2.13). The fluctuating matrix $\langle \delta M^a \delta M^b \rangle$ can be worked out from equation (2.13) and (2.14) for the given LB model.

2.2 Lattice Boltzmann for a binary fluid

A deep quench of mixed fluids can separate the fluids into distinct regions of each component. (This is the spinodal decomposition.) The later dynamics of coarsening fluids falls into three regimes distinguished by the growth rates of domains: diffusive, viscous hydrodynamic and inertial hydrodynamic. During the late (post diffusion) stages of the demixing process, fluid flow arise from a finite pressure difference across the interface between two fluids: $\Delta P = \sigma H$, where σ is the interfacial tension and H is the interfacial curvature.

In the theoretical approach to this process of spinodal decomposition, the kinetic equations of "Model H" provide the thermodynamics and the coarsening dynamics for the binary fluid. In development of simulation methods, Swift *et al.*[24] suggested an LB model which includes the term for the ordering kinetics of a binary fluid, and Kendon[25] contributed simulations for the coarsening of a binary fluid in 3D by using the code *Ludwig*. In this section, the theoretical approach for demixing fluids is discussed, and then the corresponding LB algorithm will be explained.

2.2.1 Thermodynamics: the spinodal decomposition

The spinodal decomposition for a binary fluid stems from the simple Ginzburg-Landau free energy function for the order parameter ϕ:

$$F[\phi] = \int d\mathbf{r}[V(\phi) + \frac{1}{2}\kappa|\nabla\phi|^2]. \tag{2.17}$$

Here ϕ is the conserved order parameter defined by $\phi = (n_A - n_B)/(n_A + n_B)$ with $\rho = n_A + n_B$ fluid density; n_A and n_B are densities of each fluid. The $V(\phi)$ comes from a general Landau expansion; for a symmetric binary fluid, $V(\phi) = \frac{1}{2}A\phi^2 + \frac{1}{4}B\phi^4$. The remaining term, called the gradient free energy, arises from an increase of the free energy when the field ϕ slowly varies in space. The prefactors A, B, and κ controls the fluid-fluid interfacial tension σ and the interfacial width ξ.

From equation (2.17) one can first deduce a dynamic equation of motion for $\phi(\mathbf{r})$ appropriate to the case where only ϕ is conserved. The local rate of displacement of the order parameter for the conservation condition is

$$\frac{\partial\phi(\mathbf{r})}{\partial t} = -\nabla \cdot \mathbf{j}, \tag{2.18}$$

where $\mathbf{j}$ denotes the flux driven by the thermodynamic force (chemical potential μ), $\delta F/\delta\phi$. With the flux $\mathbf{j}$ associated with the linear coefficient, M ("mobility"), the dynamic equation (‘Cahn-Hilliard’ equation for “Model B”) is given by

$$\begin{aligned} \mathbf{j}(\mathbf{r}) &= -M\nabla\mu, \\ \frac{\partial\phi}{\partial t} &= \nabla\cdot\left[M\nabla\frac{\partial F}{\partial\phi}\right] \\ &= M\left[\kappa\nabla^2\phi - \frac{dV(\phi)}{d\phi}\right]. \end{aligned} \tag{2.19}$$

The interfacial tension σ and the interfacial width ξ can be calculated from the static situation in equilibrium. This obeys $\frac{d\phi}{dt} = 0$ so that using equation (2.19), the static profile is obtained as

$$\kappa\nabla^2\phi = \kappa\frac{d^2\phi}{dx^2} = \frac{dV(\phi)}{d\phi}, \tag{2.20}$$

where $\nabla^2\phi$ is rewritten as $d^2\phi/dx^2$ in one dimension and the order parameter varies between $\phi = -\phi^*$ for $x \to -\infty$ and $\phi = +\phi^*$ for $x \to \infty$. Here ϕ^* is the magnitude of equilibrium order parameter, where the minima of $V(\phi)$ are found. For the protocol of spinodal decomposition (or phase separation), the model potential $V(\phi)$ presents a symmetric double well (seen in Figure 2.2). The equilibrium values of the order parameter ϕ^* are derived from the given $V(\phi)$:

$$\begin{aligned} \frac{\partial V}{\partial\phi} = A\phi + B\phi^3 = 0 \\ \phi(\phi^2 + \frac{A}{B}) = 0. \end{aligned} \tag{2.21}$$

According to the sign of the prefactor A, the model is determined in either the mixing or the demixing regime by the solutions:

$$\phi = 0 \quad for \quad A > 0 \ (T > T_c) \tag{2.22}$$

$$\phi = \pm\phi^* \quad for \quad A < 0 \ (T < T_c). \tag{2.23}$$

Here, the magnitudes of equilibrated order parameters are $\phi^* = \pm\sqrt{-\frac{A}{B}}$ and T_c is the critical temperature.

The surface energy per unit area σ associated with interfaces is computed by subtracting the bulk energy from the total energy:

$$\sigma = \int[\frac{1}{2}\kappa(\frac{d\phi}{dx})^2 + V(\phi) - V(\phi^*)]dx = \kappa\int_{-\infty}^{+\infty}\left(\frac{d\phi}{dx}\right)^2 dx. \tag{2.24}$$

From equation (2.20), the interfacial profile is given by

$$\phi/\phi^* = \tanh(x/\xi), \tag{2.25}$$

where the interfacial width ξ is measured by

$$\xi = \left(\frac{-2\kappa}{A}\right)^{1/2}. \tag{2.26}$$

With the given free energy in equation (2.17), the interfacial tension (or surface energy) is obtained as $\sigma = (-8\kappa A^3/9B^2)^{1/2}$; the chemical potential obeys $\mu = A\phi + B\phi^3 - \kappa\nabla^2\phi$.

2.2.2 Kinetic equation for a binary fluid

The time evolution of the order parameter for "Model H" is governed by the Cahn-Hilliard equation written as

$$\frac{\partial\phi}{\partial t} + \mathbf{v}\cdot\nabla\phi = M\nabla^2\mu, \tag{2.27}$$

where $\mathbf{v}$ is the fluid velocity, M is the mobility, and μ is chemical potential. In the above equation, the second left term is the advection of the order parameter to account for the transport of the order parameter by hydrodynamics. The right term is the diffusive term. The fluid velocity $\mathbf{v}$ obeys the Navier-Stokes equation for an isothermal/incompressible fluid which includes an extra force term arising from the chemical potential of ϕ in equation (2.2):

$$\rho\left(\frac{\partial\mathbf{v}}{\partial t} + (\mathbf{v}\cdot\nabla)\mathbf{v}\right) = \eta\nabla^2\mathbf{v} - \nabla p - \phi\nabla\mu = \eta\nabla^2\mathbf{v} - \nabla\mathbf{P}^{th}. \tag{2.28}$$

Here $\mathbf{P}^{th}$ is the thermodynamic pressure tensor consisting of two parts: an isotropic part and a chemical part. The isotropic part is given as $p\delta_{\alpha\beta} = \frac{1}{3}\rho\delta_{\alpha\beta}$ in lattice Boltzmann model. The chemical pressure tensor is deduced from the term $\phi\nabla\mu$ coming from the free-energy change per unit volume that accompanies the transport of a fluid region with order parameter ϕ over a distance for which change in the chemical potential is $\delta\mu$. Alternatively the chemical potential gradients act as a driving force on the fluid. Hence this force, $\mathbf{F} = -\phi\nabla\mu$, can be considered as the divergence of a 'chemical' pressure tensor: $\phi\nabla\mu = \nabla\cdot\mathbf{P}^{chem}$. Here the chemical pressure tensor is

$$P^{chem}_{\alpha\beta} = \delta_{\alpha\beta}\left[\phi\frac{dV}{d\phi} - V - \kappa\phi\nabla^2\phi + \frac{1}{2}\kappa|\nabla\phi|^2\right] + \kappa(\partial_\alpha\phi)(\partial_\beta\phi). \tag{2.29}$$

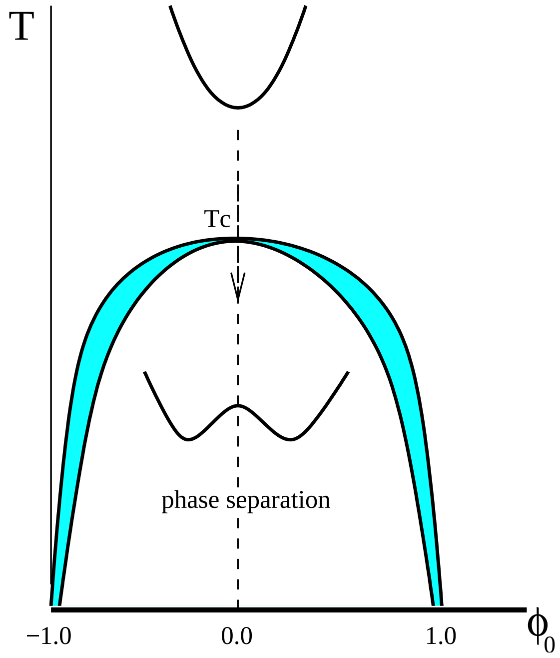

Figure 2.2: The phase diagram governing spinodal decomposition. The x axis is the initial order parameter $\phi_0 = (n_A - n_B)/(n_A + n_B)$. The mixed phase is found in the region above T_c and the potential curve is single-welled with the zero minimum value. The region below T_c under the line is for the phase separation which has the double-well potential curve with minima found at positions $\pm\phi^*$. (The colour region is for nucleation, but that is not discussed in this thesis.)

Therefore, in Cartesian coordinates for LB, the thermodynamic pressure tensor is rewritten as

$$P_{\alpha\beta}^{th} = \left(\frac{1}{3}\rho + \frac{1}{2}A\phi^2 + \frac{3}{4}B\phi^4 - \kappa\phi\nabla^2\phi - \frac{1}{2}\kappa\nabla\phi^2\right)\delta_{\alpha\beta} + \kappa(\partial_\alpha\phi)(\partial_\beta\phi). \tag{2.30}$$

2.2.3 Dynamic equation of LB for a binary fluid

For the ordering kinetics for the ϕ, a second distribution function g_i is introduced in the original LB framework alongside f_i, such that

$$\phi = \sum_i g_i. \tag{2.31}$$

Recall the velocity distribution f_i in equations (2.5)-(2.7):

$$\rho = \sum_i f_i$$
$$\rho v_\alpha = \sum_i f_i c_{i\alpha}$$

$$\Pi_{\alpha\beta} = \quad \textstyle\sum_i f_i c_{i\alpha} c_{i\beta}, \tag{2.32}$$

where the stress tensor $\Pi_{\alpha\beta}$ is derived from equation (2.29) as

$$\Pi_{\alpha\beta} = \rho v_\alpha v_\beta - \eta_{\alpha\beta\gamma\epsilon} \nabla_\gamma v_\epsilon + P^{th}_{\alpha\beta}. \tag{2.33}$$

The time-evolution equations for the pair of distribution functions, f_i and g_i, involve the two single-relaxation parameters, τ_1 and τ_2:[25]

$$f_i(\mathbf{r} + \mathbf{c}_i \Delta t, t + \Delta t) - f_i(\mathbf{r}, t) = -(f_i - f_i^{(eq)})/\tau_1, \tag{2.34}$$

$$g_i(\mathbf{r} + \mathbf{c}_i \Delta t, t + \Delta t) - g_i(\mathbf{r}, t) = -(g_i - g_i^{(eq)})/\tau_2. \tag{2.35}$$

The relaxation time τ_1 is determined by the fluid viscosity with $\eta = (2\tau_1 - 1)\rho/6$, and the other relaxation time τ_2 is set to unity in *Ludwig*. The equilibrium distribution functions, $f_i^{(eq)}$ and $g_i^{(eq)}$ can be derived from equation (2.31)-(2.33) with the condition that the order parameter is advected by hydrodynamics as in equation (2.27):

$$\sum_i f_i^{(eq)} c_{i\alpha} c_{i\beta} = P^{th}_{\alpha\beta} + \rho v_\alpha v_\beta, \tag{2.36}$$

$$\sum_i g_i^{(eq)} c_{i\alpha} c_{i\beta} = \tilde{M} \mu \delta_{\alpha\beta} + \phi v_\alpha v_\beta. \tag{2.37}$$

The parameter $\tilde{M}$ is set by the order-parameter mobility M as $\tilde{M} \Delta t(\tau_2 - 1/2) = M$ so that $\tilde{M} = 2M$[25]. In practice, instead of the single relaxation times used in equations (2.34) and (2.35), multiple relaxation times and a reprojection similar to equation (2.9) are used[12].

2.3 Colloids in LB

Figure 2.3(a) presents the mapping of a spherical colloid with a physical radius a_0 given by an input value onto a lattice grid. The boundary nodes denoted $\{\mathbf{r_b}\}$ for the surface are half way between pairs of lattice nodes near the distance a_0 from the centre of the particle. For an isolated solid object, a full complement of links obeys the conditions:

$$\sum_b w_{c_b} \mathbf{c}_b = \mathbf{0} \tag{2.38}$$

and

$$\sum_b w_{c_b} (\mathbf{r}_b \times \mathbf{c}_b) = \mathbf{0}, \tag{2.39}$$

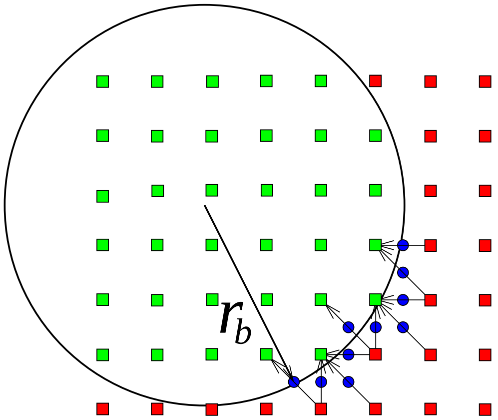

Figure 2.3: Boundary nodes of a solid particle[12] with a radius a_0. Blue circles are boundary nodes; (green and red) squares are lattice nodes. The boundary links are indicated by arrows (velocity vectors) cutting the boundary surface.

where w_{c_b} are again the quadrature weights appropriate for the boundary links.

When a solid colloid moves with the linear velocity $\mathbf{U}$ and the angular velocity $\mathbf{\Omega}$, the fluid distribution function is updated by the bounce-back on links algorithm (BBL) which is described by Ladd[15, 70]. The following subsections discuss the treatment of BBL and the force and torque of the momentum transfer in detail. In order to understand the physics of moving colloids defined by the boundary nodes, the hydrodynamic radius a_h will be defined and the calibration of a_h will be discussed in the next subsection. The remaining subsection describes the lubrication corrections for particles in close contact.

2.3.1 Bounce-Back on Links

A set of links $\{\mathbf{c}_b \Delta t\}$ connects lattice nodes inside and outside of the surface. When particles move with the velocity $\mathbf{U}$ and the angular velocity $\mathbf{\Omega}$, the total mass has to be conserved. As using the boundary condition, the incoming distribution f_b is updated by

$$f_{b'}(\mathbf{r}, t+\Delta t) = f_b^*(\mathbf{r}, t) - 2 w_{c_b} \rho_0 \mathbf{u}_b \cdot \mathbf{c}_b / c_s^2 \tag{2.40}$$

where the second term in right side is the mass transfer due to moving the object; f_b^* is the postcollision distribution at position $\mathbf{r}$ and time t in the direction $\mathbf{c}_b$ and $\mathbf{c}_{b'} = -\mathbf{c}_b$. f_b^* is obtained after collision stage in equation (2.8) as

$$f_i^* = f_i + \sum_j L_{ij}(f_j - f_j^0). \tag{2.41}$$

The local velocity of the particle surface is written as $\mathbf{u}_b = \mathbf{U} + \mathbf{\Omega} \times \mathbf{r}_b$. The above procedure for redistributing f_b is performed at the stage between the collision step and the propagation step in Section 2.1.1.

For one link, the hydrodynamic force on a moving particle can be calculated from momentum transfer as

$$\mathbf{F}^H(\mathbf{r}_b, t + \frac{1}{2}\Delta t) = \frac{\Delta L^3}{\Delta t}\left[2f_b^* - 2w_{c_b}\rho_0 \mathbf{u}_b \cdot \mathbf{c}_b / c_s^2\right]\mathbf{c}_b, \tag{2.42}$$

where ΔL is the lattice spacing unit and Δt is the lattice time unit. The corresponding torque $\mathbf{T}^H$can be obtained as $\mathbf{r}_b \times \mathbf{F}^H(\mathbf{r}_b, t + \frac{1}{2}\Delta t)$. For one object, the total hydrodynamic forces are obtained from the sums of $\mathbf{F}^H$ and $\mathbf{T}^H$ respectively for all links. Then, the total force and torque for one object can be written as a combination of the linear velocity and the angular velocity:

$$\mathbf{F}^H = \mathbf{F}_0 - \zeta^{FU} \cdot \mathbf{U} - \zeta^{F\Omega} \cdot \mathbf{\Omega}, \tag{2.43}$$

$$\mathbf{T}^H = \mathbf{T}_0 - \zeta^{TU} \cdot \mathbf{U} - \zeta^{T\Omega} \cdot \mathbf{\Omega}. \tag{2.44}$$

Here the velocity independent force and torque at the half-time step are written as

$$\mathbf{F}_0(t + \frac{1}{2}\Delta t) = \frac{\Delta L^3}{\Delta t}\sum_b 2f_b^* \mathbf{c}_b, \tag{2.45}$$

$$\mathbf{T}_0(t + \frac{1}{2}\Delta t) = \frac{\Delta L^3}{\Delta t}\sum_b 2f_b^* (\mathbf{r}_b \times \mathbf{c}_b). \tag{2.46}$$

The friction coefficients, ζ^{FU}, ζ^{TU}, $\zeta^{F\Omega}$ and $\zeta^{T\Omega}$ are given as

$$\zeta^{FU} = \frac{2\rho\Delta L^3}{c_s^2 \Delta t}\sum_b w_{c_b}\mathbf{c}_b\mathbf{c}_b, \tag{2.47}$$

$$\zeta^{F\Omega} = \frac{2\rho\Delta L^3}{c_s^2 \Delta t}\sum_b w_{c_b}\mathbf{c}_b(\mathbf{r}_b \times \mathbf{c}_b), \tag{2.48}$$

$$\zeta^{TU} = \frac{2\rho\Delta L^3}{c_s^2 \Delta t}\sum_b w_{c_b}(\mathbf{r}_b \times \mathbf{c}_b)\mathbf{c}_b, \tag{2.49}$$

$$\zeta^{T\Omega} = \frac{2\rho\Delta L^3}{c_s^2 \Delta t}\sum_b w_{c_b}(\mathbf{r}_b \times \mathbf{c}_b)(\mathbf{r}_b \times \mathbf{c}_b). \tag{2.50}$$

2.3.2 Dynamics of Colloids in LB

Using the hydrodynamic forces calculated above, the particle velocities are updated by the following:

Table 2.1: Hydrodynamic radius a_h according to input radii a_0 and fluid viscosities in $D3Q19$, calibrated by Kevin Stratford[14]. See also [15].

η	a_0			
	1.25	2.30	3.71	6.21
1/6	1.02	2.19	3.64	6.19
1/10	1.10	2.30	-	-
1/100	1.31	2.46	3.87	6.39
1/1000	1.42	2.57	4.00	6.51

$$\begin{bmatrix} \mathbf{U}(t+\Delta t) \\ \mathbf{\Omega}(t+\Delta t) \end{bmatrix} = \begin{bmatrix} \mathbf{U}(t) \\ \mathbf{\Omega}(t) \end{bmatrix} + \begin{bmatrix} \frac{m}{\Delta t} + \zeta^{FU} & \zeta^{F\Omega} \\ \zeta^{FU} & \frac{I}{\Delta t} + \zeta^{T\Omega} \end{bmatrix}^{-1} \times \begin{bmatrix} \mathbf{F}_0 - \zeta^{FU}\mathbf{U}(t) - \zeta^{F\Omega}\mathbf{\Omega}(t) \\ \mathbf{T}_0 - \zeta^{TU}\mathbf{U}(t) - \zeta^{T\Omega}\mathbf{\Omega}(t) \end{bmatrix}. \tag{2.51}$$

Here m is the mass of the solid particle and I is its moment of inertia. The friction coefficients, $\zeta^{FU}, \zeta^{F\Omega}, \zeta^{TU}$ and $\zeta^{T\Omega}$ are shown in equations (2.47)-(2.50). The $\mathbf{F}_0$ and $\mathbf{T}_0$ are the total force and torque which are sums of the hydrodynamic force and torque and the extra forces calculated from interacting potentials of particles.

2.3.3 Calibration of hydrodynamic radius

When a particle with a radius a_0 moves with a constant velocity U in a stationary solvent, the hydrodynamic radius a_h can be obtained simply from the drag force, $F_d = 6\pi\eta a_h U$. In LB, the hydrodynamic force[70, 71] acting on moving colloids with a input radius a_0 in lattice units can be calculated from equation (2.42) and it should be equal to the drag force $F_d = 6\pi\eta a_h U$, where a_h is the hydrodynamic radius (or Stokes radius). For lattice systems, this is a fluctuating quantity, but its mean value can be deduced by the relation $\langle a_h\rangle = \langle F^h\rangle/6\pi\eta U$, where $\langle\cdots\rangle$ is an average over time. For a finite system of size Λ, the hydrodynamics radius is calculated as

$$\langle a_h\rangle = \frac{\langle F^h\rangle}{6\pi\eta U}\left[1 - 2.837(a_0/\Lambda) + 4.19(a_0/\Lambda)^3 - 27.4(a_0/\Lambda)^6\right], \tag{2.52}$$

where the term [...] is for the finite size correction[70]. From now, we use a_h to denote this mean value.

For hard-sphere colloids in continuous space, the hydrodynamic radius a_h is equal to the input radius a_0. However, in lattice systems, there is a discrepancy between a_0 and a_h, which can depend on the viscosity η. Table 2.1 shows the data of a_h measured for various viscosities η and input radii a_0. For convenience, all simulations should have the parameters such that a_h is set as the same length as the input radius a_0. Thus we

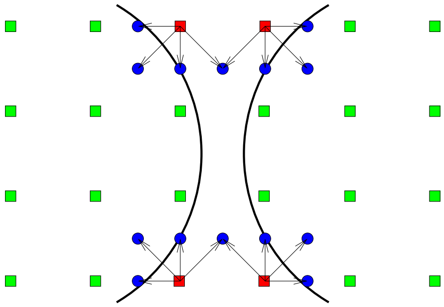

Figure 2.4: Close particles on lattice grids. Those are not satisfied with the conditions in equations (2.38), (2.39) for closed objects by the boundary links.

choose the optimal viscosity and the input radius as $\eta = 0.1$ and $a_0 = 2.3$. Since a_h is now matched with a_0, only a_h will be mentioned below when discussing simulation parameters of the systems that this thesis studies.

2.3.4 BBL for particle close to contact

As seen in Figure 2.4, when particles are close, some boundary links are lost. Thus the total mass is not conserved; the total mass transfer of particles from equation (2.40) is written as

$$\Delta M = -\frac{2\Delta L^3 \rho}{c_s^2}\left[\mathbf{U}\cdot\sum_b w_{c_b}\mathbf{c}_b + \mathbf{\Omega}\cdot\sum_b w_{c_b}\mathbf{r}_b\times\mathbf{c}_b\right]. \tag{2.53}$$

For the conservation laws in Stokes flow, particles defined by equations (2.38) and (2.39) ensure that the total mass transfer is zero, $\Delta M = 0$, but in close contact of particles, the mass transfer is not zero, $\Delta M \neq 0$. This is easily corrected by redistributing the $f_{b'}$ of equation (2.40) subtracting the term of ΔM:

$$f_{b'} = f_b^* - 2w_{c_b}\rho\mathbf{u}_b\cdot\mathbf{c}_b/c_s^2 - w_{c_b}\rho\frac{\Delta M}{A}, \tag{2.54}$$

where $A = \Delta L^3\rho\sum_b w_{c_b}$.

Also the force and the torque from redistribution of mass are obtained as

$$\mathbf{\Delta F} = \frac{\Delta L^3\rho}{\Delta t}\left[-\frac{\Delta M}{A}\sum_b w_{c_b}\mathbf{c}_b\right], \tag{2.55}$$

and

$$\mathbf{\Delta T} = \frac{\Delta L^3\rho}{\Delta t}\left[-\frac{\Delta M}{A}\sum_b w_{c_b}\mathbf{r}_b\times\mathbf{c}_b\right]. \tag{2.56}$$

From equation (2.43) and (2.44), the total force and torque with the redefinition of mass conservation can be rearranged to give new friction coefficients which are slightly different from equation (2.47) - (2.50):

$$\zeta^{FU} = -\frac{2\rho\Delta L^3}{c_s^2\Delta t}\sum_b w_{c_b}(\mathbf{c}_b - \overline{\mathbf{c}}_b)\mathbf{c}_b, \tag{2.57}$$

$$\zeta^{F\Omega} = -\frac{2\rho\Delta L^3}{c_s^2\Delta t}\sum_b w_{c_b}\mathbf{c}_b(\mathbf{r}_b \times \mathbf{c}_b - \overline{\mathbf{r}_b \times \mathbf{c}_b}), \tag{2.58}$$

$$\zeta^{TU} = -\frac{2\rho\Delta L^3}{c_s^2\Delta t}\sum_b w_{c_b}(\mathbf{r}_b \times \mathbf{c}_b)(\mathbf{c}_b - \overline{\mathbf{c}}_b), \tag{2.59}$$

$$\zeta^{T\Omega} = -\frac{2\rho\Delta L^3}{c_s^2\Delta t}\sum_b w_{c_b}(\mathbf{r}_b \times \mathbf{c}_b)(\mathbf{r}_b \times \mathbf{c}_b - \overline{\mathbf{r}_b \times \mathbf{c}_b}). \tag{2.60}$$

where

$$\overline{\mathbf{c}}_b = \frac{\sum_b w_{c_b}\mathbf{c}_b}{\sum_b w_{c_b}} \tag{2.61}$$

and

$$\overline{\mathbf{r}_b \times \mathbf{c}_b} = \frac{\sum_b w_{c_b}\mathbf{r}_b \times \mathbf{c}_b}{\sum_b w_{c_b}}. \tag{2.62}$$

2.3.5 Lubrication forces

When the gap between particles is less than $h_c \simeq 0.1a_h$, a breakdown occurs in the calculation of hydrodynamic interactions in equation (2.55) and (2.56). This error can be fixed by adding a normal lubrication force for two particles which have radii, a_1 and a_2 and linear velocities, $\mathbf{U}_1$ and $\mathbf{U}_2$ respectively[15]:

$$\mathbf{F} = -6\pi\eta\frac{a_1^2 a_2^2}{(a_1+a_2)^2}\left(\frac{1}{h} - \frac{1}{h_c}\right)\mathbf{U}_{12}\cdot\hat{\mathbf{R}}_{12} \ , \quad h < h_c \tag{2.63}$$

$$= 0 \ , \quad h > h_c. \tag{2.64}$$

Here $\mathbf{U}_{12} = \mathbf{U}_1 - \mathbf{U}_2$, $h = |\mathbf{R}_{12}| - a_1 - a_2$ is the gap between two particles and the unit vector $\hat{\mathbf{R}}_{12} = \mathbf{R}_{12}/|\mathbf{R}_{12}|$. However, in our simulations, this normal lubrication force is generally not used because the repulsive short-range potential keeps particles at distance larger than $0.1a_h$.

For colloids in a closed box with solid walls the specification can be completed by including a normal lubrication force between colloids and walls defined as

$$\mathbf{F}_\alpha = -6\pi\eta a_h^2\left(\frac{1}{h_\alpha} - \frac{1}{h_{lub}}\right) \ , \quad h_\alpha < h_{lub} \tag{2.65}$$

$$= 0 \ , \quad h_\alpha > h_{lub}, \tag{2.66}$$

where the subscript α is Cartesian coordinate components: x, y and z. Thus h_x is the gap between a particle surface and the box wall lying normal to the x direction.

2.4 The Simulation potentials for particles

Choosing suitable interaction potentials is essential to the design of simulation models for colloids. Particles in LB employ the general molecular dynamic algorithm to update their states by forces and torques via interacting potentials. Especially, in LB, the short-range interaction is chosen not only in light of the simulated model, but also to reduce the computational error at close contact of particles. In a solid particle defined by its boundary links on a lattice, the soft-sphere potential is modified to be a function of the gap distance of surface-surface of colloids for preventing overlapped particles.

Another important potential is the long-range dipolar interaction between magnetic particles. The dipole is a source of a magnetic field $\mathbf{B}(\mathbf{r})$ which falls as $1/r^3$, where r is distance. To derive the dipole-dipole interaction potential, we start from the general equation of magnetic field of a dipolar source. For the computational implementation for a periodic boundary box, the Ewald summation is used for the long-range interaction, and it will be described later.

2.4.1 Short-range potential

A simple soft-sphere potential is given by

$$U^{ss}(r) = \gamma \left(\frac{r_0}{r}\right)^{\nu}, \tag{2.67}$$

where the distance r is the centre-to-centre distance of two particles and γ, r_0 and ν are the short-range parameters; as ν is increased, U^{ss} becomes harder. This soft-sphere potential naturally has a long tail. However, to save a computational cost, a truncation method using 'cut-and-shift' with the cutoff distance r_c is used and it can be rewritten as

$$U^{sc}(r) = U^{ss}(r) - U^{ss}(r_c) - (r - r_c)\left(\frac{dU^{ss}}{dr}\right)_{r=r_c}. \tag{2.68}$$

To embed this in LB, a modification of this basic form is needed; the distance r is substituted by the gap separation $h = r - 2a_h$, the cutoff is $h_c = r_c - 2a_h$ and the scale parameter $h_0 = r_0$. So the short-range potential for colloidal particles on the lattice is given as

$$U^{sc}(h) = U^{ss}(h) - U^{ss}(h_c) - (h - h_c)\left(\frac{dU^{ss}}{dh}\right)_{h=h_c}. \tag{2.69}$$

The parameters, γ, h_0, ν and h_c, are chosen for each simulation model and this information will be mentioned in "Simulation parameters" in each chapter. The force between two particles is calculated via

$$\mathbf{F}_{ij}(h) = -\left[\frac{dU^{ss}(h)}{dh} - \left(\frac{dU^{ss}}{dh}\right)_{h=h_c}\right]\hat{\mathbf{h}}_{ij}, \tag{2.70}$$

where $\hat{\mathbf{h}}_{ij}$ is the unit vector for surface-to-surface of particles i and j.

2.4.2 Long-range dipolar interaction

A magnetic dipole can be viewed as two equal and opposite point monopoles. In the case of a magnetically polarised substance, uniform magnetisation creates an effective surface density of monopoles on the ends of the body. The magnetic dipole moment $\mathbf{m}$ can be defined as

$$\mathbf{m} = M(a_d d)\hat{\mathbf{d}}, \tag{2.71}$$

where M is the magnetisation, $\hat{\mathbf{d}}$ is the unit vector of the polarised direction of the substance, and $a_d d$ is the volume of the element.

At a position $\mathbf{r}$ from the centre of a magnetic dipole, the external field emanated by the magnet can be found by Coulomb's law[37] and it results in

$$\mathbf{B}(\mathbf{r}) = \frac{\mu_0}{4\pi r^3}\left[-\mathbf{m} + 3(\mathbf{m}\cdot\hat{\mathbf{r}})\hat{\mathbf{r}}\right], \tag{2.72}$$

where μ_0 is vacuum permeability, the dipole moment is $\mathbf{m} = m\hat{\mathbf{d}}$ and $\hat{\mathbf{r}}$ is the unit vector of $\mathbf{r}$. Note that the magnetic field $\mathbf{B}(\mathbf{r})$ in equation (2.72) is distinguished from the vector field $\mathbf{H}(\mathbf{r})$ via the relation, $\mathbf{B}(\mathbf{r}) = \mu_0\mathbf{H}(\mathbf{r})$.

Let us think of a dipolar particle with a dipolar vector $\mathbf{m}_i = m_i\hat{\mathbf{s}}_i$ subject to an external magnetic field, $\mathbf{B}_0$, which can be considered as two types: $\mathbf{B}_0(\mathbf{r})$ as a function of position r and constant $\mathbf{B}_0$ as an uniform field in space.

The force on $\mathbf{m}_i$ can be given by

$$\mathbf{F}_i = (\mathbf{m}_i \cdot \nabla)\mathbf{B}_0, \tag{2.73}$$

and the torque is derived as

$$\mathbf{T}_i = \mathbf{m}_i \times \mathbf{B}_0. \tag{2.74}$$

By a vector identity, $(\mathbf{m}\cdot\nabla)\mathbf{B}_0$ is rewritten as

$$\mathbf{F}_i = \nabla(\mathbf{m}_i \cdot \mathbf{B}_0) - \mathbf{m}_i \times (\nabla \times \mathbf{B}_0). \tag{2.75}$$

If there is no flow of electric current, $\nabla \times \mathbf{B}_0$ is zero. The $\mathbf{F}_i$ is also deduced from the energy E_h by $\mathbf{F} = -\nabla E_h$. Therefore the energy can be defined from equation (2.75)

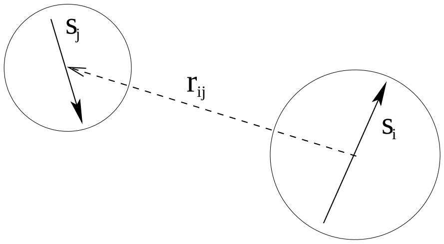

Figure 2.5: The pair dipolar interaction. In simulations, a point dipole is embedded in the centre of each sphere.

as $E_h = -(\mathbf{m} \cdot \mathbf{B}_0)$ that one regards as the interacting energy $U^d(\mathbf{r})$ for two dipoles. Consequently, the dipole-dipole interaction for two dipoles, $\mathbf{m}_i = m_i\hat{\mathbf{s}}_i$ and $\mathbf{m}_j = m_j\hat{\mathbf{s}}_j$, with the centre-to-centre distance $\mathbf{r}_{ij}$ is written as

$$U^d_{ij}(\mathbf{r}_{ij}) = \frac{\mu_0}{4\pi}\frac{m_i m_j}{r^3_{ij}}\left[\hat{\mathbf{s}}_i \cdot \hat{\mathbf{s}}_j - 3(\hat{\mathbf{s}}_i \cdot \hat{\mathbf{r}}_{ij})(\hat{\mathbf{s}}_j \cdot \hat{\mathbf{r}}_{ij})\right], \tag{2.76}$$

where the prefactor $\mu_0/4\pi$ is 10^{-7}H/m in SI units. For many body systems, the total external field, $\mathbf{B}^t_0$, acting on one particle can be superposed by the $\mathbf{B}_0$ from all dipoles except the dipole itself. Calculating the force and the torque is quite straightforward from the $\mathbf{B}^t_0$. The direct calculation using equations (2.73) and (2.74) is possible for the nonperiodic system in all dimensions. For the periodic boundary condition, the Ewald summation technique is used for the calculation of the long-range part of the dipolar interactions.

2.4.3 Ewald summation for the long-range dipolar interaction

Ewald summation[19, 72] is an efficient method to compute the long-range electrostatic interactions for a periodic system. The original method of Ewald summation[73] was for the ionic crystal system, but it can be readily extended to other systems: charge-dipole, dipole-dipole, and charge-quadrupole.

To satisfy the periodic boundary condition, the dipolar potential with periodic image boxes can be considered and rewritten as

$$U^d = \sum_{\mathbf{n}}{}' \left(\sum_{1\le i<j\le N} \frac{m_i m_j}{r'^3_{ij}}\left[\hat{\mathbf{s}}_i \cdot \hat{\mathbf{s}}_j - 3(\hat{\mathbf{s}}_i \cdot \hat{\mathbf{r}}'_{ij})(\hat{\mathbf{s}}_j \cdot \hat{\mathbf{r}}'_{ij})\right]\right), \tag{2.77}$$

where the prime on the summation denotes that the sum is over all periodic images $\mathbf{n}$ and the distance between particles for all image boxes is $\mathbf{r}'_{ij} = \mathbf{r}_{ij} + \mathbf{n}\Lambda$, where Λ is the box length. For the long-range potential in equation (2.76), this summation[74] is only conditionally convergent. To improve the convergence, the dipole is replaced by the Gaussian dipolar distribution as

$$\rho_i^d(r) = (\mathbf{m}_i \cdot \nabla)\alpha^3 \exp(-\alpha^2 r^2)/\pi^{3/2} \tag{2.78}$$

where the convergence factor α decides the width of the distribution and must be determined to maximise numerical accuracy[75]; α can be chosen to ensure that terms of order $\exp(-\alpha^2 L^2)$ are negligible. Here, r is the position relative to the centre of the distribution.

The dipolar interaction potential evaluated by Ewald technique consists of three parts: the real space part for the short-range contribution, the Fourier space part for the long-range contribution and the self-energy correction term. The short-range interaction is easily summed in real space truncated by the cutoff r_c, but the long-range is the problem; so this part is treated by using the sum in Fourier space. The final term for the self energy correction, which arises from the Gaussian distribution acting on its own centre at $\mathbf{r}_i$, should be subtracted from the total summation.

As a result, for monodisperse dipolar particles where the strength of dipoles for all particles is the same , $m_i = \sqrt{\frac{4\pi}{\mu_0}}\mu$, the total potential energy[19] is obtained as

$$\begin{aligned} U^d = \quad & \mu^2 \sum_{i,j;r_{ij}<r_c} [b_1(r_{ij})(\hat{\mathbf{s}}_i \cdot \hat{\mathbf{s}}_j) - b_2(r_{ij})(\hat{\mathbf{s}}_i \cdot \hat{\mathbf{r}}_{ij})(\hat{\mathbf{s}}_j \cdot \hat{\mathbf{r}}_{ij})] \\ + \quad & (4\pi\mu^2/\Lambda^3)\sum_{i,j}\sum_{k\neq 0}(1/k^2)(\hat{\mathbf{s}}_i \cdot \mathbf{k})(\hat{\mathbf{s}}_j \cdot \mathbf{k})\exp(-k^2/4\alpha^2)\cos(\mathbf{k}\cdot\mathbf{r}_{ij}) \\ - \quad & (2\alpha^3\mu^2 N/3\sqrt{\pi}), \end{aligned} \tag{2.79}$$

Here,

$$\begin{aligned} b_1(r) &= \operatorname{erfc}(\alpha r)/r^3 + (2\alpha/\sqrt{\pi})\exp(-\alpha^2 r^2)/r^2, \\ b_2(r) &= 3b_1(r) + (4\alpha^3/\sqrt{\pi})\exp(-\alpha^2 r^2), \end{aligned}$$

where erfc() is the complementary error function[76] and the Fourier space component $\mathbf{k}$ is given as $\mathbf{k} = \frac{2\pi}{\Lambda}(n_x, n_y, n_z)$ for $-\Lambda \le n_x, n_y \le \Lambda$ and $0 \le n_z \le \Lambda$.

When one applies this technique to model systems, the medium surrounding the systems[77] should be specified as either a conducting medium (infinite dielectric constant, $\epsilon' = \infty$) or the vacuum atmosphere ($\epsilon' = 0$). For the vacuum condition, the extra term, $\frac{2\pi\mu^2 N}{3L^3}|\sum_{j=1}^{N}\hat{\mathbf{s}}_j|^2$, is added in equation (2.79).

In the limit $\alpha \to 0$ without periodic image boxes, the equation (2.79) reduces to the simple dipole result as

$$U^d = \mu^2 \sum_{i<j} \frac{1}{r_{ij}^3} \left[\hat{\mathbf{s}}_i \cdot \hat{\mathbf{s}}_j - 3(\hat{\mathbf{s}}_i \cdot \hat{\mathbf{r}}_{ij})(\hat{\mathbf{s}}_j \cdot \hat{\mathbf{r}}_{ij}) \right]. \tag{2.80}$$

2.4.4 Force and torque for the dipolar interaction

In the system with many dipoles, from equations (2.72)-(2.74), the force $\mathbf{f}_i$ and the torque $\mathbf{t}_i$, acing on a dipolar particle i, can be derived as

$$\mathbf{f}_i = \sum_{j(\neq i)} \frac{\mu_i \mu_j}{r_{ij}^4} \left[(\hat{\mathbf{s}}_i \cdot \hat{\mathbf{s}}_j)\hat{\mathbf{r}}_{ij} - 5(\hat{\mathbf{s}}_{ij} \cdot \hat{\mathbf{r}}_{ij})(\hat{\mathbf{s}}_{ij} \cdot \hat{\mathbf{r}}_{ij})\hat{\mathbf{r}}_{ij} + (\hat{\mathbf{s}}_j \cdot \hat{\mathbf{r}}_{ij})\hat{\mathbf{s}}_i + (\hat{\mathbf{s}}_i \cdot \hat{\mathbf{r}}_{ij})\hat{\mathbf{s}}_j \right], \tag{2.81}$$

$$\mathbf{t}_i = \sum_{j(\neq i)} \frac{\mu_i \mu_j}{r_{ij}^3} \left[(\hat{\mathbf{s}}_i \times \hat{\mathbf{s}}_j) - 3(\hat{\mathbf{s}}_j \cdot \hat{\mathbf{r}}_{ij})(\hat{\mathbf{s}}_i \times \hat{\mathbf{r}}_{ij}) \right] \tag{2.82}$$

For a periodic boundary conditions in the Ewald summation[78], the force $\mathbf{f}_i^{ew}$ and the torque $\mathbf{t}_i^{ew}$ are calculated from the equation (2.79) and these also consist of two parts: the short-range part worked out from equations (2.81) and (2.82) for the condition $r_{ij} < r_c$ and the long-range part in Fourier space. However the last constant term for the self correction in equation (2.79) vanishes. Therefore, the resulting expressions are

$$\begin{aligned} \mathbf{f}_i^{ew} = & \sum_{j(\neq i);r_{ij}<r_c} \mu^2 [a_2(r_{ij})(\hat{\mathbf{s}}_i \cdot \hat{\mathbf{s}}_j)\hat{\mathbf{r}}_{ij} - a_3(r_{ij})(\hat{\mathbf{s}}_{ij} \cdot \hat{\mathbf{r}}_{ij})(\hat{\mathbf{s}}_{ij} \cdot \hat{\mathbf{r}}_{ij})\hat{\mathbf{r}}_{ij} \\ & + a_2(r_{ij})(\hat{\mathbf{s}}_j \cdot \hat{\mathbf{r}}_{ij})\hat{\mathbf{s}}_i + a_2(r_{ij})(\hat{\mathbf{s}}_i \cdot \hat{\mathbf{r}}_{ij})\hat{\mathbf{s}}_j] + \frac{4\pi\mu^2}{\Lambda^3} \sum_{\mathbf{k}\neq 0} \mathbf{k}(\mathbf{k} \cdot \hat{\mathbf{s}}_i) \exp\left(\frac{-k^2}{4\alpha^2}\right) \\ & \left[\left(\sum_j (\mathbf{k} \cdot \hat{\mathbf{s}}_j) \cos(\mathbf{k} \cdot \mathbf{r}_j) \right) \sin(\mathbf{k} \cdot \mathbf{r}_i) - \left(\sum_j (\mathbf{k} \cdot \hat{\mathbf{s}}_j) \sin(\mathbf{k} \cdot \mathbf{r}_j) \right) \cos(\mathbf{k} \cdot \mathbf{r}_i) \right] \end{aligned} \tag{2.83}$$

and

$$\begin{aligned} \mathbf{t}_i^{ew} = & \sum_{j(\neq i);r_{ij}<r_c} \mu^2 \left[a_1(r_{ij})(\hat{\mathbf{s}}_i \times \hat{\mathbf{s}}_j) - a_2(r_{ij})(\hat{\mathbf{s}}_j \cdot \hat{\mathbf{r}}_{ij})(\hat{\mathbf{s}}_i \times \hat{\mathbf{r}}_{ij}) \right] \\ & - \frac{4\pi\mu^2}{\Lambda^3} \sum_{\mathbf{k}\neq 0} \exp\left(\frac{-k^2}{4\alpha^2}\right) (\hat{\mathbf{s}}_i \times \mathbf{k}) \\ & \left[\left(\sum_j (\mathbf{k} \cdot \hat{\mathbf{s}}_j) \cos(\mathbf{k} \cdot \mathbf{r}_j) \right) \sin(\mathbf{k} \cdot \mathbf{r}_i) - \left(\sum_j (\mathbf{k} \cdot \hat{\mathbf{s}}_j) \sin(\mathbf{k} \cdot \mathbf{r}_j) \right) \cos(\mathbf{k} \cdot \mathbf{r}_i) \right] \end{aligned} \tag{2.84}$$

Here

$$\begin{aligned} a_1(r) &= \mathrm{erfc}(\alpha r)/r^3 + (2\alpha/\sqrt{\pi})\exp(-\alpha^2 r^2)/r^2, \\ a_2(r) &= 3a_1(r)/r + (4\alpha^3/\sqrt{\pi})\exp(-\alpha^2 r^2)/r, \\ a_3(r) &= 5a_2(r)/r + (8\alpha^5/\sqrt{\pi})\exp(-\alpha^2 r^2)/r. \end{aligned}$$

2.4.5 Dimensionless parameter for magnetic colloids

In the study of magnetic colloids in thermal solvents, the dimensionless parameter λ can be defined to represent the ratio of dipolar strength and thermal agitation from solvents:

$$\lambda = \frac{\mu_0}{4\pi}\frac{m^2}{k_B T D^3}. \tag{2.85}$$

This is called the "dipolar coupling constant"; in equation (2.85), the vacuum permeability is given as $\mu_0 = 4\pi \times 10^{-7}\mathrm{Hm}^{-1}$, m is the strength of magnetic dipole moment, the Boltzmann constant is $k_B = 1.38\times10^{-23}\mathrm{NmK}^{-1}$, and D is the diameter of particles. For a spherical magnetic particle, the strength of dipole moment is defined as $m(x) = \frac{\pi}{6}M_s x^3$, where M_s is the bulk magnetisation (or saturation magnetisation) of the magnet core and x is its diameter and is important to control a dipolar strength for magnetic colloids in thermal solvents. In experiments for ferrofluids[79, 5], each colloid consists of a magnet core with diameter x and the surfactant layer with the thickness $\sigma_0 \sim 2\mathrm{nm}$ to prevent the irreversible aggregation. So the diameter of magnetic colloid is given as $D = x + 2\sigma_0$. For example, to manufacture spherical magnetic colloids with $\lambda = 4$, the diameter of a magnetised core should be $x \sim 17\mathrm{nm}$ in the case of magnetite (Fe_3O_4), the most widely studied material for ferrofluids. The bulk magnetisation of magnetite is given as $M_s = 4.8 \times 10^5\mathrm{Am}^{-1}$ at $T = 293\mathrm{K}$.

In simulations, the dipolar coupling constant can be also defined: $\lambda = \mu^2/k_B T D^3$, where $\mu = \sqrt{\frac{\mu_0}{4\pi}}m$. In contrast to real magnetic colloids with a diameter x, the simulation model colloids address a point dipole with the dipolar strength μ and the dipolar unit vector $\hat{\mathbf{s}}_i$ embedded in the centre of each colloid (as seen in Figure 2.5). In general, despite this difference, the study of magnetic colloids requires the dipolar coupling constant as the parameter to be matched in both simulations and experiments.

2.5 Summary

The lattice Boltzmann method is a versatile way to simulate complex fluid flows since it effectively calculates the hydrodynamic forces through Navier-Stokes equations. From a single fluid and a binary fluid, this chapter described how the lattice Boltzmann framework has been created by use of the kinetic equations. It was also shown that the thermal solvent achieved by FLB[69] recovers the hydrodynamics in the discrete model and the fluctuations satisfy the fluctuation-dissipation theorem.

For modelling colloidal systems, the surface of a solid colloid is mapped onto the lattice half way between a pair of lattice nodes at the input radius a_0 from the centre of the colloid. Moving objects can update the incoming velocity distributions by the bounce-back on links algorithm and the hydrodynamic forces can be calculated acting on solid objects. The calibration of the hydrodynamic radius a_h found the discrepancy between a_h and a_0 depending on fluid viscosities; in LB, we chose a_0 to coincide with a_h at a certain viscosity. In the case of particles in close contact, lubrication corrections can be used for correcting the numerical error. For Brownian colloidal simulations, FLB is employed to transfer thermal energy to colloids whose motion is diffusive.

The interaction potentials can be used to classify the kinds of colloids present. For the short-range interaction, the modified soft-sphere type is used to ensure colloids do not overlap at the hard-core radius; all our simulations use this short-range potential. The long-range dipolar interaction characterises magnetic particles for modelling a ferrofluid. Also the dimensionless parameter λ was defined to express the dipolar strength of magnetic colloids in thermal fluids.

The next chapters 3, 4, and 5 will show the results of the complex fluid systems simulated by the lattice Boltzmann methods. Chapter 3 is for colloids in a binary fluid experiencing a phase separation. The next two, Chapters 4 and 5, will show magnetic particles in a single and binary fluid. All models use Brownian colloids which is accomplished by FLB.

Chapter 3

Colloids in a Binary Fluid

This chapter will discuss the simulation results of colloids in a binary fluid undergoing spinodal decomposition. This thesis extends a previous study[1] that successfully predicted the formation of a new emulsified system, the bicontinuous interfacially-jammed emulsion gel ("bijel") in a symmetric quench with spherical colloids which have no long-range interactions. Through the extensive analyses given below, the process for the arrest of demixing fluids by colloids will be quantified and the mechanism will be discussed.

For emulsions stabilised by colloids, the basic idea is inspired by the wetting property of colloids at the fluid-fluid interfaces. Wetting properties are generally quantified by the contact angle determined by three interfacial tensions between a solid and oil, between a solid and water, and between oil and water. These three interfacial tensions can lead to the stability of a solid colloid placed on an interface[2, 29, 30, 31]. For example in a colloid which has two equal solid-fluid interfacial tensions, the contact angle is 90°, called "neutral wetting". Solid colloids trapped at interfaces have high energy barriers arising from capillary forces[80]. Even if colloids of radii in nanometers are considered, the energy barrier for detachment, is very large compared to k_BT so that the local minimum of the free energy is deep compared to k_BT. So colloids at interfaces are trapped efficiently. For bijels, the simulation model[1] has used neutral wetting spherical colloids with the interfacial tension σ. For a single spherical colloid at the fluid-fluid interface, the fluid-fluid interfacial energy is reduced by $\sigma\pi a^2$, where πa^2 is the area of a disc on the interface covered by the colloid. Therefore moving a spherical colloid to the bulk of either fluid requires an energy as much as the capillary energy, $\epsilon = \sigma\pi a^2$ so that $\epsilon/k_BT \gg 1$. In practice, LB simulations choose the capillary energy to match one achievable in experiment. Section 3.1 will discuss the LB parameters to be adapted to address the stability of colloids at the fluid-fluid interfaces.

In recent experimental work, bijels[4, 36, 34] have been made from a roughly equal-volume immiscible fluid pair: 2,6 lutidine (2,6-dimethylpyridine)-water, with 2% concentration of silica colloids. The lutidine-water mixture has a lower critical temperature point and heating causes the fluids to demix. The initially dispersed colloids in the single-phase fluids are created by agitation, using an ultrasound probe. Upon warming above the critical point for the spinodal decomposition, the separated fluids sweep out domains and colloids become trapped on the fluid-fluid interfaces. As the surface area decreases due to the coarsening dynamics, colloids are jammed together at interfaces. Eventually the bijel is obtained and it endures in a stable formation for a month.

Broadly the mechanism for bijel formation in experiment agrees with the hypothesis that inspired the simulations of [1]. In these simulations, a random initial state, with mean order parameter ψ_0, is generated at an initial temperature T_i where the single phase fluid is found (as seen in Figure 2.2). Suspended colloids are dispersed in this initial fluid. After deeply quenching below the spinodal line for the spinodal decomposition, the phase separation occurs in the fluids and eventually colloids are arrested at the fluid-fluid interfaces. Then coarsening dynamics reduces the surface area covered by these colloids.

For a pure binary fluid, the coarsening dynamics[81] is governed by "Model H" consisting of three dynamical regimes: diffusive, viscous hydrodynamics and inertial hydrodynamics. However, our simulations do not address the regime of inertial hydrodynamics which can be reached by varying the parameters in free energy.

In the early stage known as the "diffusive" regime, the thermodynamics of spinodal decomposition is determined by the free energy functional in equation (2.17); three parameters, A, B and κ in $F[\phi]$, determine the values of the interfacial width ξ and the interfacial tension σ. In the kinetics, the domain growth rate is observed as $L(t) \sim t^{1/3}$ for domain sizes up to $L \simeq (M\eta)^{1/2}$. The next process, "viscous hydrodynamic", is controlled by fluid viscosities; the domain size obey $(M\eta)^{1/2} \ll L \ll 100\eta^2/\rho\sigma$. (Here the prefactor 100 was found by Kendon *et al.*[25].) The time evolution of the growing domain is faster than the diffusive motion of coarsening: $L(t) \sim t^1$. Because this coarsening dynamics reduces the surface area, any colloids on the fluid-fluid interface become jammed together; this leads to a slow growth rate and in practice makes the size of domains remain smaller than $100\eta^2/\rho\sigma$ (as seen in Figure 3.3).

Evidence of a cooperative interplay of coarsening and colloid dynamics is also found in motions of colloids. The initial state at T_i provides the environment for colloids to diffuse: $R(t) \sim t^{1/2}$, where $R(t)$ is a root mean square displacement (RMSD). However, after the diffusive regime of fluid phase separation has ended, the coarsening as $L(t) \sim t^1$ creates a faster motion of colloids trapped at interfaces which continues until these colloids are jammed closely on the surface. In Section 3.3, motions of colloids are quantified by several measurements to see the time-dependent dynamics through the two-time RMSD. We also examine the interfacial ordering of colloids by the radial distribution function $g(r)$.

In the condition for the stability of colloids at the fluid-fluid interfaces, allowing for the curved geometry of these interfaces, the energy barrier to detach a colloid must include the geometry-dependent parameter α, so that total energy barrier is obtained as $\alpha\epsilon$, where $\epsilon = \pi\sigma a^2$ is the capillary energy and a is the radius of a colloid. The geometry-dependent parameter α is contributed by a crowded monolayer of particles causing complex curvature of local interfaces during coarsening. In the simple case for a particle on a flat surface, the energy barrier to separate a particle corresponds to $\alpha = 1$. In contrast, for a complicated geometry, α is hard to estimate precisely due to the complicated energy landscape. However if a layer might have pathways allowing sequential particle expulsion while continuously decreasing surface area, it would correspond to $\alpha = 0$. In Section 3.4, the parameter α is directly estimated from an activation energy calculated from the simulations at high temperatures, and a mechanism for residual dynamics at late times will be discussed.

This Chapter consists of four parts. In the next Section, the simulation parameters are discussed to interpret the corresponding parameters in laboratory experiments. In Section 3.2 and 3.3, the results for basic analyses of coarsening and motion of colloids will be shown. The final Section will show the analyses for the residual dynamics and present the direct estimation for α.

3.1 Simulation methods and parameters

Our simulations for colloids in a binary fluid are performed using the LB for a binary fluid in Section 2.2, the fluctuating LB for Brownian motions in Section 2.1.2, and the bounce-back on links (BBL) method for colloids on lattice grids as seen in Section 2.3. The protocol for a deep quench can be controlled by parameters, A, B and κ, in the free-energy function of equation (2.17). The initial mixed state at $T_i = \infty$ is set up as a randomly mixed single phase with a certain value of the conserved mean order parameter ψ_0. As discussed in Section 2.2.1, the minus sign of A drives the phase separation of the demixing fluids. A symmetric double well potential is used, with B having the same magnitude as A but with opposite sign; specifically, $-A = B = 0.002$ is chosen. With the last parameter $\kappa = 0.0014$, the interfacial width ξ and the interfacial tension σ are given as $\xi = 1.14$ and $\sigma = 1.58 \times 10^{-3}$ in lattice units (LU). For the LB section of the code, the fluid density and the viscosities of both fluids are $\rho = 1$ and $\eta = 0.1$ respectively. The fluid temperature is set as $k_B T = 2.133 \times 10^{-5}$ LU, within the range that ensures the stability of the fluctuating LB[69]. Monodisperse colloids are used with the radius $a_h = 2.3$, although ideally this size should be much larger than ξ for fully accurate simulation of colloids trapped at fluid-fluid interfaces. However, this size is acceptable for accuracy, and required for the efficiency of our LB simulations[1].

With the interfacial tension and the colloid radius given above, the capillary energy is obtained as $\epsilon = 0.026$ in LU so that $\epsilon/k_BT = 1230$.

In a colloid-free binary fluid, the hydrodynamic coarsening in the late stage obeys the dynamical scaling hypothesis[25], $L/L_0 = f(t/t_0)$, where the characteristic length (L_0) and time (t_0) scales are defined as

$$\begin{aligned} L_0 &= \eta^2/(\rho\sigma), \\ t_0 &= \eta^3/(\rho\sigma^2). \end{aligned}$$

With the parameters used in this work, the characteristic length and time can be calculated as $L_0 = 6.33$ LU and $t_0 = 401$ LU respectively. In a laboratory experiment, these parameters in LB can be interpreted to represent systems such as a short-chain hydrocarbon/water or hydrocarbon/alcohol mixture with $\rho = 10^3$ kg m^{-3}, $\eta = 9.3 \times 10^{-4}$ Pa s and $\sigma = 6.1 \times 10^{-2}$ Nm^{-2}. Hence the characteristic scales are given as $L_0 = 14$ nm and $t_0 = 0.22$ ns. Equating the simulated temperature $k_BT = 2.133 \times 10^{-5}$ LU to room temperature, 300 K, gives the practical radius $a_h = 5.1$ nm. In practice for a given particle size a_h, we can match to experiment the dimensionless control parameters: $\epsilon/k_BT = 1230$ and $a_h/L_0 = 0.363$. We also match τ_B/t_0, where $\tau_B = 6\pi\eta a_h^3/k_BT$ is the Brownian time for a single diffusive colloid. However all dimensionless control parameters of potential relevance can not be fully matched. For example, the Reynolds number, $Re = (dL/dt)\rho a_h/\eta$, can not be made as small as the true physical value, but it is smaller than unity, which is sufficient in simulations[82].

To design the type of hard-sphere-like colloids used in this work, only the short-range potential in equation (2.69) is considered with the parameters set as $\gamma = 10k_BT$, $h_0 = 0.1$, $\nu = 1.0$ and $h_c = 0.25$. In comparison to a perfect hard sphere, the cutoff h_c produces a larger effective particle size, $a_T > a_h$, so that is reflected in the positions of peaks in $g(r)$. The lubrication correction in equations (2.63) and (2.64) is not used in this work because this repulsive short-range cutoff is enough to keep the hydrodynamic interaction accurate even at close contact.

Most simulations in this chapter have used the $D3Q19$ model in a simulation volume $\Lambda^3 = 128^3$ with periodic boundary conditions. The volume $\Lambda^3 = 64^3$ was also used to explore some morphologies in a closed box with solid walls. The latter included a normal lubrication force for colloids within the cutoff $h_{lub} = 0.5$ between the plane of the wall and the surface of the colloid[15] (see Section 2.3.5).

For a large system of $\Lambda^3 = 128^3$ at a colloid volume fraction $\phi = 0.20$, a single run requires ~ 56 hours (so that $t_{final} = 10^6$ LU) on 256-processor 700MHz PowerPc 440 machine[83]. The runs with a small volume, $\Lambda^3 = 64^3$, have been done on a single Intel core2 2.4GHz for which $t_{final} = 10^5$ LU requires around 54 hours.

3.2 Coarsening dynamics of a binary fluid

This section focuses on the characteristics of domains in a binary fluid with various different initial ψ_0. The mean conserved order parameters are given as $\psi_0 = 0.0$, 0.1, 0.2, 0.3 and 0.4. These correspond to the volume ratios of two fluids, 50 : 50, 55 : 45, 60 : 40, 65 : 35 and 70 : 30. In most cases, the volume fraction of (monodisperse) particles is set as $\phi = 0.20$. To check the effect of concentration of particles, the time evolution of domain growth with $\phi = 0.25$ is also measured, to enable comparison with domain growth for $\phi = 0.20$.

In the morphology of fluid domains with colloids, one can expect a crossover between bicontinuous and dropletlike structures according to the volume ratio of the fluids. In principal, even at $\psi_0 = 0$, depercolated structures, like droplets, can originate from a viscosity mismatch of fluids, and from an asymmetry in the phase diagram. This work has the same viscosity value for the two fluids and a symmetric phase diagram, so that only volume asymmetry ($\psi_0 \neq 0$) can cause dropletlike structures. In addition, the case of a closed box is studied to see as well if the walls influence domain morphologies. Like the previous study[1], the time evolution of domain growth is measured at various ψ_0 with a particle fraction ϕ.

3.2.1 Domain morphology

In the spinodal decomposition of a colloid-free binary fluid, the threshold, ψ_p, where bicontinuity is lost, is found at $\psi_p \simeq 0.44 \pm 0.04$[84] theoretically, experimentally and by simulation. At ψ_0 around ψ_p, on quenching into the spinodal region, the initial diffusion forms a bicontinuous pattern, but at a later stage, when the coarsening is controlled by viscosity, the bicontinuous domain breaks into droplets.

Figure 3.1 presents the snapshots for $\psi_0 = 0.0, 0.1, 0.2, 0.3$ and 0.4 with $\phi = 0.20$ at $t = 5 \times 10^5$ LU corresponding to $t = 275$ ns in a periodic box. Although all configurations sustain these domain morphologies until the end of the time window, a slow residual dynamics is found to reduce their surface area. This slow dynamics is observed in the time evolution of domain growth. The following sections will discuss the residual slow dynamics.

In Figure 3.1(a), the bicontinuous domains present for $\psi_0 = 0$ remain even at $\psi_0 = 0.3$, which has strong asymmetry. In contrast, the quench of $\psi_0 = 0.4$ shows a dropletlike phase in Figure 3.1(b). Therefore, the threshold ψ_p lies between $\psi_0 = 0.3$ and $\psi_0 = 0.4$ for bicontinuity in a binary fluid with colloids. In the case of a closed box in a volume $\Lambda^3 = 64^3$, $\psi_0 = 0.0$ and 0.4 are considered to compare domain morphologies with the systems with a periodic boundary condition. Figure 3.2 shows the domain morphologies with $\psi_0 = 0.0$ and 0.4 at $t = 2 \times 10^5$ LU (corresponding to $t = 110$ ns);

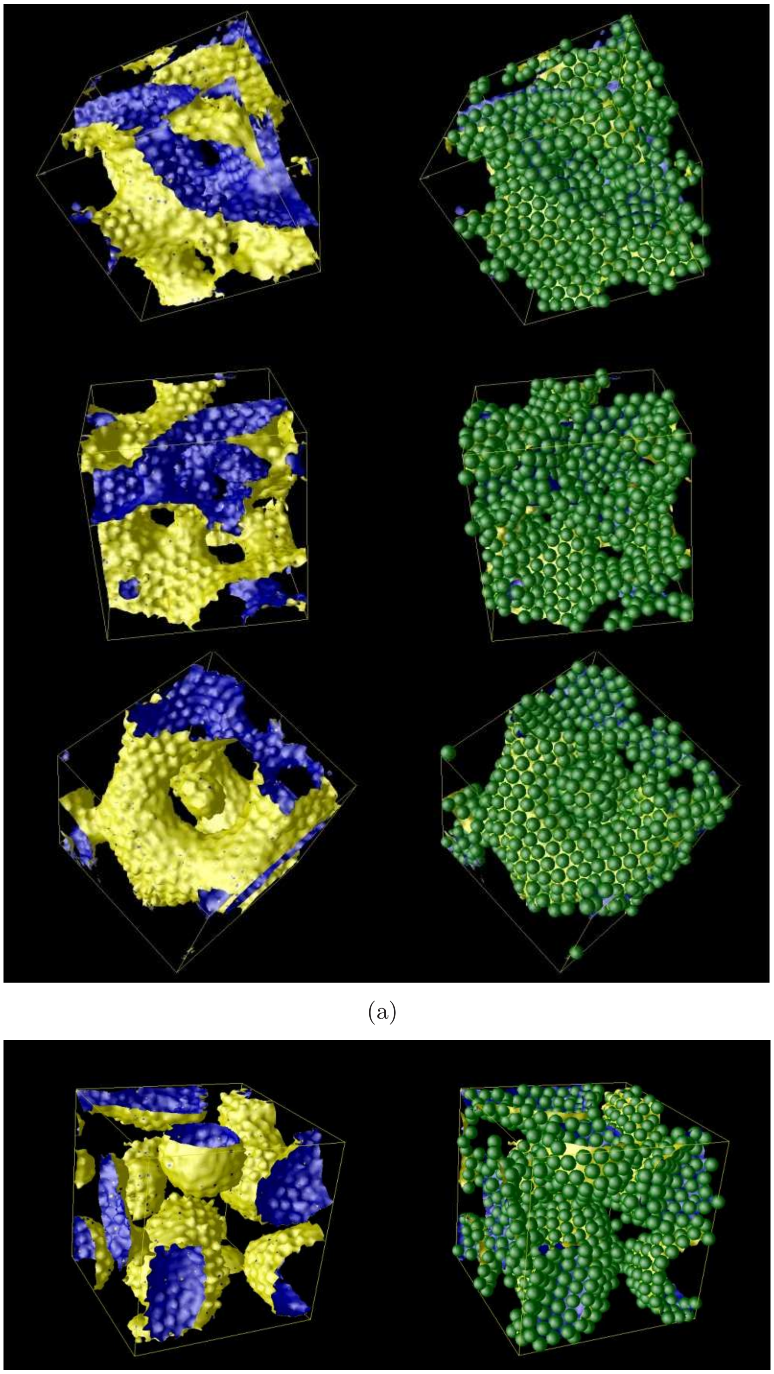

(a)

(b)

Figure 3.1: The morphologies in a periodic box for various ψ_0; lattice size $\Lambda = 128$ cropped to $\Lambda = 64$. The right side shows the fluid-fluid interfaces plus colloids given as spheres with a radius a_h. The left is the same image without particles and it shows the clear domain morphologies. (a) (top to bottom) $\psi_0 = 0.0, 0.1, 0.2$ and 0.3 for $\phi = 0.20$. (b) $\psi_0 = 0.4$ for $\phi = 0.20$.

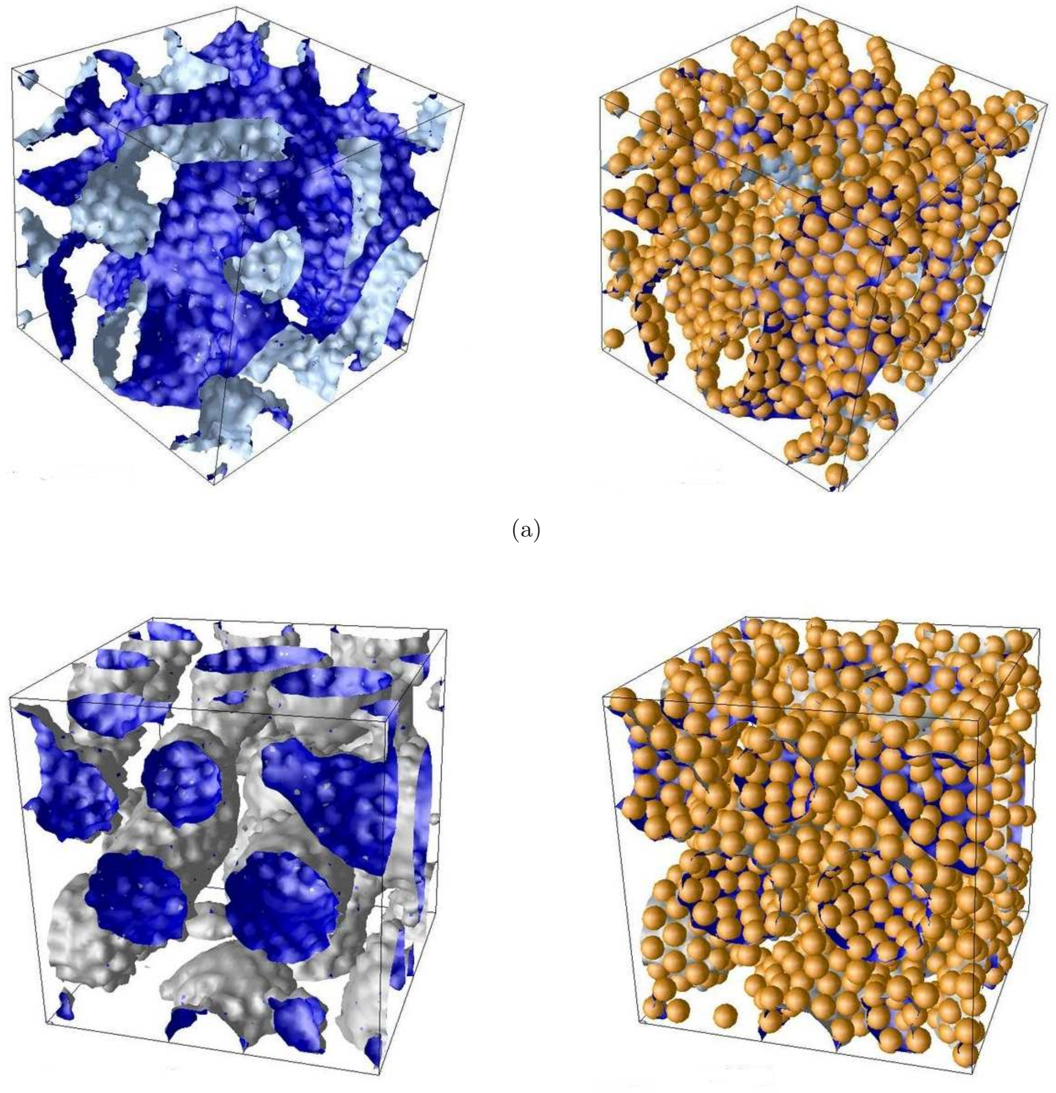

(a)

(b)

Figure 3.2: The morphologies in a closed box with solid walls. The right side shows the fluid-fluid interfaces plus colloids given as spheres with a radius a_h. The left is the same image without the particles and it shows the clear domain morphologies. (a) symmetry: $\psi_0 = 0.0$. (b) asymmetry: $\psi_0 = 0.4$. The boundary condition on the fluid order parameter at the solid walls is that of neutral wetting.

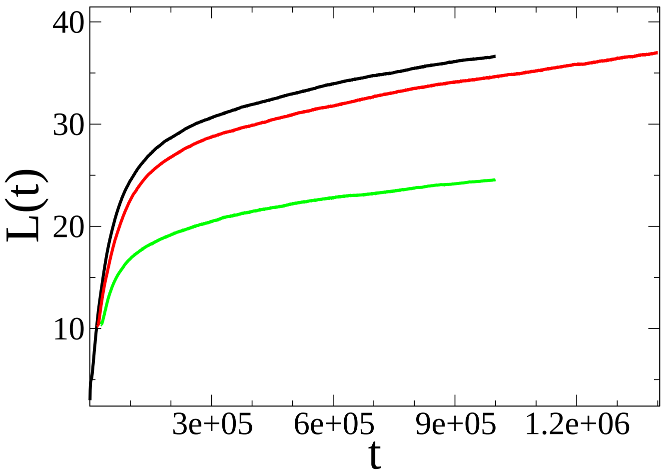

Figure 3.3: The time-evolution of domain size $L(t)$ for various quenches; (topmost curve) symmetric quench $\psi_0 = 0.0$ with $\phi = 0.20$; asymmetric quenches of $\psi_0 = 0.4$ with $\phi = 0.20$ (middle curve) and $\phi = 0.25$ (lowest curve). The lattice size is $\Lambda = 128$. The LB time scale $t = 10^6$ LU corresponds to $t = 549$ ns in lab; the domain length $L = 40$ LU corresponds to $L = 88.4$ nm in lab.

the main morphologies with symmetry and asymmetry are maintained, even though the neutral wetting condition holds between a solid wall and the fluid-fluid interfaces. Therefore, although neutral wetting might promote bicontinuity in principle, its effect on ψ_p is small in practice.

3.2.2 Domain growth kinetics

In the phase ordering kinetics, one can define the characteristic length scale $L(t)$ of the demixing domains[25] in a system with periodic boundary conditions as

$$L(t) = 2\pi \frac{\int S(k,t)dk}{\int kS(k,t)dk} \tag{3.1}$$

where $k = |\mathbf{k}|$ and $\mathbf{k}$ is a wavevector in Fourier space and $S(k,t)$ is the equal-time structure factor defined as

$$S(k,t) = \langle \delta\psi_k(t)\delta\psi_{-k}(t)\rangle. \tag{3.2}$$

Here, $\delta\psi_k(t) = \psi_k(t) - \psi_0$ and $\langle\cdots\rangle$ is an average over a shell at a fixed k.

Figure 3.3 shows the results of time evolution of $L(t)$ for a symmetric quench with $\phi = 0.20$ and asymmetric quenches with $\phi = 0.20$ and 0.25. These runs have time windows extending until $t = 10^6$ LU (double that of the previous study[1]), which is around one Brownian time as $\tau_B \simeq 10^6$ LU. The run with $\psi_0 = 0.4$ and $\phi = 0.20$ has been extended still further to $t = 1.4 \times 10^6$. However with our mapping of parameters, these time windows are still very short ($t = 0.55$ μs and $t = 0.77$ μs) in laboratory time. The $L(t)$ curve for a symmetric quench with $\phi = 0.20$ is the topmost line in Figure 3-3. This curve is similar to that found in the previous work[1]. After $t = 2 \times 10^5$ LU, the slow growth rate is observed in both studies; however, permanent arrest is not found in either. The domain size L reported here is larger than in the previous study due to the smaller effective radius a_T in this work. The $L(t)$ curves for asymmetric quenches with different particle fractions ($\psi_0 = 0.4$ with $\phi = 0.20$ and 0.25) are also presented in Figure 3.3. These lead to the droplet morphologies seen in Figure 3.1(b). Higher particle concentration makes the droplets smaller so that the domain length, L, is shorter than one with less concentration at any given time t. The droplet structures also have slow residual dynamics after a long time has elapsed (especially after $t = 2 \times 10^5$) and the next section will discuss these slow residual dynamics by the extensive analyses of colloidal motion. For $L(t)$ in a closed box, one cannot use the equation (3.1) but $L(t)$ can be determined from the spatial correlation function of $\psi(\mathbf{r})$ in real space[85, 86, 87] as also explained in Appendix D; this confined system has strong finite size effects. This thesis does not consider the analysis of $L(t)$ for non-periodic systems.

3.3 Dynamics of colloids at intermediate time

In the last Section, the characteristic length scale $L(t)$ showed continuously increasing domains of fluid at long times, $t \geq 2 \times 10^5$, instead of the fully steady state, originally envisaged in [1] as the result of colloidal arrest on the fluid-fluid interfaces. This section discusses colloidal motions, aiming to explain these slow residual dynamics. Since the simulations have a runtime of $t < \tau_B$, note that only the "intermediate" time regime is studied here. The final regime, $t \gg \tau_B$, still remains to be discussed.

To understand the slow dynamics, it is assumed that three candidates are involved: 1. the colloids slowly make a semi-crystal structure on the fluid-fluid surfaces allowing closer packing; 2. rearrangement due to the continuous ejection of particles from the interfaces caused by the smallest geometric barrier parameter α for a crowded layer; 3. numerical artefact in LB.

In this study, monodisperse spherical particles only are simulated. To see the time-evolution of configurations of colloids, a radial distribution function (RDF) $g_\Delta(r, t_i)$ is measured by averaging $g(r, t)$ over a time interval Δt starting from various initial times

t_i. Thus the time-dependent RDF is defined as

$$g_\Delta(r, t_i) = \frac{1}{\Delta t}\int_{t_i}^{t_i+\Delta t} g(r, t), \tag{3.3}$$

where $g(r, t)$ is a RDF at time t. The simulation results for g_Δ will be shown in Section 3.3.1 for the interfacial ordering of colloids. This allows us to probe candidate 1 above.

During the coarsening, it could be interesting to measure the contact angles of colloids on the interfaces with time. However, defining the exact interfaces on the lattice grid is very difficult at the crowded particles on the surface. Thus instead of measuring contact angles, a new time-dependent quantity is defined as the number of particles that have been ejected from the fluid-fluid interfaces. The detail will be shown in Section 3.3.2. In addition, the effect of thermal noise is studied there by switching off the stochastic term in equation (2.12) at $t = 4 \times 10^5$ LU. After switching off noise, colloids lose the property of Brownian motion, so that the motion of colloids becomes only dependent on hydrodynamic forces of fluids.

The second candidate, particle detachment, depends crucially on the parameter α. This is estimated directly from the activation energy and it will be discussed in Section 3.4.1. The interplay of the coarsening and the jamming smooths out the geometrical features with time so that α is time-dependent. Ideally α should be measured for time scales larger than one Brownian time, τ_B.

The final candidate, a numerical artefact of LB, cannot be totally ignored in our simulations. Particularly for the stabilisation of particles at fluid-fluid interfaces, the colloid radius should ideally be much greater than the interfacial width: $a_h \gg \xi$. However, in practice in LB, a_h is not too much larger than ξ as $a_h = 2.3$ and $\xi = 1.14$. It is possible that shallowly attached particles at interfaces could escape too easily to become free in the bulk fluids. However in previous work[1] high resolution tests of ripples and cylinders coated with colloids did not find any ejection of particles. To solve this issue requires the simulations of a full bijel with $a_h \gg 2.3$. But this is out of reach with current computational resources as a factor 2 radius increase requires a 10-fold increase in computational power.

3.3.1 Interfacial ordering

Figure 3.4 shows $g_\Delta(r, t_i)$ and time-evolution of the height of the first peak for a symmetric and an asymmetric quench with $\phi = 0.20$. The radial distribution function $g(r, t)$ measure the spatial ordering as

$$g(r, t) = \frac{2\Lambda^3}{N^2}\left\langle \sum_{i,j} \delta(r - r_{ij}) \right\rangle, \tag{3.4}$$

where r_{ij} is the distance between a pair of particles, i and j, and N is the number of colloids. This $g(r,t)$ is used to calculate $g_{\Delta}(r,t_i)$ in equation (3.3). The initial time t_i is given as $t_i/10^5 = 0.5n$, where $n = 1, 2, ..., 19$, and the time window for the average $\Delta t = 0.5 \times 10^5$ LU. The averaging over this time window reduces noise to acceptable levels while allowing the slow evolution of $g(r)$ to be detected.

Figures 3.4(a) and 3.4(b) show $g_{\Delta}(r,t_i)$ at $t_i/10^5 = 9.5$ for $\psi_0 = 0.0$ and 0.4. Clear peaks are found at the positions corresponding to hexagonal lattice scaled to the effective radius a_T. These peaks gradually increase with time in Figure 3.4(d). After $t = 2 \times 10^5$ LU where slow dynamics are found, the first peak tends to increase as particles slowly form a more crystalline layer.

After the thermal noise was switched off at $t = 4 \times 10^5$ LU, the $g_{\Delta}(r,t_i)$ for a symmetric quench is shown in Figure 3.4(c); the height of peaks is higher in comparison with the peak height of a symmetric quench with noise (seen in Figure 3.4(a)). This effect can be explained by the presence of metastable minima in the complicated energy landscape of the bijel. Less thermal energy allows it to fall into a local minimum of the total energy (the sum of the interfacial energy and interparticle energy). Therefore the height of peaks is sharper, but their positions are not changed. This probably means the layer of particles on the surface was effectively trapped in a state, close to a local metastable minimum, even prior to switching off the thermal noise.

3.3.2 Particle ejection

To quantify the ejection of particles, a free particle in either bulk fluid is identified as one which is not in contact with the fluid-fluid interface. In practice, a free particle is determined by the sign of the order parameter $\psi(\mathbf{r})$ within a distance $a_h + \sqrt{3}$ from the center of a particle. If all order parameters have the same sign, it is a free particle.

Figure 3.5 shows the time evolution of $N_f(t)$, the number of free particles. In Figure 3.5(a), showing both symmetric and asymmetric quenches, the $N_f(t)$ monotonically increases throughout the slow dynamics regime after $t = 2 \times 10^5$. The $N_f(t)$ in the dropletlike phase is remarkably higher than one in the bicontinuous phase. The higher ejection rate in the droplet phase results in a smaller surface area of the droplet compared to the bicontinuous phase. In the asymmetric case, most of the free particles are in the continuous phase rather than inside of droplets. This suggests that the droplets prefer detachment from the exterior surface. For a symmetric quench, the fraction of free particles in each fluid is almost equal.

Figure 3.5(b) shows the $N_f(t)$ switching off the thermal noise at $t = 4 \times 10^5$ LU in a symmetric quench. Soon after switching off noise, there is no significant ejection. However, at much late times, some ejection occurs. It is possibly happening when the

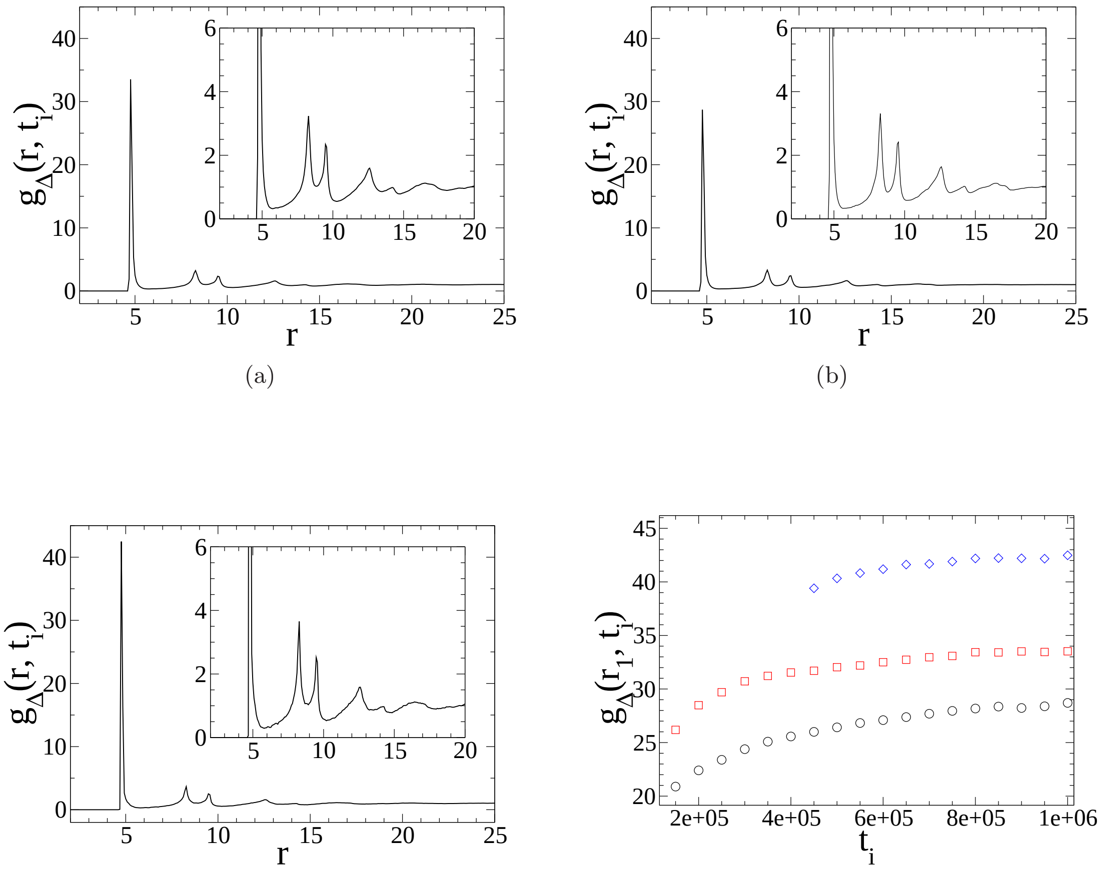

(a) (b)

(c) (d)

Figure 3.4: Late time $g_\Delta(r)$ for colloidal particles; the data is time averaged over the interval $9.5 \times 10^5 < t < 10^6$. (a) $\psi_0 = 0.4$. (b) $\psi_0 = 0.0$. (c) $\psi_0 = 0.0$ with thermal noise switched off at $t = 4 \times 10^5$. (d) time evolution of the first peak height for conditions (a)-(c) (bottom to top).

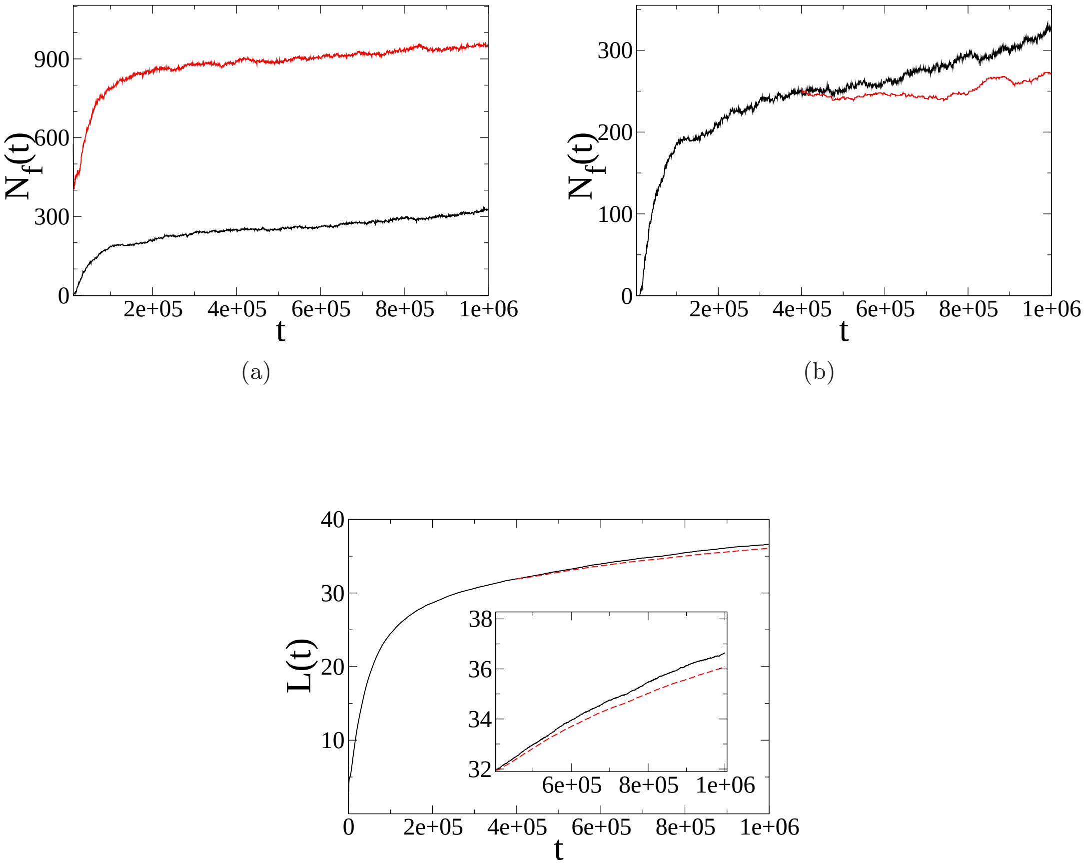

(a)

(b)

(c)

Figure 3.5: (a)Time evolution of the number of free particles $N_f(t)$ for droplets ($\psi_0 = 0.4$, upper curve) and a bicontinuous phase ($\psi_0 = 0.0$, lower curve) with $\Lambda = 128^3$, $\phi = 0.20$. (b) The upper curve is the same data for a bicontinuous phase (lower curve in Figure 3.5(a)) compared with the case where noise is switched off in $t = 4 \times 10^5$ (lower curve). (c) $L(t)$ data in Figure 3.5(b); (solid line) a symmetric quench; (dash line) the data after thermal noise is switched off. The inset of (c) is a zoom-in for the late times.

local force to drive the coarsening dynamics is enough to overcome the energy barrier to detach a colloid shallowly contacted to the fluid-fluid interface. The motion of a domain wall is driven by the mean curvature, H, having the relation as $\Delta P = \sigma H$, where ΔP is a finite pressure difference. In equilibrium, the H is zero for symmetric quenches so that the force acting to reduce curvature to $H = 0$ leads to the coarsening dynamics. In the situation after switching off the thermal noise, the geometry of interfaces covered by particles without Brownian motion controls the remaining coarsening dynamics, and leads not only the late-time ejection in Figure 3.5(b) but also a slow growth rate in Figure 3.5(c).

3.3.3 Colloid dynamics

Colloids in a thermal solvent exhibit Brownian motion with $R(t) \sim t^{1/2}$. For colloids in a binary fluid undergoing the demixing of fluids, one can expect time-dependent deviations from this according to the coarsening dynamics which defines the chance for colloids to be arrested and to be jammed at interfaces. The initial motion for colloids at T_i exhibits diffusive behaviour. Later the particles are trapped at the fluid-fluid interfaces. The velocity of trapped particles is first accelerated by the coarsening dynamics up to the speed of the moving interfaces, $dL(t)/dt \sim \sigma/\eta$, before the beginning of the residual slow dynamics, when the interfaces arrest. The transition time is around $t = 2 \times 10^5$ LU in Figure 3.3.

From the definition of RMSD (root mean square displacement), the time-dependent heterogeneous motions of particles can be quantified by the RMSD $R(t, t_w)$ between various waiting times "t_w" and later times $t_w + t$:

$$\langle R(t, t_w) \rangle = \left[\frac{1}{N} \sum_{i=1}^{N} |\mathbf{r}_i(t_w + t) - \mathbf{r}_i(t_w)|^2 \right]^{1/2} . \tag{3.5}$$

Figures 3.6(a) and 3.6(b) present the data for RMSD at the various t_w in symmetric and asymmetric quenches. In both cases the RMSD at a fixed time t monotonically decreases with t_w since the system is slowing down continuously at late time. For late waiting times, diffusive motion is seen in both the RMSD curves.

To examine the effect of thermal noise, the RMSD, after switching off the thermal noise, is measured and the data is shown in Figure 3.6(c) to compare with the data with the thermal noise, still present.

For $0 < t < 10^4$, there is clear evidence of a crossover in motion from diffusive ($R \sim 10^{-3}\ t^{1/2}$) to ballistic ($R \sim 10^{-5}\ t^1$) after switching off the noise in Figure 3.6(c). The motion without noise originates from the flow of particles by the residual coarsening of fluid-fluid interfaces. The RMSD data also show that the particle motion after $t = 10^4$ is slower than the motion with thermal noise, despite the change from diffusive to ballistic character.

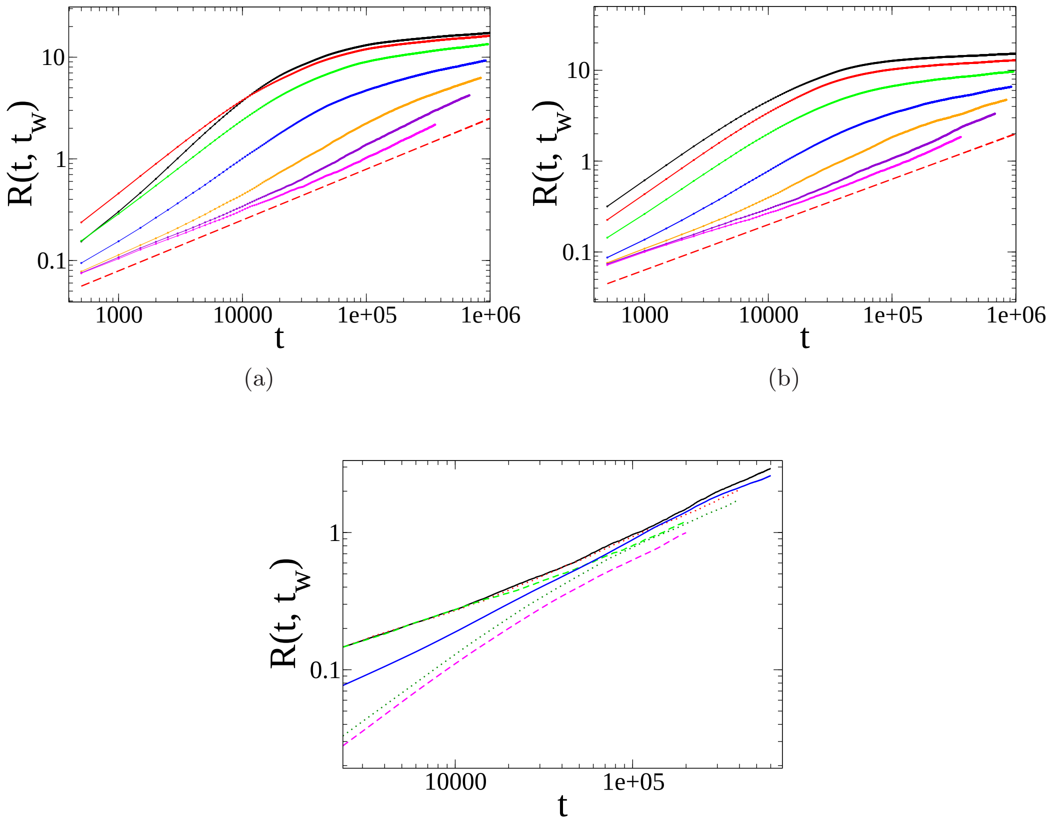

(a)

(b)

(c)

Figure 3.6: Log-log plots of $R(t, t_w)$, for $t_w/10^4 = 2^n$, $n = 0, 1, 2, ..., 6$ with (a) $\psi_0 = 0.4$ and (b) $\psi_0 = 0.0$. (c) curves for $t_w/10^5 = 4, 6$ and 8 at $\psi_0 = 0.0$ are compared with and without thermal noise switched off at $t = 4 \times 10^5$. Solid lines are at $t_w/10^5 = 4$; dotted lines are at $t_w/10^5 = 6$; Dashed lines are $t_w/10^5 = 8$; Upper three curves are for the data with thermal noise; other three curves below are for the data without thermal noise. Straight line in (a,b) represents diffusive motion with slope 1/2.

3.3.4 Droplet dynamics

Figure 3.7 presents the time evolution of a single droplet obtained within the quench at $\psi_0 = 0.4$ in $\Lambda^3 = 128^3$. The shape of the stable droplets covered by the colloids is determined by the number of particles trapped at the interface at early times, while a stable droplet of a colloid-free binary fluid will inevitably have a spherical shape. However, for the droplet covered by colloids, local crystallinity is clearly found on the

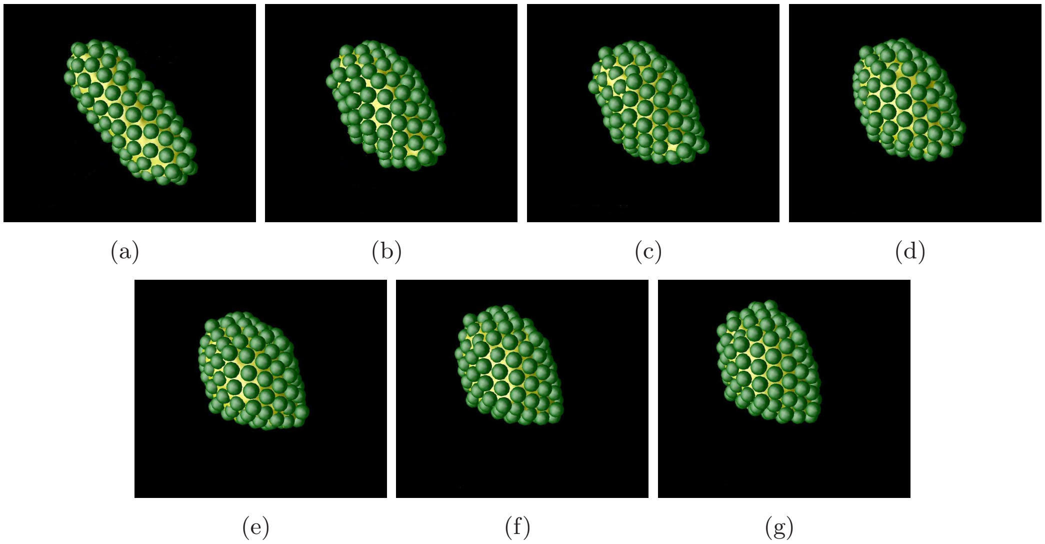
(a) (b) (c) (d) (e) (f) (g)

Figure 3.7: Snapshots for time evolution of a droplet shape; (a) $t = 1 \times 10^5$; (b) $t = 2 \times 10^5$; (c) $t = 3 \times 10^5$; (d) $t = 4 \times 10^5$; (e) $t = 5 \times 10^5$; (f) $t = 10 \times 10^5$; (g) $t = 14 \times 10^5$.

facets of a droplet. The ellipsoidal shape is maintained after $t \sim 5 \times 10^5$ LU, and for the droplet (with ~ 120 particles) shown in Figure 3.7, no particle ejection occurs after $t \sim 5 \times 10^5$. In the similar system such as a liquid-gas system, colloidal-armoured gas bubbles[88, 89, 90] have both the spherelike shape and the nonspherical shape in experiments.

3.4 Discussion of mechanism and residual dynamics

In Section 3.2 and 3.3, the analysis for the behaviour of particles showed that the slow dynamics in the domain growth for $t > 2 \times 10^5$ results from the semi-crystallisation of particles on the surface and from the ejection of particles at the fluid-fluid interfaces. In the case of switching off the thermal noise, it was found that Brownian motion does not completely stop the ejection of particles; the remaining coarsening still plays a role in the slow domain growth. Therefore the residual slow dynamics presumably arise from the interplay of the crystallisation and the remaining coarsening. The RMSD results also support this conclusion in both the thermal and athermal cases.

To understand the residual dynamics, remember that the simulation time window in this work is not much longer than Brownian time scale, $\tau_B \simeq 10^6$ LU. This relatively short time scale could be responsible for the residual dynamics; after particles have joined the fluid-fluid interfaces, they require some time to achieve the local equilibrium with respect to the interfacial energy and inter-particle energy. Even if the interfaces are nearly flat (α is not small), until $t \simeq \tau_B$, continuous ejection of some particles which are attached shallowly to the interfaces can occur. These particles have relatively low detachment energy barriers. Afterwards, particle ejection could decrease and then finally stop. Indeed α seems to be time-dependent, decreasing with the ejection of particles and the coarsening of fluids. Also a broad distribution of energy barrier heights could cause very slow "aging" dynamics on Brownian time scales. In the rest of this Section, the geometry-dependent parameter α will be discussed to explain the residual dynamics.

3.4.1 Direct estimated activation energy barrier

An activation barrier E_A to particle ejection can be estimated from the Arrhenius equation as applied to the ejection rate r: $r(T) = r_0 \exp(-E_A/k_BT)$. Here r_0 is generally a diffusive factor, called the"attempt frequency", with the unit s^{-1} given as $r_0 \simeq \tau_B^{-1} \propto k_BT$. In practice, this expression becomes reliable when $t \gg r_0^{-1}$ so that the escape process is sampled on time scales large compared to the attempt frequency for the barrier crossing process. On the other hand, even though r_0 is generally temperature-dependent, one can expect a temperature-independent rate reduction in the case of the crowded layers. Entropic barriers in the crowded layers could reduce the diffusivity leading to a decrease of the attempt frequency so that detachment requires a longer time scale to be seen. In this case, the rate reduction is temperature-independent as it is entropy-controlled, not energy-controlled. Thus this contribution is not directly visible in E_A.

For calculation of E_A, the runs with $\psi_0 = 0.0$ with $\phi = 0.20$ are simulated at eight higher temperatures up to $k_BT = 2 \times 10^{-4}$ LU. The highest temperature 2×10^{-4} LU is the upper limit to ensure accurate simulations in LB[69] and the corresponding Brownian time is $\tau_B \simeq 10^5$ LU which is 10 times smaller than τ_B at $k_BT = 2.133 \times 10^{-5}$ LU. (The latter corresponds to the room temperature ~ 300 K in a lab.) In the final stage (after $10\tau_B$) with $k_BT = 2 \times 10^{-4}$ LU, 20% of particles become free in either fluid, compared to the number of particles initially trapped at the interfaces.

At each temperature, the ejection rate r is deduced from the number of trapped particles on the interfaces with time, $N_T(t)$. This can be obtained by subtracting $N_f(t)$ from the total number of particles $N = N_T + N_f$.

In a simple activated process, the trapped particles N_T can be formulated as a function of time: $N_T(t) = N_0 \exp(-rt)$, where N_0 is the initial number of particles on the interface. Figure 3.8 shows the number of trapped particles against t in log-linear scales as seen in Figure 3.8(a), and against t/τ_B in log-linear scales as seen in Figure 3.8(b). In the early time region of Figure 3.8(a), curvature is seen at all temperatures.

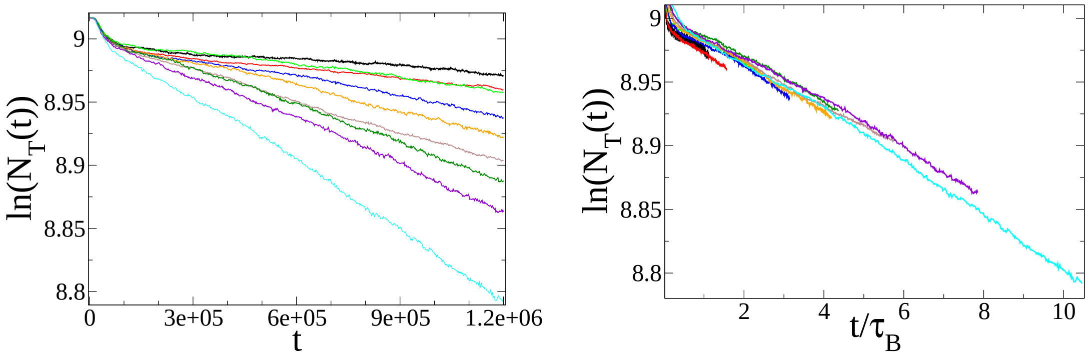

(a)

(b)

Figure 3.8: Number of trapped particles N_T in log-linear plot for temperatures (from top to bottom at extreme right) $10^5 k_B T = 2.13, 3^\dagger, 4.5, 6, 8, 11^\dagger, 12.5, 15$ and 20. Those marked with †symbol are averaged over two runs; the variation in the late-time slope is about ±10%. (a) $\ln(N_T(t))$ vs t. (b) $\ln(N_T(t))$ vs t/τ_B, where τ_B is the Brownian time for each corresponding temperature.

Especially for $t < 10^5$, the curves look overlapped, but in the plot on the scale t/τ_B instead of t, the overlapped curves are not seen anymore but the same shape of curves at all temperatures are found. In both Figures 3.8(a) and 3.8(b), straight slopes are clearly found only at the late times, $t/\tau_B \geq 3.5$, and at higher temperatures. Thus reliable ejection rates $r(T)$ can be obtained at four temperatures. In regard to the local thermal equilibrium of particles, $t/\tau_B \geq 3.5$ is a reasonable scale to be satisfied with our assumption mentioned above, that particles take some time to achieve such equilibrium.

From the ejection rate r found in Figure 3.8, two different analyses are considered, with r_0 either temperature dependent or not. The standard analysis of the Arrhenius plot assumes that r_0 is diffusive and linear in temperature. In this analysis, E_A is estimated by fitting the plot with $\ln(r/k_B T)$ versus $1/k_B T$. However, the results of this fit in Figure 3.9(a) are quite poor; the E_A is 7.0×10^{-5} with an uncertainty $\pm 2.0 \times 10^{-5} (\sim 30\%)$. Interestingly better results are obtained by the fitting assumed by non-diffusive r_0. This can be explained if the barrier-crossing attempt rate is fixed by the coarsening dynamics of interfaces rather than only the diffusion of the particles. Figure 3.9(b) is the Arrhenius plot with non-diffusive r_0; it gives an activation barrier $E_A = 2.2 \times 10^{-4} \pm 1.6 \times 10^{-5}$ and $r_0 = 5.5 \times 10^{-7} \pm 7 \times 10^{-8}$.

Our previous simulations had $k_B T = 2.133 \times 10^{-5}$ LU corresponding to 300 K in the lab. Although the running at this temperature for $t/\tau_B \geq 3.5$ is out of our simulation window, the E_A could be estimated by considering all data after $t > 6 \times 10^5$ LU. Figure 3.9(c) shows ejection rates at all temperature after $t > 6 \times 10^5$ LU. On decreasing

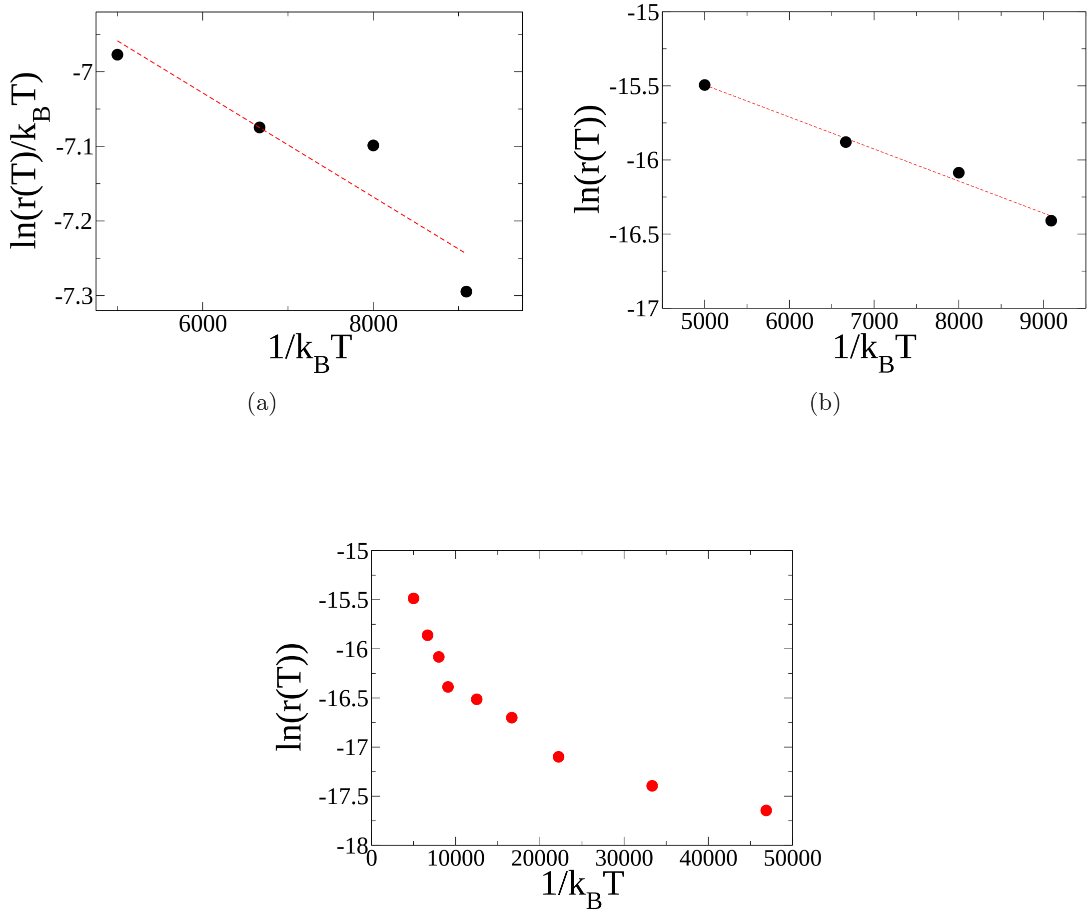

(a)

(b)

(c)

Figure 3.9: Arrhenius plots for the four highest temperatures. Dotted line is the result of linear least square fit. (a) plot of $\ln r/k_B T$ vs $1/k_B T$ for the standard analysis with r_0 assumed to be diffusive. (b) plot of $\ln r$ vs $1/k_B T$ for r_0 assumed to be non-diffusive. (c) plot of $\ln r$ vs $1/k_B T$ for non-diffusive r_0 fitted after $t > 6 \times 10^5$ at all temperatures.

temperature, increasing errors are found in r fitted after $t > 6 \times 10^{-5}$: the error of r at $k_BT = 2.133 \times 10^{-5}$ LU is 2.5 times larger than at $k_BT = 2 \times 10^{-4}$ LU, but the error bar is smaller than the size of symbol in Figure 3.9 so that the error could not been plotted together. Despite the relatively poor statistics, analysis of these curves would lead to systematically smaller scopes at lower T, so that a smaller E_A than the one quoted above is obtained at $k_BT = 2.133 \times 10^{-5}$ LU.

In summary, by analysing data within the temperature range studied (up to 2×10^4 LU), we find $E_A < 10k_BT$ for $k_BT = 2.133 \times 10^{-5}$ LU, corresponding to lab temperature for 5 nm particles. Using E_A to calculate the $\alpha\epsilon$ with $\epsilon/k_BT = 1230$, the geometry-dependent parameter α is given as $\alpha \leq 8 \times 10^{-3}$. This is very close to zero but not exactly zero. This small α might come from weakly attached particles whose ejection rate is due to the very low barriers in the late time window, $3.5\tau_B \leq t \leq 10\tau_B$.

3.4.2 Domain growth kinetics at high temperatures

Figure 3.10 shows the time evolution of domain growth with time scaled as t/τ_B at all temperatures. At the three lowest temperatures (for $10^5 k_BT = 2.133, 3$ and 4.5) in Figure 3.10(a), the domains gradually grow but do not have any particular trend in growth rate. Interestingly, for higher temperatures within the time window $t/\tau_B \geq 3.5$ in Figure 3.10(b), the domain size grows as "apparent" power law with $L(t) \sim (t/\tau_B)^\beta$, where $\beta = 0.25 \pm 0.01$. At two intermediate temperatures shown in Figure 3.10(a), this power law appears for $t/\tau_B \geq 3.0$, although the run time in these cases was not long enough to obtain ejection rates. However the apparent power law does not match any relevant theory in growth kinetics[84, 91, 92, 93]. Also, the range of L for which the apparent power law is seen remains quite narrow (a factor of 2). Presumably the behaviour of domain growth might be related to the activated process to eject particles. This is consistent with the onset of the power law regime after an indication time that scales with τ_B ($t/\tau_B \geq 3.5$). Thus, the growth kinetics of colloids in a binary fluid remains a open question.

3.5 Conclusions

This chapter presented in detail new LB simulations of nanoparticles in a binary fluid undergoing demixing after a deep quench at various initial fluid compositions ψ_0. Across various volumes of the two fluids, the threshold for the depercolation to droplets was found as $0.3 < \psi_p < 0.4$ which is somewhat lower than that for a colloid-free binary fluid. In domain growth kinetics, although a wider time window ($t = 10^6$ LU) was chosen for this work than in previous studies[1], we did not obtain a permanent arrested

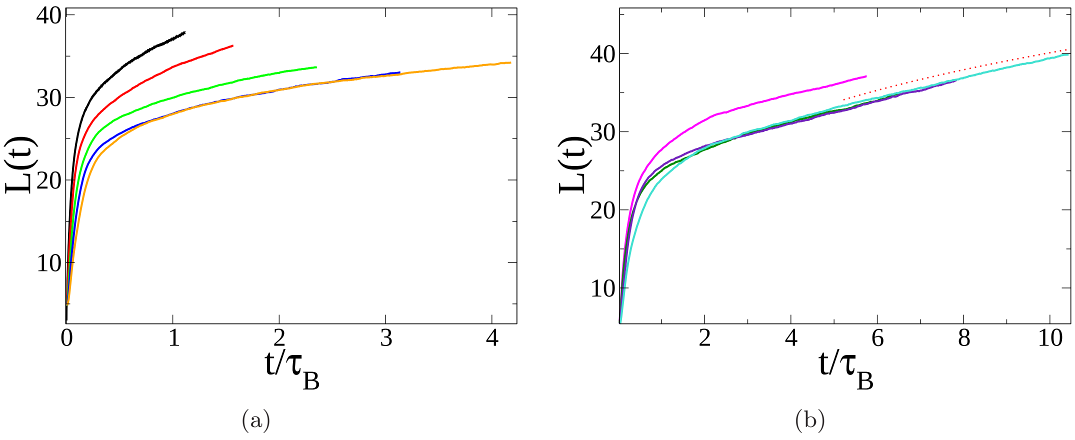

(a)

(b)

Figure 3.10: Time evolution of domain size at temperatures: (a)$10^5 k_B T = 2.13, 3^\dagger, 4.5, 6$ and 8. (b) $10^5 k_B T = 11^\dagger, 12.5, 15$ and 20. Those marked with †symbol are averaged over two runs; the variation in the late-time slop is about ±10%. The red dashed line shows the power law with the exponent $\alpha = 0.25 \pm 0.01$. Colours of lines are matched with the lines in Figure 3.8. The domain length $L = 40$ LU corresponds to $L = 88.4$ nm in lab.

state. Slow residual dynamics were found for the late time regime ($t > 2 \times 10^5$ LU) giving domain growth for both symmetric and asymmetric quenches. To explain these slow residual dynamics, we presented extended analyses for the post-arresting dynamics of colloids during the intermediate time scales, $t \simeq \tau_B$. These slow dynamics appear to involve particle ejection, and particle rearrangement to produce local crystallisation at interfaces for packing. The pair correlation functions, $g(r)$, reveal that colloids rearrange toward the higher packed ordering and the height of the first peak at late time slowly increases. During the intermediate time regime, the Brownian particles do not achieve local thermal equilibrium so that they can escape from the interfaces. Therefore the number of free particles present continuously increases. The time evolution of a single droplet shows relaxation toward the ellipsoidal shape including facets with local crystallisation.

In contrast to our simulations showing the slow evolution, the bijels in experiments sustain their stable arrested structures for a month, far beyond the time scales accessible in LB simulation. It is possible that ejection of particles results from tenuous contact between particles and also involves a numerical artefact in LB combined with the complex geometry of interfaces during the coarsening dynamics of fluids. In LB the size of colloids and the interfacial width do not obey $a_h \gg \xi$. Increasing a_h by a factor 2 costs a 10-fold increase in computational power currently. The complicated geometry of interfaces is estimated from the activation energy E_A deduced from the ejection rates at various temperatures up to $k_BT = 2 \times 10^{-4}$ LU (shown in Section 3.4.1). Remembering that the E_A is set as the energy barrier to detach a particle, $\alpha\epsilon$, the geometry-dependent parameter α was obtained as ~ 0.008 leading to a much smaller effective energy barrier to eject particles than the corresponding barrier for a single particle on a flat interface. This small activation barrier might be caused by a breakdown of local equilibrium for arrested colloids during short time scales compared to their Brownian time τ_B. This could produce a population of weakly bound particles at interfaces until time $t \gg \tau_B$.

Section 3.4.2 discussed the growth kinetics at various temperatures. At high temperatures for $t/\tau_B \geq 3.5$, an apparent power law growth is found as $L(t) \sim (t/\tau_B)^{0.25\pm0.01}$ over a factor 2 interval in domain size. Since we do not understand the residual dynamics causing behaviour, it remains an open question to investigate in detail this aspect of the growth kinetics of the bijel.

Chapter 4

Magnetic Colloids in a Single Fluid

During the last two decades, many simulations of colloidal ferrofluids ("magnetic colloids in a single solvent") have confirmed that dipolar colloids form particular aggregated structures aligned like chains. Exploiting the development of computational power, the equilibrium phase behaviour[7, 8, 94, 95] and dynamical processes of chain-like structures[96, 97] have been investigated by several simulation methods: molecular dynamics (MD)[53, 98, 99, 79], Brownian dynamics (BD)[100, 101, 97] and Monte Carlo (MC)[49, 9, 102]. Among these recent simulation works, only Mériguet *et al.*[101] have considered indirectly the hydrodynamic interactions using Brownian dynamics to study the orientational relaxations in charge-stabilised ferrofluids. However, none of these studies fully considers hydrodynamic forces, derived from a solvent, acting on magnetic colloids.

In this chapter, LB simulations for colloidal ferrofluids are investigated to see how fully many-body hydrodynamic interactions play roles in equilibrium and transient dynamics for cluster formation. In contrast to the Brownian dynamics used by Mériguet *et al.*[101], our LB method calculates the full hydrodynamic forces deduced by the momentum transfer of moving solid particles in fluids. The detail of our LB method was discussed in Section 2.3. Generally speaking in Stokes flow, it is well-known that the hydrodynamic interactions acting on colloids only affect their dynamics, but not equilibrium structural properties. Thus, this chapter has regard to three points: the structural properties and the dynamics in equilibrium, and transient motions during formation of clusters. First, the structural properties of magnetic colloids in equilibrium are studied by LB, BD and MC. We use BD, in which many-body hydrodynamic interactions are absent, so all simulations in LB are compared with those in BD to check the effect of hydrodynamic interactions. In addition, MC data[103] is compared with data for equilibrium statistics found by BD and LB in order to check the accuracy of static properties.

In colloidal ferrofluids, one of the most interesting features is the aggregated structures based on a nose-to-tail formation[44]. This originates from the long-range dipolar interactions, which depend anisotropically on the positions of dipoles and orientation of dipole moments, but which tend to make dipoles aligned in low energy states. In the case of two dipolar hard spheres, the lowest energy state is found at the nose-to-tail configuration with the bonding dipolar energy $-2\lambda k_BT$, where λ is the dipolar coupling constant discussed in Section 2.4.5. In a bulk ferrofluid, the phase of magnetic colloids is controlled by the particle fraction ϕ and the dipolar coupling constant λ[6, 7] (see Figure 1.4). In this chapter, all simulations have been done in conditions of ϕ up to 20% and λ up to 8. For accurate simulations in a periodic boundary box, the long-range dipolar interactions are accomplished by Ewald summation. The following Section 4.1 will discuss the detailed simulation parameters for magnetic colloids and a fluid. Especially, the parameters of the short-range potential will be discussed in detail, because the short-range potential used in LB simulations is chosen not only to prevent the overlap of colloids but also to reduce the discretisation error in noise forces at close contact of colloids.

In the simulation results, Section 4.2 presents the equilibrium static properties which are quantified by the radial distribution functions, the equilibrium energies including the long-range potential energy, U^d/Nk_BT, and the short-range potential energy, U^{sc}/Nk_BT. The data from both LB and BD are presented alongside the data from MC to check the accuracy in equilibrium. Also the equilibrium dynamics are measured through the dynamic correlators which describe the relaxations of particles by translational and rotational modes. These correlators represent the time-relaxation of structure in Fourier space q from which the diffusion coefficients are obtained as a function of q according to the time scales for Brownian motions (short-time Brownian and long-time Brownian).

In dilute colloidal systems with hydrodynamic interactions[104], the relaxations can be divided into three regimes by the time scale for the diffusion relaxation ($\tau_D \equiv 6\pi\eta a^3/k_BT$) and the velocity relaxation time ($\tau_v \equiv m/6\pi\eta a \sim 2a^2\rho/9\eta$) which is the same scale of the fluid momentum relaxation time ($\tau_\eta = a^2\rho/\eta$). These three regimes are the pre-Brownian, the short-time Brownian and the long-time Brownian; the characteristics of these motions are clearly seen at the dynamic correlators. Especially the diffusive behaviour is observed as the exponential decay in the dynamic correlators. For $t \ll \tau_v$, the motion of colloids are evolved by the collision with fluids, so that non-diffusive motion appears. After this ballistic motion, colloids are diffusive before they encounter other particles. So on increasing the concentration of colloids, the duration of this short-time diffusive motion is shortened due to caging by neighbouring colloids. Generally short-time motion has the time scale "$\tau_v \ll t \ll \tau_D$". Lastly, for a long time ($t \gg \tau_D \equiv 6\pi\eta a^3/k_BT$), colloids show the diffusive motion characterised by a distance comparable to a radius of colloid. In comparison with the distance that particles travel on the long-time Brownian time scale, particles hardly move during the short-time

Brownian regime.

However, hydrodynamic effects are observed even at the short-time Brownian timescale. Indeed, from the short-time diffusion coefficients ($D_s(q)$) and the static structure factor ($S(q)$), the "hydrodynamic factor" $H(q)$ can be calculated. In contrast, $H(q)$ is always unity in colloidal systems without any hydrodynamic interactions. In Section 4.3, we will discuss the relaxations of dynamic correlators and the hydrodynamic effect on the short-time Brownian regime by comparing LB and BD simulations for the various λ.

In Section 4.4, transient dynamics will be discussed to quantify the process of cluster formation after quenching from configurations equilibrated with $\lambda = 0$ to ones with $\lambda \neq 0$. In a previous study in 2D Brownian dynamics simulations of dipolar fluids[97], the aggregation kinetics has been monitored using the time-evolution statistics of cluster sizes. Using the same analysis as for the 2D model, the probabilities of cluster sizes are measured here in LB and BD runs for 3D ferrofluids. The relaxation of energetic quantities will be also discussed to support our interpretation of the aggregation process. Therefore, Section 4.5 will discuss the transient scattering functions to see time-dependent correlations at various initial times t_w for each ϕ and λ.

4.1 Simulation parameters

In LB simulations for colloidal ferrofluids, monodisperse colloids (with a radius $a = a_h = 2.3$ LU) are used in a fluid of temperature $k_BT = 5 \times 10^{-5}$ LU and viscosity $\eta = 1/40$ LU. These choices optimise the computational efficiency and stability. The thermal fluid is handled by the fluctuating lattice Boltzmann method (discussed in Section 2.1.2) on a $D3Q19$ lattice. For comparison, a simple BD algorithm of matched bare particle diffusively D_0 is used to simulate dipolar colloids. The detail of the BD algorithm is presented in Appendix A.

With this parameter set for a, k_BT and η, the relaxation times are calculated as

$$\begin{aligned}
\tau_v &= m/6\pi\eta a_h \sim 2a^2\rho/9\eta \sim 50 \text{ LU}, \\
\tau_\eta &= a^2\rho/\eta \sim 210 \text{ LU}, \\
\tau_D &= 6\pi\eta a^3/k_BT \sim 115{,}000 \text{ LU},
\end{aligned}$$

where τ_v is the velocity relaxation time, τ_η is the fluid momentum relaxation time for local equilibrium around a particle (whose time scale is similar to τ_v), and τ_D is the diffusive relaxation time. For a single particle, the translational diffusion coefficient is given as $D_0 = 4.6132 \times 10^{-5}$ LU.

To achieve magnetic colloids in a periodic box, Ewald summation is used to calculate the long-range dipolar interactions in Section 2.4.2. As mentioned previously, the short-range part of the interaction potential is designed to reduce the error of noise for close contact colloids. The following section will discuss the parameters for interaction potentials for magnetic colloids in detail.

4.1.1 Interaction potentials for magnetic colloids

To specify our magnetic colloids, the total potential is given as the sum of the short-range potential $U^{sc}(h_{ij})$ and the long-range potential $U^{d}(\mathbf{r}_{ij}, \hat{\mathbf{s}}_i, \hat{\mathbf{s}}_j)$:

$$U_{ij} = U^{sc}(h_{ij}) + U^{d}(\mathbf{r}_{ij}, \hat{\mathbf{s}}_i, \hat{\mathbf{s}}_j), \tag{4.1}$$

where $\mathbf{r}_{ij}$ is the centre-to-centre vector of the pair particles, i and j, and $\hat{\mathbf{s}}_i$ is the unit vector of the dipole on a particle i. The distance h_{ij} is the surface-to-surface separation for particle pair i and j, given as $h_{ij} = r_{ij} - 2a$ with $r_{ij} = |\mathbf{r}_{ij}|$.

In LB simulations for colloids, the choice of parameters for $U^{sc}(h_{ij})$ in Section 2.4.1 is an important issue for equilibrium static structures represented by the radial distribution functions and total energy. Colloidal Brownian motion in LB is induced by the thermal lattice fluid surrounding the colloids. However close-contact particles feel a lack of thermal fluctuation due to losing lattice points in the gap between colloids (see Figure 2.4). This makes an inevitable error in the short-range ordering, detectable in $g(r)$ and equilibrium energies, even though this effect is ignorable for the long-time Brownian motion and the static structure factor. To reduce this error, a fairly repulsive short-range potential is used, with the parameters $\gamma = k_BT$, $h_0 = 1.0$ and $h_c = 1.2$ in equation (2.69), to prevent loss of lattice points. More detail of the parameter steering will be shown in the following.

Short-range potential

For accurate simulations, we searched for the optimal parameters for short-range potential using the comparison with $g(r)$ in equilibrium. Figure 4.1 shows three sets of the short-range parameters examined to find the most effective parameters. Most test runs ignore the long-range interactions which means $\lambda = 0$; only the particle fraction $\phi = 0.10$ is considered, in $\Lambda^3 = 64^3$. The steepest curve, SP1, is the parameter set used to simulate colloids or magnetic colloids in a binary fluid in Chapters 3 and 5. However, in Figure 4.2(a), the curves of $g(r)$ obtained by LB and BD show significant discrepancy for distances $r/(2a) < 1.5$. The equilibrium energy, U^{sc}/Nk_BT, also shows a discrepancy between 0.0098 (LB) and 0.0113 (BD). In the case with long-rang dipolar interactions, e.g. $\lambda = 4$, the energies in LB do not agree with those in

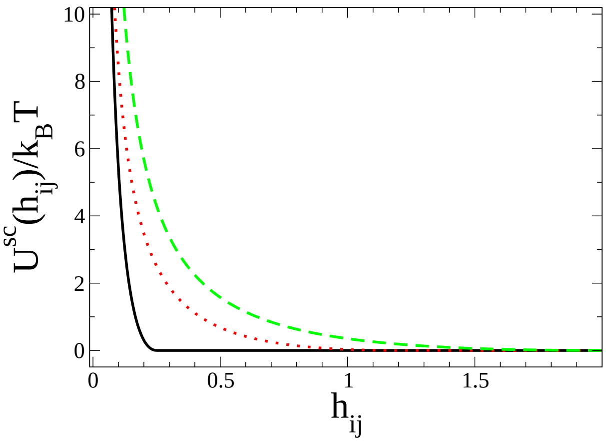

Figure 4.1: Short-range potentials $U^{sc}(h_{ij})$: (Black solid line) "SP1" has $\gamma = 10k_BT$, $h_0 = 0.15$, $\nu = 1.0$ and $h_c = 0.25$; (red dotted line) "SP2" has $\gamma = k_BT$, $h_0 = 1.0$, $\nu = 1.0$ and $h_c = 1.2$; (green dashed line) "SP3" has $\gamma = k_BT$, $h_0 = 1.4$, $\nu = 1.0$ and $h_c = 2.0$.

BD: for U^d/Nk_BT, we find values -4.214 (LB) and -3.788 (BD); for U^{sc}/Nk_BT, 0.062 (LB) and 0.060 (BD).

Figure 4.2(b) shows the data of $g(r)$ in LB and BD runs with the parameter set SP3. Both have good agreement for all range of distance $r/2a$. However, the particle repulsion is now quite "soft". The middle curve 'SP2' in Figure 4.1 is also examined as a candidate for a better compromise between efficiency and approximately hard-core behaviour. This set 'SP2' is proved quite acceptable and is actually chosen below for all simulations to study colloidal ferrofluids. In Section 4.2, the static structure properties will be presented for runs by LB, BD and MC: Figures 4.4-4.6 will show the radial distribution functions; the equilibrium energies will be seen at Table 4.1. In each case, agreement between the methods is satisfactory. Thus parameter set 'SP2' is an accurate and efficient choice to set up the generic model for ferrofluids used in this work.

To model specific ferrofluids numerically, the short-range potential is determined by the type of ferrofluid. For instance, in contrast to ferrofluids consisting of magnetic colloids made by magnetite(Fe_3O_4) in hydrocarbons, the charge-stabilised ferrofluids, using magnetic colloids produced by an iron-core plus organic acid shell[46, 47, 105], have a screened Coulomb interaction. For modelling such ferrofluids, a Yukawa repulsive potential should use alongside the long-range dipolar interactions and the effect of this soft repulsive short-range potential cannot be ignorable[100, 101]. However, in this chapter, the main interest is the process of chain formations so that we choose the rather simple short-range potential SP2 as our generic model. In comparison with the Yukawa repulsive potential, the short-range potential SP2 is closer to a hard sphere

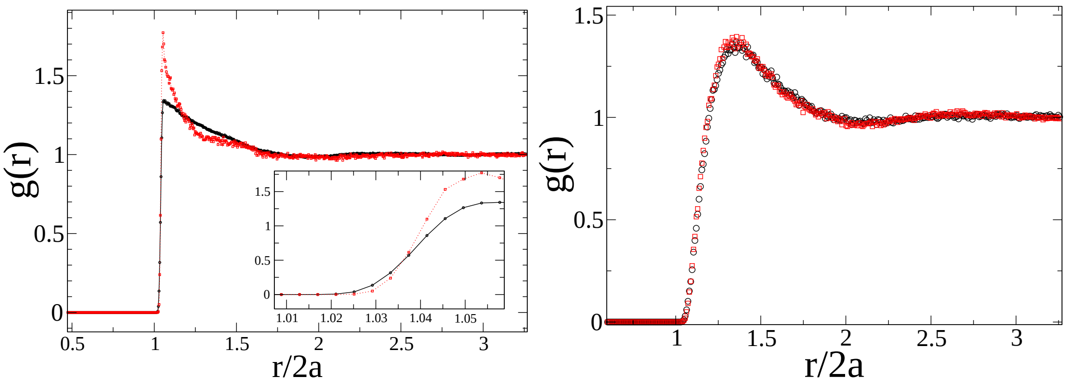

(a) SP1

(b) SP3

Figure 4.2: Radial distribution function $g(r)$ for $\lambda = 0$: (black) BD and (red) LB. Inset in Figure 4.2(a) is the zoom-in figure of $g(r)$.

potential even in the case of fairly strong repulsive interaction.

Long-range potential

The long-range interaction, $U^d(\mathbf{r}_{ij}, \hat{\mathbf{s}}_i, \hat{\mathbf{s}}_j)$ in equation (2.76), can be rewritten in terms of the dipolar coupling constant λ as

$$U^d(\mathbf{r}_{ij}, \hat{\mathbf{s}}_i, \hat{\mathbf{s}}_j) = 8\lambda k_B T a^3 \left[\frac{(\hat{\mathbf{s}}_i \cdot \hat{\mathbf{s}}_j) - 3(\hat{\mathbf{s}}_i \cdot \hat{\mathbf{r}}_{ij})(\hat{\mathbf{s}}_j \cdot \hat{\mathbf{r}}_{ij})}{r_{ij}^3} \right]. \tag{4.2}$$

Using equation (4.2), the simple configurations for two dipoles can be classified according to dipolar energies: the lowest energy is $U^d = -2\lambda k_B T$ when two dipoles are aligned parallel at a separation $2a$, in the "nose-to-tail" structure. The second lowest energy structure is the "side-by-side", arrangement of antiparallel dipoles, perpendicular to $\mathbf{r}$, which has $U^d = -\lambda k_B T$. A positive dipolar energy is deduced as $U^d = \lambda k_B T$ for "side-by-side" parallel dipoles.

Figure 4.3 shows the total interaction potentials for $\lambda = 0,\ 4$ and 8 in both the nose-to-tail state and the side-by-side parallel state of two dipoles. Despite the fairly repulsive short-range potential "SP2", the characteristics of a dipole-dipole interaction among hard-core particles is still found in this model for ferrofluids. In this chapter, we only consider three values for the dipolar coupling constant as $\lambda = 0,\ 4$ and 8. Values of λ up to $\simeq 4$ are easily available in experiments, whereas higher values are possible but unusual to study numerically and experimentally[5, 7]. (The critical point between rings or chains and networks is at around $\lambda = 6$ and the volume fraction $5\% \sim 6\%$ for hard-sphere magnetic particles. Values $4 < \lambda < 6$ are dynamically significant to make

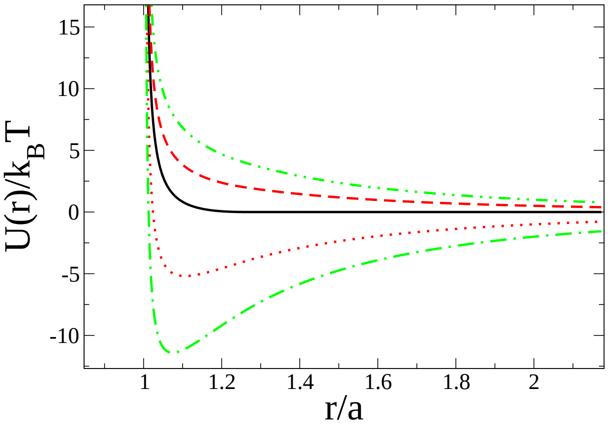

Figure 4.3: Total interaction potential U_{ij}. Green lines are for $\lambda = 8$: (green dash-dot-dotted line) side-by-side parallel; (green dash-dotted line) nose-to-tail. Red lines are for $\lambda = 4$: (red dashed line) side-by-side; (red dotted line) nose-to-tail. Black solid line is for $\lambda = 0$. The selected short range interaction in SP2.

these aggregated structures[5, 7].)

In numerical practice, a periodic box is used to simulate the colloidal ferrofluids using the Ewald summation to calculate the long-range dipolar interaction, as shown in Section 2.4.3. In LB and BD simulations, the parameters for Ewald summation are given as $r_c = 16$ and $\alpha = 0.15625$. From the given α and r_c, the wavevectors for the Fourier part of Ewald summation are obtained from $\mathbf{k} = (2\pi/\Lambda)(n_x, n_y, n_z)$ with $n_x, n_y, n_z \leq 8$ and $n_x, n_y, n_z \leq 16$ for $\Lambda^3 = 64^3$ and 128^3 respectively. The Ewald summation boundary condition at infinity was chosen to be "conducting", representing an infinite dipolar susceptibility of the surroundings[74, 77]. To generate the equilibrium structures in accordance with Boltzmann statistics, the canonical (NVT) Monte Carlo simulations[19, 103] were performed in the cubic box with periodic boundary conditions. The long-range dipolar interaction is again handled by the Ewald summation with conducting boundary condition, the convergence parameter $\alpha\Lambda = 5.6$ and wavevectors $\mathbf{k} = (2\pi/\Lambda)(n_x, n_y, n_z)$ with $n_x, n_y, n_z \leq 6$. For the static properties in equilibrium, the MC runs were performed from $t = 2 \times 10^5$ MC cycles to $t = 5 \times 10^5$ MC cycles.

4.1.2 Computational resource

The LB and BD simulations have been done on a cluster of 3GHz Intel Dual-core processors[106]. For a large system $\Lambda^3 = 128^3$ at a volume fraction $\phi = 0.10$, a single run by LB up to $\sim 10^6$ time steps required 56 hours on 64 cores, while a single run by BD required 112 hours on 8 cores of the same cluster machine. For a system size $\Lambda = 64^3$ at $\phi = 0.10$, a single run by LB up to $\sim 10^6$ time steps needed 38 hours on

8 cores of a same cluster and a run by BD required 19 hours on a single core process. Thus, to generate the data on fully equilibrium samples, a small system $\Lambda^3 = 64^3$ is used to run for $t \geq 2 - 3 \times 10^6 \simeq 25\tau_D$ at $\lambda = 8.0$. To obtain good statistics on the transient dynamics, a large system of $\Lambda^3 = 128^3$ was used.

4.2 Static structure in equilibrium

This section presents the equilibrium static properties of LB, BD and MC, in each case for $\lambda = 0.0$, 4.0 and 8.0 with the particle volume fraction $\phi = 0.10$. These properties for magnetic colloids are quantified by four radial distribution functions and the dimensionless energies of short-range interaction and long-range interaction. As a result, we confirm that the data from LB and BD have good agreements with the data generated by MC. This provides an important check to see that our LB algorithm generates the Boltzmann distribution for thermal equilibrium properties, even if a careful treatment to choose the parameters for the short-range potential is demanded to reduce the discretisation error for the noise. (As stated previously, all these results use the parameter set SP2.)

4.2.1 Equilibrium energy

Table 4.1 shows the data for time-averaged energy in equilibrium resulting from various simulation runs. The data from LB and BD in $\Lambda^3 = 64^3$ are averaged after full equilibration, $t > 30\tau_D$. For $\lambda = 0$ and $\lambda = 4$, LB and the other methods have remarkably good agreement and the energy data for $\lambda = 8$ are also in quantitatively good agreement with errors less than 5%. Systems with the volume fraction $\phi = 0.20$ are simulated in a larger volume, $\Lambda^3 = 128^3$. These have run until $\sim 7\tau_D$ and the energy data in Table 4.1 are averaged over the time window from $6\tau_D$ to $7\tau_D$. The corresponding energy curves against time are presented below in Figure 4.14. However, within the simulation time window used when $\Lambda^3 = 128^3$, the curves for energies are still undergoing slow relaxation to make aggregated clusters as shown in section 4.5. Thus, these discrepancies of energies at $\phi = 0.20$ represent the systematic error from incomplete equilibration, and do not test the accuracy of our LB algorithm.

4.2.2 Radial distribution functions

Figures 4.4(a), 4.5 and 4.6 show the radial distribution function $g(r)$ and the projections of the dipolar pair distribution functions onto rotational invariants[107], which are measured in the various simulation runs. These measurements are obtained only for

Table 4.1: Equilibrium energy data for LB, BD and MC runs. The quoted statistical errors are estimated on the basis of a standard deviation. The system volumes are reported in lattice units for LB and BD runs, while the MC volumes are reported in units of the hard-core radius a (equal to 2.3 in LU).

λ	ϕ	N	V	Method	U^d/Nk_BT	U^{sc}/Nk_BT
0	0.10	529	64^3	LB	-	0.08671 ± 0.00028
0	0.10	529	64^3	BD	-	0.0870 ± 0.0004
0	0.10	529	$22156a^3$	MC	-	0.08757 ± 0.0001
4	0.10	529	64^3	LB	-2.929 ± 0.003	0.2923 ± 0.0006
4	0.10	529	64^3	BD	-2.964 ± 0.002	0.2935 ± 0.0006
4	0.10	529	$22156a^3$	MC	-2.8830 ± 0.0008	0.2850 ± 0.0002
8	0.10	529	64^3	LB	-11.811 ± 0.002	1.1692 ± 0.0007
8	0.10	529	64^3	BD	-11.609 ± 0.002	1.1253 ± 0.0007
8	0.10	529	$22156a^3$	MC	-11.565 ± 0.003	1.1196 ± 0.0006
4	0.20	8239	128^3	LB	-3.966 ± 0.001	0.5140 ± 0.0004
4	0.20	8239	128^3	BD	-3.902 ± 0.001	0.4970 ± 0.0006
4	0.20	529	$11079a^3$	MC	-4.1895 ± 0.0008	0.4534 ± 0.0002
8	0.20	8239	128^3	LB	-11.833 ± 0.003	1.233 ± 0.001
8	0.20	8239	128^3	BD	-11.646 ± 0.003	1.188 ± 0.002
8	0.20	529	$11079a^3$	MC	-11.677 ± 0.003	1.1925 ± 0.0006

$\phi = 0.10$ in $\Lambda^3 = 64^3$, since full equilibrium is not achieved in the runs in a larger system ($\Lambda^3 = 128^3$) as reported in Table 4.1.

The radial distribution functions (RDFs)[10, 102] are given as

$$g(r) = \frac{\Lambda^3}{N^2 2\pi r^2}\left\langle \sum_{i<j} \delta(r - r_{ij}) \right\rangle, \tag{4.3}$$

$$h_{110}(r) = \frac{3\Lambda^3}{N^2 2\pi r^2}\left\langle \sum_{i<j} \delta(r - r_{ij})(\hat{\mathbf{s}}_i \cdot \hat{\mathbf{s}}_j) \right\rangle, \tag{4.4}$$

$$h_{112}(r) = \frac{2}{3}\frac{\Lambda^3}{N^2 2\pi r^2}\left\langle \sum_{i<j} \delta(r - r_{ij})[3(\hat{\mathbf{s}}_i \cdot \hat{\mathbf{r}}_{ij})(\hat{\mathbf{s}}_j \cdot \hat{\mathbf{r}}_{ij}) - (\hat{\mathbf{s}}_i \cdot \hat{\mathbf{s}}_j)] \right\rangle, \tag{4.5}$$

$$h_{220}(r) = \frac{5}{2}\frac{\Lambda^3}{N^2 2\pi r^2}\left\langle \sum_{i<j} \delta(r - r_{ij})[3(\hat{\mathbf{s}}_i \cdot \hat{\mathbf{s}}_j)^2 - 1] \right\rangle. \tag{4.6}$$

Figure 4.4(a) shows $g(r)$ for $\lambda = 0$ in LB, BD and MC; the other three RDFs are not presented, but show fluctuating curves near zero. That means there is no orientational ordering of dipoles. The $g(r)$ in real space corresponds to the structure factor $S(q)$ in Fourier space. To see the detailed short-range ordering, the $g(r)$ is more precise than $S(q)$. On the other hand, $S(q)$ is more suitable to see any long-range ordering, because a wavevector q is reciprocal to a distance r in real space. In the test run with SP1 as

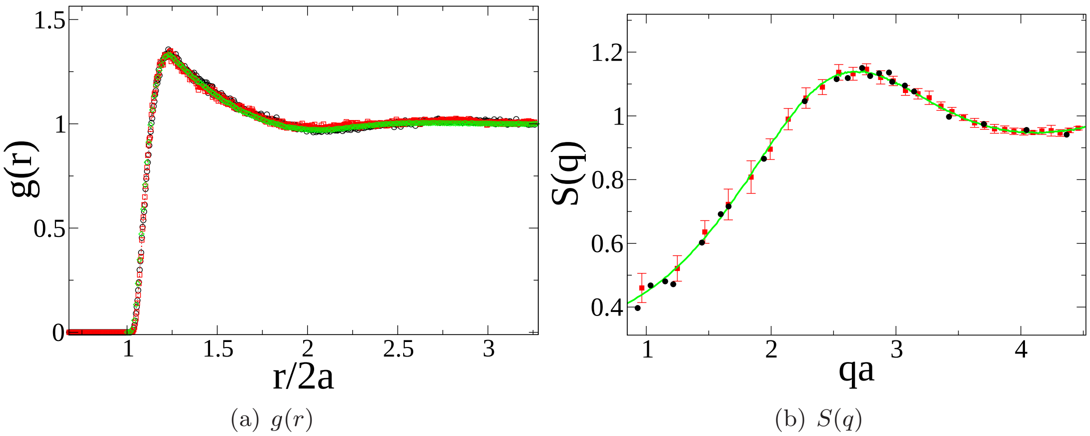

(a) $g(r)$

(b) $S(q)$

Figure 4.4: (a) Radial distribution function at $\lambda = 0.0$. Black open circle is BD, red open square is LB and green open diamond is MC. (b) Static structure factors in LB with SP1 (black circle) and SP2 (red square), and MC (green line).

the short-range potential, we found that the static structure factors do not show any discrepancy (Figure 4.4(b)) despite these being visible in $g(r)$ (Figure 4.2(a)).

In Figure 4.5, the RDFs for $\lambda = 4$ also show adequate agreement between all methods, even if LB and BD have slight discrepancies from the the MC data at the position of the nearest neighbour. However, for $\lambda = 8.0$, a clear discrepancy between LB and other two methods is seen in Figure 4.6. It is about 10% at the first peak in all the RDFs. This error is consistent with the energy discrepancies in Table 4.1; it could be also explained by the discrepancy of noise error for close particles with strong interaction forces in $\lambda = 8$. Bearing in mind the other sources of error in LB[82], this error is considered acceptable, though only just.

Generally, the RDFs present the spatial orderings of particles in real space r reflecting the total energy of a certain configuration with given interaction potentials. For $\lambda = 0$, it shows the short-range ordering corresponding to the short-range potential. At a fixed ϕ, increasing λ generates the higher short-range ordering throughout the plots of RDFs shown in Figures 4.5 and 4.6; the data of $g(r)$ show that more short-range ordering is obtained at $\lambda = 8.0$.

Contrary to a simple aggregation for drops of particles simulated with Lennard-Jones potential or Stockmayer potential[19], dipolar colloids combine to form chainlike structures based on nose-to-tail. These structures are quantified by the other three RDFs which include factors that describe orientational ordering. The RDF $h_{110}(r)$ helps to recognise the parallel or anti-parallel alignment between the pairs of dipoles, as it depends on the angle between two dipoles in equation (4.4). The RDF $h_{112}(r)$

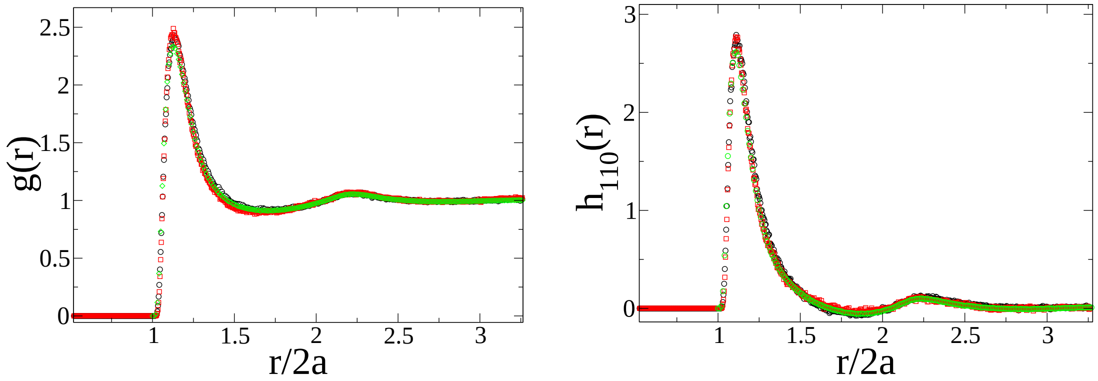

(a) $g(r)$

(b) $h_{110}(r)$

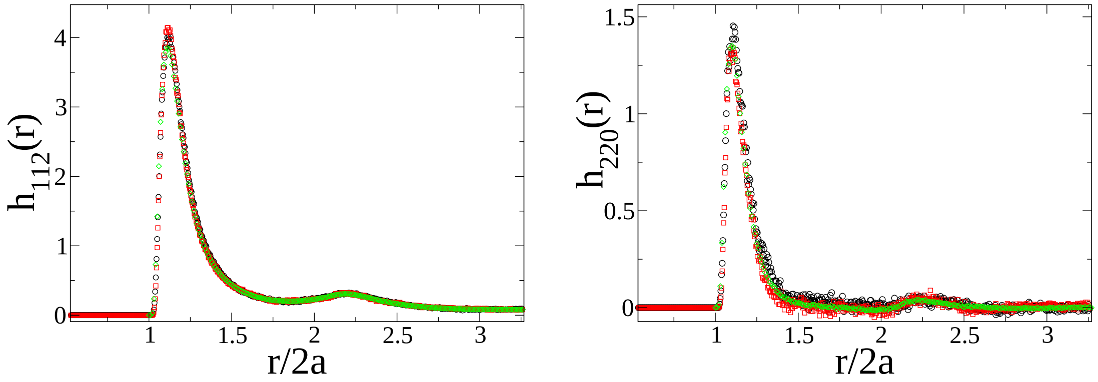

(c) $h_{112}(r)$

(d) $h_{220}(r)$

Figure 4.5: Radial Distribution functions: $g(r), h_{110}(r), h_{112}(r)$ and $h_{220}(r)$, for $\lambda = 4.0$ and $\phi = 0.10$. Black open circle is BD, red open square is LB and green open diamond is MC.

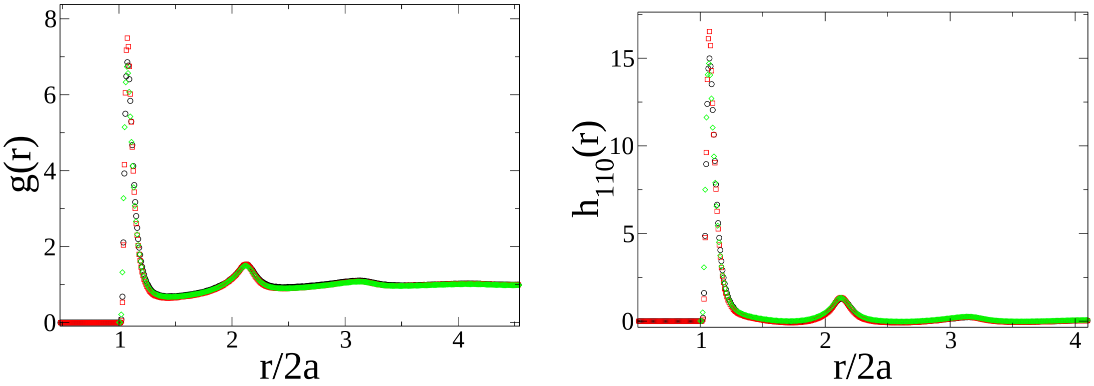

(a) $g(r)$ (b) $h_{110}(r)$

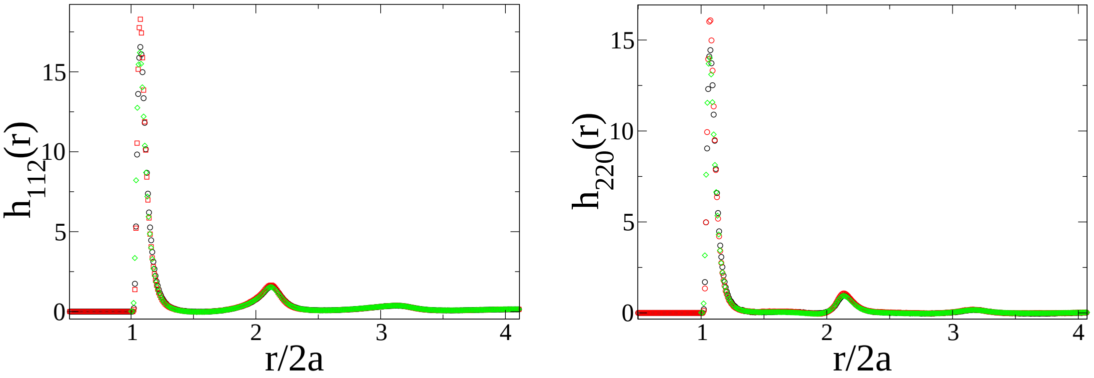

(c) $h_{112}(r)$ (d) $h_{220}(r)$

Figure 4.6: Radial Distribution functions: $g(r), h_{110}(r), h_{112}(r)$ and $h_{220}(r)$, for $\lambda = 8.0$ and $\phi = 0.10$. Black open circle is BD, red open square is LB and green open diamond is MC.

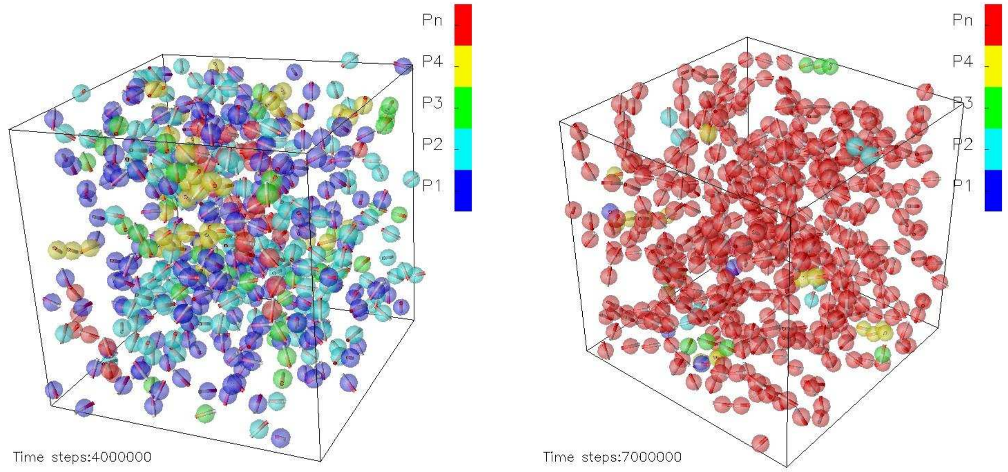

(a) $\lambda = 4$ (b) $\lambda = 8$

Figure 4.7: Snapshots from LB simulations of $N = 529$ colloids at a volume fraction $\phi = 0.10$. Each particle is colour-coded to reflect the total number of particles in the cluster to which it belongs: (dark blue) monomers; (light blue) dimers; (green) trimers; (yellow) tetramers; (red) clusters with 5 or more particles. The quantitative criterion used to define clusters in given in Section 4.4.2.

is proportional to the dipolar potential energy at a distance r with the factor giving decay as $1/r^3$ omitted. The RDF $h_{220}(r)$ quantifies the extent of nematic ordering. As a signature of structures of the nose-to-tail chains, the RDFs contain positive peaks at the inter-particle distances $\sim 2a \times n$, where $n = 1, 2, ...$ For confirmation of the chain structures, Figure 4.7 presents the two snapshots in equilibrium from LB simulations for $\lambda = 4$ and 8. The colours are classified by the number of particles in the cluster from monomer to 2-5 particles; those show clear chain structures.

4.2.3 Orientational order parameters

Any macroscopic alignment, caused by the long-range dipolar interactions, can be quantified by the orientational order parameters: the nematic order parameter $N2$ and the polarisation P. Usually at higher volume fractions ($\sim$ 50%) above $\lambda \sim 2.5$, there is a phase transition[7] from isotropic phase to a polar nematic phase, the so-called ferromagnetic state. We will show the data for orientational ordering in a bulk system within the given conditions of ϕ up to 0.20 and λ up to 8.

The $N2$ and P are defined by the second-rank order tensor, $\mathbf{Q}$,[108] which is given as

$$\mathbf{Q} = \frac{1}{2N}\sum_{i=1}^{N}(3\hat{\mathbf{s}}_i\hat{\mathbf{s}}_i - \mathbf{I}) \qquad (4.7)$$

where $\mathbf{I}$ is the second-rank unit tensor and $\hat{\mathbf{s}}_i$ is the dipolar unit vector of a particle i. The diagonalisation of the tensor $\mathbf{Q}$ produces three eigenvalues and three eigenvectors. The highest eigenvalue is the second-rank order parameter (or nematic order parameter), $N2$, and the corresponding normalised eigenvector is the director $\hat{\mathbf{n}}$[109]. For oriented states, e.g. ferro or antiferro phases aligned perfectly, the nematic order parameter $N2$ is unity; on the other hand, it is zero for an isotropic phase.

Using $\hat{\mathbf{n}}$, the polarisation P can be calculated as

$$P = \left| \frac{1}{N} \sum_{i=1}^{N} \hat{\mathbf{s}}_i \cdot \hat{\mathbf{n}} \right| . \tag{4.8}$$

The polarisation P distinguishes a ferro-phase from an antiferro phase or an isotropic phase[110]. In the case with $N2 \sim 1$, P could signify either ferro $(+1)$ or antiferro (-1) orders.

Table 4.2 shows the nematic order parameter $N2$ and the polarisation P in various simulation runs. For the parameters given with λ up to 8 and $\phi = 0.10$, all data appear to describe isotropic phases. However, the data from MC for $\phi = 0.20$ have big discrepancy with the data from LB and BD simulations. This can be explained by finite size effect due to the small number of particles in these MC simulations. In contrast to LB and BD simulations, which use a fixed system box Λ^3, we use the fixed number of particles, $N = 529$, to simulate MC runs. (These control the particle fraction by reducing the system volume Λ^3.) The orientational order parameter $N2$ obtained from $\mathbf{Q}$ in equation (4.7) show a strong N-dependency, which is expected to vary as $\sim 1/\sqrt{N}$ in an isotropic phase[110]. As shown in the table, this scaling is obeyed for $N2$, but with worse agreement for P.

4.3 Dynamic correlators in equilibrium

This section will discuss the collective relaxation of dipoles in space and time in equilibrium. In the last section, we monitored the ordering into chains on varying λ through the radial distribution functions and the snapshots. This section will discuss how the dipoles that form clusters relax translationally and rotationally in equilibrium. Those relaxations are quantified by the dynamic correlators via intermediate scattering functions, $S(q,t)$ and $F(q,t)$, that dynamic light scattering enables to measure in experiments. Here, we only investigate dynamic correlators for $\lambda = 0, 4$ and 8 with $\phi = 0.10$ in $\Lambda^3 = 64^3$.

In addition, the effect of hydrodynamic interactions is investigated by comparing the data for dynamic correlators from LB and BD runs; this hydrodynamic effect is

Table 4.2: Orientational order parameters, $N2$ and P. The quoted statistical errors are estimated on the basis of a standard deviation.

λ	ϕ	N	V	Method	$N2$	P	$N2^\dagger$	$P^\dagger$
0	0.10	529	64^3	LB	0.0361 ± 0.0002	0.0198 ± 0.0003	0.8303	0.4554
0	0.10	529	64^3	BD	0.0352 ± 0.0002	0.0120 ± 0.0002	0.8096	0.276
0	0.10	529	$22156a^3$	MC	0.03514 ± 0.00008	0.0208 ± 0.0001	0.8082	0.4784
4	0.10	529	64^3	LB	0.0375 ± 0.0003	0.0376 ± 0.0004	0.8625	0.8648
4	0.10	529	64^3	BD	0.0403 ± 0.0003	0.0424 ± 0.0006	0.9269	0.9752
4	0.10	529	$22156a^3$	MC	0.0379 ± 0.0001	0.0333 ± 0.0003	0.8717	0.7659
8	0.10	529	64^3	LB	0.0463 ± 0.0002	0.0164 ± 0.0002	1.0649	0.3772
8	0.10	529	64^3	BD	0.0558 ± 0.0003	0.0348 ± 0.0004	1.2834	0.8004
8	0.10	529	$22156a^3$	MC	0.0559 ± 0.0006	0.055 ± 0.002	1.2857	1.2650
4	0.20	8239	128^3	LB	0.0115 ± 0.0003	0.0078 ± 0.0003	1.0438	0.7080
4	0.20	8239	128^3	BD	0.0091 ± 0.0002	0.0063 ± 0.0003	0.8260	0.5718
4	0.20	529	$11079a^3$	MC	0.0402 ± 0.0001	0.0426 ± 0.0006	0.9246	0.9798
8	0.20	8239	128^3	LB	0.0184 ± 0.0001	0.0185 ± 0.0004	1.6702	1.6792
8	0.20	8239	128^3	BD	0.0164 ± 0.0002	0.0104 ± 0.0006	1.4886	0.9440
8	0.20	529	$11079a^3$	MC	0.0564 ± 0.0007	0.083 ± 0.002	1.2972	1.909

† notes the data, multiplied by $\sqrt{N}$.

clearly found for short-time Brownian motions. We present the short-time diffusion coefficients as a function of wavevector q, and also the static structure factors, in LB and BD simulations. Combining these, a non-unity hydrodynamic factor ($H(q)$) is obtained in the results from LB. That will be discussed in Section 4.3.3.

To improve the statistics of our data, overlapped sampling[76] is used to average correlators, which are measured at different initial times, and the final averaged correlators at each q are obtained by the summation of each intermediate scattering function over the same magnitude $q = |\mathbf{q}|$.

4.3.1 Translational intermediate scattering function, $S(q,t)$

The function $S(\mathbf{q},t)$ presents the density fluctuation in Fourier space q[111, 112], defined as

$$S(\mathbf{q},t) = \frac{1}{N}\langle \rho(\mathbf{q},t)\rho(-\mathbf{q},0)\rangle, \tag{4.9}$$

where $\rho(\mathbf{q},t)$ is the time-dependent density in Fourier space, calculated by Fourier transform of the density in real space, $\rho(\mathbf{r},t)$:

$$\rho(\mathbf{q},t) = \int \rho(\mathbf{r},t)\exp[-i\mathbf{q}\cdot\mathbf{r}]d\mathbf{r} = \sum_{j}^{N} \exp[-i\mathbf{q}\cdot\mathbf{r}_j(t)]. \tag{4.10}$$

(The real space density is $\rho(\mathbf{r},t) = \sum_{i=1}^{N} \delta(\mathbf{r} - \mathbf{r}_i(t))$, where $\mathbf{r}_i(t)$ is the position of a particle i.) Therefore, as considering the real part in $S(\mathbf{q},t)$, equation (4.9) is rewritten as

$$
\begin{aligned}
S(\mathbf{q},t) &= \frac{1}{N}\langle\sum_{j}^{N}\exp[-i\mathbf{q}\cdot\mathbf{r}_j(t)]\sum_{l}^{N}\exp[i\mathbf{q}\cdot\mathbf{r}_l(0)]\rangle && (4.11)\\
&= \frac{1}{N}\langle[\sum_{j}^{N}\cos(\mathbf{q}\cdot\mathbf{r}_j(t))\sum_{l}^{N}\cos(\mathbf{q}\cdot\mathbf{r}_l(0))+\sum_{j}^{N}\sin(\mathbf{q}\cdot\mathbf{r}_j(t))\sum_{l}^{N}\sin(\mathbf{q}\cdot\mathbf{r}_l(0))]\rangle. && (4.12)
\end{aligned}
$$

Here, the wavevector $\mathbf{q}$ is given as $\frac{2\pi}{\Lambda}(x,y,z)$, where Λ is the one-dimensional length of a cubic box and x, y, and z are integers for $-\Lambda \leq x,\ y \leq \Lambda$, and $0 \leq z \leq \Lambda$. At $t=0$ in equation (4.12), $S(\mathbf{q},0)$ is the static structure factor $S(\mathbf{q})$. The t-dependent relaxations of $S(q,t)$ can represent the stochastic dynamics of sinusoidal density fluctuations as a function of the wavelength $2\pi/q$ which can distinguish the dynamics in terms of a characteristic length d chosen as a diameter of particle. For $2\pi/q \ll d$, $S(q,t)$ can show the collective diffusion motion. At $2\pi/q \approx d$, the structural relaxation of the particle in the environment formed by neighbouring particles can be observed. For $2\pi/q \gg d$, the simple self diffusion of individual particles can be seen in $S(q,t)$. These q-dependent characteristics can be also interpreted for the rotational relaxation function, $F(q,t)$. In this chapter, we consider three different wavevectors to be plotted for dynamic correlators to see how dipoles belonging to chains are relaxed in equilibrium: one close to the peak ($q=q^*\approx 2\pi/d$), one larger and one smaller. (The q^* corresponding to the interparticle distance is mainly considered for the dynamic correlators. Additionally, for transient motions on the way to equilibrium, the dynamic correlators at q^* can show the relaxation and the aggregation of dipoles simultaneously; Section 4.5 will discuss this in detail.)

Figure 4.8 shows $S(q,t)$ for $\lambda=0$, 4 and 8 at $\phi=0.10$. In comparison with the $S(q,t)$ found by BD in all ranges for λ, hydrodynamic interactions delay the relaxation of $S(q,t)$ especially on early time scales. This effect is larger at smaller q and at smaller λ. The long-time relaxations are not far from exponential decays in all cases; besides, there is no sign of the decay into α and β relaxations as found in colloidal systems on approach to a glass transition[104] in Figure 4.8(d). However, at higher λ in Figures 4.8(c) and 4.8(d), the effect of hydrodynamic interactions is reduced at smaller q, because the energetic arrangement for colloidal aggregations controls the structural relaxation.

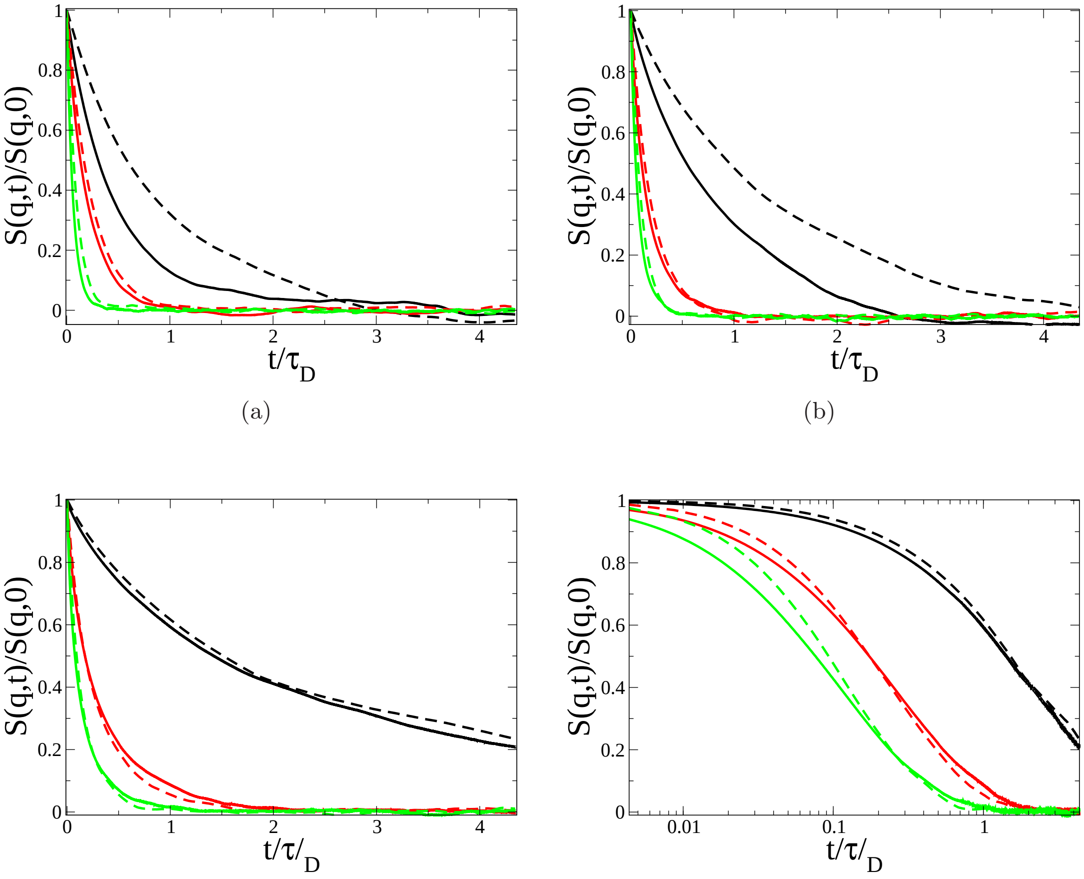

(a) (b)

(c) (d)

Figure 4.8: Translational intermediate scattering functions with $\lambda = 0, 4.0$ and 8.0. Solid lines are BD runs and dash lines are LB runs. Black is $qa = 1.1514$, green is $qa = 4.0456$. Red is q^*a at the peak of $S(q,0)$: (a) $q^*a = 2.6139$ at $\lambda = 0$, (b) $q^*a = 3.0712$ at $\lambda = 4.0$, (c) and (d) $q^*a = 3.2409$ at $\lambda = 8.0$.

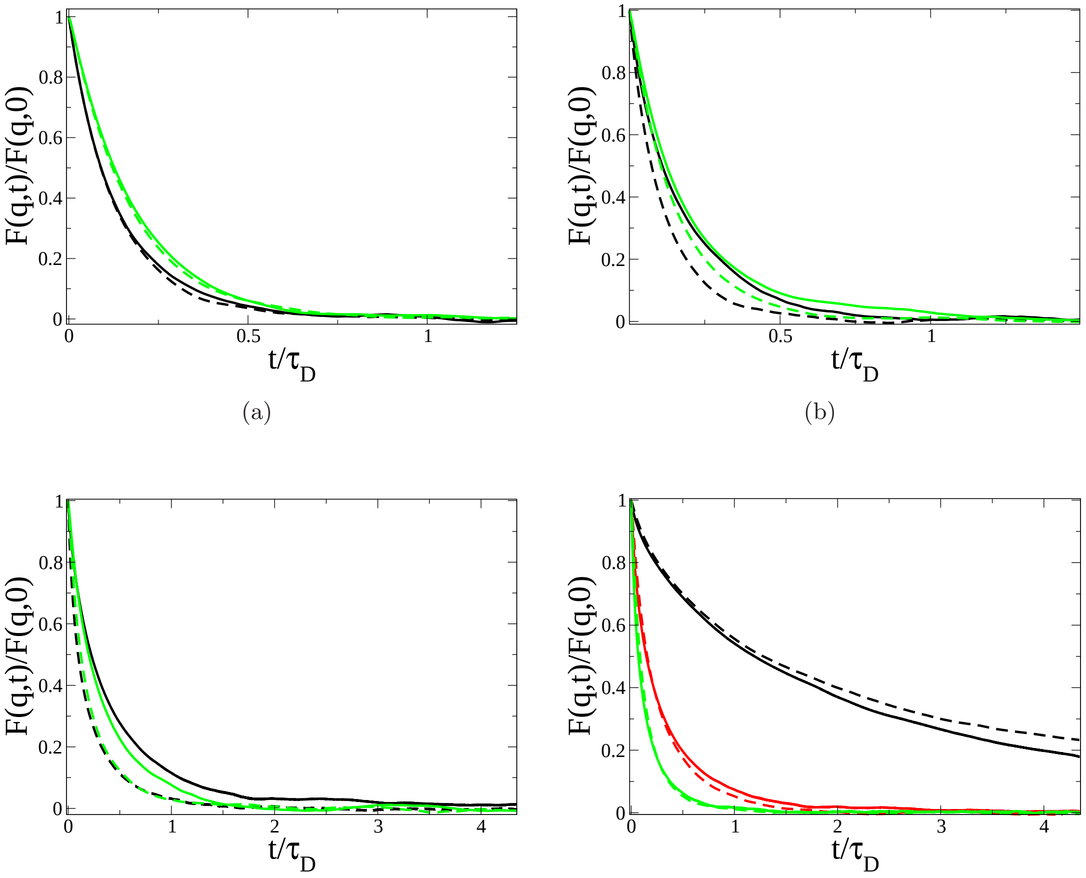

(a) (b)

(c) (d)

Figure 4.9: Orientational Relaxations in longitudinal (F_L) and transverse (F_T) correlation functions, $\phi = 0.10$ and (a) $\lambda = 0$, (b) $\lambda = 4$, and (c) $\lambda = 8$. In (a), (b), and (c), black lines are BD and green lines are LB: (solid lines) F_L; (dotted lines) F_T. In (d), solid lines are BD and dashed lines are LB: (black lines - upper) $qa = 1.1514$; (red lines - middle) $qa = 3.2409$; (green lines - lower) $qa = 4.0456$.

4.3.2 Rotational intermediate scattering functions, $F(q,t)$

The $F(q,t)$ can characterise the orientational relaxation of dipoles to form chain clusters at a wavevector q. In the similar manner to density relaxation shown in the previous section, $F(q,t)$ is derived from a wavevector-dependent dipole density, $\mathbf{M}(\mathbf{q},t) = \sum_{j=1}^{N} \hat{\mathbf{s}}_j \exp[-i\mathbf{q}.\mathbf{r}_j(t)]$ which can be divided into two components[113]: the longitudinal component and the transverse component as $\mathbf{M}_L = \mathbf{M}.\hat{\mathbf{q}}\hat{\mathbf{q}}$ and $\mathbf{M}_T = \mathbf{M} - \mathbf{M}_L$. Therefore, the three dynamic correlators of interest are given as

$$\begin{aligned} F(\mathbf{q},t) &= N^{-1}\langle \mathbf{M}(\mathbf{q},t)\cdot\mathbf{M}(-\mathbf{q},0)\rangle && (4.13)\\ F_L(\mathbf{q},t) &= N^{-1}\langle \mathbf{M}_L(\mathbf{q},t)\cdot\mathbf{M}_L(-\mathbf{q},0)\rangle && (4.14)\\ F_T(\mathbf{q},t) &= N^{-1}\langle \mathbf{M}_T(\mathbf{q},t)\cdot\mathbf{M}_T(-\mathbf{q},0)\rangle, && (4.15)\end{aligned}$$

where the $F(\mathbf{q},t)$ is the sum of $F_L(\mathbf{q},t)$ and $F_T(\mathbf{q},t)$, which are the longitudinal correlator and the transverse correlator respectively.

Figures 4.9(a)-4.9(c) show the orientational relaxations for $\lambda = 0$, 4 and 8 at $q = q^*$. The curves generally behave like $S(q,t)$ as an exponential decay with a long-time behaviour of $F(q,t) \sim \exp[-D_r(q)q^2t]$, where $D_r(q)$ is a rotational diffusion coefficient at wavevector q. The $F(q,t)$ found by LB runs relax more slowly than one by BD. At lower q, $F(q,t)$ relaxes slower. However, in contrast to the density ρ, $\mathbf{M}$ is not a conserved quantity so that this is not compelled to relax slowly for small q. The relaxation of $\mathbf{M}$ for small q suggests the slower collective rearrangement for particles that are frozen in chains. In addition, Figures 4.9(a)-4.9(c) show that the dipoles in a cluster relax more slowly on increasing the strength of dipolar interaction. (That is caused by the strong bonded dipoles inside of chains for high λ.) It is obvious that colloids in a long chain take a longer time to rotate through angle π. In both LB and BD at $\lambda = 4$ and 8, the longitudinal relaxations are slower than transverse ones. This could be explained by the slow rotational diffusion of chains with respect to the wavevector q. Slow longitudinal relaxations means that the relaxation of chains is faster along perpendicular direction to local chain orientation.

4.3.3 Short-time diffusion

For a diffusive motion of colloids, the $S(q,t)$ decays exponentially so that the (collective) short-time diffusion coefficient can be obtained as

$$D_s(q) = -\frac{1}{q^2}\left[\frac{d\ln S(q,t)}{dt}\right]_s \qquad (4.16)$$

where $[\cdots]_s$ is the time scale window in which particles move diffusively before colliding with their neighbours. For a single particle, the short-time diffusive motion is found within the time scale $\tau_\eta, \tau_v \ll t$. Figure 4.10 shows the exponential decay of $S(q^*, t)$ at short times at $\phi = 0.10$ with all three λ values, found by LB and BD runs. In the curves found by LB at the earliest times, non-exponential decays appear, but curves recover the diffusive behaviours after several relaxation times of colloid momentum and fluid viscosity. The onset of the short-time diffusive motion is delayed, yet it is ended as soon as particles collide, so that the short-time diffusive regime shortens upon increasing λ. Meanwhile, the $S(q^*, t)$ of BD runs does not have any non-diffusive behaviour during the pre-Brownian time scale, because there is no pre-Brownian timescale (beyond the basic time step of the algorithm).

In practice, the $D_s(q, N)$ is estimated by fitting a slope in the log-linear plot within a fixed time window which is identified by eye. The final data in Figures 4.11-4.13 were binned every ten wavevectors. Here, the statistical error are measured for the binned data. The $D_s(q)$ is related with the hydrodynamic factor $H(q)$[104] as

$$D_s(q)S(q) = D_0 H(q). \tag{4.17}$$

Here, D_0 is a single particle diffusion coefficient and $S(q)$ is the static structure factor. The hydrodynamic factor $H(q)$ is always unity for all q in the absence of hydrodynamic interactions. In the study of hard-sphere colloids, $H(q)$ shows dependency on the wavevector q; Segre *et al.*[114] found $0.2 \le H(q) \le 0.6$ at $\phi \simeq 0.30$ whereas $H(q^*) \simeq 0.8$ for $\phi \simeq 0.10$.

In LB simulations, the diffusion coefficient, $D_s(q)$, is known to have a strong finite size effect in periodic systems. For the case of hard spheres ($\lambda = 0$) for thermodynamic limit, it can be rectified by selecting the correction term[114, 115]:

$$\frac{D_s(q)}{D_0} = \frac{D_s(q,N)}{D_0} + \left(\frac{\eta_\infty}{\eta}\right)\left[1.7601\left(\frac{\phi}{N}\right)^{1/3} - \frac{\phi}{N}\right], \tag{4.18}$$

with particle number $N = \phi\Lambda^3/v_0$ at a fixed ϕ and a volume of spherical particle, $v_0 = \frac{4}{3}\pi a^3$. Here η_∞ is the high-frequency viscosity with suspended particles present, and η is the solvent viscosity. For the evaluation of equation (4.18) in our ferrofluids model, the recipe by Ladd[70, 71] is used to measure the high-frequency viscosities in the fully equilibrated systems. Appendix B discusses the method to measure η_∞ and the results in detail. There, the ratio η_∞/η is obtained to be 1.0532, 1.0717 and 1.1687 for $\lambda = 0$, 4 and 8 respectively at the particle volume fraction, $\phi = 0.10$. However, originally, this procedure to correct the finite-size effect was invented for hard-sphere colloids. So, its validity for the magnetic system is uncertain. Thus we plot both

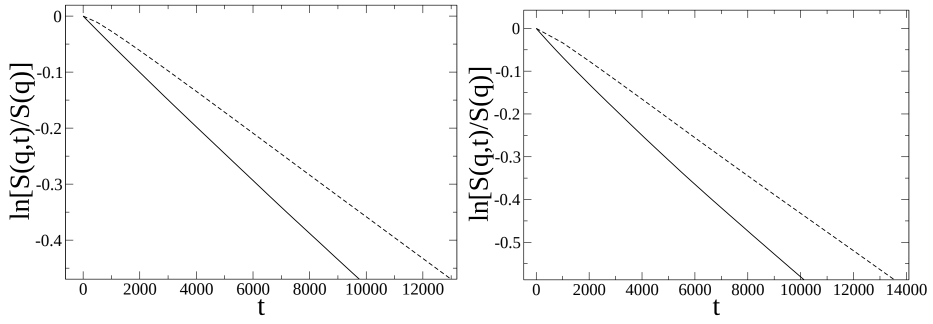

(a) $\lambda = 0$, $qa = 2.614$ (b) $\lambda = 4.0$, $qa = 3.072$

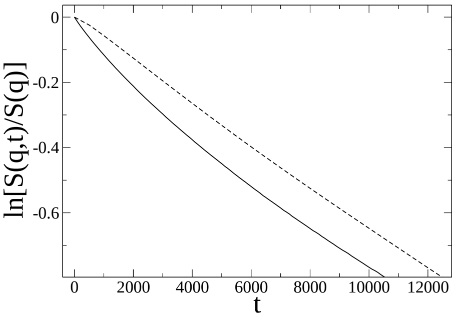

(c) $\lambda = 8.0$, $qa = 3.241$

Figure 4.10: Short time decay of $\ln[S(q,t)/S(q)]$ vs t for (a) $\lambda = 0$, (b) $\lambda = 4$, and (c) $\lambda = 8$, showing the extent of the linear regime in each case. Solid lines are BD and dash lines are LB.

$D_s(q, N)$ as actually measured and $D_s(q)$ as calculated via equation (4.18).

Figures 4.11-4.13 show the plots of $S(q)$, $D_0/D_s(q)$ and $H(q)$ measured from the translational dynamic correlators for $\lambda = 0$, 4 and 8. To check the correction effect in equation (4.18), the uncorrected curves for $D_0/D_s(q, N)$ by LB are also presented. For the data in BD, the actual calculations without any treatment are shown, because the above correction method is only for the systems with hydrodynamics; remember that our BD switches off hydrodynamic interactions. Since there is no similar method to correct for the finite size effect arising from the long-range magnetic interactions, we make no attempt to do such a correction. In the absence of hydrodynamic interactions, $H(q) = 1$ is found as required for $\lambda = 0$. But, $H(q)$ is less than unity at $\lambda = 4$ and 8, possibly suggesting that such a correction is needed.

To check the accuracy of our simulations by LB and BD, the $S(q)$ from MC is shown with ones from BD and LB. The data for $S(q)$ in LB, BD and MC have good agreements. Density fluctuations at low q are enhanced by the formation of large clusters[9]. Therefore, $S(q)$ at low q increases consistently with λ. The $H(q)$ in LB is found in the range $0.6 - 0.8$ for all three λ values. $H(q)$ also show a rising tendency a small wavevectors, $q \leq q^*/3$, but this is so far unexplained.

4.4 Transient dynamics and cluster formations

This section discusses the transient process of cluster formations following a quench from equilibrated configurations at $\lambda = 0$ to states with either $\lambda = 4$ or 8. The particle volume fractions considered are $\phi = 0.03, 0.10$ and 0.20 in $\Lambda^3 = 128^3$. The aggregation of magnetic colloids can be monitored through the energy relaxation of dipolar interactions and the cluster statistics. In this section, the data of both BD and LB will be presented to see the effect of hydrodynamic interactions.

4.4.1 Transient energy

Figure 4.14 shows the relaxations of the dipolar interaction energy as a function of time, after quenching from equilibrated configurations with $\lambda = 0$ at each particle concentration. On increasing λ, the relaxation time to reach equilibrium is increased by no more than a factor 2 in both BD and LB simulations. Compared with BD, LB shows that the hydrodynamic interactions make the relaxations slower approaching to equilibrium. Note that adding hydrodynamic interactions does not always slow down relaxations. For instance, a binary fluid has the faster phase-separation route than pure diffusion at intermediate and late times[25, 85, 86].

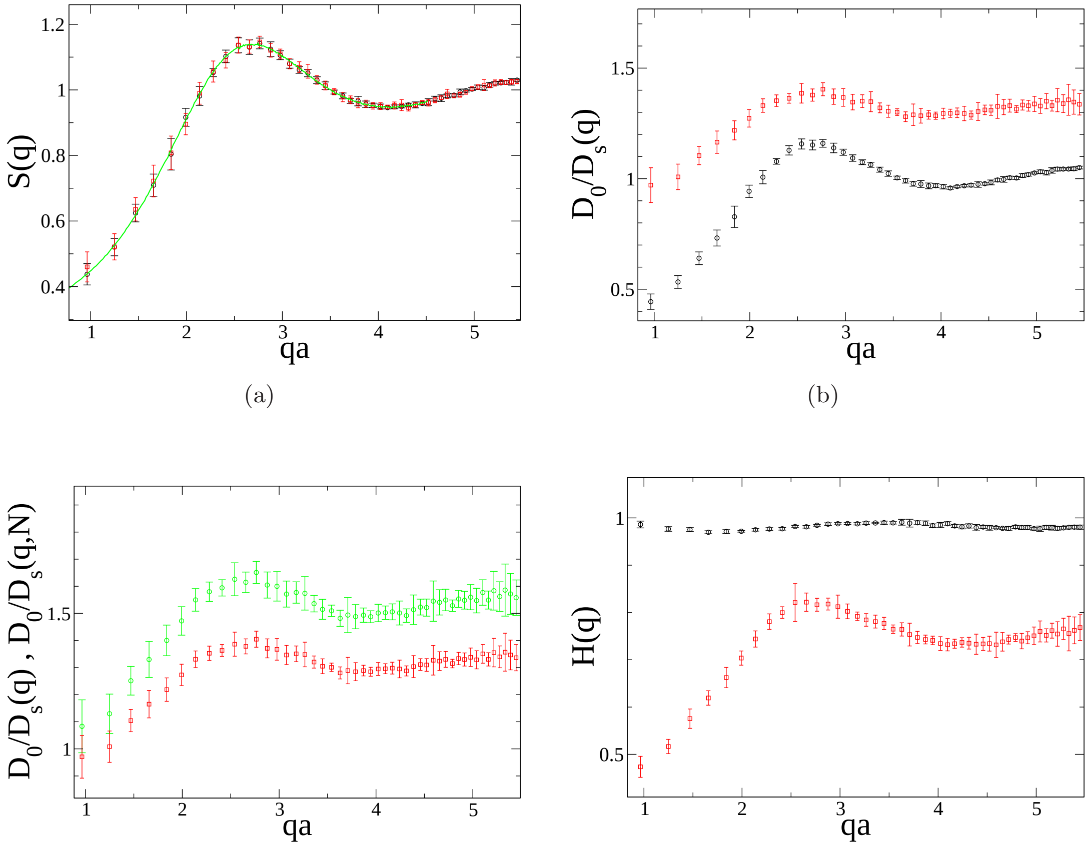

(a) (b) (c) (d)

Figure 4.11: Data for $\lambda = 0$ and $\phi = 0.10$. Black open circle is BD and red open square is LB. Green line is MC in (a). In (c), green is uncorrected $D_s(q, N)$ and red is the corrected $D_s(q)$.

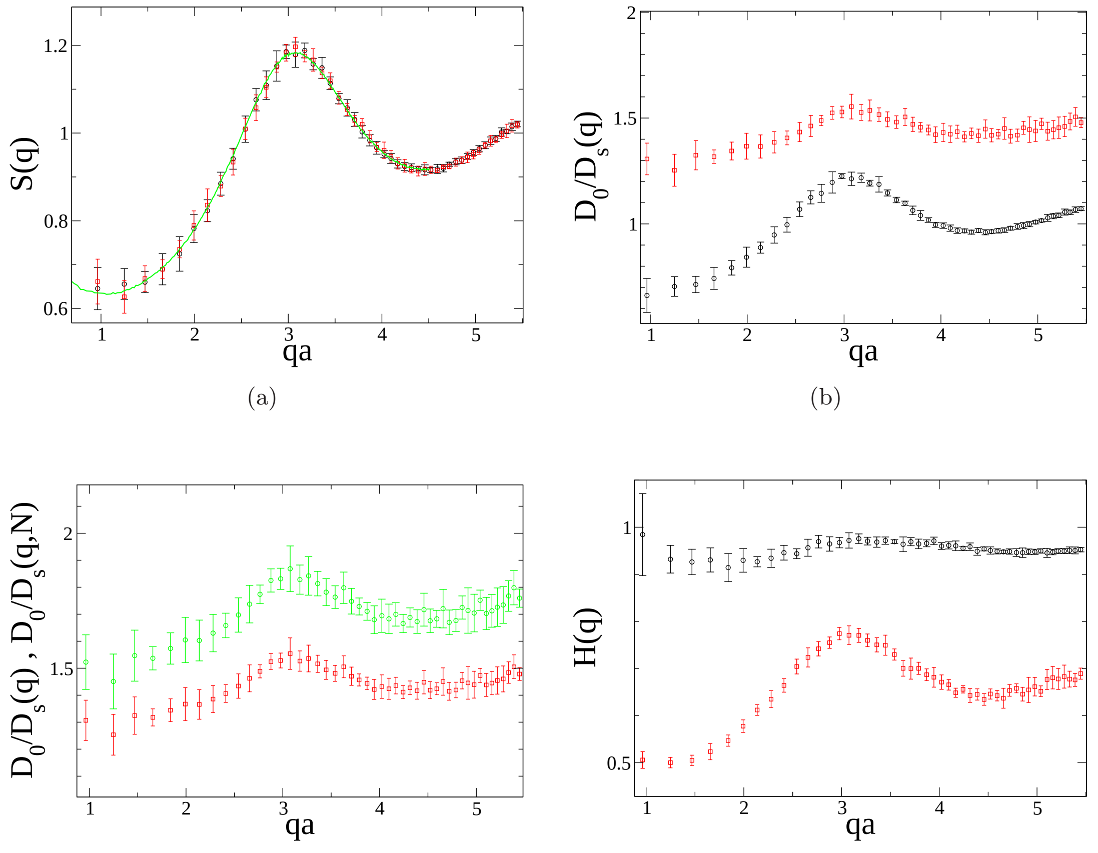

(a) (b)

(c) (d)

Figure 4.12: Data for $\lambda = 4$ and $\phi = 0.10$. Black open circle is BD and red open square is LB. Green line is MC in (a). In (c), green is uncorrected $D_s(q, N)$ and red is the corrected $D_s(q)$.

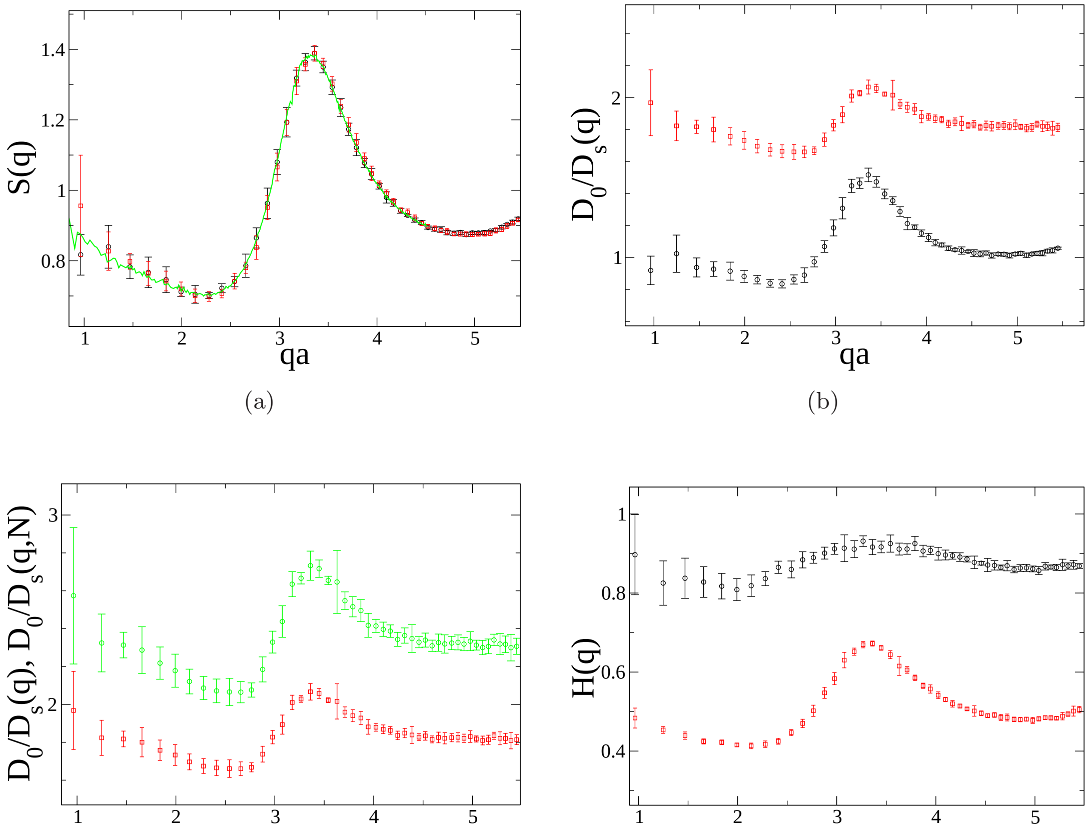

(a) (b)

(c) (d)

Figure 4.13: Data for $\lambda = 8$ and $\phi = 0.10$. Data for $\lambda = 0.0$ and $\phi = 0.10$. Black open circle is BD and red open square is LB. Green line is MC in (a). In (c), green is uncorrected $D_s(q, N)$ and red is the corrected $D_s(q)$.

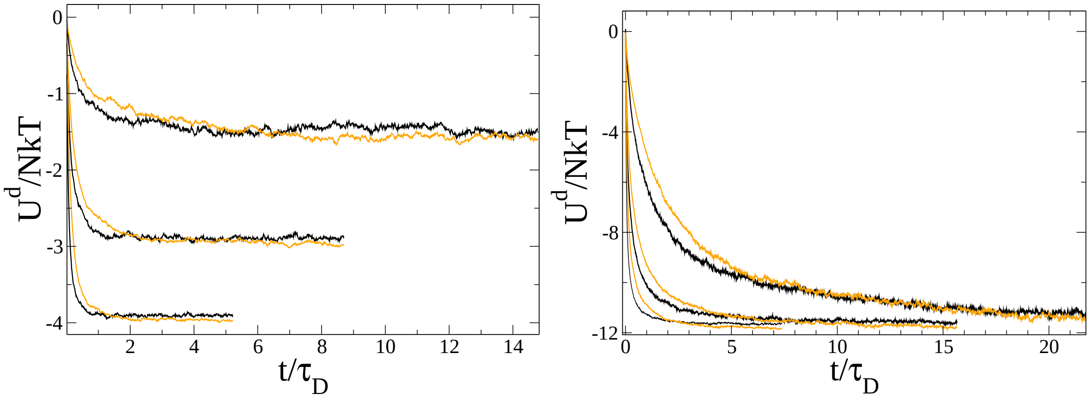

(a) (b)

Figure 4.14: Relaxation of the dipolar energy following a quench from $\lambda = 0$ to (a) $\lambda = 4$; (b) $\lambda = 8$. Black lines are BD runs and orange lines are LB runs. Pair of BD/LB curves correspond to the volume fraction of particles, $\phi = 0.03, 0.10$ and 0.20, from top to bottom.

4.4.2 Cluster statistics

We choose to define the clustering of magnetic colloids by a criterion involving a pair dipolar energy, U^d, in equation (4.2). If U^d for a pair is less than a threshold energy U^d_C, the two dipoles are defined to belong the same cluster. In hard-sphere magnetic colloids, some previous works[52, 116] have presented cluster distributions in equilibrium with various energy thresholds, $-1.7\lambda < U^d_C/k_BT < -1.4\lambda$ whose range is approximately in middle between the nose-to-tail state, -2.0λ, and the antiparallel side-by-side state, -1.0λ.

In this thesis, the soft-core repulsive potential is used for short-range interactions; we choose a threshold U^d_C determined by the geometry of dipoles based on the nose-to-tail, such that the antiparallel side-by-side structure is rejected by our $U^d_C/k_BT = -0.75\lambda$. On this basis, we found the criterion for U^d as

$$U^d/k_BT < -0.75\lambda. \tag{4.19}$$

In numerical practice, the cluster algorithm[19] is used to determine the clusters with the criterion in equation (4.19) replacing one based on the distance between two particles.

Using equation (4.19), we classify our N particles into a set of disconnected clusters. Figures 4.15-4.17 present the fraction P_n of particles, where the subscript n is the cluster size. The time evolution of P_n provides the growth trend of clusters after quenching from the equilibrated state with $\lambda = 0$. First, the P_n is measured every $t = 2000$ time steps and then all data points in Figures 4.15-4.17 are binned every 25 points for $t < 200,000$ and every 50 points thereafter. This condition for binned data is the optimal choice to resolve the peaks of $P(n)$ in the data with $\lambda = 8$.

The P_n of BD are also shown in Figures 4.15-4.17 to compare with those of LB as a check of the hydrodynamic effect in chain formation. Although the slow relaxations in P_n observed in LB are similar to those of the dynamic correlators in Section 4.3.1 and 4.3.2, there is no remarkable difference between BD simulations and LB simulations. For all λ and ϕ values, the monomer fraction P_1 decays to reach a saturated value. For $\lambda = 4$ with $\phi = 0.03, 0.10$ and 0.2, P_n for $n = 2, 3, 4$ take roughly equal times to become saturated. However, in the data for $\lambda = 8$, before P_1 reaches the steady value, peaks are found in the curves of P_2, P_3 and P_4. That means that small clusters in the early time are later assembled into large clusters. Note that $\lambda = 8$ has a large mean cluster size as $\bar{N}_p > 7$ for all particle volume fractions, while $\lambda = 4$ has small mean cluster as $\bar{N}_p < 2$. Meanwhile, in the 2 dimensional system by BD[97], a similar transient in the self assembly of chain has been found at $\phi \geq 0.20$ and $\lambda > 4$.

Figure 4.18 shows the mean number of particles per cluster $\bar{N}_p$ as a function of time: $\bar{N}_p = \frac{N_t}{\sum_c N_c}$, where N_c is the number of clusters with a size c and N_t is the total number of particles. For $\phi = 0.10$ with $\lambda = 4$ and 8, $\bar{N}_p$ at late time is reflected in the snapshots in Figure 4.7, although the small system box ($\Lambda^3 = 64^3$) is used to simulate these.

Throughout the energy relaxations and the cluster statistics, we could not find any significant discrepancy of the results between BD runs and LB runs. On the other hand, the hydrodynamic effect for cluster formation[117] has been studied in the colloidal system with a Lennard-Jones potential for the short-range attraction in an athermal fluid. That study concluded that hydrodynamic interaction makes the relaxation faster and the clusters bigger. However, in our simulations, as considering long-range dipolar interactions in a thermal fluid which influence the colloidal diffusive motion, a slower relaxation rate only is found and there is no evidence for larger clusters in LB than the ones in BD without hydrodynamic interaction.

4.5 Transient scattering functions

The last section discussed the time evolution of cluster statistics for magnetic colloids. These cluster statistics provide evidence concerning the transient process from the configuration equilibrated with $\lambda = 0$ to ones with $\lambda \neq 0$. Consistently, transient behaviour could be expected to arise in dynamic correlators for various waiting times: t_w. This section will discuss the waiting-time dependency of transient scattering

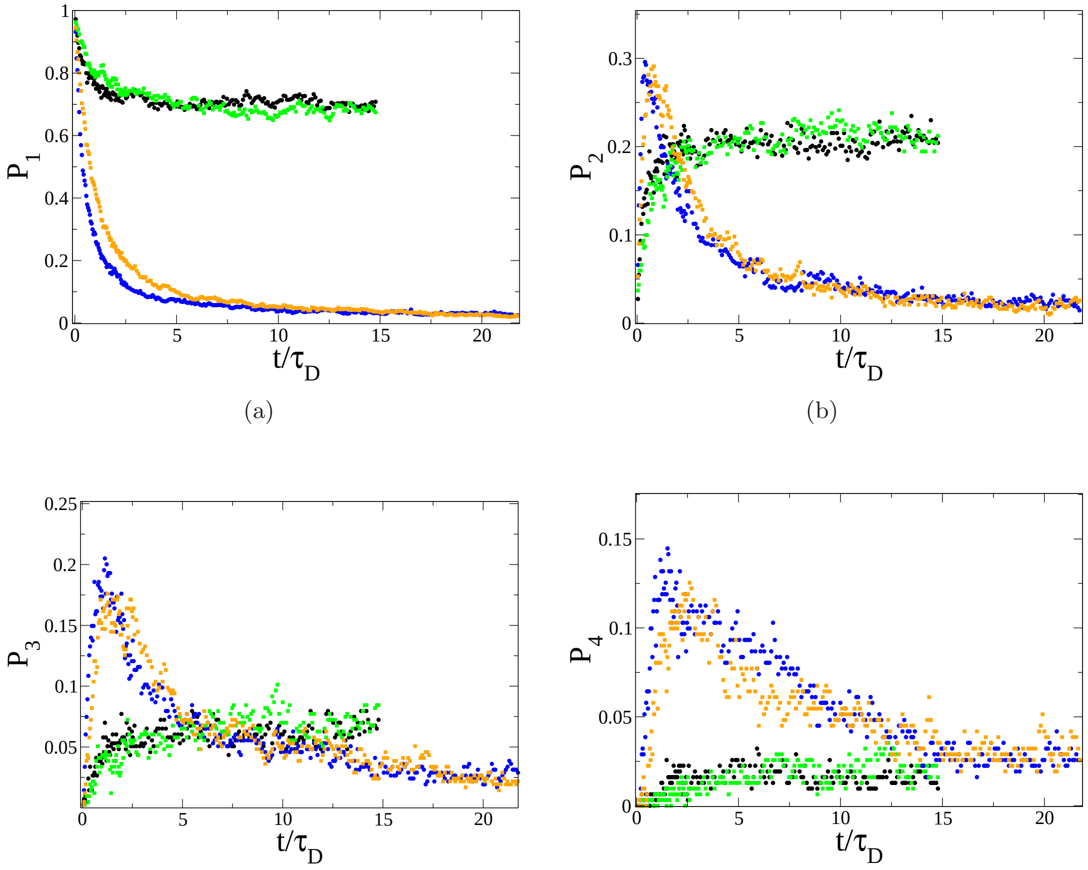

(a) (b)

(c) (d)

Figure 4.15: Relaxation of cluster probabilities $P_n(t)$ following quenches from $\lambda = 0$ to $\lambda = 4$ and 8 at $\phi = 0.03$: (black circles) BD with $\lambda = 4$; (green squares) LB with $\lambda = 4$; (blue circles) BD with $\lambda = 8$; (orange squares) LB with $\lambda = 8$.

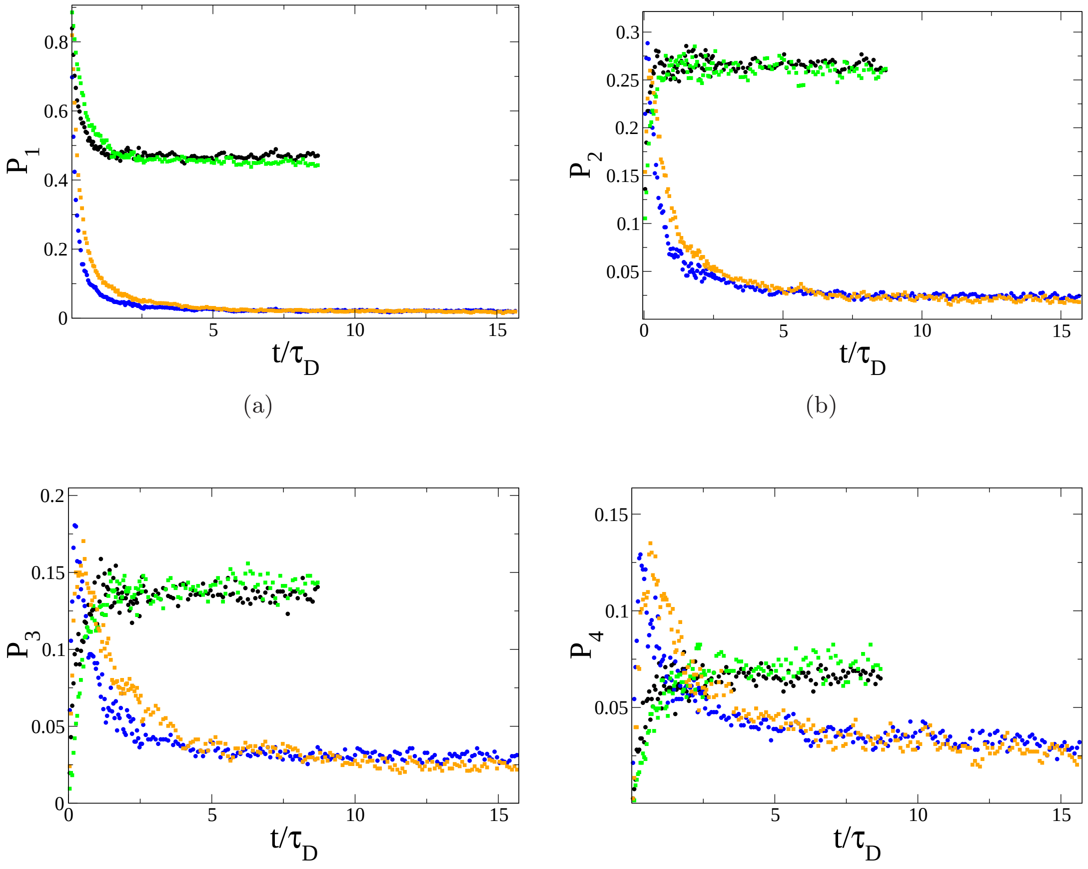

(a) (b)

(c) (d)

Figure 4.16: Relaxation of cluster probabilities $P_n(t)$ following quenches from $\lambda = 0$ to $\lambda = 4$ and 8 at $\phi = 0.10$: (black circles) BD with $\lambda = 4$; (green squares) LB with $\lambda = 4$; (blue circles) BD with $\lambda = 8$; (orange squares) LB with $\lambda = 8$.

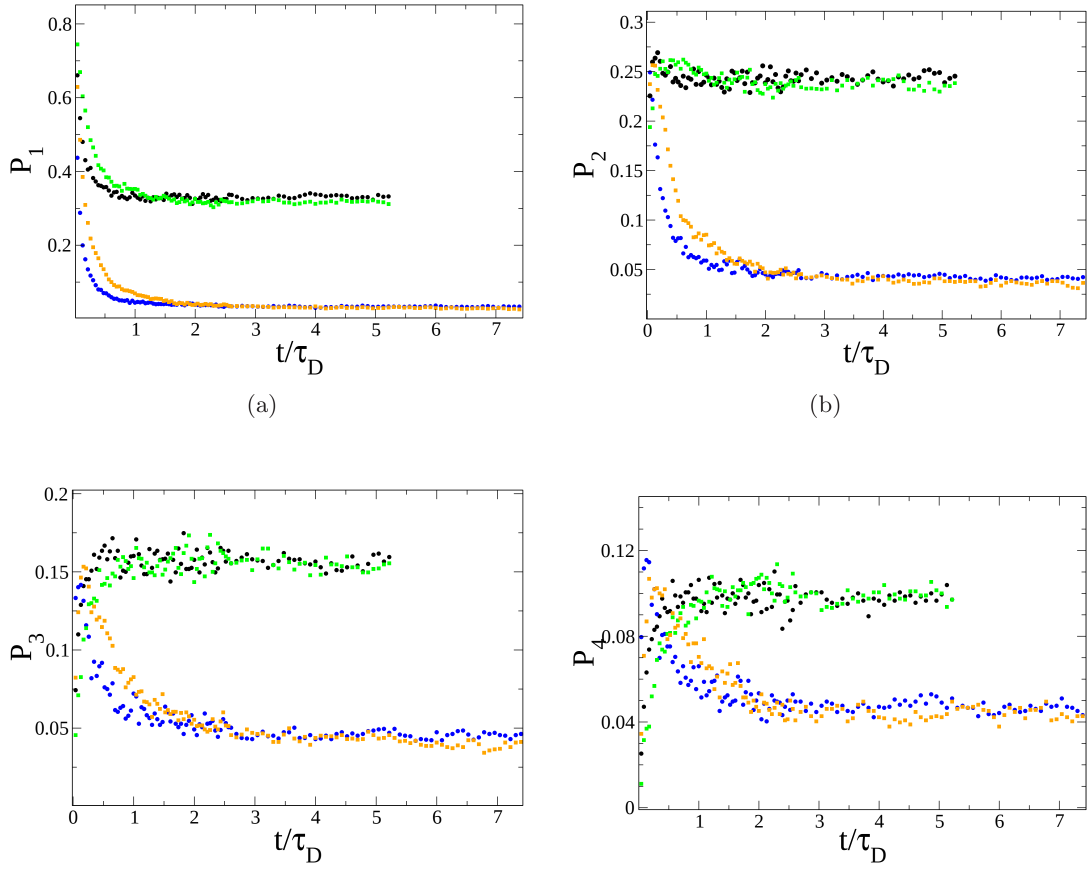

(a)

(b)

(c)

(d)

Figure 4.17: Relaxation of cluster probabilities $P_n(t)$ following quenches from $\lambda = 0$ to $\lambda = 4$ and 8 at $\phi = 0.20$: (black circles) BD with $\lambda = 4$; (green squares) LB with $\lambda = 4$; (blue circles) BD with $\lambda = 8$; (orange squares) LB with $\lambda = 8$.

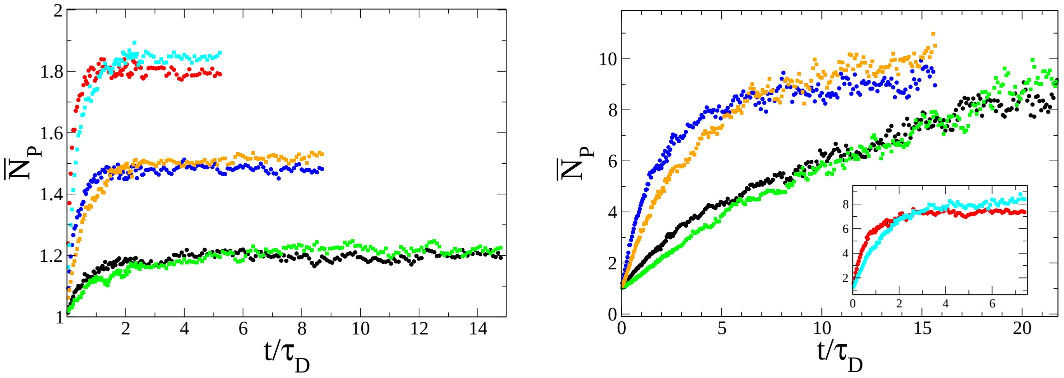

(a)

(b)

Figure 4.18: Time evolution of mean cluster size for (a) $\lambda = 4.0$ and (b) $\lambda = 8.0$ at $\phi = 0.03, 0.10, 0.20$. Black, red and blue are $\phi = 0.03, 0.10, 0.20$ in BD. Green, orange, and cyan are $\phi = 0.03, 0.10, 0.20$ in LB. Inset of (b)

functions: structure factor, translational relaxation and rotational relaxation. To observe the properties relevant for cluster assembly, the transient motions at the wavevector $q^* \approx 2\pi/d$ will be discussed. In contrast to previous sections, the LB data only are presented. (We haven't seen any important effect of hydrodynamic interactions in transient dynamics.)

4.5.1 Structure factors

Figure 4.19 shows the transient structure factors $S_\Delta(q, t_w)$ for various λ and ϕ. For good statistics from the data with $\phi = 0.03$ and 0.10, $S_\Delta(q, t_w)$ is obtained by the average over the static structure factors during a time interval Δt between a initial time t_w and a final time $t_f = t_w + \Delta t$:

$$S_\Delta(q, t_w) = \frac{1}{\Delta t} \int_{t_w}^{t_f} S(q, t) dt. \tag{4.20}$$

However, for the particle concentration $\phi = 0.20$, the large number of colloids ($N = 8239$) causes good statistics for the measurements of $S_\Delta(q, t_w)$, so that just one configuration at t_w is used to calculate $S_\Delta(q, t_w)$. The function $S_\Delta(q, t_w)$ quantifies the spatial ordering for colloids at different “waiting” times, including the long-range structures.

In Figures 4.19(a)-4.19(d), strong transient behaviours are observed in the data for $\lambda = 4.0$ and 8.0 with $\phi = 0.03$, 0.10. However, for $\phi = 0.20$ in Figures 4.19(e) and 4.19(f), relatively weak transient behaviours are seen in comparison to those for

$\phi = 0.03$ and 0.10. For $\lambda = 4$ with $\phi = 0.20$ in Figure 4.19(e), the peak near q^* is more narrow at the late waiting time and the curves for $qa < 2$ are slightly raised. At fixed $\lambda = 4$, despite increasing the particle volume fraction, the mean cluster size is less than 2. As concerning the high volume fraction effect on the static structure factor at $\phi = 0.20$ with $\lambda = 0$, the mean cluster size $\bar{N}_p \sim 1.8$ in the equilibrated configuration with $\lambda = 4$ is not crucial in terms of the positional structure of particles. In comparison with the small mean size at $\lambda = 4$, $\lambda = 8$ has large clusters so that $S_\Delta(q, t_w)$ for $qa < 2$ have a rising trend and the peak q^* is more narrow at late waiting times.

4.5.2 Translational relaxation

In contrast to pure hard-sphere diffusive particles at similar volume fraction ($0.03 < \phi < 0.20$), magnetic colloids travel for only short distance before colliding with nearby particles in the same chain. That leads to a smaller diffusion coefficient and slower relaxations at a fixed q. Section 4.3.1 discussed the equilibrium dynamics through the translational intermediate scattering function (TISF) which shows the time-independency explained in equilibrium.

In the transient dynamics, we examine the waiting-time dependency of the TISF, $S(q, t_w, t)$, which is rewritten from equation (4.11) as

$$S(\mathbf{q}, t_w, t) = \frac{1}{N} \sum_{i,j} \exp[-i\mathbf{q}\{\mathbf{r}_j(t_w + t) - \mathbf{r}_i(t_w)\}], \tag{4.21}$$

where, $\mathbf{r}_i(t_w)$ is a position of particle i at the initial time t_w.

Figure 4.20 presents the transient TISF, $S(q^*, t_w, t)$, where q^* is chosen as the highest peak of transient structure factors at late t_w in Figure 4.19. Although strong structural changes are observed at $\phi = 0.03$ and 0.10 for $\lambda = 4$ in Figures 4.19(a) and 4.19(c), the two-time relaxation curves in Figures 4.20(a) and 4.20(c) do not have any strong waiting-time dependency. For $\lambda = 8$, the curves at $\phi = 0.10$ show stronger transient behaviour than those at $\phi = 0.03$.

In Figures 4.20(e) and 4.20(f), more clear transient effects are found at high particle fraction $\phi = 0.20$ whose structure factors change relatively weakly (as seen in Figures 4.19(e) and 4.19(f)). At late t_w, the relaxations are slower; on approaching the equilibrium states corresponding to $\lambda = 4$ and $\lambda = 8$, the observed transient behaviour is getting weaker and finally the transient scattering functions are no longer dependent on t_w in equilibrium. Therefore, overlapped curves are seen at $t_w = 200,000$ and $400,000$. At these late times, more-or-less saturated curves are found in the energy relaxations as seen in Figure 4.14.

These time-dependent relaxations can be explained by the process for cluster

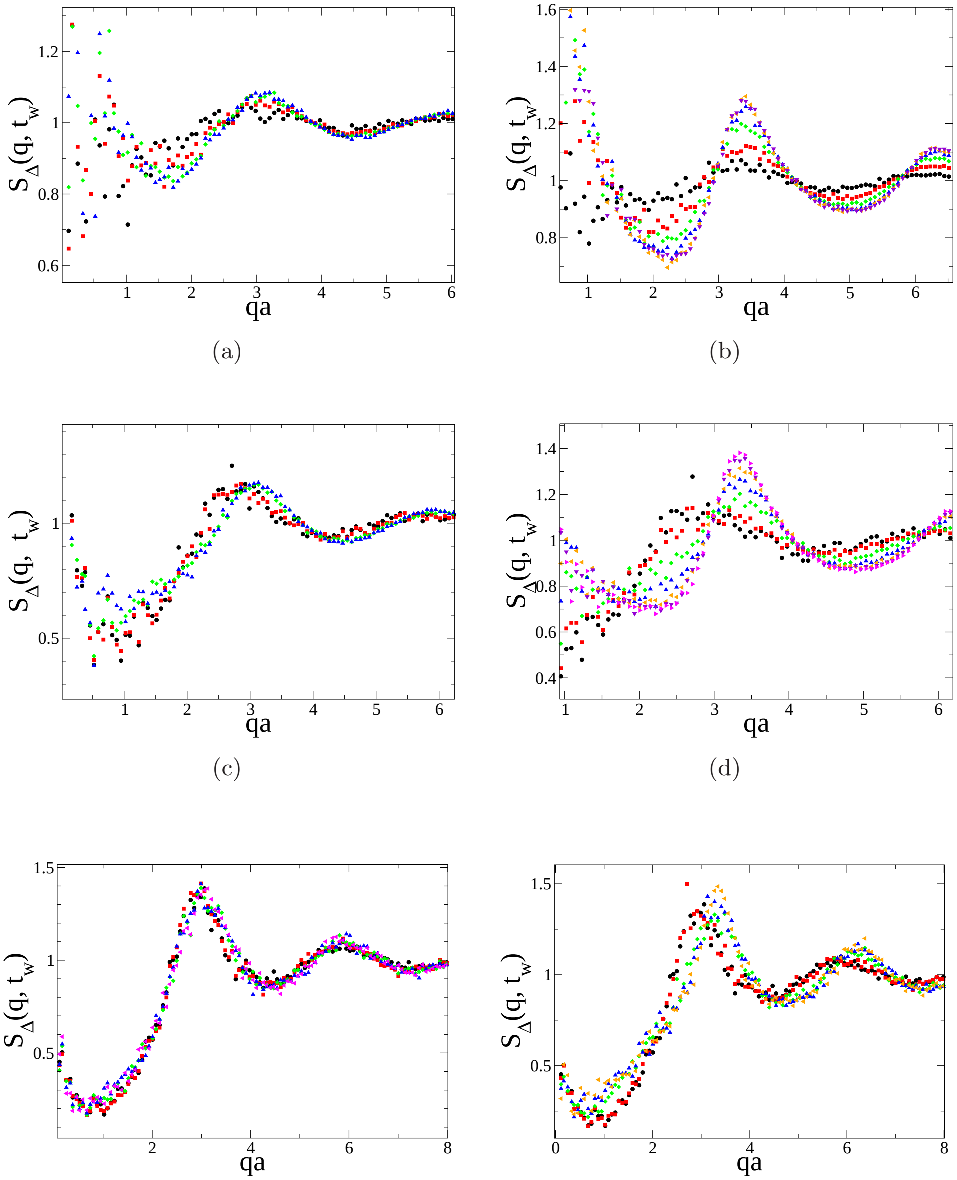

(a) (b)

(c) (d)

(e) (f)

Figure 4.19: Transient structure factors at various t_w. (a) $\lambda = 4$ with $\phi = 0.03$: (black) $t_w = 0$; (red) $t_w = 90,000$; (green) $t_w = 400,000$; (blue) $t_w = 800,000$. (b) $\lambda = 8$ with $\phi = 0.03$: (black) $t_w = 0$; (red) $t_w = 90,000$; (green) $t_w = 200,000$; (blue) $t_w = 400,000$; (orange) $t_w = 600,000$; (purple) $t_w = 800,000$. (c) $\lambda = 4$ with $\phi = 0.10$: (black) $t_w = 0$; (red) $t_w = 10,000$; (green) $t_w = 80,000$; (blue) $t_w = 200,000$. (d) $\lambda = 8$ with $\phi = 0.10$: (black) $t_w = 0$; (red) $t_w = 4,000$; (green) $t_w = 30,000$; (blue) $t_w = 70,000$; (orange) $t_w = 170,000$; (purple) $t_w = 300,000$; (magenta) $t_w = 500,000$. (e) $\lambda = 4$ with $\phi = 0.20$: (black) $t_w = 0$; (red) $t_w = 10,000$; (green) $t_w = 80,000$; (blue) $t_w = 200,000$; (magenta) $t_w = 400,000$. (f) $\lambda = 8$ with $\phi = 0.20$: (black) $t_w = 0$; (red) $t_w = 10,000$; (green) $t_w = 80,000$; (blue) $t_w = 200,000$; (orange) $t_w = 400,000$.

formations and the resulting cage effect. For $\lambda = 4$ with $\phi = 0.03$ and 0.10, only small clusters are formed as $\bar{N}_p < 2$ in equilibrium. That means the cage effect is rather weak during transient motion; so on length scales near the structure factor peak magnetic colloids still move like pure diffusive particles. Therefore strong transient behaviours are not found in Figure 4.20(a) and 4.20(c). Similarly, for $\lambda = 8.0$, the strong transient motions occur during the process of forming large clusters (as $\bar{N}_p > 7$). In addition, with increasing ϕ for $\lambda = 4$ or 8, the transient relaxation function at fixed time t increases monotonically.

4.5.3 Rotational relaxation

In a similar manner to translational correlators for transient dynamics, two-time rotational correlators can be rewritten following equations (4.13)-(4.18) as

$$\begin{aligned}
F(\mathbf{q}, t_w, t) &= \frac{1}{N} \langle \mathbf{M}(\mathbf{q}, t_w + t)\mathbf{M}(\mathbf{q}, t_w) \rangle \\
F_L(\mathbf{q}, t_w, t) &= \frac{1}{N} \langle \mathbf{M}_L(\mathbf{q}, t_w + t)\mathbf{M}_L(\mathbf{q}, t_w) \rangle \\
F_T(\mathbf{q}, t_w, t) &= \frac{1}{N} \langle \mathbf{M}_T(\mathbf{q}, t_w + t)\mathbf{M}_T(\mathbf{q}, t_w) \rangle .
\end{aligned}$$

The total rotational correlator $F(\mathbf{q}, t_w, t)$ is the sum of the longitudinal component, $F_L(\mathbf{q}, t_w, t)$, and the transverse component, $F_T(\mathbf{q}, t_w, t)$.

Figure 4.21 presents $F(q^*, t_w, t)$ for various ϕ at $\lambda = 4$ and $\lambda = 8$. Even if general characteristics for rotational relaxations are similar to ones for the translational mode in Figure 4.20, more distinct transient behaviours are now seen at $\phi = 0.03$ with $\lambda = 8$ and at $\phi = 0.10$ with $\lambda = 4$.

Figures 4.22-4.27 show the two-time rotational correlators for the longitudinal component and the transverse component at various t_w; the relaxations of chain orientation along a wavevector at q^* are slower than ones of chain orientation transverse to the wavevector. For $\lambda = 4$ with $\phi = 0.03$ (which shows no transient in translational and orientational relaxations) $F_L(q^*, t_w, t)$ and $F_T(q^*, t_w, t)$ have similar relaxation rates, although, at $t_w = 800,000$, longitudinal relaxation is slightly slower after $t > 10,000$. Except for this case, the longitudinal relaxations are dominant in orientational motions; at late waiting time t_w, the gap between two relaxation rates is getting wider.

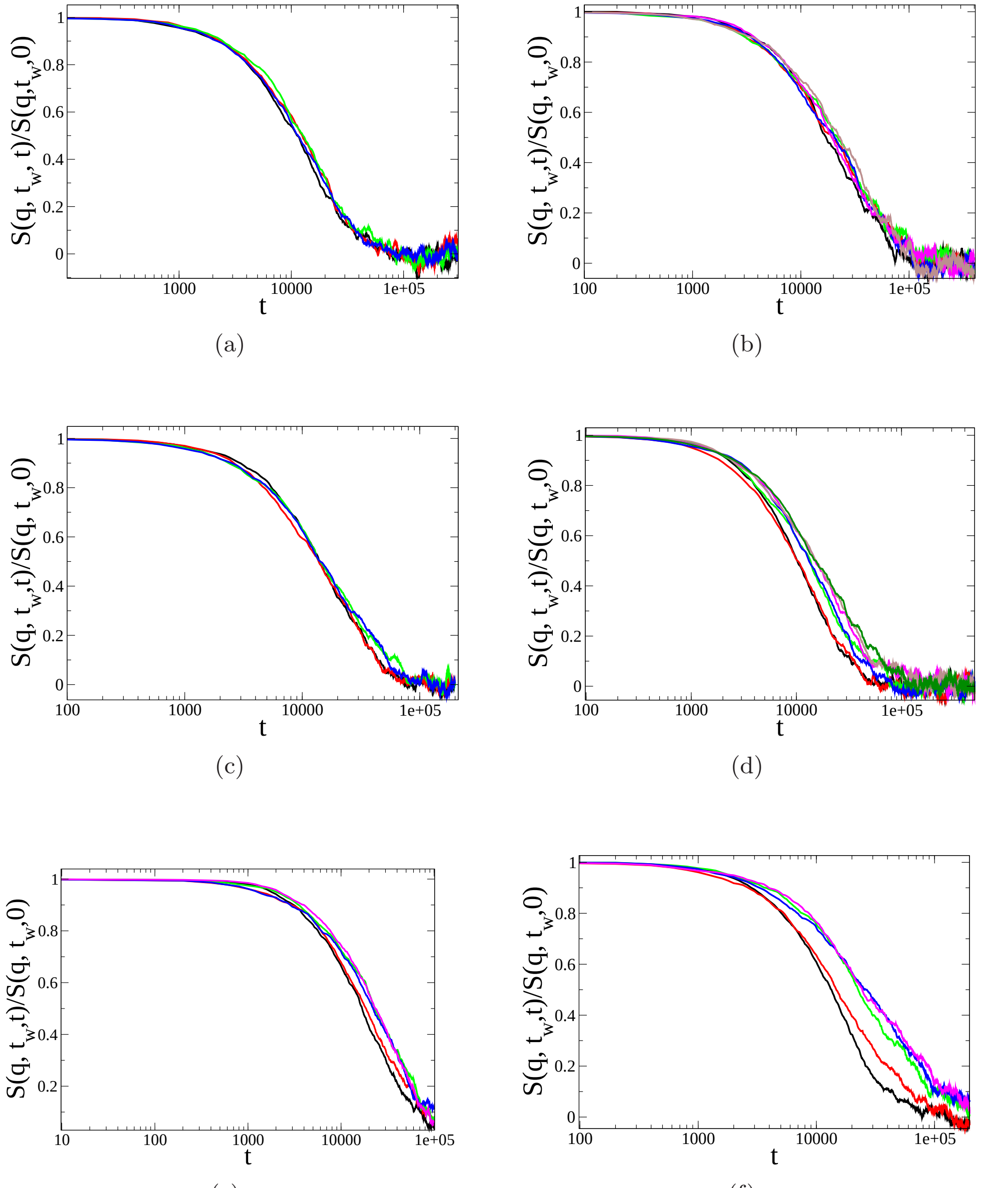

(a)

(b)

(c)

(d)

(e)

(f)

Figure 4.20: Transient relaxation on translational mode at various t_w around q^*. (a) $qa = 3.1160$ at $\lambda = 4$ with $\phi = 0.03$: (black) $t_w = 0$; (red) $t_w = 90,000$; (green) $t_w = 400,000$; (blue) $t_w = 800,000$. (b) $qa = 3.4047$ at $\lambda = 8$ with $\phi = 0.03$: (black) $t_w = 0$; (red) $t_w = 90,000$; (green) $t_w = 200,000$; (blue) $t_w = 400,000$; (orange) $t_w = 600,000$; (purple) $t_w = 800,000$. (c) $qa = 3.0579$ at $\lambda = 4$ with $\phi = 0.10$: (black) $t_w = 0$; (red) $t_w = 10,000$; (green) $t_w = 80,000$; (blue) $t_w = 200,000$. (d) $qa = 3.3548$ at $\lambda = 8$ with $\phi = 0.10$: (black) $t_w = 0$; (red) $t_w = 4,000$; (green) $t_w = 30,000$; (blue) $t_w = 70,000$; (orange) $t_w = 170,000$; (purple) $t_w = 300,000$; (magenta) $t_w = 500,000$. (e) $qa = 3.0993$ at $\lambda = 4$ with $\phi = 0.20$: (black) $t_w = 0$; (red) $t_w = 10,000$; (green) $t_w = 80,000$; (blue) $t_w = 200,000$; (magenta) $t_w = 400,000$. (f) $qa = 3.0993$ at $\lambda = 8$ with $\phi = 0.20$: (black) $t_w = 0$; (red) $t_w = 10,000$; (green) $t_w = 80,000$; (blue) $t_w = 200,000$; (orange) $t_w = 400,000$.

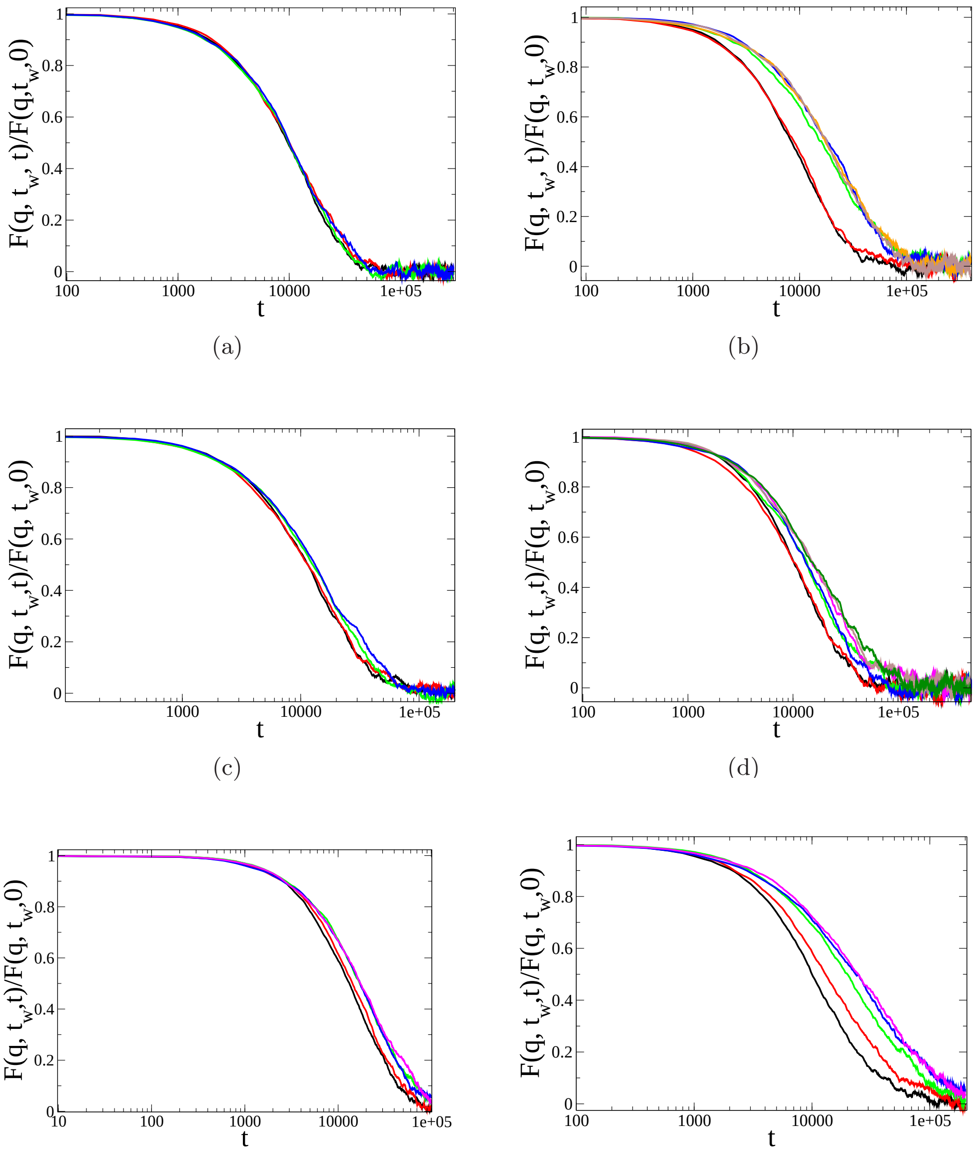

(a) (b)

(c) (d)

(e) (f)

Figure 4.21: Transient relaxation on rotational mode at various t_w around q^*. (a) $qa = 3.1160$ at $\lambda = 4$ with $\phi = 0.03$: (black) $t_w = 0$; (red) $t_w = 90,000$; (green) $t_w = 400,000$; (blue) $t_w = 800,000$. (b) $qa = 3.4047$ at $\lambda = 8$ with $\phi = 0.03$: (black) $t_w = 0$; (red) $t_w = 90,000$; (green) $t_w = 200,000$; (blue) $t_w = 400,000$; (orange) $t_w = 600,000$; (purple) $t_w = 800,000$. (c) $qa = 3.0579$ at $\lambda = 4$ with $\phi = 0.10$: (black) $t_w = 0$; (red) $t_w = 10,000$; (green) $t_w = 80,000$; (blue) $t_w = 200,000$. (d) $qa = 3.3548$ at $\lambda = 8$ with $\phi = 0.10$: (black) $t_w = 0$; (red) $t_w = 4,000$; (green) $t_w = 30,000$; (blue) $t_w = 70,000$; (orange) $t_w = 170,000$; (purple) $t_w = 300,000$; (magenta) $t_w = 500,000$. (e) $qa = 3.0993$ at $\lambda = 4$ with $\phi = 0.20$: (black) $t_w = 0$; (red) $t_w = 10,000$; (green) $t_w = 80,000$; (blue) $t_w = 200,000$; (magenta) $t_w = 400,000$. (f) $qa = 3.0993$ at $\lambda = 8$ with $\phi = 0.20$: (black) $t_w = 0$; (red) $t_w = 10,000$; (green) $t_w = 80,000$; (blue) $t_w = 200,000$; (orange) $t_w = 400,000$.

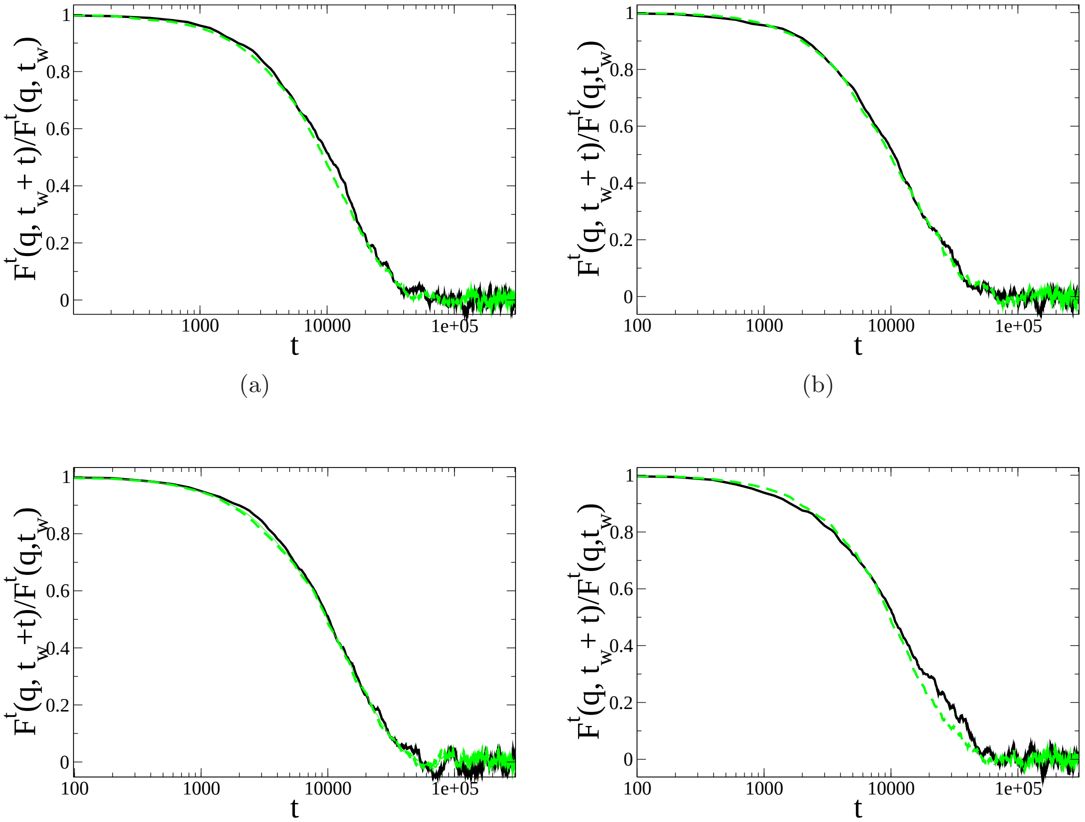

(a)

(b)

(c)

(d)

Figure 4.22: Transient relaxation on rotational mode at various t_w around q^* at $\lambda = 4$ with $\phi = 0.03$. (a) $t_w = 0$. (b) $t_w = 90,000$. (c) $t_w = 400,000$. (d) $t_w = 800,000$. Black line is longitudinal (F_L^t) and green dash is transverse (F_T^t).

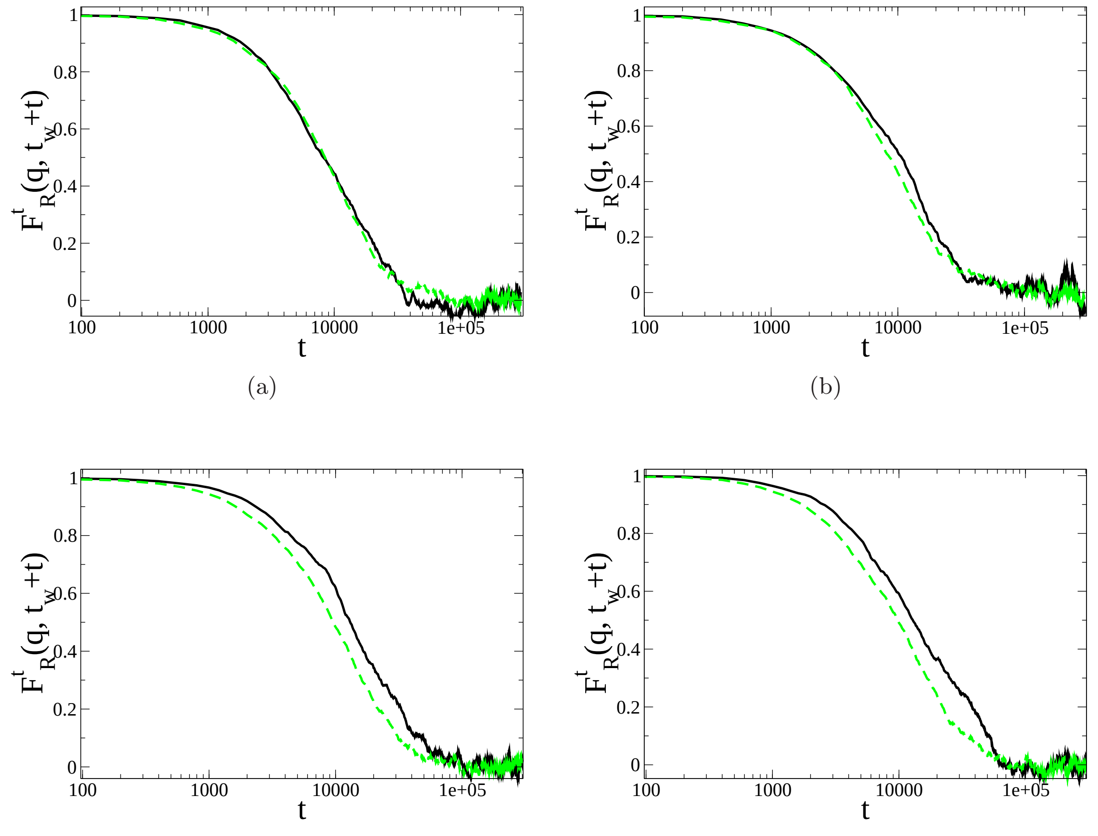

(a)

(b)

(c)

(d)

Figure 4.23: Transient relaxation on rotational mode at various t_w around q^* at $\lambda = 8$ with $\phi = 0.03$. (a) $t_w = 0$. (b) $t_w = 90,000$. (c) $t_w = 400,000$. (d) $t_w = 800,000$. Black line is longitudinal (F_L^t) and green dash is transverse (F_T^t).

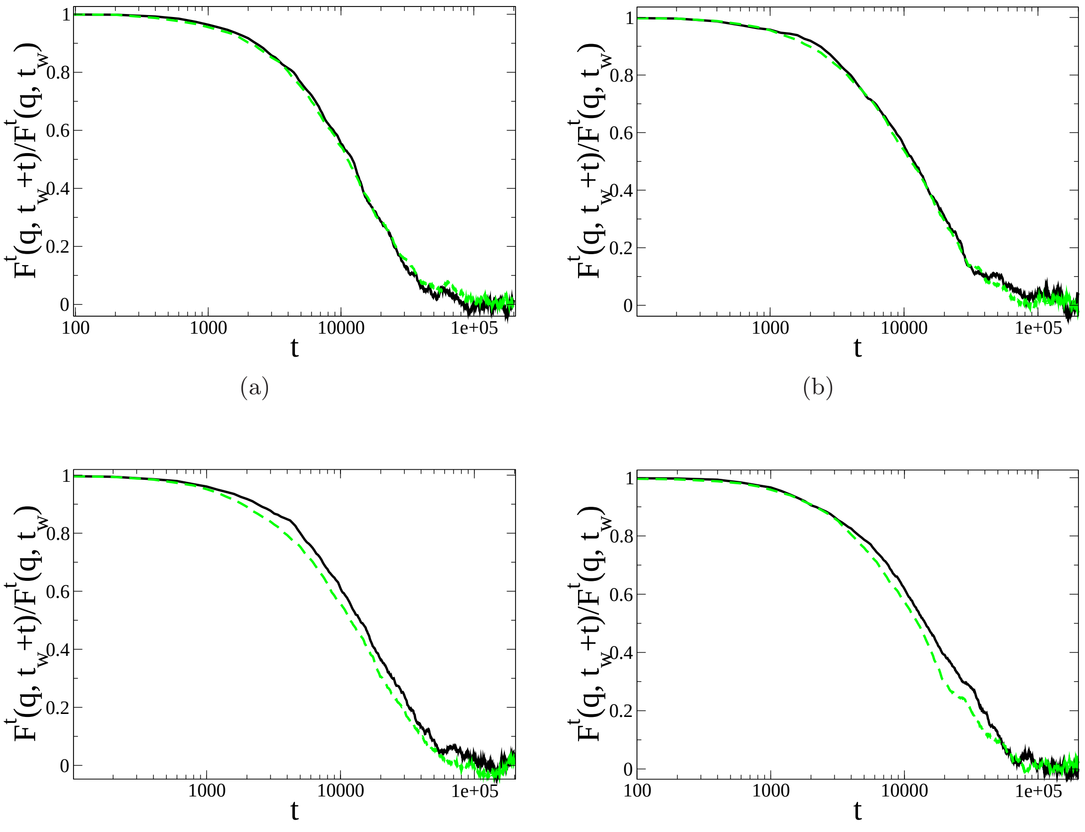

(a)

(b)

(c)

(d)

Figure 4.24: Transient relaxation on rotational mode at various t_w around q^* at $\lambda = 4$ with $\phi = 0.10$. (a) $t_w = 0$. (b) $t_w = 10,000$. (c) $t_w = 80,000$. (d) $t_w = 200,000$. Black line is longitudinal (F_L^t) and green dash is transverse (F_T^t).

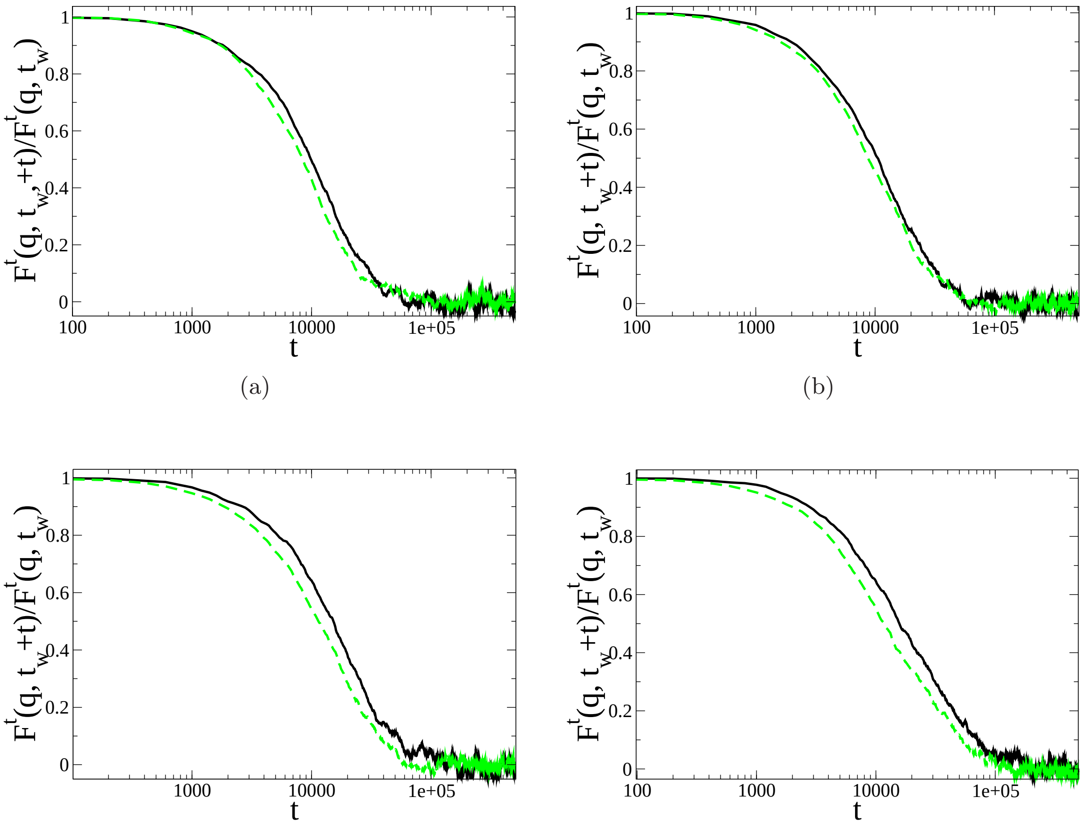

(a) (b)

(c) (d)

Figure 4.25: Transient relaxation on rotational mode at various t_w around q^* at $\lambda = 8$ with $\phi = 0.10$. (a) $t_w = 0$. (b) $t_w = 4,000$. (c) $t_w = 70,000$. (d) $t_w = 500,000$. Black line is longitudinal (F_L^t) and green dash is transverse (F_T^t).

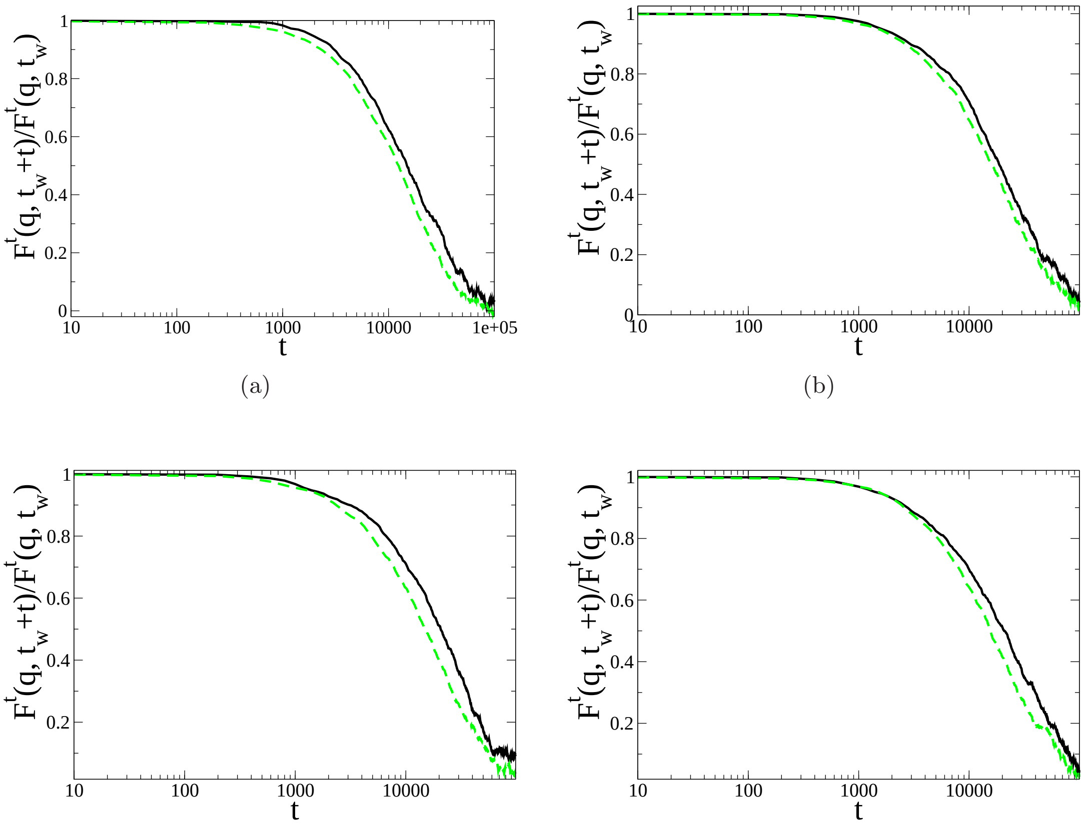

(a)

(b)

(c)

(d)

Figure 4.26: Transient relaxation on rotational mode at various t_w around q^* at $\lambda = 4$ with $\phi = 0.20$. (a) $t_w = 0$. (b) $t_w = 80,000$. (c) $t_w = 200,000$. (d) $t_w = 400,000$. Black line is longitudinal (F^t_L) and green dash is transverse (F^t_T).

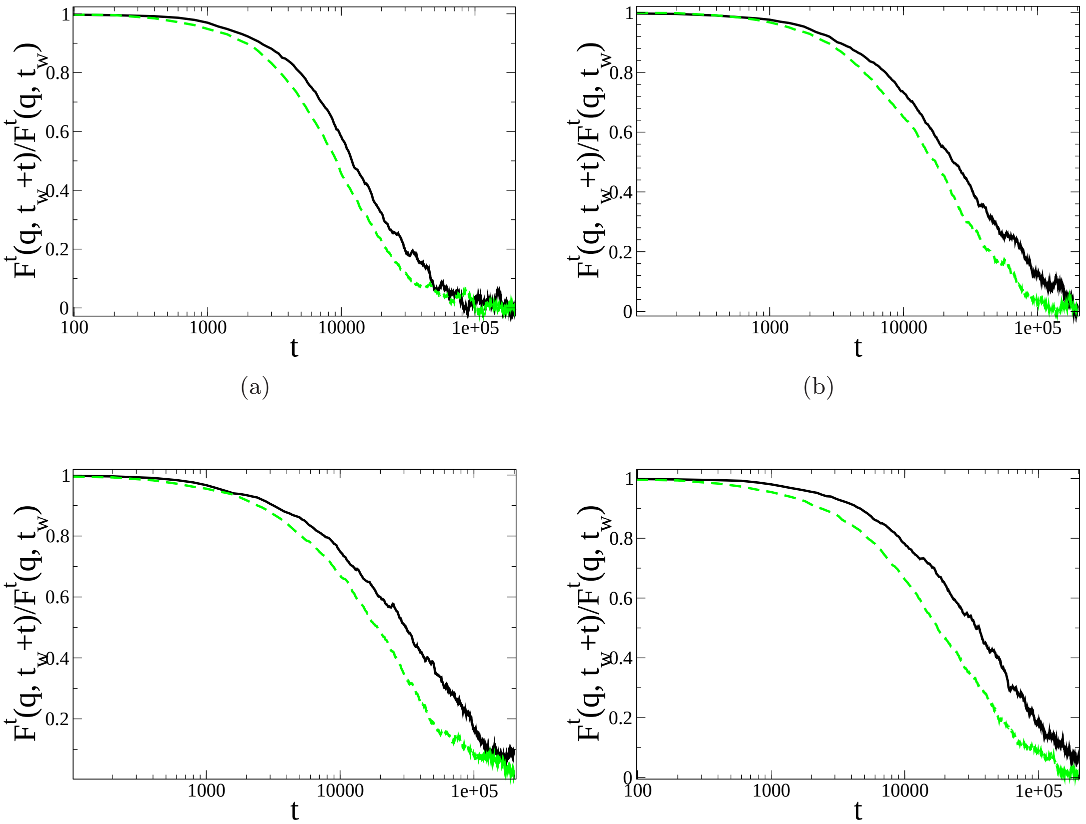

(a)

(b)

(c)

(d)

Figure 4.27: Transient relaxation on rotational mode at various t_w around q^* at $\lambda = 8$ with $\phi = 0.20$. (a) $t_w = 0$. (b) $t_w = 80,000$. (c) $t_w = 200,000$. (d) $t_w = 400,000$. Black line is longitudinal (F_L^t) and green dash is transverse (F_T^t).

4.6 Conclusions and discussions

This chapter discussed the simulations of colloidal ferrofluids via the LB method which allows for full many-body hydrodynamic effects acting on magnetic colloids. To check these hydrodynamic effects, BD simulations were also performed to compare with the results of LB runs. Data from MC runs were introduced to compare with the data of BD and LB for static structures in equilibrium. This chapter addressed the hydrodynamic effects on equilibrium dynamics, especially for the short-time Brownian regime, and on transient dynamics to form chain clusters. To ensure accurate simulations of static structures in equilibrium, we used a soft-core repulsive potential for short-range interactions to prevent the noise error that arises on close approach of particles in LB.

Static structures in equilibrium were measured by the radial distribution functions and equilibrium energies. Regardless of hydrodynamic interactions, these measurements have quantitatively good agreements with the Boltzmann statistics obtained by MC runs. However, with the strong dipolar interaction at $\lambda = 8$, a discrepancy is found at the first peak of radial distribution functions and for equilibrium energies presumably because of the noise error for close particles.

In equilibrium dynamics, the translational and rotational intermediate scattering functions were measured to see the wavevector-dependent relaxations. Here, it is found that the hydrodynamic interactions delay the relaxations and this effect is larger at smaller q and smaller λ. At high λ, we found the long-time relaxations are driven by the dipolar interactions. For rotational intermediate scattering functions, slower relaxations are observed for the longitudinal component on increasing λ. A clear effect of hydrodynamic interactions is found on the short-time diffusion coefficients in comparison with the BD data for which hydrodynamic interactions are absent. At larger λ and ϕ, a stronger hydrodynamic effect is observed, but its effect on long-time relaxation appears to be decreasing. In addition, although the full equilibration is difficult to achieve even at $\phi = 0.20$ and $\lambda = 8$, we found no evidence for a glass regime, whose signature is the presence of separate α and β relaxations in $S(q, t)$.

For transient dynamics during the process to form clusters, the size distribution of clusters as a function of time confirms the character of the transient motions, as do energy relaxations. These transient motions are also observed though the dependence of the scattering functions on waiting times, which show time-dependent behaviour.

In comparison to BD simulations, LB simulations require more computational power to achieve the same physical time scale. Also the treatment for the correct noise in LB method still remains an issue particularly for $\lambda = 8$. In our simulations, a fairly repulsive short-range potential minimises this noise error by preventing close contact for particles. For hard-sphere colloids, very high hydrodynamic forces occur when particles exist in lubrication contact. However, the soft-core repulsion in our simulations maintains the separation between particles, so that it is possible that these lubrication effects would increase the relative role of hydrodynamic interactions. To study this effect, an algorithm such as accelerated Stokesian Dynamics[23, 118] or Stokesian Dynamics[22, 119] might be more suitable than LB. Throughout several results in this chapter, we found the effect of hydrodynamic interaction is rather weak in equilibrium and during transient dynamics. However, the hydrodynamic effects could become more strongly noticeable in various nonequilibrium situations such as the rheological response to steady and/or time-dependent shearing. Hopefully, these will be studied in future work.

Chapter 5

Magnetic Colloids in a Binary Fluid

This chapter will introduce a new class of emulsions, “magnetic colloids in a binary fluid”, simulated by our LB method. Chapter 3 discussed the formation of arrested fluids by colloids, which have no long-range interactions, using a broad range of analyses in LB simulations. After a quench of the well-mixed fluids, fluids start to demix and colloids become trapped at the fluid-fluid interfaces. As the coarsening dynamics reduces the surface area between fluids, colloids become jammed at interfaces. Due to these jammed colloids, slow dynamics was observed for domain growth; local hexagonal packing or semi-crystalisation was seen for colloids at the interface. We also found domain morphologies varying from bijel to droplets by controlling ψ_0, the fraction of fluids.

Simulations for this new emulsion are accomplished by the LB method used in Chapter 3. Magnetic colloids are implemented using the long-range dipolar interactions shown in Section 2.4.2. With regard to the long-range dipolar interactions, Chapter 4 addressed the basic properties for the effect of hydrodynamic interactions on magnetic colloids in a single solvent through comparison with data from BD and MC. This confirmed that our LB method is adequate to study colloidal systems with long-range interactions. In the formation of chainlike structures in colloidal ferrofluids, the length of chains is controlled by λ (the dipolar coupling constant) at fixed particle fraction ϕ.

Concerning the aggregated structure of magnetic colloids in a binary fluid undergoing spinodal decomposition, one can look forward to seeing nose-to-tail structure among the interfacial colloids. Also we can expect an effect of external field on domain morphologies and orientational ordering of dipoles.

On the other hand, there has been no exactly corresponding study in experiment. However, Melle *et al.*[63] investigated the destabilisation of magnetic Pickering emulsions under field gradient to find a critical field strength for the stability threshold between emulsion droplets and their coalescence to form continuous fluid phases. In this chapter, we will discuss the stability of a droplet under external fields (both uniform field and gradient field). In terms of coarsening dynamics of fluids, colloids at the fluid-fluid interfaces determine the fluid morphology. So after switching on dipolar interactions and applying an external field to a stable droplet covered by randomly orientated colloids, one expects dipoles to become arranged along the direction of the external field; this could vary the droplet morphology.

In Section 5.1, simulation conditions will be briefly introduced, specifying the parameter sets for magnetic colloids in a binary fluid. In next three sections, simulation results will be discussed in detail; Section 5.2 will present the domain morphologies at various conditions, e.g. symmetric and asymmetric quenches, different temperatures to control the relaxation time and capillary energy, varying strength of dipoles, and applying an uniform external field; Section 5.3 will discuss the domain growth; and in Section 5.4, properties of magnetic colloids are quantified through the energy relaxation and dipolar ordering. Finally Section 5.5 will discuss the effect of external fields on the deformation of a droplet covered by magnetic colloids.

5.1 Simulation parameters

The simulation method used in this chapter consists of two parts. The first is the LB framework for a binary fluid. The second treats the dynamics for magnetic colloids by adding the terms of force and torque derived from the long-range dipolar interactions in the update step for velocities of particles (as seen in Section 2.3.2.).

From the initial mixed fluids with composition ψ_0 (the conserved mean order parameter), a deep quench is given by using the parameter set, $-A = B = 0.002$, in the free energy potential of equation (2.17). The last parameter in equation (2.17) is given as $\kappa = 0.0014$, so that the interfacial width and the interfacial tension are obtained as $\xi = 1.14$ LU and $\sigma = 1.58 \times 10^{-3}$ LU, respectively. The viscosity of both fluids is set as $\eta = 0.1$ in all simulations. Monodisperse colloids are used with a radius $a_h = 2.3$ LU; $\phi = 0.20$ is the concentration of colloids used in all simulations in Sections 5.1-5.3. Two temperature choices are made, with different values for the dimensionless control parameter for capillary energy, $\sigma\pi a_h^2/k_BT$, and the diffusive time τ_D for magnetic particles; one is the standard temperature $k_BT = 2.133 \times 10^{-5}$ LU which corresponds to 300 K in a lab; another is the higher temperature $k_BT = 2 \times 10^{-4}$ LU. The diffusion time τ_D at $k_BT = 2 \times 10^{-4}$ LU is 10 times faster than one at $k_BT = 2.133 \times 10^{-5}$ LU, so that we can expect faster relaxation of dipoles at $k_BT = 2 \times 10^{-4}$ LU. With the given parameters, the capillary energy is obtained as $\epsilon = 0.026$, so that the dimensionless parameters are given as $\epsilon/k_BT = 1230$ at $k_BT = 2.133 \times 10^{-5}$ LU and $\epsilon/k_BT = 130$ at $k_BT = 2 \times 10^{-4}$ LU; this means that the capillary energy still dominates for colloids at interfaces within this temperature range.

For the short-range potential of colloids, the parameter set is chosen as $\gamma = 10k_BT$, $h_0 = 0.1$, $\nu = 1.0$ and $h_c = 0.25$. All simulations in this chapter have been done in a $D3Q19$ model with the system volume $\Lambda^3 = 64^3$ with either periodic or fixed-wall boundary conditions. For the latter system, a normal lubrication force is introduced for colloids at distances $h < h_{lub} = 0.5$ between the plane of the wall and the surface of the colloid; the neutral wetting condition is maintained between a solid wall and the fluid-fluid interfaces.

To calculate the long-range dipolar interactions for a periodic boundary box, Ewald summation is used (see Section 2.4.3). The parameters are chosen as the real space cutoff $r_c = 16$ and the convergence parameter $\alpha = 0.15625$. With given α, the wavevectors for the Fourier part obeys $\mathbf{k} = (2\pi/\Lambda)(n_x, n_y, n_z)$ with $n_x, n_y, n_z \leq 8$. The conducting boundary condition is used in the Ewald summation. In a non-periodic box system, the long-range dipolar interactions can be simply calculated from equation (2.76). The corresponding force and torque, derived from the long-range dipolar equation, were shown in Section 2.4.4.

For study of the external field effect, we examine one droplet covered by colloids (as in Figure 3.7(g)) under either a uniform field or a field gradient. A uniform field $\mathbf{B}_0$ directly creates torque but not net forces on the dipoles. By aligning the dipoles, it alters the dipole-dipole interactions. In superparamagnetic colloids, Langevin theory predicts the equilibrium magnetisation as a function of uniform field strength (discussed in Appendix C). A uniform field applied within the simulation box always obeys $\nabla\cdot\mathbf{B}_0 = 0$, so that it can be used with both periodic boundary condition and nonperiodic one. On the other hand, study of field gradient effects requires care; it is hard to have a function of nonuniform field which satisfies zero-divergence of the field in a periodic box, so that only nonperiodic boundary conditions are used to study the effect of a field gradient. To allow parameter mapping onto laboratory conditions, we assume an external permanent magnet as the source for the field gradient whose form is then given as equation (2.72).

Most of simulations have been done until $t_{final} = 5 \times 10^5$ LU; this time window is enough to reach a near-steady state in $\Lambda^3 = 64^3$, so long as one disregards the slow residual dynamics discussed in Chapter 3. For a single run, one single Intel core2 2.4GHz requires 270 hours. However the parallel computation using 8 cores of a cluster of 3GHz Intel Dual-core processors[106] reduce the computational time to about 26 hours; 8 cores of IBM Power5 processor requires 63 hours to simulate a single run[120].

5.2 Morphologies of fluid domains

This section presents the morphologies of fluid domains under various conditions according to the initial volumes of fluids (ψ_0), the dipolar coupling constant (λ), the fluid temperature (k_BT) and either an absence or a presence of uniform external field

($\mathbf{B}_0$). We always use the same initial configurations with a uniformly mixed fluid phase and random positions of colloids.

The following sections will present the morphologies at two temperatures, $k_BT = 2.133 \times 10^{-5}$ LU and $k_BT = 2 \times 10^{-4}$ LU, for $\psi_0 = 0.0$ and 0.4. We set $\lambda = 4$ in these runs and study the effect of varying the relaxation time for dipolar interactions. A higher dipolar strength, $\lambda = 40$, is also examined for a symmetric quench and then the effect of uniform fields will be discussed for two different values of the strength of field.

5.2.1 Bicontinuous phase and droplet phase

In Section 3.1, the domain morphologies have been shown for colloids in a binary fluid undergoing spinodal decomposition. By controlling the initial mean order parameter ψ_0 from a symmetry to a strong asymmetry, the percolation threshold ψ_p between the bicontinuous phase and the droplet phase was estimated within the range from 0.3 to 0.4. At $\psi_0 = 0.4$, a clear dropletlike phase was found as seen in Figure 3.1(b).

After a quench of a system of magnetic colloids in a binary fluid, one can imagine that the aggregation process of magnetic colloids and the phase separation of the binary fluid occur coincidentally. In addition, the fast diffusion time at $k_BT = 2 \times 10^{-4}$ LU could induce a faster process to aggregate magnetic colloids, which in turn could influence domain morphologies.

Figures 5.1 and 5.2 present snapshots at different two temperatures, $k_BT = 2.133 \times 10^{-5}$ LU and $k_BT = 2 \times 10^{-4}$ LU. The same dipolar coupling constant $\lambda = 4$ is used for all simulations in Figures 5.1 and 5.2. Even at the higher temperature, their basic morphologies are maintained consistent with the results in Section 3.1; the bicontinuous phase is found at a symmetric quench whose volumes of fluid are 50:50; the droplet phase is obtained at an asymmetric quench with fluid volumes 70:30. Moreover, it is found that the long-range dipolar interactions make dipoles align as nose-to-tail chains on the surfaces at all cases. To see the arrangement of dipoles on the surface, one droplet is selected from the droplet phase in Figure 5.1(b). The following sections will discuss the geometry of dipoles in detail.

The morphologies of fluid domains in a closed box are seen in Figure 5.3. Comparing with fluid domains in a periodic box, fluid domains in a closed box have more strongly curved surfaces. In an asymmetric quench, sizes of droplets are smaller than ones in a periodic box. Although a closed box makes more interfaces, aligned magnetic particles are still observed at the fluid-fluid interfaces.

On increasing the dipolar strength, we expect strong interactions to make more orientational ordering of dipoles. Figure 5.4 presents the snapshot for $\lambda = 40$ in a symmetric quench at $k_BT = 2 \times 10^{-4}$ LU. We find that the dipolar strength does not affect the main morphology of the fluid domains, but that longer chains are seen along the surfaces in comparison with those for $\lambda = 4$.

5.2.2 Droplet covered by magnetic colloids

Figure 5.5 shows a droplet chosen from the snapshot in Figure 5.1(b). Magnetic particles on its surface align to reduce their interaction energies so that interesting patterns of dipoles are found on the surface. Figure 5.5(a) shows the droplet with different view points rotating by a full turn counter-clockwise; so pictures 1 and 6 are the same. The particles undergo local hexagonal ordering; their dipolar ordering is based on the nose-to-tail along the curve of surfaces. In pictures 1 and 3, larger domains are seen where dipoles are aligned parallel, but the orientations of dipoles on these two faces of the droplet are opposite. The cross-domains between these two faces (picture 2 and 4) show the change in direction of dipoles. Figures 5.5(b) and 5.5(c) show snapshots of the top and bottom of the droplet.

5.2.3 Effect of uniform external field

In the absence of an applied external field, magnetic dipoles have only local orientational correlations. However, under the external field, dipole moments partially align along the direction of the field according to the strength of field compared with thermal fluctuations. So at very high field strength, completely aligned dipoles can be expected and the total magnetisation is saturated close to unity per dipole, as predicted by Langevin theory (Appendix C). This predicts the magnetisation of colloids in terms of the dimensionless parameter $\alpha_B = \mu B / k_BT$, assuming that dipolar interactions of particles are ignorable. Although the classical Langevin theory neglects dipole-dipole interactions, a recent study of ferrofluids in a uniform field[121] has shown that this Langevin theory is still applicable in systems with moderate dipolar interactions.

Figure 5.6 shows the final snapshots for simulations under the uniform external fields, $\alpha_B = 2$ and 20 respectively. These simulations have retained the long-range dipolar interactions for magnetic particles with $\lambda = 4$. The applied uniform field is given as $\mathbf{B} = (0, 0, B_z)$ and the corresponding equilibrated particle magnetisations are 0.54 and 0.95 provided by Langevin theory. The analysis for the nematic ordering and energy relaxations will be presented in Section 5.3.

On increasing the strength of the uniform field, stretched domains of fluids along the direction of the field are observed and dipoles also form chain structures aligned along $\mathbf{B}$. However, the morphologies for $\psi_0 = 0.0$ still maintain bicontinuity for both α_B values.

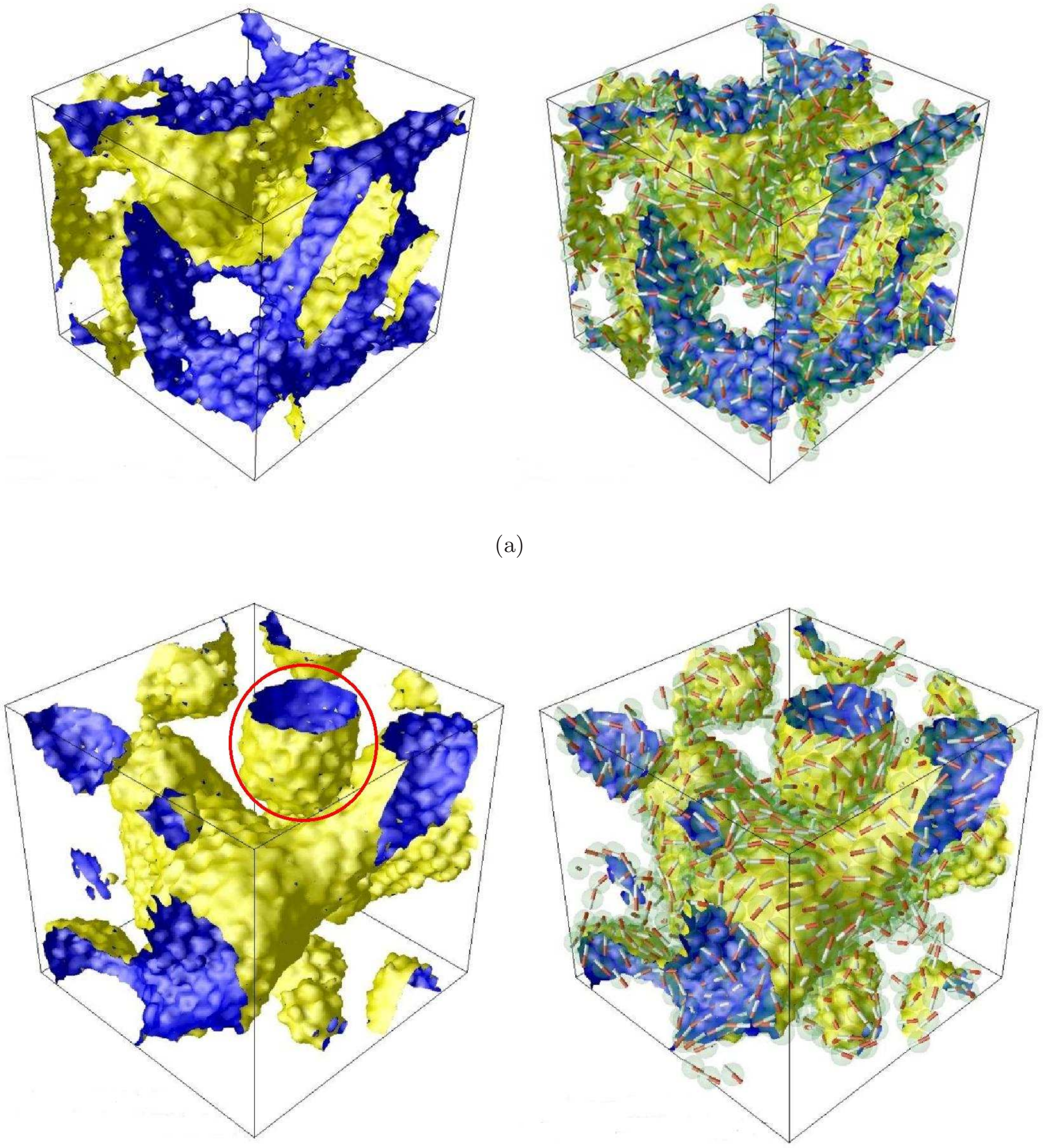

(a)

(b)

Figure 5.1: The morphologies in a system with periodic boundary conditions for $\lambda = 4$ at $k_BT = 2.133 \times 10^{-5}$ LU in $\Lambda^3 = 64^3$. The right side shows the fluid-fluid interfaces plus colloids given as spheres with a radius a. Cylinder represents a dipole whose poles are painted by red (+) and white (-). The left is the images without the particles that are shown on right side and it shows clear domain morphologies. (a) symmetric quench: $\psi_0 = 0.0$. (b) Asymmetric quench: $\psi_0 = 0.4$. One droplet (circled by red) is chosen to see the geometry of magnetic particles on the surface, discussed in Section 5.3.2.

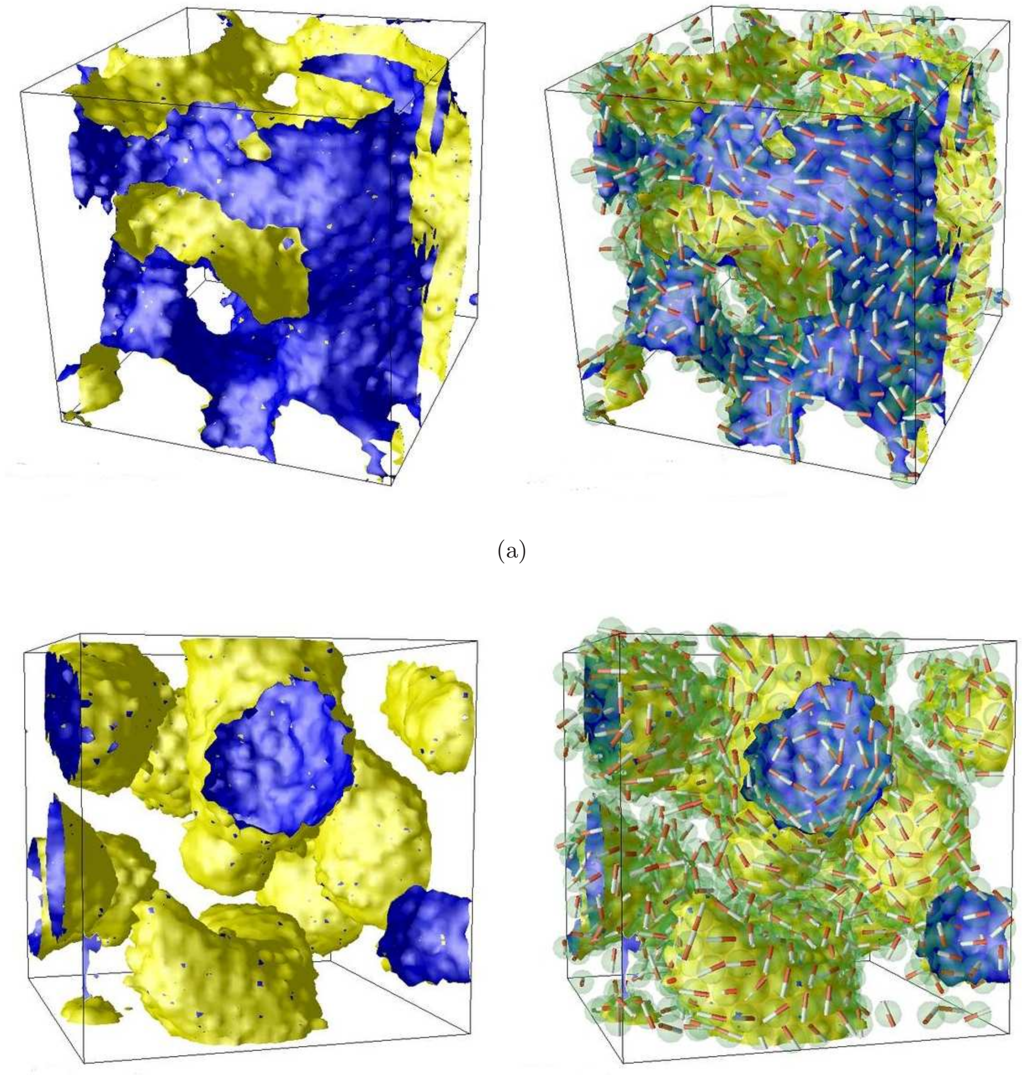

(a)

(b)

Figure 5.2: The morphologies in a system with periodic boundary conditions for $\lambda = 4$ at $k_BT = 2 \times 10^{-4}$ LU in $\Lambda^3 = 64^3$. The right side shows the fluid-fluid interfaces plus colloids given as spheres with a radius a. Cylinder represents a dipole whose poles are painted by red (+) and white (-). The left is the images without the particles that are shown on right side and it shows clear domain morphologies. (a) symmetric quench: $\psi_0 = 0.0$. (b) asymmetric quench: $\psi_0 = 0.4$.

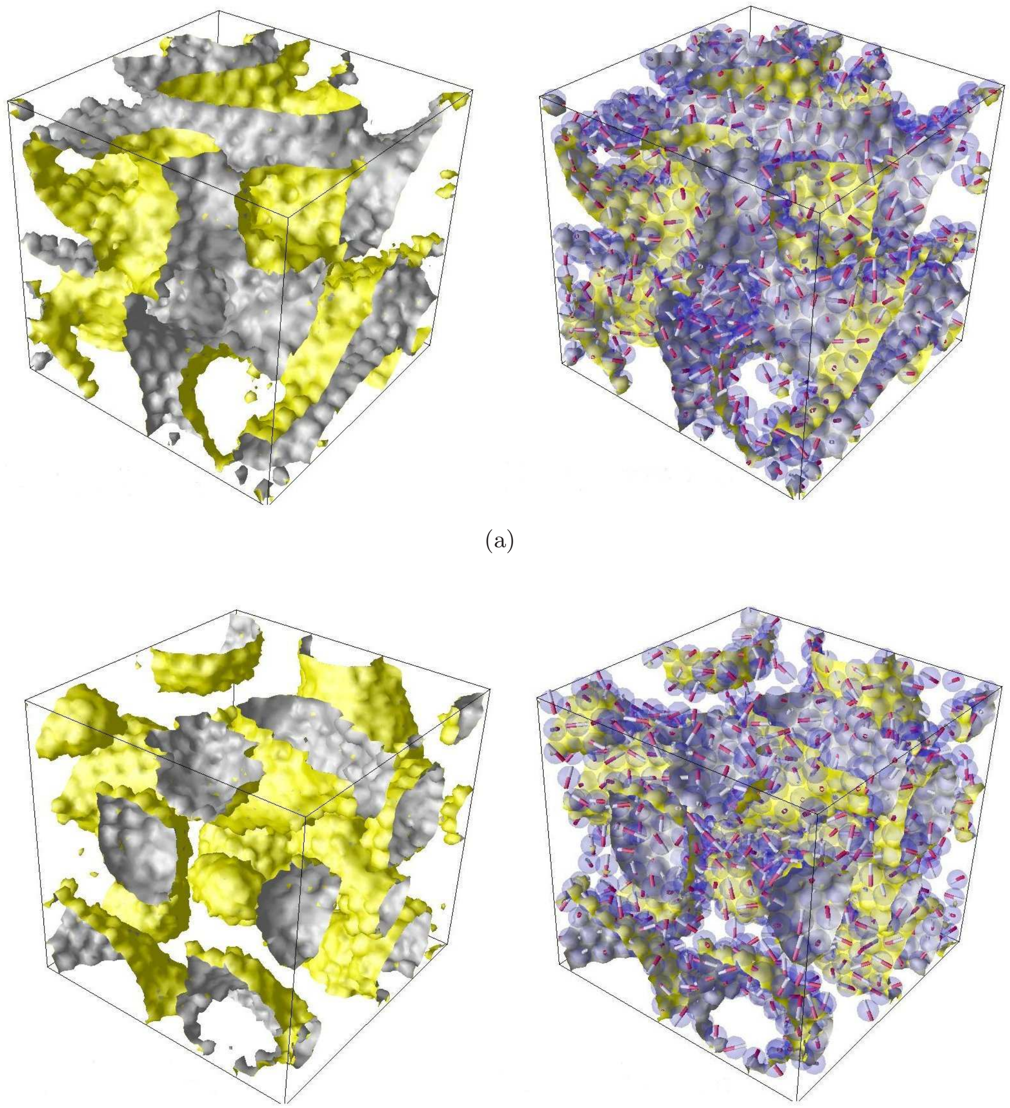

(a)

(b)

Figure 5.3: The morphologies in a closed box for $\lambda = 4$ at $k_BT = 2 \times 10^{-4}$ in $\Lambda^3 = 64^3$. The right side shows the fluid-fluid interfaces plus colloids given as spheres with a radius a. Cylinder inside of a sphere represents a dipole whose poles are painted by red (+) and white (-). The left is the images without the particles that are shown on right side and it shows the clear domain morphologies. (a) symmetric quench: $\psi_0 = 0.0$. (b) asymmetric quench: $\psi_0 = 0.4$.

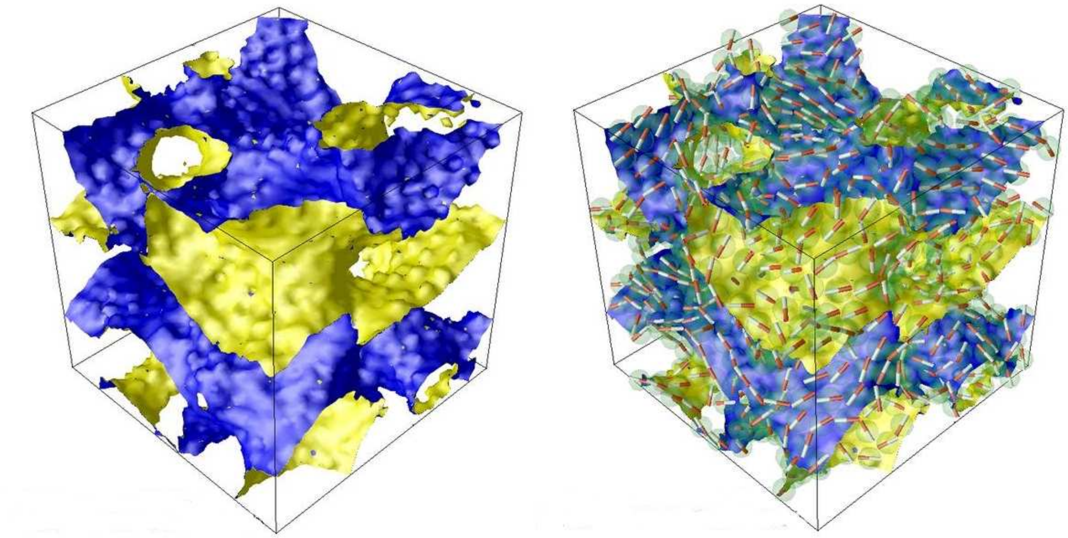

Figure 5.4: Domain morphologies for $\psi_0 = 0.0$ with $\lambda = 40$ in $\Lambda^3 = 64^3$.

5.2.4 Domain growth

The size of demixed fluid domains can be quantified by the characteristic length scale, $L(t)$, defined in equation (3.1) for a periodic box system. Figure 5.7 and Figure 5.8 present the time evolution of domain growth at various conditions shown in the last section for domain morphologies. In Figure 5.7, the curves of $L(t)$ for symmetric and asymmetric quenches are seen at different temperatures and dipolar strengths. We find that the $L(t)$ depends on k_BT and λ. In Section 3.4.2, $L(t)$ for nonmagnetic colloids showed dependency on k_BT. Consistently, with given fixed λ, the domain growth of a binary fluid with magnetic colloids also shows the same tendency. In addition, on increasing λ, larger domains are observed in Figure 5.7. That might be caused by slower relaxation of magnetic colloids at higher λ; we showed slow relaxations on translational and rotational modes for magnetic colloids belonging to chains in Chapter 4.

For the cases with applied external fields, Figure 5.8 shows the time-evolution of domain sizes for symmetric quenches at two different uniform fields, $\alpha_B = 2$ and $\alpha_B = 20$. Figure 5.8(a) presents $L(t)$ measured by the equation (3.1) for periodic boundary conditions; larger $L(t)$ is obtained at the stronger field ($\alpha_B = 20$) at any fixed time. In the domain morphologies of Figure 5.6, we found stretched domain along the direction of the field, so we measure the domain size along each axis[87]. (The detailed method to measure these L_x, L_y and L_z is discussed in Appendix D.) Figures 5.8(b)-5.8(d) show

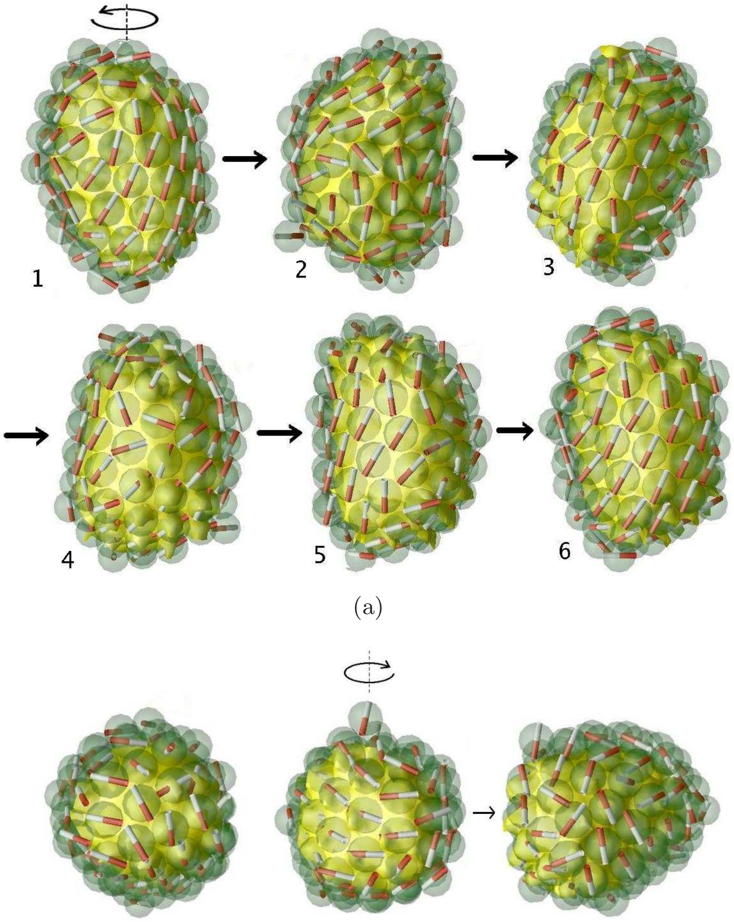

(a)

(b)

(c)

Figure 5.5: The dipolar ordering on the facets of the droplet. (a) snapshots for sides of the droplet rotating counter-clockwise. (b) Viewed from above. (c) Viewed from below.

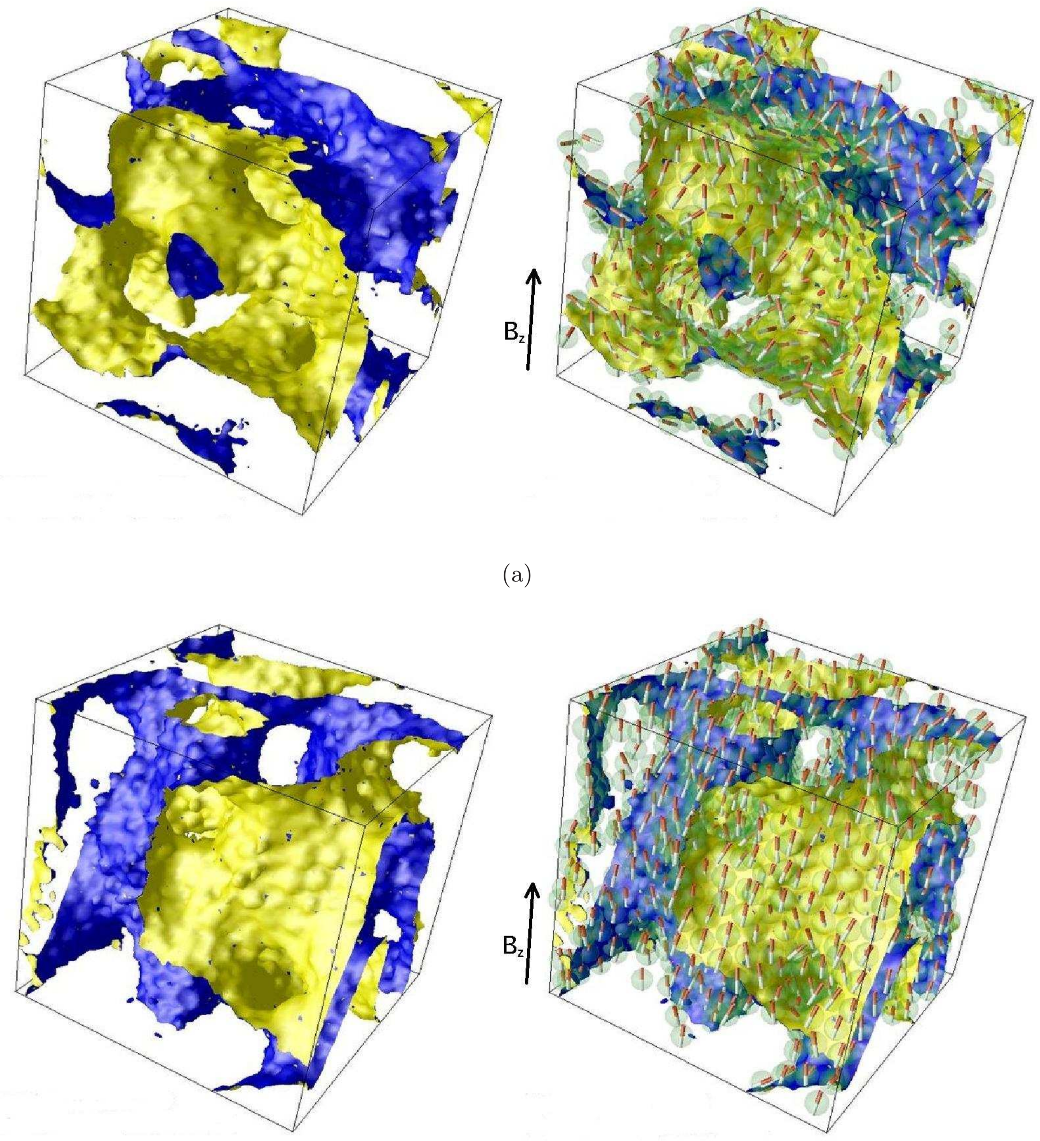

(a)

(b)

Figure 5.6: The morphologies for $\lambda = 4$ at $k_B T = 2 \times 10^{-4}$ LU in $\Lambda^3 = 64^3$. (a) $\alpha_B = 2$. (b) $\alpha_B = 20$.

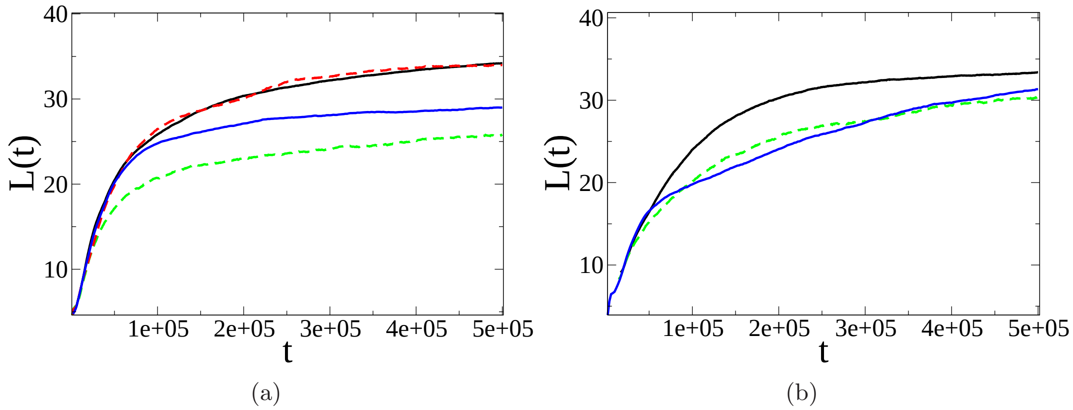

Figure 5.7: The characteristic length scale, $L(t)$. (a) a symmetric quench ($\psi_0 = 0.0$) with $\lambda = 4$: black solid is $k_BT = 2.133 \times 10^{-5}$ LU, green dash is $k_BT = 2 \times 10^{-4}$ LU and red dash is for $\lambda = 40$ at $k_BT = 2 \times 10^{-4}$ LU. Blue solid is $\lambda = 0$ at $k_BT = 2.133 \times 10^{-5}$ LU. (b) an asymmetric quench ($\psi_0 = 0.4$) for $\lambda = 4$: black solid is $k_BT = 2.133 \times 10^{-5}$ LU, green dash is $k_BT = 2 \times 10^{-4}$ LU. Blue solid is $\lambda = 0$ at $k_BT = 2.133 \times 10^{-5}$ LU. The length $L = 10$LU in simulation corresponds to $L = 22.1$nm in lab unit; the time scale $t = 5 \times 10^5$LU corresponds to $t = 247$ns in lab.

the length scales at each axis, x, y and z. For $\alpha_B = 2$ at final time step, length scales along all directions are almost isotropic with the range between 32 and 37. But, for $\alpha_B = 20$, the domain lengths show strong anisotropy; the length along z (the direction of field) is about 50% larger than lengths along the other axes, x and y.

5.2.5 Summary: characteristics of fluid domains

In the above sections, we presented the morphologies of fluid domains and the time-evolution of domain growth under various conditions. In Chapter 3, we concluded that the basic structure of fluid domains is controlled by the initial mean order parameter, ψ_0, from bicontinuous phase to droplet phase. To extend that previous study, we investigated how magnetic interactions change the morphologies of domains. As a result, although the same initial random fluid mixture was used for all simulations, different morphologies were observed, depending on temperature, strength of dipolar interactions and external field strength. However, although the presence of magnetic colloids influences the curvature of fluid surfaces, the main morphologies, bicontinuous or droplet phases, are maintained.

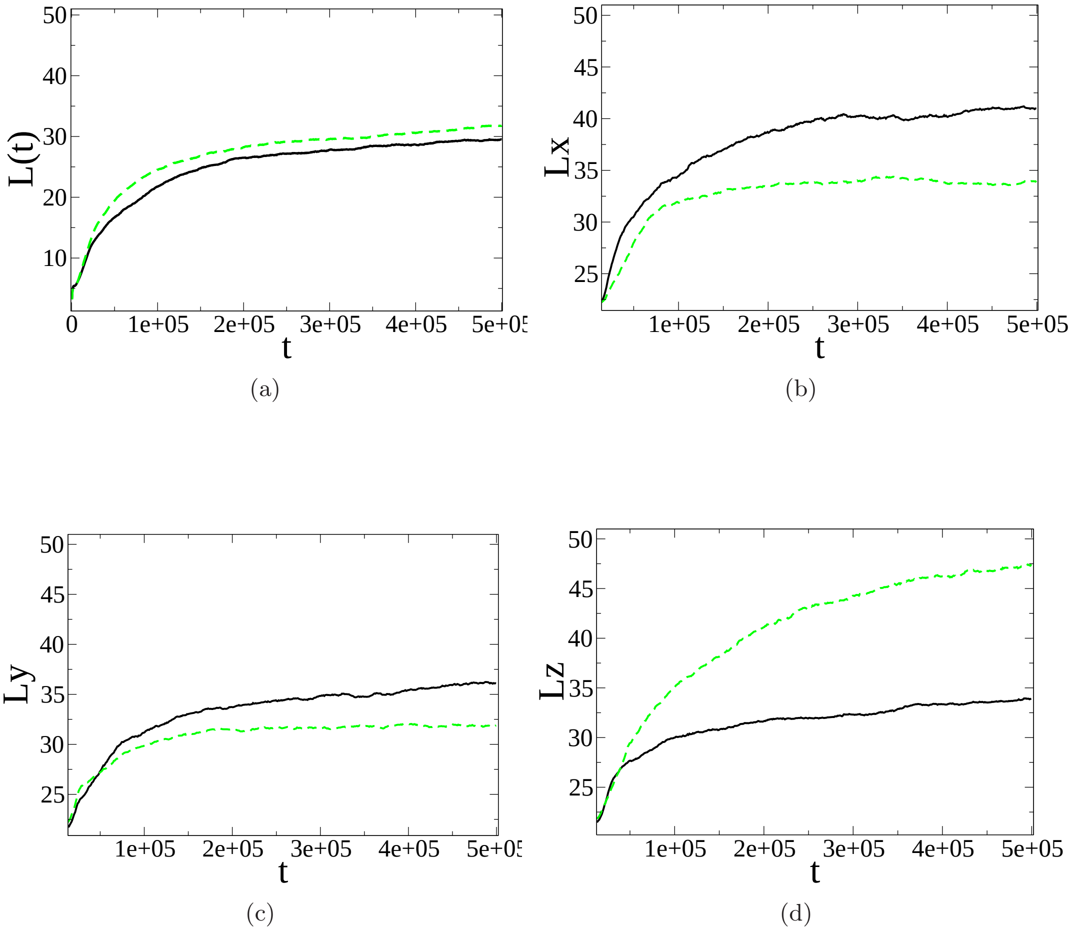

(a) (b)

(c) (d)

Figure 5.8: The characteristic length scales for applied uniform fields: black solid is $\alpha_B = 2$; green dash is $\alpha_B = 20$. (a) $L(t)$. (b) L_x. (c) L_y. (d) L_z. The length $L = 10$LU in simulation corresponds to $L = 22.1$nm in lab unit; the time scale $t = 5 \times 10^5$LU corresponds to $t = 247$ns in lab.

These domain morphologies can be quantified using the size of demixed fluid domains, through the characteristic length scale $L(t)$. In the presence of the dipolar interactions, we found the resulting chain structures to affect not only the form of the domains, but also their domain size, $L(t)$; the strongly aggregated clusters help to make larger domains of fluids at fixed time. We also obtained similar domain growth rates, depending on the detachment of colloids at interfaces as shown in Section 3.4.2, even though magnetic colloids are used instead of nonmagnetic colloids. In the absence of an external field, magnetic colloids can change the microstructures of the fluid domains, but their length scales show isotropy. In contrast, we found that an external field can create strong anisotropy of domain morphology. We examined how external fields can change the domain morphologies by controlling the arrangement of magnetic dipoles. Strong anisotropy in length scales is found for strong external uniform fields; on the other hand, at weaker fields, length scales are still isotropic. But for symmetric quenches, both cases still keep the bicontinuous structure of fluid domains.

5.3 Energy relaxation and dipolar ordering

In Chapter 4, we have investigated the equilibrium and the transient properties of colloidal ferrofluids. In contrast with colloidal ferrofluids, the post-arrested motions of magnetic colloids in a binary fluid are not free translationally due to the confinement by the capillary energy at the fluid-fluid interfaces. However, their rotational motions are rather independent of this restricted circumstance. Therefore, even if particles are localised in space, they tend to find low energy states through rotating their dipoles.

This section will address the properties of magnetic colloids in a binary fluid by measuring the energy relaxation and the nematic ordering from the simulations shown in last section. Also an individual dipolar energy is defined to see the dependency on environment such as surface geometry and neighbouring dipoles. Finally, the number of free particles as time is also measured as a function of time to see the ejection effect.

5.3.1 Energy relaxations

After a quench of a binary fluid with magnetic colloids which are equilibrated with $\lambda = 0$, the process for magnetic colloids to aggregate should arise concurrently with the phase separation to demix into each fluid. Even if particles are arrested by the fluid-fluid interfaces after the diffusive regime of the spinodal decomposition, continuing relaxations of the dipolar energy are clearly observed in Figures 5.9 and 5.10(a). In the cases with applied uniform fields, the relaxation curves for the energy of interaction with the external field are also seen in Figure 5.10(b). All curves in Figures 5.9 and

5.10 seem to approach steady states (although the curve for an asymmetric quench at $k_BT = 2.133 \times 10^{-4}$ LU is still slowing down). Table 5.1 presents the dimensionless energies averaged over the time window between 4.5×10^5 LU and $t_{final} = 5 \times 10^5$ LU at all cases. For magnetic colloids in a single fluid, the equilibrium dipolar and soft-core energies at $\lambda = 4$, $\alpha_B = 0$ and $\phi = 0.20$ are measured in Chapter 4 as $U^d/Nk_BT = -4.904 \pm 0.004$ and $U^{sc}/Nk_BT = 0.0326 \pm 0.0001$. In comparison with the latter, higher values are obtained for U^{sc}/Nk_BT in magnetic colloids in a binary fluid. That means colloids are closer to each other; that results from the jamming of colloids on surfaces. However, in the dimensionless dipolar energy, U^d/Nk_BT, no systematic trend is found at any ψ_0 and any k_BT for $\alpha_B = 0$. At $\alpha_B = 2$ and 20, the similar U^d/Nk_BT values are obtained, while U^B/Nk_BT at $\alpha_B = 20$ is much greater than one at $\alpha_B = 2$.

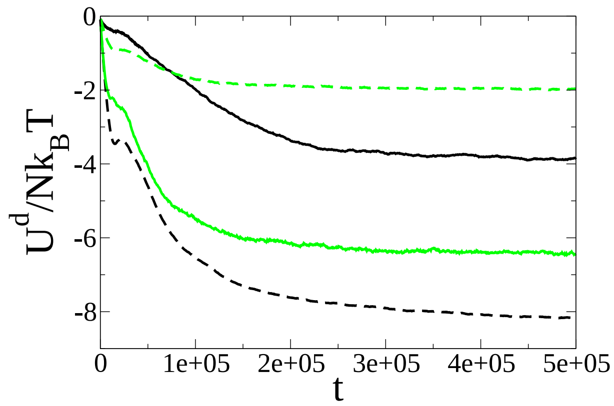

Figure 5.9: U^d/Nk_BT at $\lambda = 4$. Black is $k_BT = 2.133\times10^{-5}$. Green is $k_BT = 2\times10^{-4}$. Solid line for $\psi_0 = 0.0$. Dash is for $\psi_0 = 0.4$.

5.3.2 Local (or individual) dipolar energy

Due to the nature of the long-range and many-body dipolar interactions, magnetic particles easily become frustrated energetically. These frustrated particles usually lead to higher energy states. For magnetic colloids in a binary fluid, we could also expect frustrated behaviour of dipoles on the confined geometry of the fluid-fluid interfaces with neighbouring colloids jammed onto these surfaces.

Figure 5.11 presents two simple cases drawing a dipole surrounded by six neighbours: Figure 5.11(a) shows the diagonal case, with 60°as the angle between the vector of dipole i and the distance vector $\hat{r}_{ij}$, between dipoles, i and j; Figure 5.11(b) shows the case

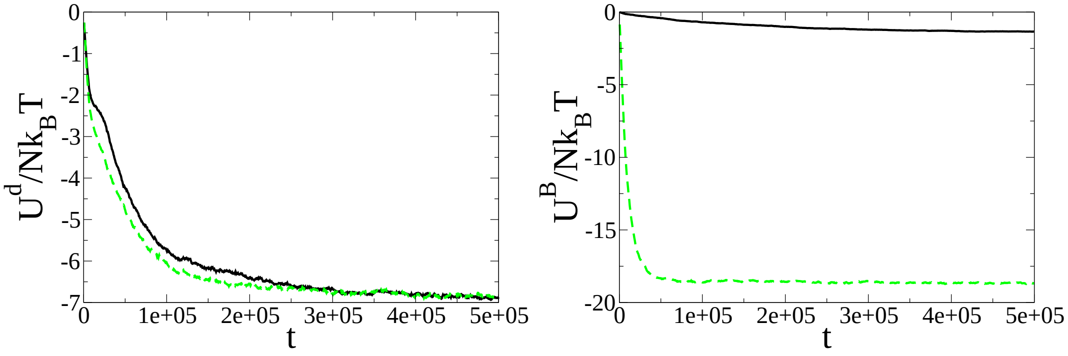

(a) (b)

Figure 5.10: (a) U^d/Nk_BT and (b) U^B/Nk_BTat $\lambda = 4$, $k_BT = 2 \times 10^{-4}$. Black solid is $\alpha_B = 2$ and green dash is $\alpha_B = 20$.

Table 5.1: Dimensionless energies.

ψ_0	k_BT	λ	ϕ	α_B	U^d/Nk_BT	U^{sc}/Nk_BT	$\dagger U^B/Nk_BT$
0.0	2.133×10^{-5}	4	0.20	0	-3.870 ± 0.001	3.067 ± 0.002	0.0
0.0	2.133×10^{-5}	0	0.20	0	0.0	2.852 ± 0.009	0.0
0.4	2.133×10^{-5}	4	0.20	0	-8.152 ± 0.001	4.400 ± 0.006	0.0
0.4	2.133×10^{-5}	0	0.20	0	0.0	2.363 ± 0.010	0.0
0.0	2.0×10^{-4}	4	0.20	0	-6.411 ± 0.003	0.419 ± 0.002	0.0
0.4	2.0×10^{-4}	4	0.20	0	-1.9761 ± 0.0009	0.388 ± 0.002	0.0
0.0	2.0×10^{-4}	40	0.20	0	-88.940 ± 0.007	2.242 ± 0.004	0.0
0.0	2.0×10^{-4}	4	0.20	2	-6.871 ± 0.003	0.428 ± 0.001	-1.3371 ± 0.0007
0.0	2.0×10^{-4}	4	0.20	20	-6.840 ± 0.003	0.424 ± 0.001	-18.658 ± 0.003

$\dagger U^B = \sum_i U_i^B$, where $U_i^B = -\mu \hat{\mathbf{s}}_i \cdot \mathbf{B}$.

with 90°for this angle. The dipole at the center in Figure 5.11(a) has lower energy than the dipole at the center in Figure 5.11(b). Similarly, this diagonal pattern is also observed at dipoles on the surfaces for domain morphologies in Section 5.1; dipoles on the fluid-fluid interfaces show nose-to-tail packings.

In general, the individual dipolar energy can be defined from equation (2.76) as

$$U_i^d = \mu^2 \sum_{i \neq j} \frac{1}{r_{ij}^3} [\hat{\mathbf{s}}_i \cdot \hat{\mathbf{s}}_j - 3(\hat{\mathbf{s}}_i \cdot \hat{\mathbf{r}}_{ij})(\hat{\mathbf{s}}_j \cdot \hat{\mathbf{r}}_{ij})]. \tag{5.1}$$

The dipolar energy for a particle i is calculated by the sum of pairwise dipolar energies with particles j within $r_c = \Lambda/2$ in real space. In the case of periodic boundary conditions, the long-range contribution for $r_{ij} > \Lambda/2$ is obtained from the Fourier space part of the Ewald summation. However, since dipolar interaction decays as $1/r^3$, the long-range contribution for $r_{ij} > \Lambda/2$ is negligible. So we calculate U_i^d/k_BT by summing over interacting particles within $r_{ij} < \Lambda/2$.

Figure 5.12 presents the same snapshots in Figure 5.1, with particles colour-coded by the strength of individual dipolar energy. In Table 5.1, the total dipolar energy for $\psi_0 = 0.4$ at $k_BT = 2.133 \times 10^{-5}$ LU is about two times lower than one for $\psi_0 = 0.0$; the colour distribution in Figure 5.12(a) accordingly depicts higher energies than one shown in Figure 5.12(b). In morphologies of fluid domains, $\psi_0 = 0.0$ shows more curved surfaces in comparison with the curvature of $\psi_0 = 0.4$, so that broad colour spectrum is monitored at individual energy for magnetic particles. Figures 5.12(c) and 5.12(d) show the histograms of U_i^d/k_BT to see the energy relaxation for the individual particle at certain times after onset of the slow relaxations in Figure 5.9. Consistently, as following total energy relaxation, this distribution is shifted to get peaks at smaller $\Delta U_i^d/k_BT$.

To find a frustrated dipole in terms of the individual dipolar energy, we do the high resolution test for a single droplet covered magnetic colloids in Figure 5.4. To select a fluid droplet and magnetic colloids covering its fluid drop in Figure 5.1(b), we first find the boundary lattice points between this droplet and the continuous phase; then magnetic colloids are chosen if their distance from boundary lattice points is less than $\sqrt{3}$. Figure 5.13(a) shows the corresponding single droplet with magnetic colloids coloured by strength of dipolar energy, U_i^d/k_BT. Through measurement for U_i^d/k_BT in equation (5.1), the highest dipolar energy is obtained as -2.93, but this corresponding dipole (red colour in Figure 5.13(a)) is actually a free particle which is in very close contact with particles on the surfaces. However, the dipole with the second highest energy is found on the surface itself, and it shows frustration with six neighbour particles forming the ring structure around it.

5.3.3 Nematic ordering parameter and magnetisation

Table 5.2 shows the nematic order parameter, $N2$, whose definition was given in Section 4.3.2 and the magnetisation, M, measured by equation (C.2). Except for the data for applied external fields, all data refer to the isotropic phases. Comparing with $\lambda \rightarrow 0$, higher orientational orderings in both N_2 and M are found at $\lambda = 4$ and 40 for all k_BT. In the cases of applied external fields, comparing with the equilibrium magnetisations by Langevin theory, M of our simulation for $\alpha_B = 2$ has the lower value than theoretical value as $M^{eq} = 0.54$. For $\alpha_B = 20$, our simulation has the slightly lower value ($M = 0.9335$) in comparison with the theoretical value ($M^{eq} = 0.95$).

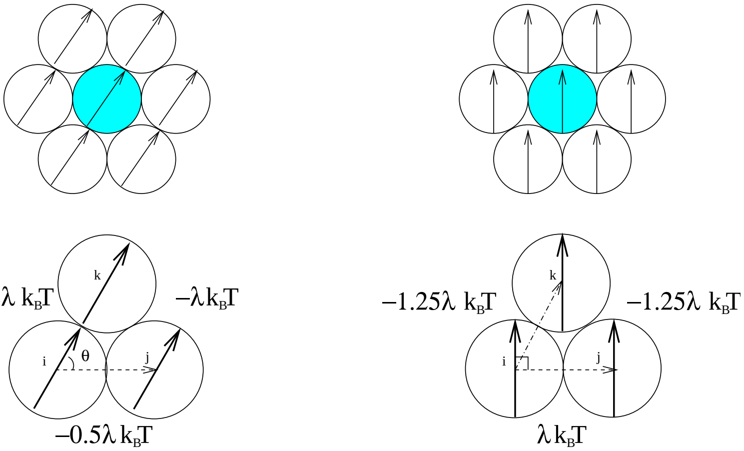

Figure 5.11: (a) the angle between the dipole and the horizontal is 60°; the individual dipolar energy is given as $-7\lambda k_B T$. (b) the angle between the dipole an the horizontal is 90°; the individual dipolar energy is given as $-3\lambda k_B T$.

5.3.4 Particle ejection

Figure 5.14 shows the number of free particles as a function of time. The definition of free particle was already introduced in Section 3.3.2. To check the effect of dipolar particles, the data for non-magnetic particles in Section 3.3.2 can be compared. A more-or-less data saturated plateau is found at $N_f(t)$ after $t > 1 \times 10^5$ LU in Figure 5.14(a) instead of the continuous ejections of non-magnetic colloids in Figure 3.5. At $t = 5 \times 10^5$ LU in a system of 'room' temperature $k_B T = 2.133 \times 10^{-5}$ LU, the fractions of free particles for non-magnetic colloids are higher than ones for magnetic particles; non-magnetic particles have 3.6% and 11.5% at $\psi_0 = 0.0$ and $\psi_0 = 0.4$ respectively, whereas magnetic particles have 2.4% and 4.9%. This smaller number of free particles suggests that the dipolar interactions attract particles to each other at the fluid-fluid interfaces.

However, in Figure 5.14(b) and 5.14(c), a continuously increasing $N_f(t)$ is observed in a system at enhanced temperature $k_B T = 2 \times 10^{-4}$ LU. Although there is ejection of magnetic particles, the rate is about one half of that for non-magnetic colloids: for a symmetric quench, 5% are free particles in magnetic colloids, but 9% are free particles in non-magnetic colloids. The dimensionless capillary energy at $k_B T = 2 \times 10^{-4}$ LU is 10 times lower than at $k_B T = 2.133 \times 10^{-5}$ LU; that means that, for Brownian particles, the escape from the fluid-fluid interfaces is 10 times easier. Thus continuous ejection in Figure 5.14(b) can be understood by the weak capillary energy. Figure 5.14(c) shows

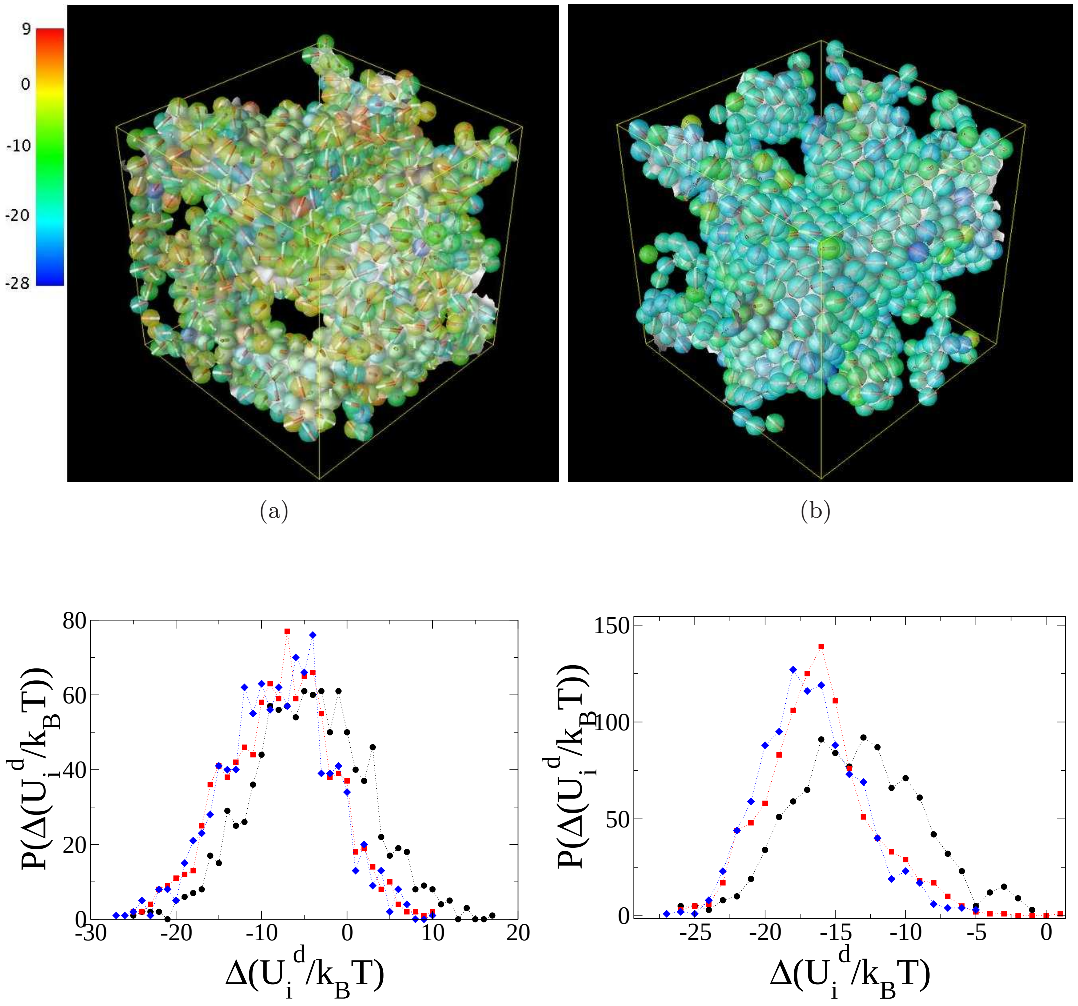

(a) (b)

(c) (d)

Figure 5.12: Individual magnetic particles are coloured by the strength of U_i^d/k_BT: (a) $\psi_0 = 0.0$ and (b) $\psi_0 = 0.4$, $k_BT = 2.133 \times 10^{-5}$ LU. The spectrum of U_i^d/k_BT is shown in the left of Figure (a). During the slow relaxation of dipolar energy, the U_i^d/k_BT distributions are shown in (c) $\psi_0 = 0.0$ and (d) $\psi_0 = 0.4$: the black circle is $t = 100,000$; red square is $t = 300,000$; blue diamond is $t = 500,000$.

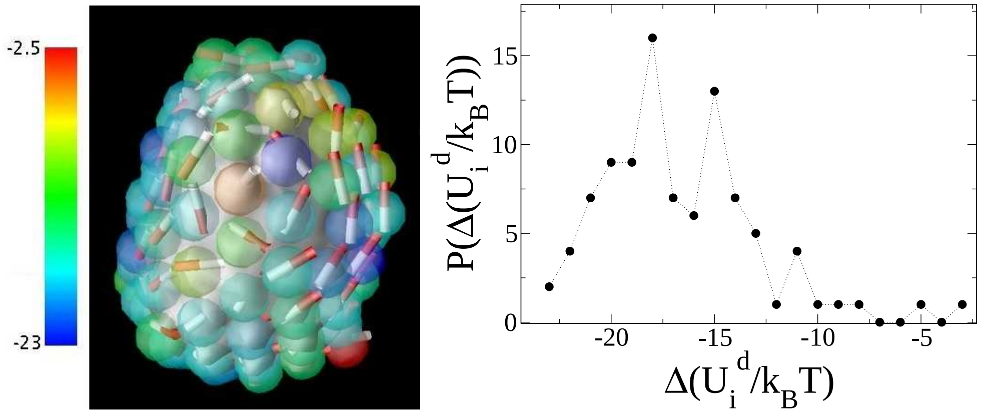

(a) (b)

Figure 5.13: (a) The directions of dipoles covering the droplet are shown with coloured particles according to U_i^d/k_BT. Here, the frustrated particle (orange colour) is found among dipoles on the surface, having the higher energy as $U_i^d/k_BT = -4.70$. (b) The local dipolar energy distribution at dipoles shown in (a).

$N_f(t)$ for $\alpha_B = 2$ and 20; this shows that the ejection of particles does not depend on the strength of applied external field in cases of $\alpha_B \neq 0$, but these fractions of $N_f(t)$ are higher than the one in $\alpha_B = 0$.

5.4 Structure deformation under external fields

For an initial droplet, the single droplet in Figure 3.7(g) is used in a closed box with $\Lambda^3 = 64^3$. The same droplet is shown in Figure 5.15(a) from a different view point. We consider paramagnetic particles which are randomly orientated initially; the neutral wetting particles cover the surface of the fluid droplet as discussed in Section 3.3.4. After switching on an external field, the dipolar long-range interactions are coincidentally switched on.

The type of external field determines the forces and torques acting on dipolar particles. A uniform field creates only torques which cause dipoles to arrange along the direction of field; a field gradient creates both forces and torques. To deform a fluid droplet, the interaction energy, arising from both dipole-dipole interaction and dipole-field interaction, should affect the rearrangement for colloids on the surfaces; also the rate for detachment of particles has an influence of these dipolar interactions in comparison with the strength of capillary energy. For uniform fields, we consider two temperatures as before: $k_BT = 2.133 \times 10^{-5}$ LU and $k_BT = 2 \times 10^{-4}$ LU. These

Table 5.2: Nematic ordering $N2$ and magnetisation M.

ψ_0	k_BT	λ	ϕ	α_B	$N2$	M
0.0	2.133×10^{-5}	4	0.20	0	0.0270 ± 0.0005	0.0554 ± 0.0003
0.0	2.133×10^{-5}	†0	0.20	0	0.0174 ± 0.0008	0.024 ± 0.001
0.4	2.133×10^{-5}	4	0.20	0	0.0496 ± 0.0003	0.0569 ± 0.0004
0.4	2.133×10^{-5}	†0	0.20	0	0.0143 ± 0.0004	0.0198 ± 0.0007
0.0	2.0×10^{-4}	40	0.20	0	0.0588 ± 0.0005	0.0756 ± 0.0002
0.0	2.0×10^{-4}	4	0.20	0	0.0657 ± 0.0005	0.0872 ± 0.0008
0.4	2.0×10^{-4}	4	0.20	0	0.0430 ± 0.0005	0.0717 ± 0.0004
0.0	2.0×10^{-4}	4	0.20	2	0.3499 ± 0.0006	0.6888 ± 0.0004
0.0	2.0×10^{-4}	4	0.20	20	0.8149 ± 0.0003	0.9335 ± 0.0001

† is actually the case for the limit of $\lambda \to 0$. ($N2$ and M therefore remain well defined.)

can control both the capillary energy and the diffusion time for particles.

To study the effect of a field gradient, we consider only the higher temperature. In addition, we introduce a buoyancy force on the fluid droplet that is chosen to balance the net force upon it caused by the field gradient. This prevents an overall translational motion of the droplet.

5.4.1 Uniform external field

Figure 5.15 presents snapshots of a droplet. The initial droplet is seen in Figure 5.15(a); we apply a strong field, given as $\alpha_B = 20$, which creates the equilibrium magnetisation 0.95 per dipole (Appendix C). For the lower temperature (high capillary energy, $\epsilon/k_BT = 1230$), the droplet snapshot after $t = 590,000$ LU is shown in Figure 5.15(b). We found that no particle ejection happens even at the final time steps; instead a slight elongation of the droplet is found along the field direction. Due to the rearrangement of magnetic colloids, the surface area of the domain is a little bit reduced from 2793 LU to 2730 LU. For the higher temperature (weak capillary energy, $\epsilon/k_BT = 130$), however, particle ejection begins at around $t = 65,000$ LU; the corresponding snapshot is seen in Figure 5.15(c). Again an elongated structure of the fluid droplet is observed. Finally 30 particles become free by $t = 590,000$ LU and a different shape of droplet more like a sphere is obtained with the smaller surface area. In conclusion, under the uniform field, the elongation of a droplet is observed in both cases with different capillary energies. The ejection of particles is seen in the case with the low capillary energy at the high temperature $k_BT = 2 \times 10^{-4}$ LU. After starting the ejection, the droplet starts to lose its initial shape as the coarsening dynamics drives to reduce the surface area of the domain.

5.4.2 Gradient external field

This study for the effect of field gradient is initially motivated by the experimental work[63]. In experiment, Melle *et al.*[63] has investigated the controllable stability of magnetic Pickering emulsions to undergo a phase transformation from droplet phase to bicontinuous phase according to strength of field gradient. When the field force is greater than the buoyancy force acting on droplets, droplets begin to move along the field direction in the continuous phase; they found the critical strength of magnetic field that droplets start to move according to concentration of particles; below this field strength, the droplets remain in a cream of the top of the sample. A stronger magnetic field far above the critical strength completely destabilises emulsions leading to a coalescence of droplets causing an evolution from the droplet phase to a bicontinuous phase. However, if the strength of gradient field is not strong enough to induce droplet movement, a slight elongation of droplets along the field direction can be observed.

The experimental magnetic Pickering emulsion is made by paramagnetic particles with a diameter 1 μm in decane (oil) and water, so that the final composition has decane droplets covered by paramagnetic particles dispersed in water. Due to the density difference between decane (oil) and water, the buoyancy force acts to keep the decane droplets afloat. To generate the magnetic gradient field, an electromagnet below the sample is used.

In simulations to examine the effect of a field gradient, we consider the same droplet also used in the study of uniform field effect shown in last section. Most of simulation conditions are same as ones in last section, but we use a field gradient generated by an external magnet whose material is the same as the ferromagnetic colloids in the simulation box. This field gradient from that magnet does not satisfy the $\nabla \cdot \mathbf{B} = 0$ for periodic boundary conditions, so that we only consider a closed box with nonperiodic conditions. To check the buoyancy effect, we introduce an artificial buoyancy force to balance the net forces of particles from the field gradient.

Comparing with the experimental setup[63], a few conditions are different in our simulation methods: the type of dipoles, the source of field gradient and the buoyancy force.

In experiment, paramagnetic particles are used instead of ferromagnetic particles, so long-range dipolar interactions are calculated from dipoles induced by an external field. In the case of using the field gradient, this induced dipole is almost independent of the applied field due to effects of saturation magnetisation. Thus we can consider a constant strength of dipoles to calculate the dipole-dipole interactions; dipolar colloids (ferromagnetic colloids) in our simulation model are adequate to simulate this induced dipolar systems as well.

The second difference is the source of external field gradient. In experiment, an electromagnet generates a field gradient acting on the sample of magnetic Pickering emulsions, while our simulations assume an external magnet made from the same material as the ferromagnetic colloids in the system box.

Final difference is a buoyancy force; whereas the buoyancy force from the density difference is of fixed value for a given stabilised droplet, our artificial buoyancy force depends on the directions and the positions of dipoles covering the droplet. The recipe for the artificial buoyancy force is the following; first, the number of lattice nodes (N_b) inside of the droplet is counted and then the forces on dipoles from the gradient field $\mathbf{B}(\mathbf{r})$ is calculated as $\mathbf{F_b}(\mathbf{r}) = \sum_i \mu{\cdot}\nabla\mathbf{B}(\mathbf{r})$, where i labels the particles; next the uniform buoyancy force is derived from $\mathbf{f}_b = \mathbf{F_b}(\mathbf{r})/N_b$ and then $-\mathbf{f}_b$ is added in the divergence of the stress tensor (shown in equation (2.33)) of the lattice nodes constituting the droplet. In addition, that means this force is time-dependent because the positions and the directions of dipoles are varied in time. The magnitude of the artificial buoyancy force varies with the strength of external field, so that we can only check the effect with or without the buoyancy force in our simulations; we do not discuss the effect of gradient field strength at a fixed buoyancy force.

Despite several differences between the experimental setup and the numerical setup, our simulation model is enough to study the effect of field gradient for magnetic emulsions. The important issue in this study is to design the field gradient whose strength in simulations corresponds to the equivalent strength in lab. As mentioned above, the gradient field in simulations is defined from the external magnet so that the field gradient as a distance is determined by the dipolar moment in equation(2.72); the size of magnet core decides the strength of dipolar moment. Assuming that the external magnet and magnetic colloids in the system box have spherical shape and are made by the same material, we can calculate the diameter of the external magnet with given strength of dipolar moment in simulations.

In these simulations, we consider $\lambda = 4$ for dipole-dipole interactions in the system box; here, the dipolar moment is given as $\mu = 0.27$ LU and $\mu(d) = 1.2348 \times 10^{-28}\mathrm{Am}^2$ with a diameter $d = 17\mathrm{nm}$ of magnet core ($\mathrm{Fe_3O_4}$) in simulation and lab respectively. For the external magnet ($\mathrm{Fe_3O_4}$) with $M = 10^3$ LU of the dipolar moment, the corresponding dipolar moment $M(D) = 4.41733 \times 10^{-15}\mathrm{Am}^2$ with a diameter $D = 260\mathrm{nm}$ is obtained in lab experiment. Therefore, using equation (2.72), the field gradient $\mathbf{B}(\mathbf{r})$ generated by $M(D)$ can be plotted. The diameter of the external magnet, D, exceeds the distance from dipole to box, but this does not matter since the lab system does not have the extra dipole but an electromagnet coil instead.

Figures 5.16(a) and 5.16(b) show the field gradient emitted from M at the position (0, 0, 0), to the simulation box with $\Lambda = 64^3$ with midpoint at the position (0, 0, 632); a clear gradient field along the z axis is found in the range of the system box, while the field strength is homogeneous at x and y axes. The corresponding strength of magnetic field at $z = 0$ is given as 0.0002 Tesla. Using the relation 1LU = 2.2nm from the characteristic length L_0, this is 300T/m, which is a reasonable strength of field gradient in a lab.

Figures 5.16(c) and 5.16(d) present the snapshots of the droplet under the field gradient shown in Figures 5.16(a) and 5.16(b) after $t = 590,000$ LU; both simulations are considered with the capillary energy $\epsilon/k_BT = 130$. In Figure 5.16(c), the ejection of particles occurs and 30% of particles becomes free in a bulk fluid; a more spherical droplet is observed like the droplet in Figure 5.15(d). In the case of the existence of the buoyancy force, Figure 5.16(d) shows that the buoyancy force resists the particle ejection on the bottom of the droplet so that its deformation is rather weaker than one without the buoyancy force, comparing with the simulation shown in Figure 5.16(c).

5.5 Conclusions

In this chapter, we presented simulations of a binary fluid with magnetic colloids undergoing a quench causing phase separation of the fluids. For both a symmetric quench and an asymmetric quench, we found the basic morphologies remain the same as for the systems with non-magnetic colloids. However, due to the long-range dipolar interaction, pattern formation is observed among the magnetic colloids on the surfaces of the fluid domains; alongside the curvature of interfacial surface, a pattern based on nose-to-tail is seen. However in the cases of the absence of the external field, globally isotropic orientational ordering is found, although approximately twice as much fluctuating nematic order is obtained in comparison with orientational ordering of the magnetic systems found in the limit $\lambda \to 0$. Using the idea of dipolar structure reflecting dipolar energy, frustrated particles are monitored as magnetic particles with higher individual dipolar energy. Especially, it is found that these frustrated particles on the surface are strongly dependent on the geometry of the surface and the neighbouring particles, through our high resolution trial for magnetic colloids covering a single droplet.

In the simulations of the existence of external uniform field and the high dipolar strength, the morphologies of fluids, e.g. bijel or droplets, are maintained even though interactions among magnetic colloids affect the residual coarsening dynamics after magnetic colloids are arrested at the interfaces. In the results for the characteristic length scales, we found strong anisotropy of domains under strong uniform fields; the stretched domain length is oriented along the direction of external field. In addition, larger domains were obtained by increasing the strength of dipoles. In comparison with the particle ejection of non-magnetic colloids, we found less ejection of magnetic colloids from the fluid-fluid interfaces; this may arise because dipolar interactions make particles strongly bonded at close contact.

In the last section, the deformation of fluid structures by the magnetic external fields, such as the uniform field and the field gradient, was discussed in the simple case of a stable droplet. On applying an external uniform field, the ejection of particles occurs at lease for modest capillary energy ($\epsilon/k_BT = 130$). Even if there is no particle ejection in the case with high capillary energy ($\epsilon/k_BT = 1230$), the droplet becomes elongated along the dipolar axis (field axis).

The study of the field gradient effect aims at a preliminary study comparing with the experimental work[63]. We found the buoyancy force resists the particle ejection on the bottom of the droplet while the final droplet without any buoyancy force results obtains more spherical shape due to the particle ejection. To understand the destabilisation of magnetic Pickering emulsions under the field gradient, further works are required in simulations. Technically, we hope to implement a precise calculation for the more realistic buoyancy force. Furthermore, simulations with two or more droplets would be needed to study the coalescence process from the droplet phase to a bicontinous phase. In addition, dependency on particle concentrations leading to smaller droplet size will be also of interest in the further work.

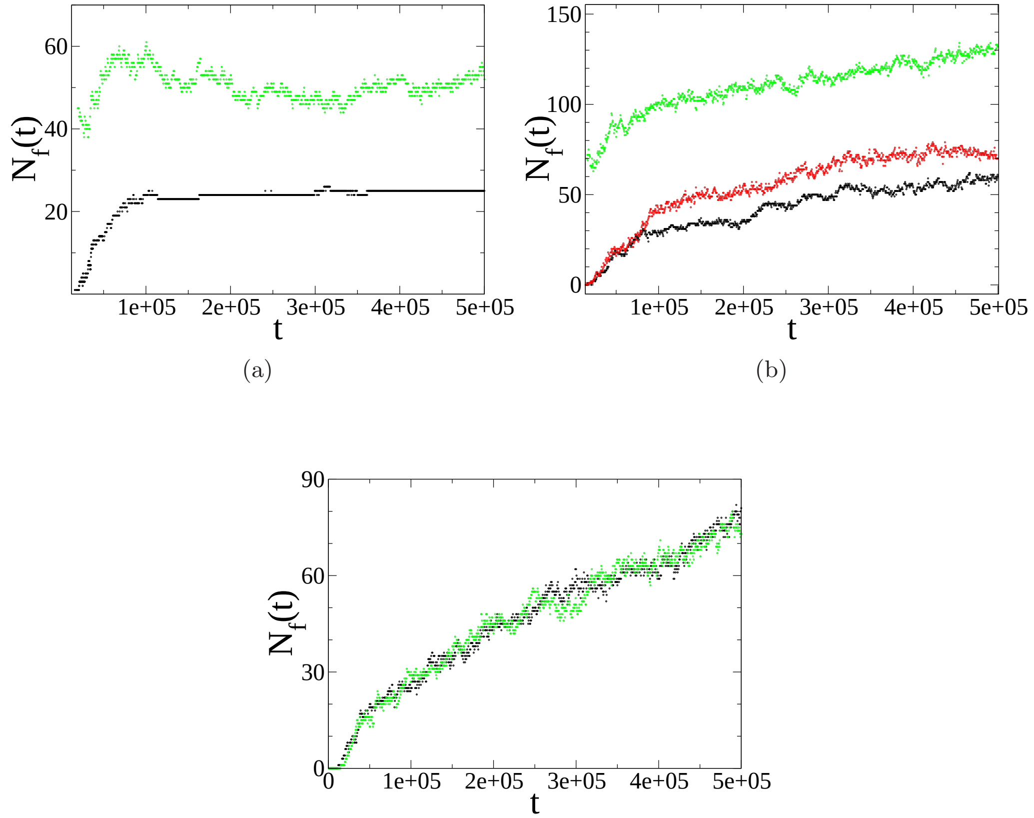

(a)

(b)

(c)

Figure 5.14: The number of free particles, $N_f(t)$. (a) $\lambda = 4$ at $k_BT = 2.133 \times 10^{-5}$; black is a symmetry and green is an asymmetry. (b) $\lambda = 4$ at $k_BT = 2 \times 10^{-4}$; black is a symmetry and green is an asymmetry. The red is $\lambda = 40$ at $k_BT = 2 \times 10^{-4}$. (c) $\lambda = 4$ at $k_BT = 2 \times 10^{-4}$; black solid is for $\alpha_B = 2$ and green dash is for $\alpha_B = 20$.

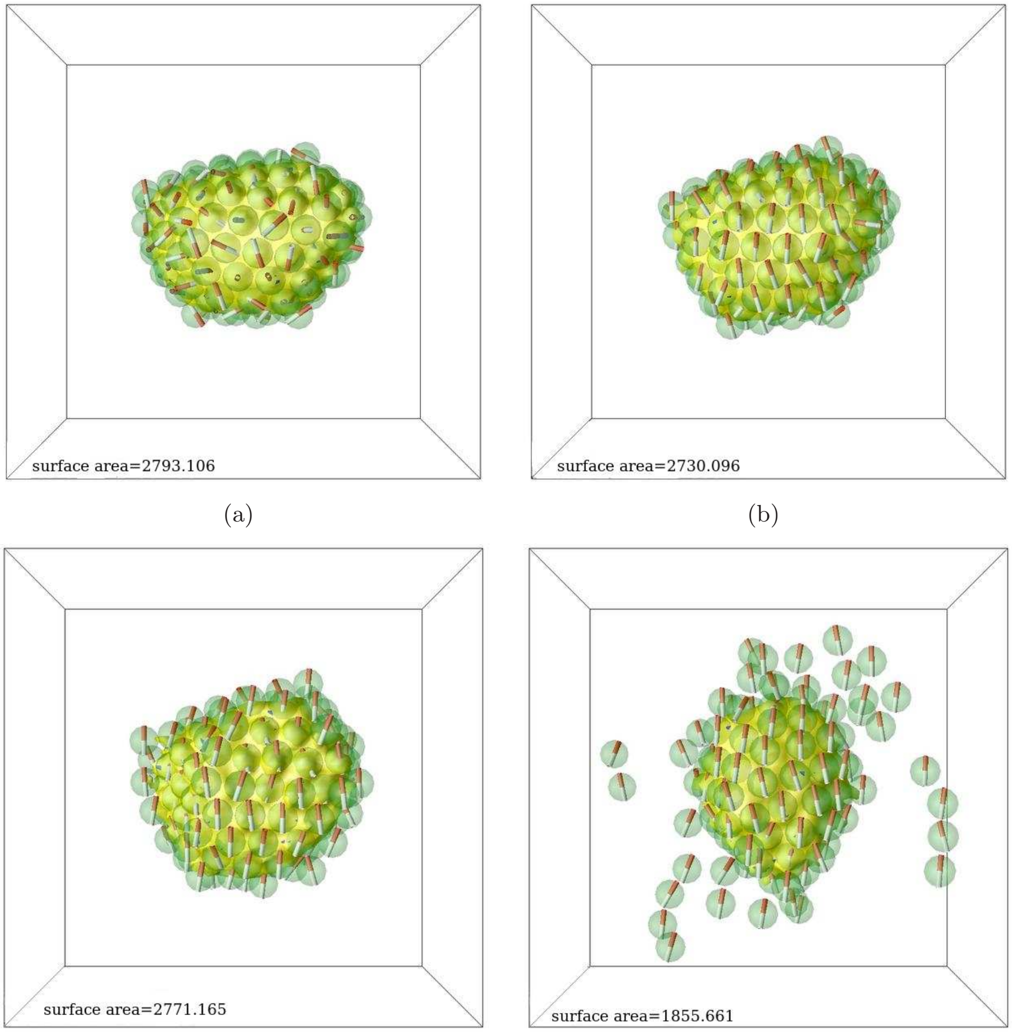

(a) (b) (c) (d)

Figure 5.15: (a) the initial droplet. (b) $t_{final} = 590,000$ LU at the capillary energy, $\epsilon/k_BT = 1230$. For the capillary energy, $\epsilon/k_BT = 123$, (c) $t = 65,000$ LU and (d) $t_{final} = 590,000$ LU.

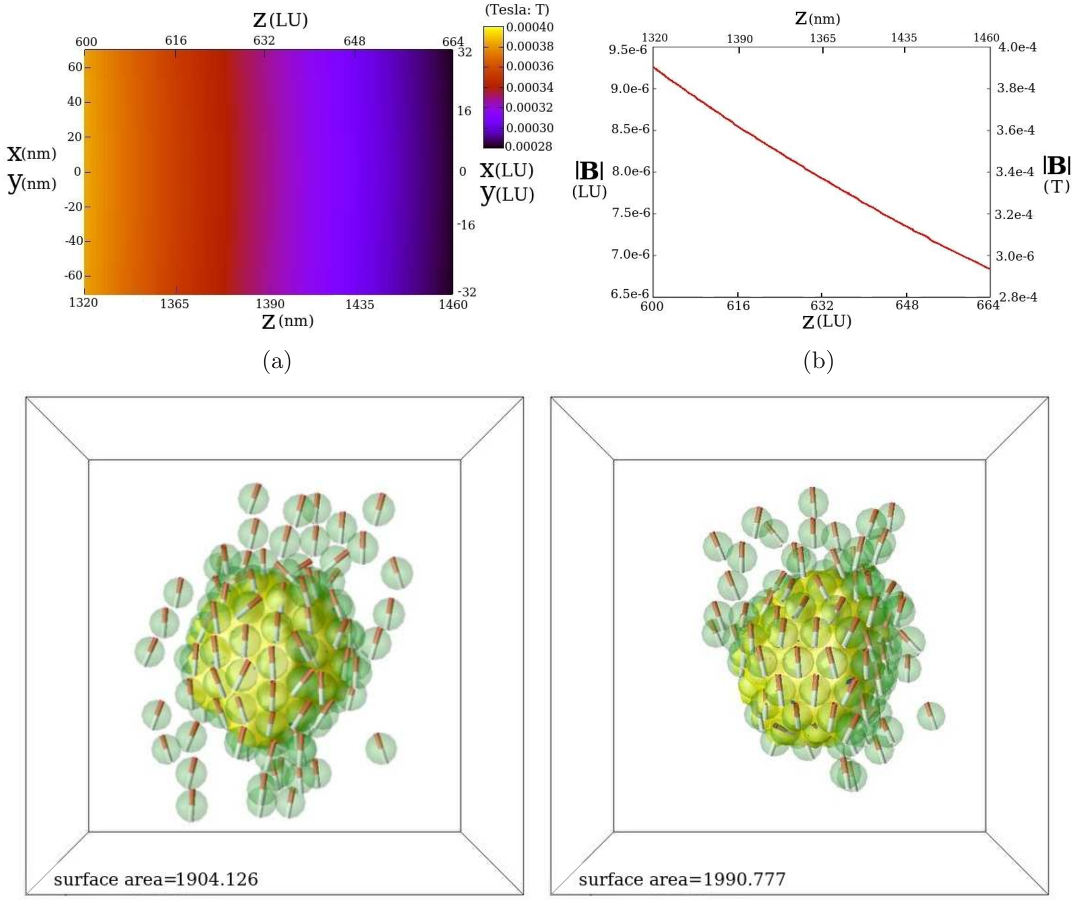

(a)

(b)

(c)

(d)

Figure 5.16: (a) The magnitude of external magnetic field: $|\mathbf{B}|$. The field strength at the bottom of the box is 300 T/m. The snapshots at $t_{final} = 590,000$ are shown in (a) the case without buoyancy and (b) the case with buoyancy.

Chapter 6

Conclusions and Further Work

In this Thesis, the simulations for colloidal complex fluids have been investigated by LB methods. Above all, we confirmed that our LB methods are remarkably efficient to simulate complex fluids including the fully hydrodynamic interactions acting on solid colloids. Compared with other techniques to calculate the hydrodynamics, e.g. computational fluid dynamics, LB provides efficiency to solve the Navier-Stokes equation for incompressible fluids by introducing discrete lattice grids. This basic lattice construction also improves the computational efficiency as it is easily developed for parallel simulation. Indeed, the LB scheme is easily compatible with other kinetic equations governing the evolution of complex fluids such as a binary fluid and moving particles in a single/binary fluid. For a binary fluid undergoing phase separation, another distribution function for the order parameter of the binary fluid is introduced along with the fluid distributions on the lattice. In colloidal systems, the dynamics of colloids follows a general Molecular Dynamics scheme and fully hydrodynamic forces are calculated by the “bounce-back on links” method for moving particles. For Brownian particles, thermal fluids are generated by the fluctuating LB algorithm; colloidal particles surrounded by thermal fluid on the lattice experience full Brownian motion. However, noise error from the discrete lattice fluid occurs for close-contact particles. To solve this problem, a repulsive short-range potential is used in the study for colloidal ferrofluids, but this issue of noise error should be considered in the future. To specify the kind of colloids, extra potentials can be added to the interaction between colloids. For magnetic colloids simulated here, the long-range dipolar interactions is calculated; in practice, Ewald summation is used for this in periodic boundary systems. In the study for colloidal ferrofluids with hydrodynamic interactions, our LB approach, incorporating the long-range dipolar interaction, generates reasonably good data in equilibrium and nonequilibrium.

In terms of research for complex fluids, LB is more adequate than other methods to study dynamical properties in equilibrium and nonequilibrium; especially, LB is outstanding to simulate complex composites including three phases such as colloids in a binary fluid. On the other hand, the static properties for colloids in equilibrium obey the Boltzmann statistics so that other methods such as Monte Carlo and Brownian Dynamics with the absence of hydrodynamics are more efficient than the LB method. In the simulations for hard-sphere colloids in a single solvent, ASD (accelerated Stokesian Dynamics) or SD (Stokesian Dynamics) is more suitable to implement full hydrodynamics without any noise error found in LB.

Among our results of LB simulations, there are several achievements to understand their dynamics and the basic structures for colloidal complex fluids: colloids in a binary fluid, colloidal ferrofluids and magnetic colloids in a binary fluid.

First, in the study for colloids in a binary fluid (as discussed in Chapter 3), LB originally predicted the new morphology of "bijel". The extensive works reported in this Thesis (and published recently) shows the droplet structure for a strong asymmetric quench; this droplet structures was observed in the recent lab experiment as well[34]. In the mechanism for arrested fluids demixing, our simulation results quantitatively agree with experimental results in terms of cooperating coarsening dynamics and particles jammed at interfaces. However, our simulations failed to reach fully arrested domains due to the short simulation time (so-called "intermediate time") related to Brownian time scale, whereas a bijel in the lab is stable for one month. Instead of fully arrested domains, slow residual dynamics is found, caused by ejection of particles at interfaces and remaining coarsening dynamics of fluid domains. To explain this slow dynamics for intermediate time scales, we directly measure the geometry-dependent parameter α throughout simulations at various temperatures; we found α as ~ 0.008 leading to a much smaller effective energy barrier to eject particles on the complicated geometry of interfaces than the corresponding barrier for a particle on a flat interface. In growth kinetics at various temperatures, an apparent power law is observed as $L(t) \sim (t/\tau_B)^{0.25\pm0.01}$ over a factor 2 interval in domain size. The growth kinetics of fluids arrested by colloids remains an open question in the future.

Secondly, in colloidal ferrofluids, the effect of hydrodynamic interactions was investigated in comparison with BD and MC simulations. On increasing the dipolar strength, controlled by dimensionless parameter λ, it is observed that magnetic colloids form larger clusters. By studying the dynamic correlators in equilibrium (defined as intermediate scattering functions in the lab), we found that hydrodynamic interactions delay the relaxations at all λ regimes and the dipolar interactions drive the long-time relaxations at high λ. Clear evidence for hydrodynamic interactions is also found in the short-time diffusion coefficients in comparison with the BD simulations. For transient dynamics during process to form clusters, the time-evolution of cluster size distribution is measured, but no significant difference is found, while slow relaxation is also seen. Transient motions are observed via two-time scattering functions which show time-dependent behaviour.

Finally, by using magnetic colloids in a binary fluid undergoing spinodal decomposition, our LB study predicts a new emulsified system, arrested demixing fluids covered by magnetic colloids. Even if the basic morphologies of fluid domains (from bicontinuity to droplets) follow those of emulsions with non-magnetic colloids on controlling the fraction of fluids, we found that these morphologies are perturbed by the structures of magnetic colloids. Especially, along the direction of external field, stretched domains are observed in the presence of a strong uniform field. We also observed interesting ordering structure, based on nose-to-tail, among magnetic particles jammed at surfaces. The dipolar directions of these jammed magnetic colloids show strong dependency on the surface geometry and neighbouring particles, so that energetically frustrated particles are observed.

Using the external magnetic field, it is possible to deform the fluid structures by using magnetic colloids which interact with the external field. Through a few test runs under uniform fields or field gradients, the preliminary study for destabilisation of a droplet was examined in Section 5.4. Both external field types can control the stability of a droplet by the arrangement of magnetic dipoles and the ejection of particles. Relating to the experiment work for the destabilisation of magnetic Pickering emulsions under a field gradient, some issues requires more simulations in further work. In experiment, coalescence of magnetic Pickering emulsions can be started from the particles pulled from the bottom of droplets when the magnetic force from an external field is stronger than the buoyancy force; also, higher concentrations of particles can respond to smaller strengths of magnetic field for moving droplets. Hopefully, these issues will be explained by further LB simulations.

Appendix A

Brownian Dynamics Algorithm

In a simple Brownian dynamics algorithm[19, 100] for dipolar colloids, the update scheme is given as

$$\mathbf{r}_i(t+\Delta t) = \mathbf{r}_i(t) + \Delta t \frac{D^t}{k_B T}\mathbf{F}_i(t) + \zeta_i^t(\Delta t) \tag{A.1}$$

$$\mathbf{s}_i(t+\Delta t) = \mathbf{s}_i(t) + \left(\Delta t \frac{D^r}{k_B T}\mathbf{T}_i(t) + \zeta_i^r(\Delta t)\right) \times \mathbf{s}_i(t). \tag{A.2}$$

Here $\mathbf{r}_i(t)$ and $\mathbf{s}_i(t)$ are respectively a position and a unit vector of dipole of particle i at time t. $\mathbf{F}_i(t)$ and $\mathbf{T}_i(t)$ are the force and the torque acting on particle i. From the long-range dipolar interactions, $\mathbf{F}_i(t)$ and $\mathbf{T}_i(t)$ are shown in equations (2.81)-(2.84). The force term corresponding to the short-range potential is easily calculated by the relation: $\mathbf{F} = -\nabla U^{sc}$, where U^{sc} is seen at equation (2.68). At a given temperature $k_B T$, translational and rotational diffusion coefficients are given respectively from the Stokes law as

$$D^t = \frac{k_B T}{6\pi\eta a}, \; D^r = \frac{k_B T}{8\pi\eta a^3}, \tag{A.3}$$

where, η is the fluid viscosity and a is the radius of particles. This correspondence allows exact matching onto LB parameters so that the only difference between LB and BD is the presence of hydrodynamic interactions in LB. In equations (A.1) and (A.2), $\zeta_i^t(t)$ and $\zeta_i^r(t)$ are random Gaussian variables with the following conditions:

$$\langle \zeta_i^t \rangle = 0, \langle \zeta_i^r \rangle = 0,$$
$$\langle \zeta_i^t \cdot \zeta_j^t \rangle = 2\Delta t D^t \delta_{ij}, \quad \langle \zeta_i^r \cdot \zeta_j^r \rangle = 2\Delta t D^r \delta_{ij}.$$

Appendix B

Shear Viscosity

The fluid viscosity η can be found from a time integral via the Green-Kubo formula[70, 71]:

$$\eta\rho\Lambda^3 k_BT = \int_0^\infty \langle \Sigma^f_{\alpha\beta}(t)\Sigma^f_{\alpha\beta}(0)\rangle dt. \tag{B.1}$$

Here Λ^3 is the system volume, k_BT is temperature, and $\Sigma^f_{\alpha\beta}(t)$ is the stress tensor; α and β are components in Cartesian coordinates.

Using the velocity distribution $f_i(\mathbf{r}, t)$ in LB, the stress tensor is defined as $\Sigma^f_{\alpha\beta}(t) = \sum_i f_i(\mathbf{r}, t)c_{i\alpha}c_{i\beta} - \sum_i f_i^{eq}c_{i\alpha}c_{i\beta}$ in equations (2.7) and (2.9). The shear components in the stress tensor are the off-diagonal terms, e.g. Σ_{xy}, Σ_{yz} and Σ_{xz}, so that, in equation (B.1),the correlations of each components are calculated and the shear viscosity is obtained by the average over all three correlations.

B.1 Shear viscosity of fluids without colloids, η

By considering the shear components for numerical calculations, equation (B.1) becomes

$$\eta = \frac{1}{3\rho\Lambda^3 k_BT}\int_0^{t_f} \langle \Sigma^f_{xy}(t)\Sigma^f_{xy}(0) + \Sigma^f_{yz}(t)\Sigma^f_{yz}(0) + \Sigma^f_{xz}(t)\Sigma^f_{xz}(0)\rangle dt, \tag{B.2}$$

where ρ is the fluid density and t_f is a final cutoff time for the integral.

To examine the measurement of viscosity from equation (B.2), two different viscosities are considered as the input values: $\eta = 1/2$ and $1/40$. The $D3Q19$ model is used with the system box, $\Lambda^3 = 64^3$. The temperature of fluid is chosen as $k_BT = 5 \times 10^{-5}$. Figures B.1(a) and B.1(b) show the results of the normalised stress-stress correlation functions. Both curves converge into zero. Using equation (B.2) and $t_f = 200$, the viscosities are found as 0.50471 for the input viscosity 0.5 and 0.02556 for the input viscosity 0.025. Moreover, Figures B.1(a) and B.1(b) show the different shapes for the relaxation curves depending on the fluid viscosities. In the Navier-Stokes equation (2.2), the shear viscosity of the fluid determines the collison

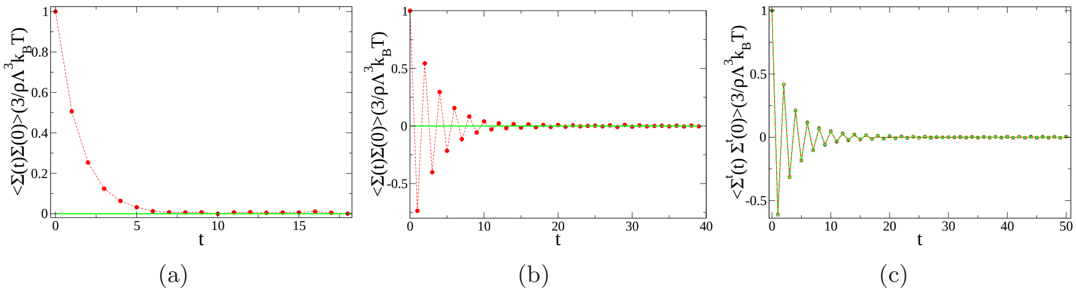

(a) (b) (c)

Figure B.1: (a) Stress-stress correlation function with $\eta = 1/2$. The corresponding collision operator ω is -0.5 which obeys under-relaxing, $-1 < \omega < 0$. (b) Stress-stress correlation function with $\eta = 1/40$. The corresponding collision operator ω is -1.74 which obeys over-relaxing, $-2 < \omega < -1$. (c) the total correlation functions for $\lambda = 0$(black), 4(red) and 8(green).

operator parameter ω:

$$\eta = -\frac{1}{6}\rho\left(\frac{2}{\omega}+1\right), \tag{B.3}$$

where, ρ is the density of fluid. This in turn determines the relaxation shape of the stress-stress correlator[70, 71].

B.2 High-frequency shear viscosity, η_∞

In the case of solid colloids in a single/binary fluid, the high-frequency shear viscosity can be calculated from the ratio of the viscosity with solid particles and the pure fluid viscosity: $\eta_\infty(\phi)/\eta$. The value of η_∞ can be computed by the integral of the total stress correlation function across the short time window, t_f:

$$\eta_\infty 3VkT = \int_0^{t_f} \langle \Sigma^t_{\alpha\beta}(t)\Sigma^t_{\alpha\beta}(0)\rangle dt \tag{B.4}$$

where $\Sigma^t = \Sigma^s + \Sigma^f$. The particle stress Σ^s is found by summing components of $\mathbf{r}_b\bar{f}(\mathbf{r}_b)$, where $\bar{f}(\mathbf{r}_b)$ is the average of all f_b shown in equation (2.2) around boundary nodes of particles. Figure B.1(c) presents the total stress correlations for $\lambda = 0$, 4 and 8. For good statistics, the correlation functions are averaged over 298900 different initial times with $t_f = 100$. Three curves in Figure B.1(c) look overlapped, but, on integrating these by equation (B.5), the high-frequency viscosities η_∞ are obtained as 0.0263301 ± 0.0003271, 0.0267933 ± 0.0002877 and 0.0292169 ± 0.0002291 respectively.

Appendix C

Langevin Theory

In ideal paramagnetism, ignoring the dipolar interaction, Langevin theory provides the equilibrium magnetisation under the uniform external field:

$$M^{eq} = M_{sat}\mathcal{L}(\alpha_B), \tag{C.1}$$

where α_B is the dimensionless parameter as the ratio of the interaction energy (for the dipole μ and the uniform field B) and the thermal energy k_BT, $\mathcal{L}$ is the Langevin function: $\mathcal{L} = \coth(\alpha_B) - 1/\alpha_B$. The saturation magnetisation is given as $M_{sat} = \mu N/\Lambda^3$. In simulation, M_{sat} is set as unity per a particle and the magnetisation M is generally defined as

$$M = \frac{1}{N}\left[m_x^2 + m_y^2 + m_z^2\right]^{1/2}. \tag{C.2}$$

Here $m_\alpha = \sum_i s_i^\alpha$, where α is x, y and z in Cartesian coordinates. Figure C.1 presents the equilibrium magnetisations with various α_B in our LB simulations. From these data, we confirm that the equilibrium mangetisation is satisfied by a Langevin curve over the whole range of α_B.

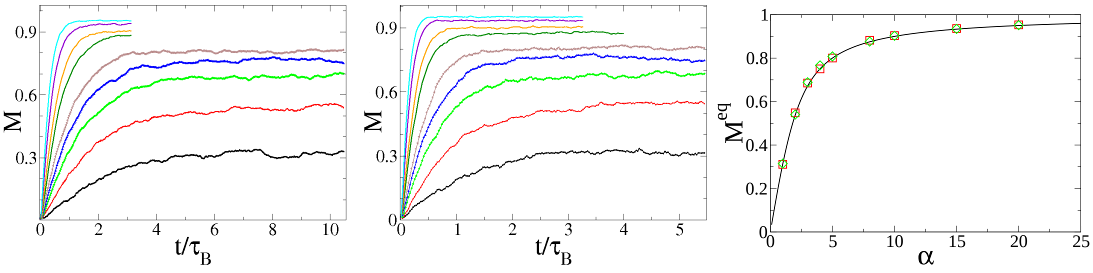

(a) (b) (c)

Figure C.1: Equilibrium magnetisation at $\alpha_B = 1, 2, 3, 4, 5, 8, 10, 15$ and 20 (from bottom to top): (a) $\tau_D = 19,111$ with the fluid viscosity $\eta = 1/600$ and (b) $\tau_D = 18,350$ with the fluid viscosity $\eta = 1/60$. (c) Langevin curve resulting from the data in Figures C.1(a) and C.1(b).

Appendix D

Measurements for domain length scales

The discrete structure factor for order parameter ψ in a binary fluid[87, 122, 123] is defined as

$$s(\mathbf{k},t) = \left\langle \frac{1}{V} \left| \sum_{\mathbf{r}} \exp(i\mathbf{k}\mathbf{r})\psi(\mathbf{r},t) \right|^2 \right\rangle. \tag{D.1}$$

Here $\mathbf{k} = \frac{2\pi}{\Lambda}(x,\ y,\ z)$, where Λ is one-dimensional length of a cubic box with the volume V.

Generally, the spherically averaged structure factor is given as

$$S(k,t) = \frac{\sum_{\hat{\mathbf{k}}} s(\mathbf{k},t)}{\sum_{\hat{\mathbf{k}}} 1}, \tag{D.2}$$

where $k = \frac{2\pi n}{\Lambda}$, $n = 0, 1, 2, ..., \Lambda$, the sum $\sum_{\hat{\mathbf{k}}}$ is over a spherical shell defined by $n - \frac{1}{2} \leq |\mathbf{k}|\frac{\Lambda}{2\pi} \leq n + \frac{1}{2}$ and $\sum_{\hat{\mathbf{k}}} 1$ is the normalisation factor. Using $S(k,t)$, the length scales can be deduced from the pth moment:

$$[k_p(t)]^p = \frac{\sum_k k^p S(k,t)}{\sum_k S(k_t)}. \tag{D.3}$$

Considering the first three moments, possible length scales are

$$\begin{aligned} R_1(t) &\sim 2\pi/k_1,\ R_2(t) \sim 2\pi/k_2^{\frac{1}{2}}, \\ R_3(t) &\sim 2\pi k_1/k_2,\ R_4(t) \sim 2\pi/k_3^{\frac{1}{3}}, \\ R_5(t) &\sim 2\pi(k_1/k_3)^{\frac{1}{2}}. \end{aligned} \tag{D.4}$$

In equation (D.4), $R_1(t)$ is equivalent to $L(t)$ in equation (3.1) to measure the domain length in periodic box. For nonperiodic systems, such as sheared system or nonisotropic domains, methods based on Fourier transforms cannot be used to measure length scales. In this case, a length scale can be deduced from $R_5(t)$ which can be evaluated in real space:

$$\begin{aligned} R_5^2 &= \frac{\sum_{\mathbf{k}} s(\mathbf{k})}{\sum_{\mathbf{k},\alpha} \sin(k_\alpha)\sin(k_\alpha)s(\mathbf{k})} \\ &= \frac{\sum_{\mathbf{r},\alpha} \psi^2(\mathbf{r},t)}{\sum_{\mathbf{r}} \partial_\alpha^D \psi(\mathbf{r},t)\partial_\alpha^D \psi(\mathbf{r},t)}, \end{aligned} \tag{D.5}$$

where ∂_α^D is the symmetric discrete derivative in direction α. To extract two or three length scales in 2D or 3D respectively, we can define a symmetric tensor written as

$$d_{\alpha\beta} = \frac{\sum_{\mathbf{r}} \partial_\alpha^D \psi(\mathbf{r},t)\partial_\beta^D \psi(\mathbf{r},t)}{\sum_{\mathbf{r}} \psi^2(\mathbf{r},t)}. \tag{D.6}$$

This tensor $d_{\alpha\beta}$ can be diagonalised to extract three eigenvalues (l_1, l_2, l_3) and three eigenvectors ($\hat{\mathbf{e}}_1$, $\hat{\mathbf{e}}_2$, $\hat{\mathbf{e}}_3$) in 3D. In practice, we calculate these eigenvalues and eigenvectors numerically, while 2D solutions are easily obtained[87]. From these eigenvalues and eigenvectors, three orthogonal length scales are:

$$L_1 = \frac{1}{l_1\xi},\ L_2 = \frac{1}{l_2\xi},\ L_3 = \frac{1}{l_3\xi} \tag{D.7}$$

where ξ is the interfacial width.

Similarily, length scales along axes x, y and z can be calculated from the tensor $d_{\alpha\beta}$ directly:

$$L_x = \frac{1}{d_{xx}\xi},\ L_y = \frac{1}{d_{yy}\xi},\ L_z = \frac{1}{d_{zz}\xi}. \tag{D.8}$$

Figure D.1 shows the example of length scales in 2D: L_1, L_2 and L_x, L_y. For an arbitrary shape of domain, the smallest eigenvalue represents the longest length scale of the domain; the other two eigenvalues in 3D give the lengths which are orthogonal to the longest length (inverse of smallest eigenvalue).

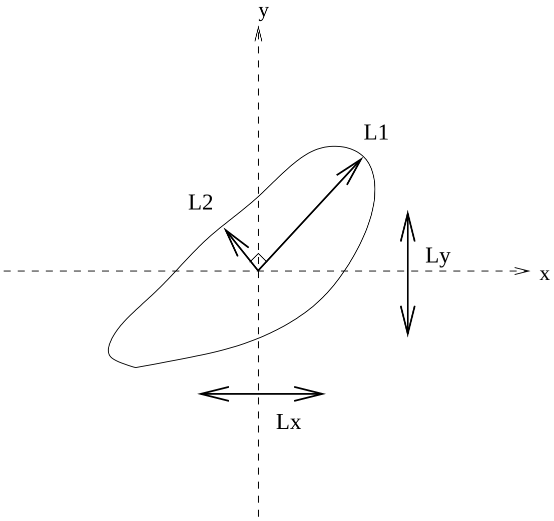

Figure D.1: The schematic picture of length scales in a simple 2D domain. Using the equation (D.7), two eigenvalues (l_1 and l_2) give two length scales L_1 and $L2$. The longer length L_1 (the smaller eigenvalue l_1) is perpendicular to the shorter length L_2 (the large eigenvalue l_2). L_x and L_y are the averaged domain lengths along x and y axes repectively.

Appendix E

Ewald Summation in *Ludwig*

E.1 Cell list in *Ludwig*

The fluid part in LB is easily parallelised by a regular domain decomposition[11]. For implementation of dynamics of colloids in LB, the "cell list"[19] is employed to reduce the $O(N^2)$ problem[13]. Figure E.1(a) presents a schematic cell list and domain in 2D. The domain is divided into cuboid cells whose width ensures that all pairwise interactions can be identified by particles in the adjacent cells. The minimum width of a cell is usually given as $2a_h+h_c$, where h_c is the surface-surface cutoff of the lubrication interaction between particles. Zero or more particles are contained in a cell.

For long-range dipolar interactions, choosing this cell width arises as an important issue to calculate the Ewald summation (discussed in Section 2.4.3). Ewald summation for the long-range dipolar interactions consists of three parts: the short-range part in real space, the long-range part in Fourier space and the self energy correction term. Among the three parts, the short-range calculation in real space is strongly restricted by the cell width. (On the other hand, the Fourier space contribution and the self energy correction term do not depend on the cell width.)

For the Ewald technique, the real space cut-off distance r_c determines the convergence factor α and the maximum Fourier space component n_{max}: $\alpha = 2.5/r_c$ and $n_{max} = \alpha^2 r_c \Lambda/\pi$[124]. This says that decreasing r_c demands more Fourier space calculation which requires more computational power.

For the real space interaction, the cell width must be larger than r_c. Thus in practice, the cell width is equal to the real space distance $r_c = 16$ in cases of the parallel computation with 8 processors in $\Lambda^3 = 64^3$ and 64 processors in $\Lambda^3 = 128^3$; also the sub-domain length is given equal to the cell width. This condition is reasonably optimised choice in our simulations. Figure E.2 shows a cartoon of particle-particle interactions in the nearest neighbouring cells.

The following section shows the implementation of the Ewald sum in *Ludwig* as written by E. Kim and K. Stratford.

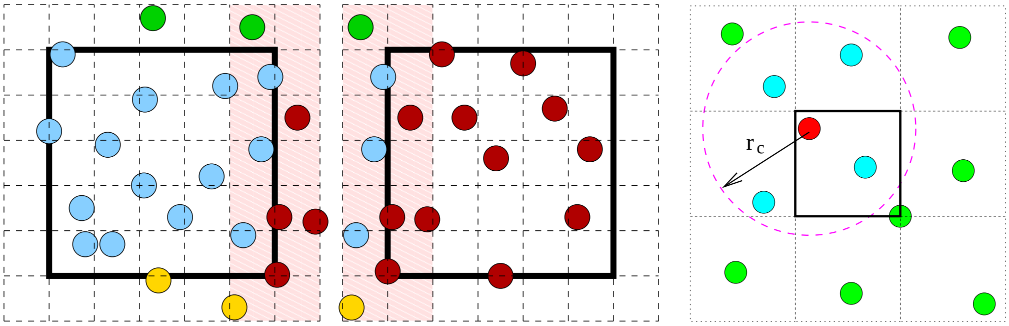

(a) (b)

Figure E.1: (a) the cell list on the basis of domain decomposition in 2D (from [13]). The thick line represents each sub-domain which consists of cells (dash lines) which constitute the cell list. (b) the long-range dipolar interactions based on the cell list; for the chosen particle (red), the dipolar energy is calculated by the short-range contribution (with cyan particles) in real space truncated by r_c and the long-range contribution (with green particles) which is calculated in Fourier space.

E.2 Codes of Ewald summation

```
void ewald_init(double mu_input, double rc_input) {

 int nk;

 rpi_      = 1.0/sqrt(PI);
 mu_       = mu_input;
 ewald_rc_ = rc_input;
 alpha_    = 5.0/(2.0*ewald_rc_);

 nk = ceil(alpha_*alpha_*ewald_rc_*L(X)/PI);

 info("\nThe Ewald sum:\n");
 info("Real space cut off is     %f\n", ewald_rc_);
 info("Ewald parameter alpha is  %f\n", alpha_);
 info("Dipole strength mu is     %f\n", mu_);
 info("Self energy (constant)    %f\n", ewald_self_energy());
 info("Max. term retained in Fourier space sum is %d\n", nk);

 nk_[X] = nk;
 nk_[Y] = nk;
 nk_[Z] = nk;
```

```
 kmax_ = pow(2.0*PI*nk/L(X), 2);
 nkmax_ = nk + 1;
 nktot_ = ewald_get_number_fourier_terms();

 info("maximum square wavevector is %g\n", kmax_);
 info("Total terms retained in Fourier space sum is %d\n\n", nktot_);

 sinx_ = (double *) malloc(nktot_*sizeof(double));
 cosx_ = (double *) malloc(nktot_*sizeof(double));

 sinkr_ = (double *) malloc(3*nkmax_*sizeof(double));
 coskr_ = (double *) malloc(3*nkmax_*sizeof(double));

 return;
}

static void ewald_sum_sin_cos_terms() {

 double k[3], ksq;
 double fkx, fky, fkz;
 int kx, ky, kz, kn = 0;
 int ic, jc, kc;
 int ncell[3];

 fkx = 2.0*PI/L(X);
 fky = 2.0*PI/L(Y);
 fkz = 2.0*PI/L(Z);

 ncell[X] = Ncell(X);
 ncell[Y] = Ncell(Y);
 ncell[Z] = Ncell(Z);

 for (kn = 0; kn < nktot_; kn++) {
   sinx_[kn] = 0.0;
   cosx_[kn] = 0.0;
 }

 for (ic = 1; ic <= ncell[X]; ic++) {
```

```
  for (jc = 1; jc <= ncell[Y]; jc++) {
    for (kc = 1; kc <= ncell[Z]; kc++) {

      Colloid * p_colloid;

      p_colloid = CELL_get_head_of_list(ic, jc, kc);

      while (p_colloid != NULL) {

        double r[3];
        kn = 0;

        r[X] = p_colloid->r.x;
        r[Y] = p_colloid->r.y;
        r[Z] = p_colloid->r.z;
        ewald_set_kr_table(r);

        for (kz = 0; kz <= nk_[Z]; kz++) {
          for (ky = -nk_[Y]; ky <= nk_[Y]; ky++) {
            for (kx = -nk_[X]; kx <= nk_[X]; kx++) {
              double udotk, kdotr;
              double skr[3], ckr[3];

              k[X] = fkx*kx;
              k[Y] = fky*ky;
              k[Z] = fkz*kz;
              ksq = k[X]*k[X] + k[Y]*k[Y] + k[Z]*k[Z];

              if (ksq <= 0.0 || ksq > kmax_) continue;

              skr[X] = sinkr_[3*abs(kx) + X];
              skr[Y] = sinkr_[3*abs(ky) + Y];
              skr[Z] = sinkr_[3*kz      + Z];
              ckr[X] = coskr_[3*abs(kx) + X];
              ckr[Y] = coskr_[3*abs(ky) + Y];
              ckr[Z] = coskr_[3*kz      + Z];

              if (kx < 0) skr[X] = -skr[X];
```

```
               if (ky < 0) skr[Y] = -skr[Y];

               udotk = dot_product(p_colloid->s, k);

               kdotr = skr[X]*ckr[Y]*ckr[Z] + ckr[X]*skr[Y]*ckr[Z]
                 + ckr[X]*ckr[Y]*skr[Z] - skr[X]*skr[Y]*skr[Z];
               sinx_[kn] += udotk*kdotr;

               kdotr = ckr[X]*ckr[Y]*ckr[Z] - ckr[X]*skr[Y]*skr[Z]
                 - skr[X]*ckr[Y]*skr[Z] - skr[X]*skr[Y]*ckr[Z];
               cosx_[kn] += udotk*kdotr;

               kn++;
             }
           }
         }
         p_colloid = p_colloid->next;
       }
       /* Next cell */
     }
   }
 }

#ifdef _MPI_
 {
   double * subsin;
   double * subcos;

   subsin = (double *) calloc(nktot_, sizeof(double));
   if (subsin == NULL) fatal("calloc(subsin) failed\n");
   subcos = (double *) calloc(nktot_, sizeof(double));
   if (subcos == NULL) fatal("calloc(subcos) failed\n");

   for (kn = 0; kn < nktot_; kn++) {
     subsin[kn] = sinx_[kn];
     subcos[kn] = cosx_[kn];
   }
```

```
   MPI_Allreduce(subsin, sinx_, nktot_, MPI_DOUBLE, MPI_SUM, cart_comm());
   MPI_Allreduce(subcos, cosx_, nktot_, MPI_DOUBLE, MPI_SUM, cart_comm());

   free(subsin);
   free(subcos);
 }
#endif

 return ;
}

double ewald_real_space_energy(double u1[3], double u2[3], double r12[3]) {

 /* u1[3] and u2[3] are dipolar vectors,
    r12[3] is the centre-to-centre separation between particles. */

 double e = 0.0;
 double r;
 double erfc(double); /* ANSI C does not define erfc() in math.h. */

 r = sqrt(r12[X]*r12[X] + r12[Y]*r12[Y] + r12[Z]*r12[Z]);

 if (r < ewald_rc_) {
   double rr = 1.0/r;
   double b, b1, b2, c;

   b1 = mu_*mu_*erfc(alpha_*r)*(rr*rr*rr);
   b2 = mu_*mu_*(2.0*alpha_*rpi_)*exp(-alpha_*alpha_*r*r)*(rr*rr);

   b = b1 + b2;
   c = 3.0*b1*rr*rr + (2.0*alpha_*alpha_ + 3.0*rr*rr)*b2;

   e = dot_product(u1,u2)*b - dot_product(u1,r12)*dot_product(u2,r12)*c;
 }

 return e;
}

double ewald_fourier_space_energy() {
```

```
double e = 0.0;
double k[3], ksq;
double fkx, fky, fkz;
double b0, b;
double r4alpha_sq;
int kx, ky, kz, kn = 0;

ewald_sum_sin_cos_terms();

fkx = 2.0*PI/L(X);
fky = 2.0*PI/L(Y);
fkz = 2.0*PI/L(Z);
b0 = (4.0*PI/(L(X)*L(Y)*L(Z)))*mu_*mu_;
r4alpha_sq = 1.0/(4.0*alpha_*alpha_);

for (kz = 0; kz <= nk_[Z]; kz++) {
  for (ky = -nk_[Y]; ky <= nk_[Y]; ky++) {
    for (kx = -nk_[X]; kx <= nk_[X]; kx++) {

      k[X] = fkx*kx;
      k[Y] = fky*ky;
      k[Z] = fkz*kz;
      ksq = k[X]*k[X] + k[Y]*k[Y] + k[Z]*k[Z];

      if (ksq <= 0.0 || ksq > kmax_) continue;

      b = b0*exp(-r4alpha_sq*ksq)/ksq;
      if (kz == 0) {
        e += 0.5*b*(sinx_[kn]*sinx_[kn] + cosx_[kn]*cosx_[kn]);
      }
      else {
        e +=     b*(sinx_[kn]*sinx_[kn] + cosx_[kn]*cosx_[kn]);
      }
      kn++;
    }
  }
}
```

```
 return e;
}

double ewald_self_energy() {

 double eself;

 eself = -2.0*mu_*mu_*(alpha_*alpha_*alpha_/(3.0*sqrt(PI)))*get_N_colloid();

 return eself;
}


void ewald_real_space_sum() {

 Colloid * p_c1;
 Colloid * p_c2;

 int    ic, jc, kc, id, jd, kd, dx, dy, dz;
 double r12[3];

 FVector r_12;
 FVector COLL_fvector_separation(FVector, FVector);
 double erfc(double);

 ereal_ = 0.0;

 for (ic = 1; ic <= Ncell(X); ic++) {
   for (jc = 1; jc <= Ncell(Y); jc++) {
     for (kc = 1; kc <= Ncell(Z); kc++) {

       p_c1 = CELL_get_head_of_list(ic, jc, kc);

       while (p_c1) {

         for (dx = -1; dx <= +1; dx++) {
           for (dy = -1; dy <= +1; dy++) {
             for (dz = -1; dz <= +1; dz++) {
```

```
id = ic + dx;
jd = jc + dy;
kd = kc + dz;

p_c2 = CELL_get_head_of_list(id, jd, kd);

while (p_c2) {

  if (p_c1->index < p_c2->index) {

    double r;

   /* Here we need r2-r1 */
    r_12 = COLL_fvector_separation(p_c2->r, p_c1->r);
    r12[X] = r_12.x;
    r12[Y] = r_12.y;
    r12[Z] = r_12.z;

    r = sqrt(r12[X]*r12[X] + r12[Y]*r12[Y] + r12[Z]*r12[Z]);

    if (r < ewald_rc_) {
      double rr = 1.0/r;
      double b, b1, b2, c, d;
      double udotu, u1dotr, u2dotr;
      double f[3], g[3];
      int i;

      /* Energy */
      b1 = mu_*mu_*erfc(alpha_*r)*(rr*rr*rr);
      b2 = mu_*mu_*(2.0*alpha_*rpi_)
        *exp(-alpha_*alpha_*r*r)*(rr*rr);

      b = b1 + b2;
      c = 3.0*b1*rr*rr + (2.0*alpha_*alpha_ + 3.0*rr*rr)*b2;
      d = 5.0*c/(r*r)
        + 4.0*alpha_*alpha_*alpha_*alpha_*b2;
```

```
udotu  = dot_product(p_c1->s, p_c2->s);
u1dotr = dot_product(p_c1->s, r12);
u2dotr = dot_product(p_c2->s, r12);

ereal_ += udotu*b - u1dotr*u2dotr*c;

/* Force */

for (i = 0; i < 3; i++) {
  f[i] = (udotu*c - u1dotr*u2dotr*d)*r12[i]
    + c*(u2dotr*p_c1->s[i] + u1dotr*p_c2->s[i]);
}

p_c1->force.x += f[X];
p_c1->force.y += f[Y];
p_c1->force.z += f[Z];

p_c2->force.x -= f[X];
p_c2->force.y -= f[Y];
p_c2->force.z -= f[Z];


g[X] = b*p_c2->s[X] - c*u2dotr*r12[X];
g[Y] = b*p_c2->s[Y] - c*u2dotr*r12[Y];
g[Z] = b*p_c2->s[Z] - c*u2dotr*r12[Z];

p_c1->torque.x += -(p_c1->s[Y]*g[Z] - p_c1->s[Z]*g[Y]);
p_c1->torque.y += -(p_c1->s[Z]*g[X] - p_c1->s[X]*g[Z]);
p_c1->torque.z += -(p_c1->s[X]*g[Y] - p_c1->s[Y]*g[X]);

/* Torque on particle 2 */

g[X] = b*p_c1->s[X] - c*u1dotr*r12[X];
g[Y] = b*p_c1->s[Y] - c*u1dotr*r12[Y];
g[Z] = b*p_c1->s[Z] - c*u1dotr*r12[Z];

p_c2->torque.x += -(p_c2->s[Y]*g[Z] - p_c2->s[Z]*g[Y]);
p_c2->torque.y += -(p_c2->s[Z]*g[X] - p_c2->s[X]*g[Z]);
```

```
                     p_c2->torque.z += -(p_c2->s[X]*g[Y] - p_c2->s[Y]*g[X]);
                   }

                 }

                 p_c2 = p_c2->next;
               }

               /* Next cell */
             }
           }
         }

         p_c1 = p_c1->next;
       }

       /* Next cell */
     }
   }
 }

 return;
}

void ewald_fourier_space_sum() {

 double k[3], ksq;
 double b0, b;
 double fkx, fky, fkz;
 double r4alpha_sq;
 int ic, jc, kc;
 int kx, ky, kz, kn = 0;
 int ncell[3];

 ewald_sum_sin_cos_terms();

 fkx = 2.0*PI/L(X);
 fky = 2.0*PI/L(Y);
```

```
fkz = 2.0*PI/L(Z);
r4alpha_sq = 1.0/(4.0*alpha_*alpha_);
b0 = (4.0*PI/(L(X)*L(Y)*L(Z)))*mu_*mu_;

ncell[X] = Ncell(X);
ncell[Y] = Ncell(Y);
ncell[Z] = Ncell(Z);

for (ic = 1; ic <= ncell[X]; ic++) {
  for (jc = 1; jc <= ncell[Y]; jc++) {
    for (kc = 1; kc <= ncell[Z]; kc++) {

      Colloid * p_colloid;

      p_colloid = CELL_get_head_of_list(ic, jc, kc);

      while (p_colloid != NULL) {

        /* Sum over k to get the force/torque. */

        double f[3], r[3], t[3];
        int i;

        r[X] = p_colloid->r.x;
        r[Y] = p_colloid->r.y;
        r[Z] = p_colloid->r.z;
        ewald_set_kr_table(r);

        for (i = 0; i < 3; i++) {
          f[i] = 0.0;
          t[i] = 0.0;
        }

        efourier_ = 0.0; /* Count only once! */
        kn = 0;
        for (kz = 0; kz <= nk_[Z]; kz++) {
          for (ky = -nk_[Y]; ky <= nk_[Y]; ky++) {
            for (kx = -nk_[X]; kx <= nk_[X]; kx++) {
```

```
double udotk, g[3];
double coskr, sinkr, ckr[3], skr[3];

k[X] = fkx*kx;
k[Y] = fky*ky;
k[Z] = fkz*kz;
ksq = k[X]*k[X] + k[Y]*k[Y] + k[Z]*k[Z];

if (ksq <= 0.0 || ksq > kmax_) continue;
b = b0*exp(-r4alpha_sq*ksq)/ksq;

/* Energy */

if (kz > 0) b *= 2.0;
efourier_ += 0.5*b*(sinx_[kn]*sinx_[kn] + cosx_[kn]*cosx_[kn]);

skr[X] = sinkr_[3*abs(kx) + X];
skr[Y] = sinkr_[3*abs(ky) + Y];
skr[Z] = sinkr_[3*kz      + Z];
ckr[X] = coskr_[3*abs(kx) + X];
ckr[Y] = coskr_[3*abs(ky) + Y];
ckr[Z] = coskr_[3*kz      + Z];

if (kx < 0) skr[X] = -skr[X];
if (ky < 0) skr[Y] = -skr[Y];

sinkr = skr[X]*ckr[Y]*ckr[Z] + ckr[X]*skr[Y]*ckr[Z]
  + ckr[X]*ckr[Y]*skr[Z] - skr[X]*skr[Y]*skr[Z];

coskr = ckr[X]*ckr[Y]*ckr[Z] - ckr[X]*skr[Y]*skr[Z]
  - skr[X]*ckr[Y]*skr[Z] - skr[X]*skr[Y]*ckr[Z];

/* Force and torque */

udotk = dot_product(p_colloid->s, k);

for (i = 0; i < 3; i++) {
```

```
                  f[i] += b*k[i]*udotk*(cosx_[kn]*sinkr - sinx_[kn]*coskr);
                  g[i] =  b*k[i]*(cosx_[kn]*coskr + sinx_[kn]*sinkr);
               }

               t[X] += -(p_colloid->s[Y]*g[Z] - p_colloid->s[Z]*g[Y]);
               t[Y] += -(p_colloid->s[Z]*g[X] - p_colloid->s[X]*g[Z]);
               t[Z] += -(p_colloid->s[X]*g[Y] - p_colloid->s[Y]*g[X]);

                kn++;
               }
             }
           }

         /* Accumulate force/torque */

         p_colloid->force.x += f[X];
         p_colloid->force.y += f[Y];
         p_colloid->force.z += f[Z];
         p_colloid->torque.x += t[X];
         p_colloid->torque.y += t[Y];
         p_colloid->torque.z += t[Z];

         p_colloid = p_colloid->next;
       }

       /* Next cell */
     }
   }
 }

 return;
}
```

Appendix F

Supporting Movies

1. fig3-1b.avi: droplet phases in asymmetric quench $\psi_0 = 0.4$ in $\Lambda^3 = 64^3$.
2. fig3-2a.avi: bijel in a closed box with solid walls.
3. fig3-2b.avi: droplet phases in a closed box with solid walls.
4. fig4-7a.avi: LB simulation of colloidal ferrofluids in $\lambda = 4$ and $\phi = 0.10$.
5. fig4-7b.avi: LB simulation of colloidal ferrofluids in $\lambda = 8$ and $\phi = 0.10$.
6. fig5-2a.avi: magnetic bijel with periodic boundary conditions for $\lambda = 4$.
7. fig5-6b.avi: bijel under uniform field ($\alpha_B = 20$) for $\lambda = 4$.
8. fig5-15c.avi: a droplet under uniform field with capillary energy ($\epsilon/k_BT = 1230$).
9. fig5-15d.avi: a droplet under uniform field with capillary energy ($\epsilon/k_BT = 130$).
10. fig5-16c.avi: a droplet under field gradient without arteficial buoyancy.
11. fig5-16d.avi: a droplet under field gradient with arteficial buoyancy.

Bibliography

[1] K. Stratford, R. Adhikari, I. Pagonabarraga, J.-C. Desplat, and M. E. Cates. Colloidal jamming at interfaces: a route to bicontinuous gels. *Science*, 309:2198–2201, 2005.

[2] R. Aveyard, B. P. Binks, and J. H. Clint. Emulsions stabilised solely by colloidal particles. *Adv, Colloid Interface Sci.*, 100-102:503–546, 2003.

[3] B. P. Binks and S. O. Lumsdon. Pickering emulsions stabilised by monodisperse latex particles: Effects of particle size. *Langmuir*, 17:4540–4547, 2001.

[4] E. M. Herzig, K. A. White, A. B. Schofield, W. C. K. Poon, and P. S. Clegg. Bicontinuous emulsions stabilized solely by colloidal particles. *Nat. Mater.*, 6:966–971, 2007.

[5] M. Klokkenburg, R. P. A. Dullens, W. K. Kegel, B. H. Erné, and A. P. Philipse. Quantitative real-space analysis of self-assembled structures of magnetic dipolar colloids. *Phys. Rev. Lett.*, 96:037203, 2006.

[6] J. J. Weis and D. Levesque. Simple dipolar fluids as generic models for soft matter. *Adv. Polym. Sci.*, 185:163–225, 2005.

[7] C. Holm and J.-J. Weis. The structure of ferrofluids: a status report. *Curr. Opin. Colloid Interface Sci.*, 10:133–140, 2005.

[8] P. J. Camp, J. C. Shelley, and G. N. Patey. Isotropic fluid phases of dipolar hard spheres. *Phys. Rev. Lett.*, 84:115–118, 2000.

[9] P. J. Camp and G. N. Patey. Structure and scattering in colloidal ferrofluids. *Phys. Rev. E*, 62:5403–5408, 2000.

[10] J. J. Weis and D. Levesque. Ferroelectric phases of dipolar hard spheres. *Phys. Rev. E*, 48:3728–3740, 1993.

[11] J.-C. Desplat, I. Pagonabarraga, and P. Bladon. Ludwig: a parallel lattice-Boltzmann code for complex fluids. *Comput. Phys. Comm.*, 134:273–290, 2001.

[12] K. Stratford, R. Adhikari, I. Pagonabarraga, and J.-C. Desplat. Lattice Boltzmann for binary fluids with suspended colloids. *J. Stat. Phys.*, 121:163, 2005.

[13] K. Stratford and I. Pagonabarraga. Parallel simulation of particle suspensions with the lattice Boltzmann method. *Comput. Math.*, 55:1585, 2008.

[14] Personal communication with Kevin Stratford.

[15] N. Q. Nguyen and A. J. C. Ladd. Lubrication corrections for lattice-Boltzmann simulations of particle suspensions. *Phys. Rev. E*, 66:046708, 2002.

[16] T. A. Witten and P. A. Pincus. *Structured Fluids.* Oxford University Press, 2004.

[17] R. A. L. Jones. *Soft Condensed Matter.* Oxford University Press, 2004.

[18] M. Karttunen, I. Vattulainen, and A. Lukkarinen (editors). *Novel Methods in Soft Matter Simulations.* Springer Berlin / Heidelberg, 2004.

[19] M. P. Allen and D. J. Tildesley. *Computer Simulation of Liquids*. Oxford Science Publications, 1986.

[20] J. K. G. Dhont. *An Introduction to Dynamics of Colloids*. Elsevier, Amsterdam, 1996.

[21] R. B. Jones and F. N. Alavi. Rotational diffusion of a tracer colloid particle: IV. Brownian dynamics with wall effects. *Physica A*, 187:436–455, 1992.

[22] J. F. Brady and G. Bossis. Stokesian Dynamics. *Ann. Rev. Fluid. Mech.*, 20:111–157, 1998.

[23] A. Sierou and J. F. Brady. Accelerated Stokesian Dynamics simulations. *J. Fluid. Mech.*, 448:115–146, 2001.

[24] M. R. Swift, E. Orlandini, W. R. Osborn, and J. M. Yeomans. Lattice Boltzmann simulation of liquid-gas and binary fluid systems. *Phys. Rev. E*, 54:5041, 1996.

[25] V. M. Kendon, M. E. Cates, I. Pagonabarraga, J. C. Desplat, and P. Bladon. Inertial effects in three-dimensional spinodal decomposition of a symmetric binary fluid mixture: a lattice Boltzmann study. *J. Fluid. Mech.*, 440:147–203, 2001.

[26] Nélido González-Segredo and P. V. Coveney. Coarsening dynamics of ternary amphiphilic fluids and the self-assembly of the gyroid and sponge mesophases: lattice Boltzmann simulations. *Phys. Rev. E*, 69:061501, 2004.

[27] G. Giupponi, J. Harting, and P. V. Coveney. Emergence of rheological properties in lattice Boltzmann simulations of gyroid mesophases. *Europhys. Lett.*, 73:533–539, 2006.

[28] C. Denniston, E. Orlandini, and J. M. Yeomans. Lattice Boltzmann simulations of liquid crystal hydrodynamics. *Phys. Rev. E*, 63:056702, 2001.

[29] S. U. Pickering. Emulsions. *J. Chem. Soc.*, 91:2004, 1907.

[30] W. Ramsden. Separation of solids in the surface-layers of solutions and 'suspensions'. *Proc. R. Soc. London, Ser. A*, 72:156–164, 1903.

[31] B. P. Binks and T. S. Horozov. *Colloidal Particles at Liquid Interfaces*. Cambridge University Press, 2006.

[32] G. J. Young. Interaction of water vapor with silica surfaces. *J. Colloid Interface Sci.*, 13:67, 1958.

[33] S. Levin, B.D. Bowen, and S. J. Partridge. Stabilization of emulsions by fine particles I. partitioning of particles between continuous phase and oil/water interface. *Colloids Surf.*, 38:325, 1989.

[34] K. A. White, A. B. Schofield, P. B. Bink, and P. S. Clegg. Influence of particle composition and thermal cycling on bijel formation. *J. Phys.: Condens. Matter*, 20:494223, 2008.

[35] P. S. Clegg, E. M. Herzig, A. B. Schofield, T. S. Horozov, B. P. Binks, M. E. Cates, and W. C. K. Poon. Colloid-stabilized emulsions: behaviour as the interfacial tension is reduced. *J. Phys.:Condens. Matter*, 17:S3433–S3438, 2005.

[36] P. S. Clegg, E. M. Herzig, S. U. Egelhaaf, A. B. Schofield, T. S. Horozov, B. P. Binks, M. E. Cates, and W. C. K. Poon. Emulsification of partially miscible liquids using colloidal particles: nonspherical and extended domain structures. *Langmuir*, 23:5984–5994, 2007.

[37] R. E. Rosensweig. *Ferrohydrodynamics*. Cambridge University Press, New York, 1985.

[38] P. Weiss. L'hypothèse du champ molculaire et la proprité ferromagnètique (the hypothesis of the molecular field and the property of ferromagnetism). *J. de Phys. Rad.*, 6:661–690, 1907.

[39] C. Kittel. Theory of the structure of ferromagnetic domains in film and small particles. *Phys. Rev.*, 70:965–971, 1946.

[40] L. Néel. Effect of thermal fluctuations on the magnetization of small particles. *C. R. Acad. Sci. (Paris)*, 228:664, 1949.

[41] L. Néel. Thermoremanent magnetization of fine powders. *Rev. Mod. Phys.*, 25:293–295, 1953.

[42] P. I. C. Teixeira, J. M. Tavares, and M. M. Telo da Gama. The effect of dipolar forces on the structure and thermodynamics of classical fluids. *J. Phys. Condens. Matter*, 12:R411–R434, 2000.

[43] B. Huke and M Lücke. Magnetic properties of colloidal suspensions of interacting magnetic particles. *Rep. Prog. Phys.*, 67:1731–1768, 2004.

[44] P. G. de Gennes and P. A. Pincus. Pair correlations in a ferro-magnetic colloid. *Phys. Kondens. Materie*, 11:189–198, 1970.

[45] P. H. Hess and Ph. H. Parker. Polymers for stabilization of colloidal cobalt particles. *J. Appl. Polym. Sci.*, 10:1915–1927, 1966.

[46] K. Butter, P. H. Bomans, P. M. Frederik, G. J. Vroege, and A. P. Philipse. Direct observation of dipolar chains in iron ferrofluids by cryogenic electron microscopy. *Nature Mater.*, 2:88–91, 2003.

[47] K. Butter, P. H. Bomans, P. M. Frederik, G. J. Vroege, and A. P. Philipse. Direct observation of dipolar chains in ferrofluids in zero field using cryogenic electro microscopy. *J. Phys.: Condens. Matter*, 15:S1451–s1470, 2003.

[48] J. J. Weis and D. Levesque. Orientational and structural order in strongly interacting dipolar hard spheres. *Phys. Rev. E*, 49:5131–5140, 1994.

[49] J. J. Weis and D. Levesque. Chain formation in low density dipolar hard spheres: a Monte Carlo study. *Phys. Rev. Lett.*, 71:2729–2732, 1993.

[50] J. J. Weis and G. N. Patey. Orientational order in simple dipolar liquids: Computer simulation of a ferroelectric nematic phase. *Phys. Rev. Lett.*, 68:2043, 1992.

[51] J. J. Weis and G. N. Patey. Ferroelectric liquid-crystal and solid phases formed by strongly interacting dipolar soft spheres. *Phys. Rev. A*, 46:7783, 1992.

[52] M. J. Stevens and G. S. Grest. Coexistence in dipolar fluids in a field. *Phys. Rev. Lett.*, 72:3696–3689, 1994.

[53] Z. Wang, C. Holm, and H. W. Müller. Molecular dynamics study on the equilibrium magnetization properties and structure of ferrofluids. *Phys. Rev. E*, 66:021405, 2002.

[54] M. E. van Leeuwen and B. Smit. What makes polar liquid a liquid. *Phys. Rev. Lett.*, 71:3991–3994, 1993.

[55] G. Ganzenmüller and P. J. Camp. Applications of Wang-Landau sampling to determine phase equilibria in complex fluids. *J. Chem. Phys.*, 127:154504, 2007.

[56] E. Dubois F. Cousin and V. Cabuil. Tuning the interactions of a magnetic colloid suspension. *Phys. Rev. E*, 68:021405, 2003.

[57] S. H. L. Klapp. Dipolar fluids under external perturbations. *J. Phys.:Condens. Matter*, 17:R525–R550, 2005.

[58] V. Cabuil. Phase behavior of magnetic nanoparticles dispersions in bulk and confined geometries. *Curr. Opin. Colloid Interface Sci.*, 5:44–48, 2000.

[59] C. Alexiou, W. Arnold, R. J. Klein, F. G. Parak, P. Hulin, C. Bergemann, W. Erhardt, S. Wagenpfeil, and A. S. Lübbe. Locoregional cancer treatment with magnetic drug targeting. *Cancer Res.*, 60:6641–6648, 2000.

[60] M. F. Kircher, U. Mahmood, R. S. King, R. Weissleder, and L. Josephson. A multimodal nanoparticle for preoperative magnetic resonance imaging and intraoperative optical brain tumor delineation. *Cancer Res.*, 63:8122–8125, 2003.

[61] C. Scherer and A. M. F. Neto. Ferrofluids: properties and applications. *Braz. J. Phys.*, 35:718–727, 2005.

[62] C. Alexiou, R. Jurgons, R. J. Schmid, C. Bergemann, J. Henke, W. Erhardt, E. Huenges, and F. Parak. Magnetic drug targeting-biodistribution of the magnetic carrier and the chemotherapeutic agent mitoxantrone after locoregional cancer treatment. *J. Drug Target.*, 11:139149, 2003.

[63] S. Melle, M. Lask, and G. G. Fuller. Pickering emulsions with controllable stability. *Langmuir*, 21:2158–2162, 2005.

[64] Sauro Succi. *The Lattice Boltzmann Equation for Fluid Dynamics and Beyond.* Clarendon Press, Oxford, 2001.

[65] L. D. Landau and E. M. Lifshitz. *Fluid Mechanics.* Pergamon Press, Oxford, 1959.

[66] D. Raabe. Overview of the lattice Boltzmann method for nano- and microscale fluid dynamics in materials science and engineering. *Modelling Simul. Mater. Sci. Eng.*, 12:R13–R46, 2004.

[67] D. D'Humiéres, I. Ginzburg, Manfred Krafczyk, Pierre Lallemand, and Li-Shi Luo. Multiple-relaxation-time lattice Boltzmann models in three dimensions. *Phil. Trans. R. Soc. Lond. A*, 360:437–451, 2002.

[68] A. J. C. Ladd. Short-time motion of colloidal particles: numerical simulation via a fluctuating lattice-Boltzmann equation. *Phys. Rev. Lett.*, 70:1339, 2001.

[69] R. Adhikari, K. Stratford, M. E. Cates, and A. J. Wagner. Fluctuating lattice Boltzmann. *Europhys. Lett.*, 71:473–479, 2005.

[70] A. J. C. Ladd. Numerical simulations of particulate suspensions via a discretized Boltzmann equation. part I. theoretical foundation. *J. Fluid. Mech.*, 271:285–309, 1994.

[71] A. J. C. Ladd. Numerical simulations of particulate suspensions via a discretized Boltzmann equation. part II. numerical results. *J. Fluid. Mech.*, 271:311–339, 1994.

[72] J.-P. Hansen. Molecular-dynamics simulations of Coulomb systems in two and three dimensions. In *Molecular Dynamics Simulations of Statistical Mechanics Systems, Proceedings of the 97th Int. "Enrico Fermi" School of Physics, North Holland, Amsterdam*, 1986.

[73] P. Ewald. Die Berechnung optischer und elektrostatischer Gitterpotentiale (Evaluation of optical and electrostatic lattice potentials). *Ann. Phys. Leipzig*, 64:253–287, 1921.

[74] S. W. de Leeuw, J. W. Perram, and E. R. Smith. Simulation of electrostatic systems in periodic boundary conditions. I. Lattice sums and dielectric constants. *Proc. R. Soc. Lond. A*, 373:27–56, 1980.

[75] D. Frenkel and B. Smit. *Understanding Molecular Simulation.* Academic press, London; New York, 2002.

[76] W. H. Press, S. A. Teukolsk, W. T. Vetterling, and B. P. Flannery. *Numerical Recipes, 2nd edition.* Cambridge University Press, 1988.

[77] S. W. de Leeuw, J. W. Perram, and E. R. Smith. Computer simulation of the static dielectric constant of systems with permanent electric dipoles. *Ann. Rev. Phys. Chem.*, 37:245, 1986.

[78] D. C. Rapaport. *The Art of Molecular Dynamics Simulation.* Cambridge University Press, Cambridge, 1995.

[79] A. O. Ivanov, S. S. Kantorovich, E. N. Reznikov, C. Holm, A. F. Pshenichnikov, A. V. Lebedev, A. Chremos, and P. J. Camp. Magnetic properties of polydisperse ferrofluids: a critical comparison between experiment, theory, and computer simulation. *Phys. Rev. E*, 75:061405, 2007.

[80] M. E. Cates, R. Adhikari, and K. Stratford. Colloidal arrest by capillary forces. *J. Phys.: Condens. Matter*, 17:S2771–S2778, 2005.

[81] A. J. Bray. Theory of phase-ordering kinetics. *Adv. Phys.*, 43:357–459, 1994.

[82] M. E. Cates, K. Stratford, R. Adhikari, P. Stansell, J.-C. Desplat, I. Pagonabarraga, and A. J. Wagner. Simulating colloid hydrodynamics with lattice Boltzmann. *J. Phys.: Condens. Matter*, 16:S3903–S3915, 2004.

[83] Bluegene in Edinburgh Parallel Computer Center (http://www.epcc.ed.ac.uk).

[84] A. Onuki. *Phase Transition Dynamics.* Cambridge University Press, Cambridge, 2002.

[85] P. Stansell, K. Stratford, J.-C. Desplat, R. Adhikari, and M. E. Cates. Nonequilibrium steady states in sheared binary liquids. *Phys. Rev. Lett.*, 96:085701, 2006.

[86] K. Stratford, J.-C. Desplat, P. Stansell, and M. E. Cates. Binary fluids under steady shear in three dimensions. *Phys. Rev. E*, 76:030501(R), 2007.

[87] A. J. Wagner and J. M. Yeomans. Phase separation under shear in two-dimensional binary fluid. *Phys. Rev. E*, 59:4366–4373, 1999.

[88] A. B. Subramaniam, M. Abkharian, L. Mahadevan, and H. A. Stone. Non-spherical bubbles. *Nature*, 438:930–930, 2005.

[89] A. B. Subramaniam, M. Abkharian, and H. A. Stone. Controlled assembly of jammed colloidal shells on fluid droplets. *Nature Mat.*, 4:553–556, 2005.

[90] A. B. Subramaniam, M. Abkharian, L. Mahadevan, and H. A. Stone. Mechanics of interfacial composite materials. *Langmuir*, 22:10204–10208, 2006.

[91] Z. W. Lai and G. F. Mazenko. Classes for growth kinetics problems at low temperatures. *Phys. Rev. B*, 37:9481, 1988.

[92] J. Lee, S. J. Lee, B. Kim, and I. Chang. Ordering kinetics in the two-dimensional classical Coulomb gas of half-integer charges on a square lattice: temperature dependent growth and roughening transition. *Phys. Rev. Lett.*, 79:2172, 1989.

[93] R. Paul, S. Puri, and H. Rieger. Domain growth in Ising systems with quenched disorder. *Phys. Rev. E*, 71:061109, 2005.

[94] T. Tlusty and S. A. Safran. Defect-induced phase separation in dipolar fluids. *Science*, 290:1328–1331, 2000.

[95] G. Ganzenmüller and P. J. Camp. Vapor-liquid coexistence in fluids of charged hard dumbbells. *J. Chem. Phys.*, 126:191104, 2007.

[96] V. V. Murashov, P. J. Camp, and G. N. Patey. Dielectric relaxation of chained ferrofluids. *J. Chem. Phys.*, 116:6731–6737, 2002.

[97] P. D. Duncan and P. J. Camp. Aggregation kinetics and the nature of phase separation in two-dimensional dipolar fluids. *Phys. Rev. Lett.*, 97:107202, 2006.

[98] Z. Wang and C. Holm. Structure and magnetic properties of polydisperse ferrofluids: a molecular dynamics study. *Phys. Rev. E*, 68:041401, 2003.

[99] J. P. Huang, Z. W. Wang, and C. Holm. Computer simulations of the structure of colloidal ferrofluids. *Phys. Rev. E*, 71:061203, 2005.

[100] G. Mériguet, M. Jardat, and P. Turq. Structural properties of charge-stabilized ferrofluids under a magnetic field: a brownian dynamics study. *J. Chem. Phys.*, 121:6078–6085, 2004.

[101] G. Mériguet, M. Jardat, and P. Turq. Brownian dynamics investigation of magnetization and birefringence relaxations in ferrofluids. *J. Chem. Phys.*, 123:144915, 2005.

[102] D. Levesque and J. J. Weis. Orientational and structural order in strongly interacting dipolar hard spheres. *Phys. Rev. E*, 49:5131–5140, 1994.

[103] All MC data have been done by Philip Camp in Chemistry at University of Edinburgh.

[104] P. N. Pusey. Colloidal suspensions. In *Liquids, Freezing and Glass Transition*. Les Houches Session LI, Volume II, Hansen, J.-P., Levesque. D., Zinn-Justin, J., Eds, North Holland, Amsterdam, 1991.

[105] G. A. van Ewijk, G. J. Vroege, B. W. M. Kuipers, and A. P. Philipse. Thermodynamic (in)stability of ferrofluid-polymer mixtures. *J. Magn. Magn. Mater.*, 252:32–34, 2002.

[106] Edinburgh Computer Data Facility (http://www.ecdf.ed.ac.uk).

[107] C. G. Gray and K. E. Gubbins. *Theory of Molecular Fluids, Vol. 1*. Oxford: Clarendon Press, 1984.

[108] C. Zannoni. *The Molecular Physics of Liquid Crystals*. Academic Press, London; New York, 1979.

[109] P. G. de Gennes. *The Physics of Liquid Crystal*. Clarendon Press, Oxford, 1974.

[110] R. Eppenga and D. Frenkel. Monte carlo study of the isotropic and nematic phases of infinitely thin hard platelets. *Molecular physics*, 52:no.6, 1303, 1984.

[111] J. P. Hansen and I. R. McDonald. *Theory of Simple Liquids*. Academic Press, New York, 1986.

[112] J. P. Boon and S. Yip. *Molecular Hydrodynamics*. Dover Publications, 1992.

[113] B. U. Felderhof and R. B. Jones. Orientational relaxation in a colloidal suspension of spheres. *Phys. Rev. E*, 48:1084–1090, 1993.

[114] P. N. Segré, O. P. Behrend, and P. N. Pusey. Short-time brownian motion in colloidal suspensions: experiment and simulation. *Phys. Rev. E*, 52:5070–5083, 1995.

[115] A. J. C. Ladd. Hydrodynamic transport coefficients of random dispersions of hard spheres. *J. Chem. Phys.*, 93:3484–3494, 1990.

[116] J. M. Tavares, J. J. Weis, and M. M. Telo da Gama. Strongly dipolar fluids at low densities compared to living polymers. *Phys. Rev. E*, 59:4388–4395, 1999.

[117] H. Tanaka and T. Araki. Simulation method of colloidal suspensions with hydrodynamic interactions: Fluid particle dynamics. *Phys. Rev. Lett.*, 85:1338–1341, 2000.

[118] A. J. Banchio and G. J. Nägele. Short-time transport properties in dense suspensions: from neutral to charge-stabilized colloidal spheres. *J. Chem. Phys.*, 128:104903, 2008.

[119] A. Satoh. Development of effective Stokesian Dynamics method for ferromagnetic colloidal dispersions (cluster-based Stokesian Dynamic method). *J. Coll. Interf. Sci.*, 255:98–106, 2002.

[120] The HPCx system (http://www.epcc.ed.ac.uk).

[121] A. O. Ivanov, S. S. Kantorovich, E. N. Reznikov, C. Holm, A. F. Pshenichnikov, A. V. Lebedev, V. Alexander, A. Chremos, and P. J. Camp. Magnetic properties of polydisperse ferrofluids: a critical comparison between experiment, theory, and computer simulation. *Phys. Rev. E*, 75:061405, 2007.

[122] C. Roland and M. Grant. Monte Carlo renormalization-group study of spinodal decomposition: Scaling and growth. *Phys. Rev. E*, 39:11971–11981, 1989.

[123] A. J. Wagner. *Theory and Applications of the Lattice Boltzmann Method*. PhD thesis, University of Oxford, 1997.

[124] W. Smith. A replicated data molecular dynamics strategy for the parallel Ewald sum. *Comp. Phys. Comm.*, 67:392–406, 1992.

Publications

E. Kim, K. Stratford, R. Adhikari and M. E. Cates. Arrest of fluid demixing by nanoparticles: a computer simulation study. *Langmuir*, **24**: 6549-6556, 2008.

E. Kim, K. Stratford, P. J. Camp and M. E. Cates. Hydrodynamic interactions in colloidal ferrofluids: A lattice Boltzmann study. *Journal of Physical Chemistry B*, **113**: 3681-3693, 2009.